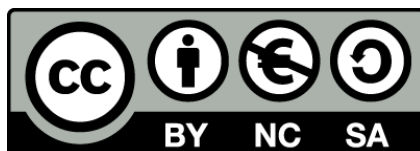




UNIVERSITAT<sub>DE</sub>  
BARCELONA

## Novel light management techniques for thin film solar cells: Nanotextured substrates and transparent conducting upconverters

Marta Llusçà Jané



Aquesta tesi doctoral està subjecta a la llicència **Reconeixement- NoComercial – Compartir Igual 4.0. Espanya de Creative Commons.**

Esta tesis doctoral está sujeta a la licencia **Reconocimiento - NoComercial – Compartir Igual 4.0. España de Creative Commons.**

This doctoral thesis is licensed under the **Creative Commons Attribution-NonCommercial-ShareAlike 4.0. Spain License.**



Universitat de Barcelona

DEPARTAMENT DE FÍSICA APLICADA I ÒPTICA

Av. Diagonal, 645, 08028 Barcelona

**Novel light management techniques for  
thin film solar cells: Nanotextured  
substrates and transparent conducting  
upconverters**

**Marta Llusçà Jané**

Memòria presentada per optar al grau de Doctor

Barcelona, Abril de 2015





DEPARTAMENT DE FÍSICA APLICADA I ÒPTICA

Av. Diagonal, 645, 08028 Barcelona

# Novel light management techniques for thin film solar cells: Nanotextured substrates and transparent conducting upconverters

Marta Llusçà Jané

Directors: Aldrin Antony; Joan Bertomeu i Balagueró;  
Programa de doctorat: Física

Memòria presentada per optar al grau de Doctor  
Barcelona, Abril de 2015



This work was also supported by the Ministerio de Ciencia e Innovación, the Ministerio de Economía y Competitividad and the European Regional Development Fund through projects CLASICO (ENE2007-67742-C04-03), AMIC (ENE2010-21384-C04-03), MICROSIL08 (PSE-120000-2008-1), INNDISOL (IPT-420000-2010-6) and the European Commission through project HELATHIS (Grant agreement no. 241378).



*Als meus pares, Marta i Jordi.*





# Contents

<b>Abstract</b>	<b>1</b>
<b>Resum</b>	<b>5</b>
<b>1 Introduction</b>	<b>9</b>
1.1 Renewable energy: state of the art . . . . .	9
1.2 An overview to the photovoltaic technology . . . . .	10
1.3 Thin film silicon solar cells . . . . .	11
1.3.1 Basic principle . . . . .	13
1.4 Transparent Conducting Oxides . . . . .	14
1.4.1 Transparent conducting ZnO . . . . .	15
1.4.1.1 Crystallographic Structure . . . . .	15
1.4.1.2 Electrical and optical properties . . . . .	16
1.4.1.3 Sputtered ZnO growth . . . . .	20
1.5 Strategies to improve energy conversion efficiency . . . . .	23
1.6 Aim and outlook of this thesis . . . . .	26
<b>2 Experimental details</b>	<b>29</b>
2.1 Deposition methods . . . . .	29
2.1.1 Magnetron sputtering . . . . .	29
2.1.1.1 Description of the equipment . . . . .	31
2.1.1.2 Targets and pellets . . . . .	32
2.1.2 Resistive thermal evaporation . . . . .	33
2.1.3 Electron beam evaporation (e-beam evaporation) . . . . .	34
2.1.4 Plasma enhanced chemical vapour deposition (PECVD) . . . . .	34
2.2 Post-deposition treatments . . . . .	36
2.2.1 Thermal annealing . . . . .	36
2.2.2 Chemical etching . . . . .	36
2.2.3 Laser treatment . . . . .	37

## Contents

2.3	Characterization techniques . . . . .	37
2.3.1	Thickness and morphology . . . . .	38
2.3.1.1	Stylus profilometer . . . . .	38
2.3.1.2	Confocal Microscope . . . . .	38
2.3.1.3	Atomic force microscopy (AFM) . . . . .	38
2.3.1.4	Scanning electron microscopy (SEM) . . . . .	39
2.3.2	Structural analysis . . . . .	40
2.3.2.1	X-ray diffraction (XRD) . . . . .	40
2.3.2.2	Transmission electron microscopy (TEM) . . . . .	42
2.3.3	Compositional analysis . . . . .	43
2.3.3.1	X-ray photoelectron spectroscopy (XPS) . . . . .	43
2.3.4	Optical characterization . . . . .	43
2.3.4.1	Spectrophotometer . . . . .	43
2.3.4.2	Photoluminescence (PL) . . . . .	44
2.3.5	Electrical characterization . . . . .	46
2.3.5.1	Four point probe . . . . .	46
2.3.5.2	Hall effect and Van der Paw method . . . . .	48
2.3.6	Device characterization . . . . .	49
2.3.6.1	Current-voltage characteristics . . . . .	49
2.3.6.2	Spectral response (SR) and external quantum efficiency (EQE) . . . . .	51
<b>3</b>	<b>Novel texturing methods for light confinement</b>	<b>53</b>
3.1	Introduction . . . . .	53
3.2	Laser texturing of front contacts . . . . .	57
3.2.1	Laser texturing: Optimization . . . . .	58
3.2.2	Laser-textured transparent and conducting AZO . . . . .	63
3.3	Nano-textured glass substrates . . . . .	67
3.3.1	Aluminum Induced Texturing (AIT) . . . . .	69
3.3.1.1	Description of the process . . . . .	70
3.3.1.2	Choice of glass substrates . . . . .	70
3.3.1.3	Preparation of the textured substrates . . . . .	71
3.3.1.4	Process optimization . . . . .	73
3.3.2	Growth of AZO on AIT substrates . . . . .	86
3.3.3	HCl texturing of AZO grown on AIT substrates . . . . .	102
3.3.4	Thin film silicon solar cells on AIT substrates . . . . .	106
3.3.4.1	a-Si:H solar cells fabricated at CIEMAT . . . . .	108

3.3.4.2	a-Si:H solar cells fabricated at UB . . . . .	114
3.3.4.3	a-Si:H/pm-Si:H tandem solar cells on AIT substrate . . . . .	118
3.4	Conclusions . . . . .	121
<b>4</b>	<b>Transparent conducting upconverters</b>	<b>123</b>
4.1	Fundamentals . . . . .	123
4.1.1	Spectral conversion . . . . .	123
4.1.2	Upconversion: Principles . . . . .	126
4.1.3	Rare earth ions . . . . .	128
4.1.4	Rare earth based upconverters for solar cells . . . . .	131
4.2	Results and discussion . . . . .	132
4.2.1	Initial trials . . . . .	133
4.2.2	Er- and Yb-doped ZnO thin films . . . . .	142
4.2.2.1	Structure and composition . . . . .	143
4.2.2.2	Optical and electrical properties . . . . .	147
4.2.3	Annealing methods on Er- and Yb-doped ZnO thin films . . . . .	154
4.2.3.1	Structure and composition . . . . .	156
4.2.3.2	Optical and electrical properties . . . . .	158
4.2.4	Laser annealing of Er- and Yb-doped ZnO thin films: Optimization . . . . .	164
4.2.5	Upconversion from transparent and conducting laser annealed ZnO:Er:Yb . . . . .	170
4.2.5.1	Morphology . . . . .	170
4.2.5.2	Structure . . . . .	171
4.2.5.3	Electrical and optical properties . . . . .	178
4.3	Conclusions . . . . .	182
<b>5</b>	<b>Conclusions</b>	<b>185</b>
	<b>Bibliography</b>	<b>193</b>
	<b>List of Symbols</b>	<b>217</b>
	<b>Curriculum Vitae</b>	<b>225</b>
	<b>Acknowledgements</b>	<b>231</b>



# Abstract

Photon management is a key factor in the development of efficient solar cells. A promising route to enhance the efficiency is to increase the photon absorption in the active layer. Higher photon absorption leads to the generation of more electron-hole pairs that would contribute to the solar cell performance. The objective of this work was to study two different light management approaches to enhance the efficiency of thin film Si solar cells. The first approach was to increase the effective path length of light by using nanotextures for light scattering and the second approach was to perform a spectral exploitation by changing the energy of the incident photons which were not absorbed other wise.

In the first approach the light path was manipulated by creating either periodic or random textured interfaces. Periodic patterns were created on the front AZO by means of direct laser ablation and amongst all the patterns assessed, the best equilibrium between haze and conductivity was achieved with a linear pattern of 10  $\mu\text{m}$  of pitch and 360 nm of groove depth that yielded to a  $R_s$  of 11  $\Omega/\text{sq}$  and a haze of 12.7% at 600 nm. However, the use of a single laser beam can not create pattern structures in the sub-micrometer range because the minimum period is limited by the laser spot dimension.

By means of the Aluminium Induced Texturing method (AIT) nanometric random textures were realised on glass substrates. In this method, a thin Al film is deposited onto a glass substrate and a redox reaction between the Al and the  $\text{SiO}_2$  of the glass is induced by high temperature annealing. The reaction products are wet-etched and the result is a uniform and rough glass surface. The process parameters such as the deposition method, the annealing time and temperature, the Al thickness and the etching conditions were varied in order to control the resultant glass roughness to achieve suitable morphologies for thin film Si solar cells. As it is an interface reaction, the most critical parameters were found to be the deposition method and the glass cleanness. The energy at which the Al

## Contents

particles reach the glass determine the adhesion and the compactness of the film which defines the degree of glass roughness. By using thermal evaporation it was possible to create morphologies based on smooth U-shaped craters (0.5 to 1  $\mu\text{m}$ ) and roughness ranging from 50 nm to 90 nm, whereas the sputtered films resulted in very rough and porous textures with  $\sigma_{rms}$  values up to 145 nm. AZO grown over the smooth U-shaped crater morphology led to a double texture with haze values above 10% at 600 nm, transparency above 84%, and  $R_s \sim 7 \Omega/\text{sq}$  whereas AZO over very rough glass resulted in a cauliflower-like surface with haze values  $>32\%$  at 600 nm,  $R_s$  around 9.5  $\Omega/\text{sq}$  and transmittance of 74%. To prove the suitability of these morphologies on solar cells, a-Si:H and a-Si:H/pm-Si:H tandem solar cells were fabricated on different AIT textures. An improvement of the short circuit current, as well as a reduction of the device reflectivity was achieved for all the AIT textures in comparison to the cells deposited on smooth glass textures.

The second approach was to create a transparent and conducting upconverter to be used on top of the rear reflector of a thin film Si solar cell. For that purpose, ZnO was doped with Er or codoped with Er and Yb ions and was post-annealed under different treatments. The unique spectral properties of rare earth (RE) elements due to their electronic configuration occur as a result of their intra 4f-4f shell transitions. In the case of Er, its excitation takes places at 1500 nm and 980 nm and the upconverted photons are emitted within the Si absorption range (410, 520, 550, 660 or 810 nm). Moreover, codoping with Yb can enhance the Er visible emission because they cooperate together due to the matching of their energy levels for  $\lambda=980$  nm. As deposited ZnO doped with RE was found to be transparent and conducting but not luminescent. In order to be optically active, the RE ions should be surrounded by 6 oxygen atoms in the form of a distorted octahedron to be optically active and REs replacing zinc in the ZnO lattice do not present this symmetry; hence, a post-deposition treatment is necessary. When the films were post-annealed in air, visible upconversion (UC) was seen at 660 nm under 980 nm laser excitation, however, the films become almost insulating. When the films were annealed in vacuum, lower UC luminescence was achieved, and the resistivity increased just 1 order of magnitude. By using CW laser radiation at the ablation limit of the material, the electrical properties were completely maintained and high UC was observed at 660, 560, 520 and 480 nm. UC lumines-

cence came from clusters of  $\text{REO}_6$  as well as from  $\text{RE}_2\text{O}_3$  inside or outside the matrix. The as-deposited films had a lack of oxygen which yielded to non luminescent samples. When annealing in air, in vacuum or by laser radiation, oxygen from the atmosphere bounded to the RE species which migrate from substitutional sites or from the grain boundaries to form RE oxides and/or  $\text{REO}_6$  complexes but only laser annealing was able to preserve the electrical properties while producing optically active centres.





# Resum

El control dels fotons és un component clau en el desenvolupament de cèl·lules solars eficients. Una via prometedora per millorar-ne l'eficiència és augmentar l'absorció de fotons en la capa activa. Com més fotons són absorbits, més alta és la probabilitat de crear parelles electró-forat i contribuir al rendiment de la cèl·lula solar.

L'objectiu d'aquesta tesi és la millora de l'eficiència de les cèl·lules solars de silici en capa prima mitjançant l'estudi de dos mètodes diferents per a l'aprofitament de la llum solar al dispositiu: texturant les interfícies per confinar la llum i emprant *upconverters* per convertir la llum incident que normalment és transmesa, en llum que serà absorbida.

En el primer mètode el camí òptic és manipulat mitjançant estructures periòdiques o aleatòries. Els patrons periòdics s'han creat al contacte frontal de ZnO:Al mitjançant ablació làser directa i amb un únic feix. Entre els diferents patrons que s'han provat, el millor equilibri entre el factor de dispersió i la conductivitat s'ha trobat per un patró lineal amb un període de  $10\ \mu\text{m}$  i una alçada de  $360\ \text{nm}$ . Els valors del factor de dispersió a  $600\ \text{nm}$  i de la resistència quadre ( $R_s$ ) han estat de  $12\%$  i  $11\ \Omega/\text{sq}$ , respectivament. Tot i així, emprar un únic feix làser no permet crear estructures nanomètriques òptimes per a cèl·lules solars de silici en capa prima, ja que el període del patró està limitat pel diàmetre del feix. En canvi, texturar aleatòriament el substrat de vidre a partir de la Texturització Induïda per Alumini (AIT), ha resultat funcionar molt millor. Aquest mètode es basa en una reacció de reducció no uniforme entre el vidre i una capa prima d'alumini gràcies a un tractament tèrmic. Posteriorment els productes de la reacció s'eliminen mitjançant un atac químic i el resultat és un vidre transparent i texturat. Els paràmetres del procés com el mètode de dipòsit, el temps i la temperatura del tractament tèrmic, el gruix de l'alumini i les condicions de l'àcid s'han variat per tal de controlar la rugositat final del vidre i crear textures adequades per a cèl·lules solars de silici en capa prima. S'ha trobat que com que la reacció té lloc a la

## Contents

interfície Al/vidre, els paràmetres més crítics són la neteja del substrat i el mètode de dipòsit. L'energia d'impacte de les partícules d'alumini contra el vidre determinen l'adhesió i la compacitat de la capa, que és el que al final defineix el grau de rugositat del vidre. Mitjançant evaporació tèrmica és possible crear morfologies basades en cràters en forma de "U" (0.5-1  $\mu\text{m}$ ) i rugositats que van des de 50 a 90 nm, mentre que les pel·lícules dipositades per polvorització catòdica produeixen textures poroses i molt rugoses amb valors de rugositat de fins a 145 nm. Les capes de ZnO:Al crescudes sobre la morfologia basada en cràters forma textures dobles amb factors de dispersió superiors al 10% a 600 nm, transmitàncies per sobre el 84% i  $R_s$  de 7  $\Omega/\text{sq}$ . D'altra banda, les capes de ZnO:Al crescudes sobre les textures molt rugoses resulten en superfícies amb morfologia en forma de coliflor amb factors de dispersió  $>32\%$  a 600 nm,  $R_s$  al voltant dels 9  $\Omega/\text{sq}$  i transmitàncies del 74%. Per comprovar que aquestes textures funcionen, s'han dipositat cèl·lules solars de a-Si:H i cèl·lules tandem de a-Si:H/pm-Si:H sobre diversos vidres texturats per AIT. En tots els casos sempre s'ha observat una millora en el corrent i una disminució en la reflectància del dispositiu comparat amb els dispositius fabricats sobre vidre pla.

El segon mètode estudiat és el fenomen de l'*upconversion* que consisteix en la conversió de fotons de baixa energia ( $E < E_g$ ), que normalment són transmesos, en fotons d'alta energia ( $E > E_g$ ) que podran ser absorbits en la zona activa; així doncs s'ha intentat fer una capa conductora, transparent i amb propietats d'*upconversion* per a substituir el ZnO:Al que normalment forma part del reflector posterior en una cèl·lula solar de silici en capa prima. Per aquest propòsit s'han estudiat capes d'òxid de zinc dopat amb erbi o co-dopades amb erbi i iterbi dipositades per polvorització catòdica magnetró sobre substrat de vidre. Les terres rares (RE) presenten unes propietats espectrals úniques degut que la seva configuració electrònica permet múltiples transicions dins de la capa 4f. En el cas de l'erbi, l'excitació esdevé a 1500 i 980 nm i els fotons convertits són emesos dins del rang d'absorció del silici (410, 520, 550, 660 or 810 nm). A més a més, co-dopar amb iterbi pot afavorir l'emissió visible de l'erbi perquè cooperen junts degut a la coincidència dels seus nivells energètics per  $\lambda=980$  nm. Les capes primes de ZnO:Er:Yb són conductores i transparents però no són luminescents. Les terres rares han d'estar envoltades de 6 àtoms d'oxigen formant un octaedre distorsionat per actuar com a centres òptics actius i si

es troben en posicions substitucionals dins de la matriu de ZnO no presenten aquesta simetria. Per aquest motiu les capes s'han sotmès a diferents tractaments tèrmics. Les capes escalfades en aire han mostrat ser fotoactives, ja que emeten a 660 nm en ser excitées amb 980 nm, però, en canvi, també deixen de ser conductores. Quan s'han escalfat en buit, també s'ha aconseguit *upconversion*, tot i que menys intensa, i la conductivitat ha disminuït només en un ordre de magnitud. Quan les capes s'han escalfat amb radiació làser just per sota el llindar d'ablació del material, aleshores s'ha aconseguit *upconversion* a 660, 560, 520 i 480 nm i les propietats elèctriques s'han mantingut invariables. L'*upconversion* prové dels centres òptics actius que es troben en complexos de REO<sub>6</sub> i en cristalls de RE<sub>2</sub>O<sub>3</sub>, tant a dins com fora de la matriu d'òxid de zinc. Les mostres sense tractament tèrmic posterior no tenen prou oxigen per formar centres òptics i per això és imprescindible que s'escalfin, o bé en aire, en buit o amb radiació làser. Gràcies a l'escalfament, l'oxigen de l'atmosfera forma enllaços amb les terres rares que migren de les seves posicions substitucionals o de les barreres de gra per formar REO<sub>6</sub> o RE<sub>2</sub>O<sub>3</sub>. Només la radiació làser és capaç de preservar la conductivitat i generar *upconversion*.



# 1 Introduction

## 1.1 Renewable energy: state of the art

World's energy demand is increasing under the pressure of growing population and due to advances in lifestyle of the emerging countries. In particular, electricity is an energy carrier that contributes significantly to improve the quality of life, and almost two thirds of the world's electricity is generated from fossil fuels. Apart from the fact that this source will be exhausted, it also causes harmful effects to the environment, thus, it is required to develop and expand other sources of electricity which are more sustainable.

In 2012, about 19% of the global energy consumption (power, heating and transport sectors) was provided by renewable energy. Of this total share, approximately 10% was supplied by modern renewable energy whereas the remaining 9% was coming from traditional biomass. Modern renewable energy makes reference to the energy coming from heat, that was 4.2%, from hydropower, that was 3.8%, and the power from wind, solar, geothermal, biomass, and biofuels accounted for approximately 2%.

The most significant growth occurred in the power sector (Fig. 1.1), with a global capacity of 1560 GW in 2013 that supposed an increase of more than 8% over 2012. Hydropower rose by 4% with a value of 1000 GW, while other renewables collectively grew nearly 17% to an estimated 560 GW. Globally, hydropower and solar photovoltaics (PV) accounted for about one-third of renewable power capacity, followed closely by wind power (29%). For the first time, more solar PV (39 GW) than wind power capacity was added worldwide [1].

Despite the fact that photovoltaics has enjoyed extraordinary growth during the last decade with overall growth rates above 50% per year, and a total PV electricity generation of 139 GW in 2013, it is still a small contributor to the worldwide energy consumption and a continuous improvement of the current solar cell technologies will be necessary in the

## 1 Introduction

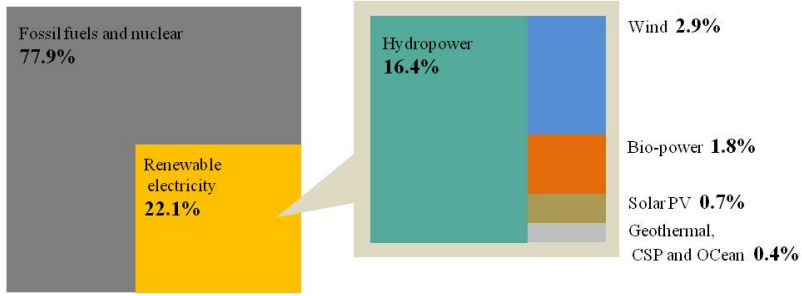


Figure 1.1: Renewable energy share of global electricity production in 2013 [1].

coming decades to become a more leading electricity provider [1].

### 1.2 An overview to the photovoltaic technology

The photovoltaic effect is the basic physical process through which a semi-conducting material converts light into electric current: a photon is absorbed just if its energy is higher than the band gap of the material ( $E_g$ ), then, its energy is transferred to an electron of an atom of the semiconductor device enabling it to escape from its normal position to become part of the current in an electrical circuit. Photovoltaic solar cells are semiconductor devices that operate by directly converting sunlight into electricity. Depending on the material, very different efficiencies can be obtained as well as very different manufacturing costs.

Nowadays, silicon wafer technology dominates the 85% of the photovoltaic market [2]. Silicon is non-toxic, cheap and the second most abundant element on the Earth's crust. The most developed Si PV technology is based on monocrystalline silicon (c-Si) with efficiencies as high as 25.6% for laboratory cells and 22.9% for commercial modules [3], even though, the main disadvantage is the high manufacturing cost associated with the silicon purification and growth of the single crystal wafers. On the other hand, polycrystalline silicon (p-Si) wafers are cheaper to manufacture, they are made from similar silicon material except that instead of being grown into a single crystal, they are melted and as the material cools it crystallizes randomly forming many different crystal sizes. The efficiency of

energy conversion is slightly lower, (20.4% in laboratory cells and 18.5% for modules [3]) but the manufacturing process is simpler.

An interesting alternative to silicon wafer technology, is the so-called second generation solar cells, based on thin film technology. This technology consists of the deposition of different semiconducting layers that permit to spend between 100 and 1000 times less material, as well as the use of large area substrates such as glass, flexible plastic or metal. In the current market, the dominating thin film technology is based on cadmium telluride (CdTe) followed closely by silicon thin film solar cells with a global capacity production of 2.1 GW and 2.0 GW, respectively. But even though CdTe modules present efficiencies as high as 17.5% [3], cadmium's toxicity and tellurium's low availability promote silicon-based thin films as the favourite candidate within this technology. There are two kinds of thin film silicon solar cells, hydrogenated amorphous silicon (a-Si:H) and microcrystalline silicon ( $\mu$ c-Si:H). The band gap of a-Si:H is 1.7-1.8 eV and has shown a record laboratory efficiency of 10.1% [3]. These solar cells are less than 1  $\mu$ m thick and present degradation problems under light exposure. On the other hand,  $\mu$ c-Si:H with a band gap of 1.1 eV has shown a record efficiency of 11% [3] and do not degrade. Further details are given in Sec. 1.3. Other semiconductor absorber materials that use thin film technology are GaAs, InP and CIGS among others. Though they present record efficiencies they are expensive to manufacture.

Currently, other cheap technologies are being developed trying to reduce the manufacturing costs by increasing efficiencies while maintaining the economic and environmental cost advantages of thin film deposition techniques and these are the third generation solar cells. Technologies associated with this generation include new materials such as polymers, perovskites, and also new concepts such as multijunction solar cells, up-and down-converters, nanostructured materials, light concentrator systems and hot carriers solar cells, etc. [4–6].

## 1.3 Thin film silicon solar cells

As mentioned in the last section, thin film silicon solar cells are divided into two categories depending on the structure of the material: amorphous silicon and microcrystalline silicon. The a-Si:H consist of a disordered network



## 1 Introduction

of Si-Si and Si-H bonds, whereas the  $\mu\text{c-Si:H}$  consists of silicon crystals of few nanometers in size, spread in an amorphous phase. These different materials present different optical and electronic properties, as well as different metastable behaviour. Amorphous silicon has a quasi-direct band gap of 1.7-1.8 eV which can thus absorb light until a maximum wavelength of 800 nm, but its absorption coefficient is fairly high in the short wavelength range allowing the use of very thin layers (400 nm). On the other hand,  $\mu\text{c-Si:H}$  with an indirect band gap of 1.1 eV leads to a higher absorption range up to 1100 nm. As a consequence of the indirect band gap the absorption of light generally requires a change in momentum by the absorption or emission of a phonon and hence the absorption coefficient is lower, and thicker layers are required (1.5  $\mu\text{m}$ ). Another important difference between these two materials is in their electrical properties. The high density of dangling bonds present in amorphous silicon leads to a poor conductivity and this is normally improved through hydrogen passivation. The drawback is that the passivated bonds degrade under illumination impacting in the solar cell efficiency which decreases with time. This type of degradation is known as Staebler-Wronski effect [7]. On the contrary, since only a small fraction of the microcrystalline silicon is in the amorphous phase, solar cells from this material do not suffer such degradation effect.

Another possibility is a tandem solar cell that is a combination of both a-Si:H and  $\mu\text{c-Si:H}$  [8]. This *micromorph* concept allows more efficient partitioning of the solar spectrum, the shortest wavelengths are absorbed by the top amorphous cell and the longer wavelengths are absorbed by the bottom microcrystalline cell. As a result, the efficiencies are higher than those made of single junctions. In this kind of structure, where the subcells are connected in series, the whole device performance is limited to the lowest generated photocurrent, moreover, the amorphous top cell needs to be thin enough to avoid light degradation.

In any case, it is necessary to improve the light trapping techniques in order to reduce the *i*-layer thickness and generate enough current to get higher efficiencies.

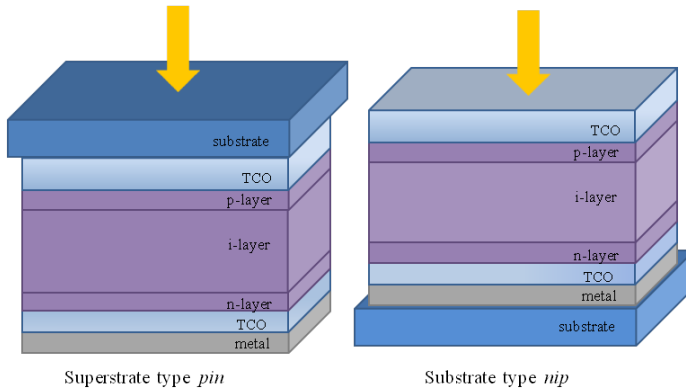


Figure 1.2: Schematic structure of a single junction silicon thin film solar cell in a) superstrate configuration ( $pin$ ) and b) substrate configuration ( $nip$ ).

### 1.3.1 Basic principle

Solar cells are optoelectronic devices that convert sunlight into electricity. Thin film silicon solar cells are composed of several thin semiconducting layers deposited on a substrate. A  $p$ -type (positively doped), an intrinsic (non-doped) and an  $n$ -type (negatively doped) Si layers are stacked together in order to create an internal electric field across the intrinsic region. When a photon strikes the device it will be absorbed if its energy is higher than the band gap of the material, then, it will excite an electron from the valence to the conduction band leaving a hole behind. The electron and hole pairs will be separated by means of the internal electric field and two electrodes will be used to collect them before they recombine.

Silicon thin film solar cells can have two different configurations depending on the order of growth of the layers involved: the  $pin$  structure called superstrate and the  $nip$  structure called the substrate configuration (see Fig. 1.2). In both cases the silicon layers are sandwiched between two conductive electrodes, the front electrode that needs to be transparent, and the back electrode that has to be highly reflective. Furthermore the  $p$ -layer is always located at the front side in order to make the holes travel shorter distances as they have lower mobility than electrons.

In case of  $pin$  solar cells, the light enters the device, first, through a

## 1 Introduction

transparent substrate (like glass) and then through the front electrode which is a transparent and conducting oxide (TCO). Commonly used materials are tin oxide doped with fluorine ( $\text{SnO}_2\text{:F}$ ) [9], and zinc oxide doped with aluminium ( $\text{ZnO:Al}$ , AZO) [10] or boron ( $\text{ZnO:B}$ , BZO) [11].

For *nip* solar cells, the light enters the device through the layers and the substrate does not need to be transparent. In such a case, indium tin oxide (ITO) is generally used as the front electrode. It is worth noting that when a TCO is deposited over a device some restrictions have to be taken into account given that the deposition conditions (like temperature or power) could damage the underlying layers.

In both structures the back contact consists of a reflective metal such as Al or Ag and another thin TCO placed between the metal and the *n*-type Si layer whose function is to enhance the reflectance of the non-absorbed light that reaches the back contact. Some of the important properties of TCOs are explained in the following section.

### 1.4 Transparent Conducting Oxides

Transparent and conducting oxides are a unique class of materials due to their high transparency in the solar spectra and high conductivity. These materials have found wide spread use in flat panel displays, photovoltaics and flexible electronics enabling in their role as transparent contacts. Commonly used TCOs such as  $\text{SnO}_2\text{:F}$  (FTO),  $\text{ZnO:Al}$  (AZO) and ITO are *n*-type degenerate semiconductors with a band gap higher than 3 eV and are doped up to carriers concentrations of  $n > 1.5 \times 10^{21} \text{ cm}^{-3}$  (50 to 100 times lower than the carrier concentration in metals). Because of their high mobilities of  $\mu < 100 \text{ cm}^2\text{V}^{-1}\text{s}^{-1}$ , TCOs exhibit resistivities as low as  $10^{-4} \Omega \text{ cm}$  [12].

As mentioned above, thin film solar cells require two transparent conducting oxide layers, the front TCO that acts as the front electrode and the back TCO as a part of the back side reflector.

The front TCO needs to be highly transparent, preferably more than 85% in the wavelength region where the photovoltaic absorber layers are active, sheet resistance lower than  $10 \Omega/\text{sq}$ , a low contact resistance with the *p*-type Si layer and an optimized surface morphology that could scatter the incoming light into the silicon absorber layer but free from sharp edges

that could cause shunting in the cell [13]. Besides, a textured front TCO will act as an efficient anti-reflecting coating due to the refractive index grading at the interface TCO/Si. The back TCO needs also to be transparent and conducting and it is mainly used to improve the back reflector optical properties and to act as a diffusion barrier [14].

Apart from the aforementioned requirements, the TCOs should possess chemical inertness to atomic hydrogen which is produced during the amorphous and microcrystalline silicon deposition processes using plasma enhanced chemical vapour deposition (PECVD). Moreover, thinking of large scale production, the material should also be non-toxic, abundant and possess low processing cost. Hence, taking into account these considerations, a potential candidate for transparent contacts in thin film solar cells is based on ZnO.

### 1.4.1 Transparent conducting ZnO

Zinc oxide doped with Al or B has been widely studied as an *n*-type transparent and conducting electrode for thin film solar cells due to its high transparency in the visible and near infrared region and low resistivity ( $<10^{-3} \Omega \text{ cm}$ ). Moreover it is easily dopable, resistant against hydrogen-rich atmospheres, easy to texture, low cost, abundant and non-toxic [15].

#### 1.4.1.1 Crystallographic Structure

Zinc oxide is an oxidic compound which occurs in nature as the mineral zincite. Though it normally shows a hexagonal wurtzite lattice, it can also be grown in zincblende or rocksalt structure [15]. The wurtzite crystal structure can be characterized by two lattice constants  $a$  and  $c$  and in the case of ZnO, they are  $a=0.3250 \text{ nm}$  and  $c=0.5207 \text{ nm}$  [16]. In the hexagonal unit cell which contains two ZnO molecules, zinc atoms are surrounded by oxygen atoms nearly in a tetrahedral configuration as shown in Fig. 1.3. The Zn-O distances in  $c$  direction are a little bit shorter than the distances to the other three oxygen atoms. The wurtzite crystal structure does not have inversion symmetry along the  $c$ -axis, so the  $(001)$  and  $(00\bar{1})$  planes are Zn or O terminated, respectively. The bonding in ZnO is largely ionic with the corresponding radii of  $0.074 \text{ nm}$  for  $\text{Zn}^{2+}$  and  $0.140 \text{ nm}$  for  $\text{O}^{2-}$ ; these polar bonds lead to planes of positively charged Zn or negatively

## 1 Introduction

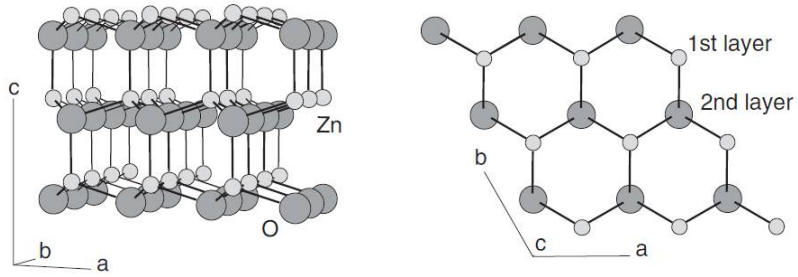


Figure 1.3: The hexagonal wurtzite structure of ZnO. Left: Perspective view perpendicular to the  $c$ -axis. Right view: View along the  $c$ -axis. reprinted from [18], with permission from Elsevier.

charged O perpendicular to the  $c$ -axis. This polarization of the atomic planes together with the absence of inversion symmetry gives rise to some unique properties of ZnO: piezoelectricity, spontaneous polarization and anisotropic etching behaviour [17].

### 1.4.1.2 Electrical and optical properties

#### Electrical properties

ZnO is a direct band gap semiconductor with a gap of 3.4 eV. The low lying valence bands ( $E-E_V \approx -8.5$  eV) belong to Zn 3d states and the upper valence bands (-5 to 0 eV) are composed of O 2p bonding levels. The lowest conduction bands are strongly localized at Zn 3s levels [17].

Stoichiometric ZnO is not a degenerately doped material and thus it is practically an insulator at room temperature. However it is relatively easy to raise the charge carrier concentration and get an  $n$ -type semiconductor by three different mechanisms, intrinsic, extrinsic or hydrogen doping.

Intrinsic doping makes reference to the lack of stoichiometry during the ZnO growth: oxygen vacancies or zinc interstitial lattice sites give rise to shallow donor states just below the conduction band. In other words, because some Zn to O bonds are missing, the resultant Zn to Zn bond is weaker and energies smaller than the band gap can excite electrons from the valence to the conduction band [17]. However, intrinsically doped ZnO

is not stable under ambient atmosphere because of the chemisorption of oxygen at the grain boundaries [19].

Extrinsic doping consists of introducing foreign elements to the lattice replacing Zn sites with ions of an additional valence electron in the outer shell. In the case of ZnO this can be generally done by using elements of group 13 such as  $B^{3+}$ ,  $Al^{3+}$ ,  $Ga^{3+}$  and  $In^{3+}$ , i.e. for zinc sites, leaving an additional weakly bond electron [20]. The binding energies of these electrons are in the range 50-65 meV and are much smaller than the energy required to excite an electron from the valence to the conduction band (3.4 eV).

Another possibility is the hydrogen doping that consists in the incorporation of hydrogen into the crystal lattice [15].

The electrical transport in polycrystalline TCOs is mainly limited by two mechanisms: the ionized impurity scattering and the scattering at the grain boundaries. The first scattering mechanism is caused by the ionized extrinsic dopants, therefore, the higher the carrier concentration, the lower the mobility. It has been reported by Ellmer *et al.* [18] that this is the predominant scattering mechanism if the carrier concentration is higher than  $10^{19} \text{ cm}^{-3}$ . The other scattering mechanism takes place at the grain boundaries. In polycrystalline ZnO the majority of defects are localized at the boundaries between the grains. These defects create intermediate states within the band gap that lead to traps for the free carriers inside the grains. In turn, a depletion or accumulation region for *n*-type or *p*-type materials, respectively, is formed. A charge carrier must overcome this potential barrier to take part in the material conduction [15, 18, 21].

### Optical properties

While considering the optical spectrum of transparent conducting oxides, (Fig. 1.4 a), three regimes can be distinguished, the ultraviolet (UV), the visible (VIS) and the near-infrared (NIR) part. The first one makes reference to the region below the band gap of the material, thus, for  $\lambda < 400$  nm. In this region the incoming photons with energies higher than the band gap are strongly absorbed by the electrons to transit between the valence and the conduction band [17].

## 1 Introduction

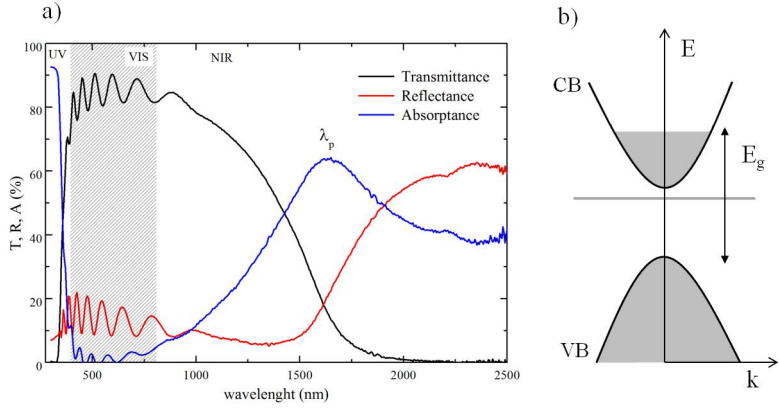


Figure 1.4: a) Optical spectra and b) Schematic electronic structure of a typical transparent conducting oxide. Shaded areas denote occupied states.

For a film with thickness ( $d$ ), reflectance ( $R$ ) and total transmittance ( $T$ ), the absorption coefficient ( $\alpha$ ) of the film can be expressed by the Eq. 1.1 [22]:

$$T = \frac{(1 - R)^2 \exp(-\alpha d)}{1 - R^2 \exp(-\alpha d)} \quad (1.1)$$

In the case of a strongly absorbing medium (where the product  $\alpha d$  is very large), one can neglect the second term in the denominator and  $\alpha$  can be extracted from Eq. 1.2:

$$T \approx (1 - R)^2 \exp(-\alpha d) \quad (1.2)$$

Moreover, for direct transitions, as in the case of ZnO, the absorption coefficient can be deduced from Eq. 1.3 [22]:

$$\alpha h\nu = B(h\nu - E_g)^{1/2} \quad (1.3)$$

where  $h\nu$  is the incident photon energy,  $E_g$  is the band gap energy and  $B$  is a constant. The optical band gap energies of the films can be deduced from the Tauc plot of  $(\alpha h\nu)^2$  against  $h\nu$  by extrapolating to zero the linear portion of the  $(\alpha h\nu)^2$  curve.

Burstein [23] and Moss [24] observed that increasing the carrier density in a semiconductor leads to a shift in the absorption edge to smaller wavelengths and they explained that this increase in the band gap was due to fully occupied energy states in the conduction band and, according to Pauli's exclusion principle, new states must be at higher unoccupied energies. Fig. 1.4 b) exhibits a schematic electronic structure of a doped semiconductor with fully occupied states in the lower energies of the conduction band.

The second regime (VIS) comprises the wavelength range 400-1000 nm, in this range the photon energy is too low and the TCO is transparent. In addition, oscillations in the optical spectra appear due to constructive and destructive interferences that arise from the reflectance at both flat surfaces air/TCO and TCO/glass. These interference fringes disappear in the case of randomly textured surfaces.

The third regime (NIR) is the region where  $\lambda > 1000$  nm. As seen in Fig. 1.4 a) the transmittance decreases and the reflectance increases, this effect is due to the absorption by the free carriers which is described by the Drude model [25]. At frequencies below the plasma frequency ( $\omega_p$ ) of the free electron gas the incident light is reflected. The plasma frequency can be expressed as:

$$\omega_p = \sqrt{\frac{nq_e^2}{\varepsilon\varepsilon_0m^*}} \quad (1.4)$$

where,  $\varepsilon$  is the relative permittivity of the TCO,  $\varepsilon_0$  is the permittivity of free space,  $m^*$  is the effective mass of an electron in the semiconductor material,  $q_e$  the fundamental charge of an electron and  $n$  is the charge carrier density. Each frequency can be converted into wavelength using  $\lambda = 2\pi c/\omega$ , where  $c$  is the speed of light. At very high electron densities the transparency can even decrease in the visible range [17].

To summarize, from the optical point of view, there are positive and negative things in doping ZnO: the optical band gap increases which allows more ultraviolet light to be transmitted but the plasma frequency shifts to higher wavelengths which increases the free carrier absorption for longer visible and near infrared wavelengths.

## Luminescence of ZnO



## 1 Introduction

Photoluminescence in ZnO thin films consists of an intense UV peak followed by a visible broadband luminescence [26–30]. The UV peak is assigned to the band-to-band excitonic recombination (also called excitonic band) and the visible wide band is related to defects within the band gap [26–33]. The shape and position of this visible band depend on the defect state populations. For instance, if the emission is green is mostly associated with oxygen vacants [30]. However, some authors assign it to zinc interstitials [34]. When the emission is yellow, orange and red, it is associated to an excess of oxygen [30, 35], oxygen interstitials [36–38] or zinc vacancies [35]. But orange-red emission is less common than green and yellow emissions [29]. These different behaviours on the ZnO luminescence results from the different preparation methods and post-annealing treatments employed, but, overall, most authors coincide that green emission is associated to oxygen vacancies and orange-red emission to an oxygen excess. Chen *et al.* also demonstrated that upon post-annealing in O<sub>2</sub>, the green band changed into the yellow band and the yellow band into the orange-red one [39].

### 1.4.1.3 Sputtered ZnO growth

ZnO thin films can be prepared by a variety of techniques such as magnetron sputtering, chemical vapour deposition, spray pyrolysis and molecular beam epitaxy, etc., but sputtering has been reported to be the best method concerning high conductivity and transparency [40]. Moreover sputtered ZnO thin films present a very smooth surface. When sputtered ZnO is doped with Al in order to be used as the front contact of a solar cell, then HCl etching is used to texture the films. Within this work all the ZnO-based thin films have been deposited by means of magnetron sputtering. The working principle and the equipment characteristics are explained in Chapter 2, Sec.2.1.1. This section explains some of the processes that take place during film growth as well as a model connecting the electrical and optical properties of sputtered ZnO thin films to the growth conditions and a study on the hydrochloric acid (HCl) etching behaviour of rf sputtered ZnO:Al films.

The energy at which the particles reach the substrate is the most

important quantity to characterize the growth process [41]. Sputtered atoms and clusters travel from the target to the substrate, first across the plasma and then across the vacuum. During their path they might collide deviating their direction and decreasing their energy. If the particles have low kinetic energy, they can diffuse along the substrate surface until the lowest energy site to which to bond. But if they have high kinetic energy, they will get implanted into the growing film without diffusion. Moreover the high energy particles could end up with the re-sputtering of the growing film. Another process that can occur during the growth is the formation of big clusters that might create shadowed areas that will decrease the growth rate. In addition, desorption processes can also take place from the growing surface if the particles have enough energy. All these mechanisms depend strongly on the substrate temperature, the working pressure, the power, the dopant concentration and the film thickness (deposition time) [41].

### Modified Thornton model

Kluth *et al.* [42] adapted the Thornton model [43] to magnetron sputtered ZnO films. The Thornton model consists of three different growth zones (Zone 1, 2 and 3) as a function of the ratio between the substrate temperature and the melting point of the material, and the pressure during deposition. Kluth *et al.* [42] exchanged the temperature ratio into the substrate temperature and the pressure with the temperature axis and Zone 3 was not considered. Moreover the modified model, includes a study on the HCl etching behaviour of rf sputtered ZnO:Al films on glass substrates.

According to Thornton's initial model, higher compactness is achieved with higher substrate temperature and lower pressure. Zone 1 consists of relatively loosely packed material. When the substrate temperature is low, the absorbed atoms do not have enough mobility so crystallites grow according to the incident sputter flux and voids are formed between grains. As pressure is increased, the mobility of the adatoms is further decreased and even at higher temperatures the result is still the same loosely packed material of Zone 1.

Zone 2 is characterized for having large columnar grains, shadowing is negligible and recrystallization may occur. In this zone, higher mobilities

## 1 Introduction

can be achieved ought to the larger grain sizes. Zone T is the transition area between Zone 1 and 2.

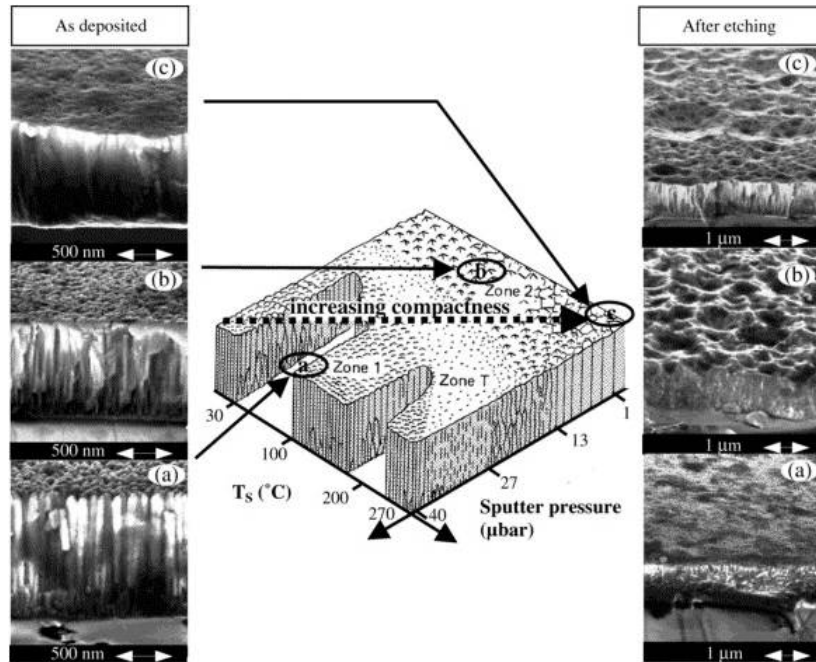


Figure 1.5: Modified Thornton model for the growth of sputtered ZnO:Al layers. Reprinted from Thin Solid Films [42], with permission from Elsevier.

Fig. 1.5 represents the modified Thornton model by Kluth *et al.*, with an extension to the etching behaviour. Three types of morphologies can be distinguished depending on the growth conditions (a, b and c). The etch to morphology (a) leads to surfaces with very similar appearance to unetched ZnO:Al, and etching morphologies (b) and (c) result in crater formations with large opening angles, the difference between (b) and (c) is the crater surface coverage, in type (b) the surfaces are homogeneously covered whereas type (c) is just partly covered [42].

## 1.5 Strategies to improve energy conversion efficiency

Shockley and Queisser developed a detailed balanced model based on the calculation of the maximum theoretical efficiency of a single junction solar cell [44]. It is called the Shockley-Queisser (SQ) limit and was calculated by examining the electrical energy extracted per incident photon considering just one semiconductor material under non-concentrated sunlight. The limit assumes that all photons with energies greater than the band gap are completely absorbed, that the sun and the cell act as ideal black bodies with temperatures of 6000 K and 300 K, respectively, that the only recombination loss is radiative and that carriers have infinite mobility.

The limit gives maximum solar energy conversion efficiency around 30% for a single  $p$ - $n$  junction with a band gap of 1.1 eV. That means that from all the power contained in the sunlight that strikes this cell (about 1000 W/m<sup>2</sup>), only 30% could be converted into electricity [44].

Despite the detailed balance method, real-world devices experience other unavoidable losses that limit solar cells performance. Fig. 1.6 presents a scheme on the major loss processes that limit the efficiency in single-junction solar cells [45].

The most significant loss mechanisms are thermalization losses (process 1) and non-absorbed photons (process 2). When the cell absorbs a photon with energy significantly higher than its band gap, the excess energy is dissipated as heat by thermalization of the electron and hole to the edges of the conduction and valence bands. This process is considerable in solar cells with small band gaps. In process 2, photons with energies lower than the band gap of the semiconductor are not absorbed and cannot generate electron-hole pairs, thus, these photons are not involved in the energy conversion process. This transmission losses contribute more for wide band gap solar cells [46]. Both of these losses (1 and 2) are thus related to the spectral mismatch of the energy distribution of photons in the solar spectrum and the band gap of the semiconductor material. The losses are around 23% due to thermalization and 33% due to spectral mismatch, which means that more than half of the incident solar energy is not exploited by the cell [47].

## 1 Introduction

Slighter loss mechanisms are related to collection losses, because not all charge carriers that are generated in a solar cell are collected at the electrodes. Process 3 shows recombination losses which include radiative, Auger or Shockley-Read-Hall recombination. The carriers recombine in the bulk, at the interfaces, and/or at the surfaces of the junction. This loss process can be minimized through maintaining high minority carrier lifetimes in the semiconductor material. Other losses are represented by processes 4 and 5 and make reference to the junction and contact voltage losses. These ones can be relatively small [45].

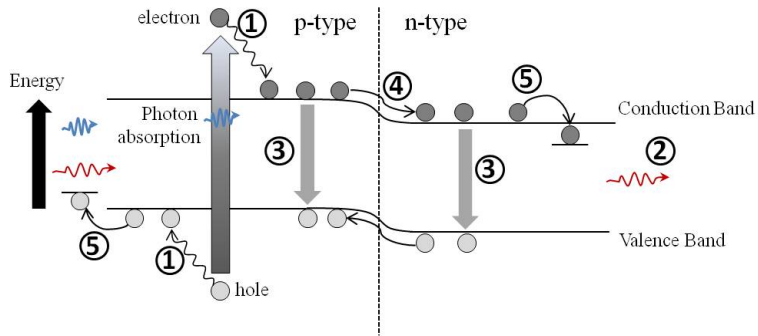


Figure 1.6: Loss processes in a standard solar cell: (1) lattice thermalisation loss, (2) non-absorbed below band gap photons, (3) recombination loss, (4) and (5) junction and contact voltage losses [45].

Several approaches have been suggested to overcome mainly processes 1 and 2. For example using multiple energy levels like in the case of tandem solar cells [48], or by spectral conversion of the sunlight, which consists in the absorbance of photons from the incident solar spectrum and the re-emission at energies more suitable for the solar cell [5, 6].

Also thermal approaches have been done, in which the incident spectrum is allowed to heat up carriers or other particles in the absorber, from which the energy will be extracted. Among all these strategies just tandem solar cells have demonstrated notable improvements in efficiency in comparison to single junction solar cells, and theoretical studies have been done by Green that described an upper efficiency limit ranging from 30% to 68.2% for one and for infinite number of band gaps, respectively, under uncon-

## 1.5 Strategies to improve energy conversion efficiency

concentrated sunlight [4]. Moreover the application of up and downconversion mechanisms are predicted to exceed the SQ limit [5, 6].

Different types of spectral conversion can be distinguished: when two or more sub band gap photons produce a higher energy photon it is called upconversion [6] when one high energy photon is transformed into one lower energy photon is called downshifting and when it is transformed in two lower energy photons it is a downconversion process [6]. Research on spectral conversion is focused in quantum dots, organic dyes, transition metal ion systems and rare earth ions [46]. Upconversion attracts a lot of attention because it uses photons that are normally transmitted through the solar cell to produce photons that may be absorbed.

In the case of thin film silicon solar cells, when the thickness of the absorber layer is made very thin, the path length of light inside the solar cell needs to be increased to get absorbed. This fact demands either light scattering interfaces or the multiple light pass within the device. Commonly, in thin film silicon solar cells the most used light confinement strategies are the use of highly reflective back contacts and to texture the substrate or the layers that form the cell. In that case, the refractive index varies progressively and the reflection losses are decreased. Moreover, light trapping is caused by the scattering at the different interfaces and the net result is an increased optical path for the incident light [49].

In the case of thin film solar cells with *pin* configuration (superstrate structure), the most commonly method for light trapping is to texture the front TCO and this is normally done by means of the deposition method or through chemical etching after the deposition of the front TCO. One of the most common used substrates is Asahi-U that consists of a glass covered with a rough layer of  $\text{SnO}_2:\text{F}$  grown by chemical vapour deposition at atmospheric pressure (APCVD). Other alternatives are to use ZnO based front TCOs, where the surface roughness of the TCO films can be achieved by the deposition process, such as ZnO:B grown by Low Pressure Chemical Vapour Deposition (LPCVD) [11] or by HCl etching of sputtered ZnO:Al [10]. In the *nip* configuration (substrate structure), the TCO can be textured over the smooth reflector or can be deposited over nanotextured rough metallic surfaces (typically Ag) which can be obtained by sputtering at high substrate temperature [50–52].

Another option is to texture the substrate. In the case of a glass sub-

## 1 Introduction

strate it can be textured by dipping in HF or using stamping processes in which the glass is heated at high temperature and a mold is pressed over it with the desired texture [53]. And for plastic substrates, a texture can be achieved by etching with oxygen plasma [54] or by the hot-embossing of the polymeric substrates using desired master textures [55].

### 1.6 Aim and outlook of this thesis

The objective of the present work was to study different light management strategies to enhance the efficiency of thin film silicon solar cells.

The first approach was to manipulate the light path within the cell by creating periodic or random textured surfaces. The periodic structures were created at the front AZO through laser ablation and the random textures were performed on the glass substrate by means of the Aluminium Induced Texturing method (AIT).

The second approach was to convert the incoming photons to photons that match better the Si absorption spectrum and this was done using upconversion mechanisms. The aim was to create a transparent and conducting upconverter to be used as the TCO of the back reflector of a Si thin film solar cell. ZnO:Er:Yb thin film has been optimized for that purpose.

The thesis is structured in 5 chapters. This first chapter is an introduction to the fundamental knowledge required to understand the results. Then, in Chapter 2, the experimental details of the equipments and characterisation tools are explained, Chapters 3 and 4 contain all the results and finally, Chapter 5 summarizes the conclusions.

In particular, Chapter 3 deals with the aforementioned approach on creating light trapping structures. After an introduction on light trapping schemes, a very brief study based on periodically textured ZnO:Al is presented. These periodic structures have been achieved by means of laser ablation at Centro Láser UPM of Madrid. Next, a detailed research work is presented on the AIT method, first, an accurate optimization of the process is exposed, then, ZnO:Al is grown over some of the optimized textures and finally the feasibility of this textures on solar cells is presented; a-Si:H solar cells have been grown at the research centre CIEMAT and at UB, and a-Si:H/pm-Si:H tandem solar cells have been deposited at *Laboratoire de Physique des Interfaces et des Couches Minces* at the *École Polytechnique*

in Palaiseau, France.

Chapter 4, presents the second approach: a study of ZnO doped with rare earth ions as a transparent and conducting upconverter. After an introduction on the basics of upconversion, the first experiments on sputtered ZnO:Er are exposed, and according to these first results in which it is found that an annealing treatment is required to achieve upconversion, the next sections are based on a comparison between different annealing methods performed on a thick ZnO:Er:Yb film. These methods include air annealing, vacuum annealing and also laser annealing. Specifically, the last part of this chapter includes an optimization of the laser annealing process in order to achieve upconversion without damaging the film. All the laser annealing experiments have been performed at Centro Láser UPM of Madrid and the luminescence characterization of the samples have been done by the group of Electro-Photonics Division of the Micro- and Nanoscopies and Nanotechnologies for Electronic and Photonic Devices (MIND) of the Electronics Department of the UB.





## 2 Experimental details

In this chapter, the deposition methods, post-deposition treatments and characterization techniques that have been employed along this thesis, are described. Sec. 2.1 focuses on the deposition methods and brings special attention to the magnetron sputtering technique that was widely used for the two different research topics of this thesis: to deposit the Al films and ZnO:Al transparent contacts of Chapter 3 and to deposit all the rare earth-doped ZnO films of Chapter 4. In Sec. 2.2 the post-deposition treatments are just briefly explained because further details are given within the corresponding chapters and in Sec. 2.3 the characterization tools employed to study the morphology, structure, optical and electrical properties are enumerated and briefly described.

### 2.1 Deposition methods

This section starts with the magnetron sputtering, where the working principle, the equipment characteristics and the description of all the targets and pellets that have been employed, are presented. In the next subsections other deposition techniques such as the resistive thermal evaporation, the electron beam evaporation and the different PECVD reactors used to grow the solar cells, are explained.

#### 2.1.1 Magnetron sputtering

Sputtering is the release of particles from a surface induced by the bombardment of high energy ions. The target surface is eroded by the arriving ions via momentum exchange, and the surface material is ejected in the form of neutral particles; either as individual atoms, clusters of atoms or molecules. The ions are generated by a radio-frequency (rf) or direct current (dc) glow discharge in a noble gas atmosphere (normally Ar) between a cathode (the target) and an anode (substrate and chamber walls).

## 2 Experimental details

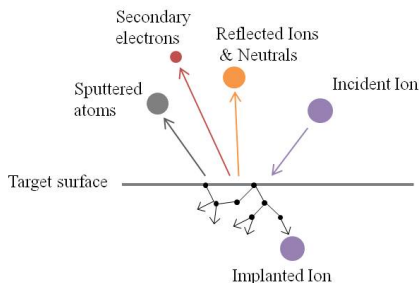


Figure 2.1: Processes occurring at the target surface due to the impact of high energy particles [18].

The positively charged Ar ions are accelerated towards the cathode and, if they have energy greater than the surface binding energy, target atoms are ejected in vapour phase and deposited on a substrate to form a film. The sputtering atmosphere consists of a mixture of ions, electrons and neutral gas atoms. The energy at which the Ar atoms impact on the target surface is in the order of 100 eV and it leads to a collision cascade within the target surface which ends up in the emission of target atoms (mostly neutral atoms) at energies of few electronvolts [18]. A scheme on the processes occurring at the target surface is depicted in Fig.2.1.

The properties of the ejected material depend on the atomic mass, kinetic energy and angle of the impinging ions as well as on the target material. An important parameter of the sputtering process is the sputtering yield, which is the average number of atoms ejected from the target per incident ion. The sputtering yield for an oxidized target is smaller than that of a metallic target.

Magnetron sputtering uses magnets behind the cathode that cause travelling electrons to spiral along the magnetic field lines, thus, a higher amount of collisions take place and the ionization process is enhanced, as a result, higher deposition rates are achieved [56]. The magnetic field strength is adjusted in such a way that just the electrons are influenced by the magnetic field but not the Ar ions. The magnetic field confines the electrons in helical orbits in front of the target yielding in very high

ionization efficiency.

### 2.1.1.1 Description of the equipment

The confocal magnetron sputtering was a commercially available *ATC-ORION 8 HV* from *AJA International, Inc.* The system was placed in a clean room ISO 7 (10000 class) and it consisted of a single chamber of 34.7 cm of diameter and 39.8 cm of height equipped with 3 magnetron guns tilted  $3^\circ$  off normal directed to the rotating substrate.

The chamber could reach a base vacuum as low as  $1 \times 10^{-5}$  Pa by using a turbo molecular pump ( $500 \text{ l s}^{-1}$ ) backed by a dry primary pump, and Ar and  $\text{O}_2$  could be introduced and controlled by two different mass flow controllers limited to 20 sccm. During the sputtering process, the pressure was regulated by a three position gate valve and a capacitance manometer was used to measure the pressure.

The system could handle substrates of sizes up to  $10 \times 10 \text{ cm}^2$  that could be heated up to  $850^\circ\text{C}$  by 3 halogen lamps placed behind the holder plate. The motorized substrate holder could rotate till 20 rpm and the target to substrate distance could be adjusted between 11.7 and 18 cm. The magnetron sputtering guns hosted targets of 7.62 cm (3 inch) in diameter that were protected by metallic chimneys and flip-top shutters. Either rf (300 or 600 W) with poles changing at a frequency of 13.56 MHz or dc (750 W) adjustable power sources could be applied to the cathodes. The magnets were placed underneath the target over a magnetic field return plate and were subjected in a Cu backing plate which is water cooled (see Fig. 2.2). 18 magnets were placed tracing the target perimeter oriented with the north pole touching the magnetic plate, and one magnet was placed in the center oriented in the other direction. Between the magnets and the target there was a very thin Cu mesh to improve the heat conduction.

For conductive targets (like Al), a constant dc voltage can be applied because when the positively charged ions strike the surface the resulting charges can move freely throughout the material preventing any charge build up. On the other hand, for insulating targets (like ZnO), the conduction bands will not allow free charge movement, the charge will remain localized and over time it will build up causing arcing or even a plasma

## 2 Experimental details

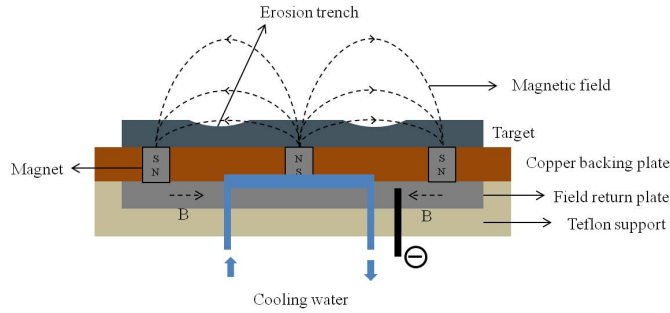


Figure 2.2: Schematic cross section of the magnetron sputtering gun.

stop. Alternating the electric field, like in rf, makes the electrons to be drawn at the cathode neutralising the charged ions. A high frequency is used so that the heavy ions cannot follow the switching fast enough and only electrons hit the surface to neutralize charge, the rf voltage can be coupled through any kind of impedance so that targets do not need to be conductors [56].

With steady state dc power (no oscillations), there is no need for impedance matching but for rf, impedance matching is very important to provide the best power transfer from the generator to the plasma chamber. In this equipment an *MC2* automatic impedance matching network from *Seren* is used in conjunction with the rf power supply.

To avoid the time consuming process of cleaning the chamber walls, ultra high vacuum aluminium foil from *All Foils, Inc.* was used to cover the walls and was periodically changed. The chimneys and the substrate holder were cleaned by sand blasting after several depositions or while changing the target material. After the sand blasting they were rinsed with isopropanol and heated in an oven at temperatures above 100°C. The process conditions for every set of samples are detailed in the corresponding chapters.

### 2.1.1.2 Targets and pellets

Table 2.1 summarizes all the targets and pellets that have been used to deposit the different films by magnetron sputtering. In Chapter 3, the

Table 2.1: Targets and pellets classified by chapters. Chapter 3: Al films as a part of the Aluminium Induced Texturing method to texture glass substrates and AZO films as front TCOs over the textured surfaces. Chapter 4: Targets and pellets used to create transparent and conducting upconverters.

Chapter	Material	Purity	Size	Supplier
Chapter 3	ZnO:Al <sub>2</sub> O <sub>3</sub> (98:2 wt)	99.99%	3"×0.25"	Neyco
	Al	99.999%	3"×0.25"	AJA
Chapter 4	ZnO	99.999%	3"×0.25"	Neyco
	ZnO:Er <sub>2</sub> O <sub>3</sub> :Yb <sub>2</sub> O <sub>3</sub> (89:1.2:9.8 wt)	99.99%	3"×0.25"	Neyco
	Er <sub>2</sub> O <sub>3</sub> (pellets)	99.99%	0.5"×0.1"	Alfa Aesar
	Yb <sub>2</sub> O <sub>3</sub> (pellets)	99.99%	0.5"×0.1"	Alfa Aesar

targets were used to deposit the Al films as a part of the Aluminium Induced Texturing method and the AZO films as front TCOs. In Chapter 4, the objective was to grow ZnO:Er or ZnO:Er:Yb thin films. For that purpose, pellets were used to dope the ZnO films. The doping content was adjusted by placing one or more pellets on the erosion area of the target surface as shown in Fig. 2.3 and once the layer's composition was optimized, custom-made single targets with the respective compositions were procured.

The pellets were fabricated by pressing Er<sub>2</sub>O<sub>3</sub> or Yb<sub>2</sub>O<sub>3</sub> powder with a force of 4 Ton during 10 min by means of a manual hydraulic press and were subsequently annealed at 800°C during 4 h under an oxygen gas atmosphere.

### 2.1.2 Resistive thermal evaporation

In resistive thermal evaporation the source material is heated in vacuum until it starts evaporating by means of an electrical current passing through a filament (the resistance) where the material is placed. Al rods 99.99% pure and 2 mm of diameter were placed into tungsten helical filaments and were heated above the Al melting point of 660°C. The evaporated atoms were transported through a vacuum of  $5 \times 10^{-3}$  Pa to get deposited on the substrate that was at 15.5 cm above the filament. Quartz crystal thickness monitor *Leybold XTM/2 Inficon* was used to control the thickness during

## 2 Experimental details

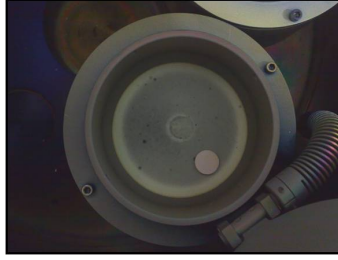


Figure 2.3: Top view of the ZnO target with the Er<sub>2</sub>O<sub>3</sub> pellet placed on the erosion area.

deposition. A thermal evaporation equipment (*Veeco VE-400*) was used for the deposition of the Al layers, either as a part of the back reflector of *pin* type solar cells or over glass substrates as part of the AIT process mentioned in Chapter 3.

### 2.1.3 Electron beam evaporation (e-beam evaporation)

E-beam evaporation is a process whereby a source material is heated in vacuum by a beam of electrons above its sublimation temperature causing it to evaporate. A filament placed below the crucible that contains the source material is heated by applying a large voltage. Thus, electrons are drawn from the filament and focused on the source material using bending magnets.

A *PFEIFFER Vacuum Classic 500* e-beam evaporator was used to deposit the Al films on Borofloat glass substrates. The deposition pressure and the applied filament voltage were  $5 \times 10^{-3}$  Pa and 10 kV respectively and the Al films were grown at a deposition rate of 13 nm/min. The thickness was measured through a quartz crystal microbalance. More details on the process are explained in Chapter 3.

### 2.1.4 Plasma enhanced chemical vapour deposition (PECVD)

PECVD is the most commonly used technique for the deposition of hydrogenated amorphous and microcrystalline silicon thin film solar cells. It

is a glow discharge technique in which a plasma of the reactive gases is created between two parallel discharge plates at an excitation frequency of usually 13.56 MHz. The gas molecules dissociate under the influence of the plasma, they react to form the film material and deposit themselves on the substrate.

Amorphous silicon solar cells with *pin* configuration were fabricated at CIEMAT in Madrid where a conventional RF-PECVD (13.56 MHz) reactor from *MV Systems Inc.* with two separate chambers was used to grow the films. The structure consisted of 7.5 nm *p*-type a-SiC:H, 5 nm carbon-graded buffer layer, 400 nm thick intrinsic absorber and 30 nm of *n*-type a-Si:H layer. Further details on the preparation conditions, as well as on the optoelectronic and structural characteristics of the different a-Si:H alloys used are described elsewhere [57].

Amorphous silicon solar cells were also fabricated at UB using a multi-chamber PECVD reactor from *Elettrovava*. The equipment consists of two chambers for PECVD and a loading and transfer chamber. To avoid dopant contamination, *p*- and *n*- type silicon were deposited in one chamber, while the other chamber was used solely for intrinsic silicon deposition. Silane was used as the precursor gas for silicon deposition and trimethylborane and phosphine were introduced for *p*- and *n*-type doping in silicon, respectively. More information about the growth of thin film solar cells by means of PECVD can be found elsewhere [13]. The deposition was performed at a temperature of 200°C with a power density of 40 mW/cm<sup>2</sup> and the thickness of *p*-, *i*- and *n*- type layers were ~15, ~200 and ~15 nm respectively. In some of the cells, where ZnO:Al front contacts were used, a microcrystalline *p*-type film of ~25 nm was introduced between the front contact and the *pin* a-Si:H solar cell in order to minimize the potential barrier that appears because of the band gap differences between the ZnO:Al and the a-Si *p*-type film. More details on the deposition conditions are explained in Chapter 3.

Amorphous silicon/polymorphous silicon (a-Si:H/pm-Si:H) tandem solar cells were deposited at the *Laboratoire de Physique des Interfaces et des Couches Minces* from the École Polytechnique in Palaiseau, France. The reactor was a home-made conventional RF-PECVD with a mono chamber cluster configuration. Every layer (*p*-, *i*- or *n*-type) was fabricated in a different plasma box inside the same chamber. Details on the reactor can be found elsewhere [58]. The tandem cell consisted of a top cell of a-Si:H



## 2 Experimental details

with a  $p$ -type  $\mu\text{c-SiO}_x$  layer, 65 nm thick intrinsic a-Si:H layer and a  $n$ -type  $\mu\text{c-SiO}_x$  film, and then, a bottom pm-Si:H cell made also with a thin  $p$ -type  $\mu\text{c-SiO}_x$  layer, a pm-Si intrinsic layer of 500 nm and a  $n$ -type  $\mu\text{c-SiO}_x$  film. The whole tandem solar cell was deposited at a temperature of 150°C and all the layers were grown at pressures in the range 266-293 Pa except the  $i$ -type a-Si that was grown at 21 Pa. The cells were finished with a back contact of 0.126 cm<sup>2</sup> that consist of 80 nm of AZO and 300 nm of sputtered Ag. Information on the properties of pm-Si:solar cells can be found elsewhere [59].

## 2.2 Post-deposition treatments

In this section the equipments used for the post-deposition treatments are briefly explained: the first subsection comments on the different ovens that have been used for the thermal annealings, the second one, points out the chemical etching processes, and the last subsection enumerates in a table the lasers that have been employed, classified by chapters and with their main features.

### 2.2.1 Thermal annealing

Depending on the size of the sample to post-anneal, two different ovens were used. In the case of samples larger than 2×5 cm<sup>2</sup> a *Thermo Scientific M110* muffle furnace with a chamber of 9 l and capable to reach 1100°C was employed, whereas for smaller samples a tubular quartz furnace with a diameter of 2.6 cm and a maximum annealing temperature of 800°C was used. The vacuum annealing treatments were performed in a PCVD reactor capable of annealing up to 1000°C, the temperature was controlled by a pyrometer and the vacuum pressure was kept at 2×10<sup>-4</sup> Pa.

### 2.2.2 Chemical etching

Different acid solutions have been employed for different purposes. Orthophosphoric acid (H<sub>3</sub>PO<sub>4</sub>) 85% and hydrofluoric acid (HF) 40% provided by *Panreac Quimica S.L.U.* have been used as a part of the AIT process. More details on the etching procedure are given in Chapter 3.

## 2.3 Characterization techniques

Hydrochloric acid (HCl) 37% also from *Panreac Quimica S.L.U.* was used to roughen the relatively flat as-deposited ZnO layers by magnetron sputtering in order to introduce light trapping features. The etching rate of the solution depends on the quality of the layer, etchant, concentration and temperature [15]. HCl of 0.5 wt.%, 1 wt.% and 2 wt.% was used at room temperature to texture ZnO:Al layers. Samples were dipped during different times in the solution and were quickly rinsed with deionised water and dried with nitrogen.

### 2.2.3 Laser treatment

All laser treatments were performed at *Centro Láser UPM* of Madrid. In Chapter 3 the objective was to use laser radiation to ablate the AZO surface and create a periodically textured transparent conducting oxide. In Chapter 4 the lasers were used to anneal the rare earth doped ZnO films.

The lasers used are summarized in the following table and classified by chapters:

Table 2.2: Lasers used for the sample treatments and their characteristics classified by chapters. In Chapter 3 the laser was used to texture the ZnO:Al films and in Chapter 4 it was employed to annealed the rare earth doped ZnO samples.

Chapter	Laser commercial name	Laser characteristics
Chapter 3	<i>Spectra Physics HIPPO</i>	DPSS Nd:YVO <sub>4</sub> <b>355 nm</b> Average Power: 5 W @ 50 kHz Pulse duration :15 ns Pulse frequency:15-300 kHz Scanner head
Chapter 4	<i>Spectra Physics Millennia</i>	DPSS Nd:YVO <sub>4</sub> <b>532 nm CW</b> Power:15 W Scanner head, XYZ stages

## 2.3 Characterization techniques

In this section the equipments and techniques used to evaluate the morphology, the structure, the composition and the optical and electrical properties of the samples are explained.

### 2.3.1 Thickness and morphology

#### 2.3.1.1 Stylus profilometer

In the stylus profilometer a diamond tip scans in contact-mode the sample surface following its morphology, and a position transducer converts the tip movements into height values producing surface profiles. A surface profiler (*Dektak 3030*, *Veeco*) equipped with a  $25\ \mu\text{m}$  diameter stylus was used to determine the thickness of the Al films of Chapter 3. The vertical resolution of the equipment was of 1 nm and the associated error was of  $\pm 10$  nm, which was the standard deviation of a set of measures taken at the same point. To measure the thickness a step was created by removing a piece of *Kapton*® tape that was placed on the substrate prior to deposit the Al film.

#### 2.3.1.2 Confocal Microscope

A confocal microscope uses point illumination and a pinhole aperture before the detector to eliminate out-of-focus light. Light from above and below the plane of focus of the object is eliminated from the final image, thus the reconstruction of the 3D image is achieved by scanning series of optical slices from different focus levels in the specimen. In this thesis a *SENSOFAR Plμ 2300* confocal microscope equipped with two *EPI* objectives  $20\times$  and  $150\times$  with optical resolution of  $0.35\ \mu\text{m}$  and  $0.14\ \mu\text{m}$ , respectively, have been used either to study the topography or to determine the thickness of all the transparent films. To create the steps in the TCO films a lift-off technique combining ink marker and isopropanol was employed. The confocal microscope technique could not be used for measuring the Al thickness because the reflection difference between the substrate and the Al film made the detector saturate.

#### 2.3.1.3 Atomic force microscopy (AFM)

AFM is a widely used technique for surface characterization at a nanometric scale. A tip is scanned across the sample surface whereas a laser light incident on the back of the cantilever is deflected differently as the surface features change; this deflection is measured using a photodiode [60]. From the resultant topographic maps it is possible to obtain parameters

that give information about the vertical and lateral sizes of the grains or structures that form the surface that enable to compare quantitatively the different sample surfaces. One of the most used parameters is the root mean square roughness ( $\sigma_{rms}$ ), that gives information about the vertical features and is defined as:

$$\sigma_{rms} = \sqrt{\frac{1}{N} \sum_{i=1}^N (z_i)^2} \quad (2.1)$$

where  $N$  is the total number of data points and  $z_i$  is the vertical distance from the average line of the  $i^{th}$  data point.

However the  $\sigma_{rms}$  makes no distinction between peaks and valleys and does not account for the lateral distribution of surface features. A more complete description is provided by the Power Spectral Density (PSD) of the surface topography. It is obtained from the Fast Fourier Transform of the images and performs a decomposition of the surface profile into its spatial wavelengths and allows the comparison of roughness measurements over different spatial frequency ranges.

The atomic force microscope images were taken using a *Pacific Instruments* system and the software for data analysis was *XEI 1.7.3* of *Psia Inc* from which the  $\sigma_{rms}$  and the PSD values were obtained.

### 2.3.1.4 Scanning electron microscopy (SEM)

SEM consists in focussing an electron beam on a sample and forming an image from the detected scattered electrons. From the interaction between the electron beam and the atoms of the sample's surface, various signals can be produced such as X-rays, cathodoluminescence and secondary and backscattered electrons. From these signals it is possible to get information about the sample's topography, composition and structure. In particular, secondary electrons produce the SEM topography images. Typically areas ranging from 1 cm to 5 microns in width can be imaged by scanning the sample surface with magnifications from  $20\times$  to  $30,000\times$  and spatial resolutions between 50 to 100 nm. Insulating samples have to be covered with thin layers of carbon or gold to avoid the surface to get charged [61].

The images presented in this work were taken using a *NOVA NANOSEM 230* from *FEI Electron Microscopes* taken at the Nanotechnology Platform

## 2 Experimental details

of the Institute for Bioengineering of Catalonia (IBEC). The microscope is an ultra-high resolution SEM which enables both high and very low kV imaging and enables a resolution of 1 nm at 15 kV. Images at different magnifications were taken to study the sample's roughness in Chapter 3.

### 2.3.2 Structural analysis

#### 2.3.2.1 X-ray diffraction (XRD)

XRD is a nondestructive analytical technique to study the crystal structure of solids. The principle consists of illuminating the sample by a beam of X-rays at a known wavelength ( $\lambda$ ) and angle ( $\theta$ ) of inclination and measure the diffracted angles of the scattered beam. The atoms cause the incident beam to diffract and when the Bragg's law is fulfilled Eq. 2.2, constructive interferences are formed and an intensity peak can be measured.

$$2d \sin \theta = m\lambda \quad (2.2)$$

where  $d$  is the distance between lattice planes and  $m$  is the diffraction order.

In this study, the diffractometer used was a *PANalytical X'pert PRO MRD Alpha1* used in Bragg-Brentano geometry ( $\theta - 2\theta$  scans) and all the scans were made using Cu  $K_{\alpha 1}$  radiation ( $\lambda=1.5406 \text{ \AA}$ ). While scanning through different angles, peaks in the diffraction pattern appear when Bragg's condition is verified and from the intensity, position and widths of those peaks, a whole range of information such as structure, orientation, crystallite size and stresses can be deduced. Experimentally determined data are usually compared with the Joint Committee on Powder Diffraction Standards (JCPDS) data base. For ZnO, card No 36-1451, for Er<sub>2</sub>O<sub>3</sub>, card No 08-0050 and for Yb<sub>2</sub>O<sub>3</sub>, card No 41-1106 are used.

From the intensity of the peaks, the relative contribution of the different crystallographic orientations can be estimated and from the peak's position the lattice constants can be identified: from Eq. 2.2 the interplanar spacing  $d$  and the reflecting planes (hkl) can be deduced. When a hexagonal crystal system is observed, such in the case of ZnO, the lattice parameters  $a$  and  $c$  can be calculated following Eq. 2.3. Along this work, the main diffracted peak measured for the sputtered ZnO based samples corresponded to (002) planes, where  $h=0$ ,  $k=0$  and  $l=2$  but other crystallographic orientations

could also be observed corresponding to (100) or (101), etc. The lattice parameter values could be obtained from the following equation:

$$\frac{1}{d^2} = \frac{4}{3} \left( \frac{h^2 + hk + k^2}{a^2} \right) + \frac{l^2}{c^2} \quad (2.3)$$

for (002),

$$c = 2d \quad (2.4)$$

and for (100),

$$a = \frac{2}{\sqrt{3}}d \quad (2.5)$$

By comparing the lattice parameter values to the standard undoped ZnO (JCPDS card No 36-1451) it is possible to obtain information on the crystal lattice deformation and determine if the lattice suffers from a compressive or tensile stress.

The width of the peaks is characterized by the full width at half maximum (FWHM) and smaller FWHM values indicate better film quality. The crystallite size ( $D$ ) and microstrain ( $e$ ) can be deduced from the peak's profile fitting by using the single-line approach method [62]: a diffraction line is conceived as a convolution of a Gaussian and a Lorentzian profile (i.e. as a Voigt function), where the Gaussian component is due to microstrain and the Lorentzian component is due to finite crystallite size. The crystallite size  $D$  (volume-weighted domain size in the direction perpendicular to the reflecting lattice planes) and the width of the microstrain distribution  $e$  in the diffracting volume can be estimated according to Eq. 2.6 and Eq. 2.7 respectively:

$$\beta_L = \frac{\lambda}{D \cos \theta} \quad (2.6)$$

$$\beta_G = 4e \tan \theta \quad (2.7)$$

where  $\lambda$  is the X-ray wavelength,  $2\theta$  is the Bragg angle of reflection,  $\beta_L$  is the breadth of the Lorentzian component and  $\beta_G$  is the breadth of the Gaussian component.  $\beta_L$  and  $\beta_G$  were directly obtained by XRD peak profile fitting with *WinPLOTR* [63] software.

The crystallite sizes should not be considered as absolute values since XRD is sensitive to any crystallographic defects including extrinsic and

## 2 Experimental details

intrinsic dopants. Hence, in this work the crystallite sizes will be treated as a simple indicator of the crystal quality to compare within series.

### 2.3.2.2 Transmission electron microscopy (TEM)

TEM is a microscopy technique that images the electrons transmitted through an ultra-thin layer.

The technique consists of accelerating electrons to nearly the speed of light towards the sample. When an electron beam passes through the ultra-thin material, electrons are scattered, then a system of electromagnetic lenses focuses the scattered electrons into a magnified and high resolution image [64].

In order to obtain very thin layers of TCO material for cross section imaging, two different preparation methods have been employed. One option is to glue two pieces of the sample head to head to obtain a "sandwich" (with the layers in the center and the glass substrate on each side). Then the "sandwich" is mechanically polished until the stack is 30  $\mu\text{m}$  thick and finally is slimmed with an ion bombardment system. This bombardment was done through an Ion Milling  $\text{Ar}^+$  at low temperature in order to avoid the recrystallization as well as changes in the microstructure. More information on the samples preparation can be found elsewhere [65]. Another option is to use a Focused Ion Beam (FIB) to create the electro-transparent cross-section sample. A FIB system uses a finely focused beam of Ga ions that employed at high beam current can be used for milling. A thin layer of Au is placed over the area of interest to prevent charging effects in the SEM, and then, a specific area of the sample is selected. This chosen area is coated with a metal film (Pt) to protect the surface during ion milling. Once the milling has been performed all around the chosen area, a lift-out technique with an Omniprobe is used to extract the ultra thin lamella from the sample. A final step using bombarding with Ar plasma is required to achieve a clean and electro-transparent sample. The FIB system used in this work was a FEI Strata 235 Dual Beam System.

TEM micrographs were obtained with a microscope *JEOL J-2100*. The microstructural study as well as the analysis of the electron diffraction patterns were performed with the *Digital Micrograph* and *Diffpack* software.

### 2.3.3 Compositional analysis

#### 2.3.3.1 X-ray photoelectron spectroscopy (XPS)

XPS is used to determine the quantitative atomic composition and the chemical state of the measured material. The process works by irradiating the sample with monochromatic X-rays, and counting the emitted photo-electrons whose energies are characteristic of the elements within the sampling volume.

The kinetic energy (KE) of the emitted electrons is given by:

$$KE = h\nu - BE - \Phi_{sp} \quad (2.8)$$

where  $h\nu$  is the energy of the photon, BE is the binding energy of the atomic orbital from which the electron originates and  $\Phi_{sp}$  is the spectrometer work function. Thus, by measuring the KE of the photoelectrons, the equation above can be used to translate this energy into BE of the electrons [66].

XPS analysis was performed using a *PHI 5500 Multitechnique System* (from *Physical Electronics*) with a monochromatic X-ray source (Al  $K\alpha$  line, with an energy of 1486.6 eV and at a power of 350 W) placed perpendicular to the analyzer axis and calibrated using the  $3d_{5/2}$  line of Ag with a full-width at half-maximum (FWHM) of 0.8 eV. XPS spectra were recorded after sputtering the sample surface with an  $Ar^+$  ion source (4 keV energy). The composition was calculated from the integrated peak areas of the spectra and a Shirley background subtraction was carried out before proceeding to analyze the chemical composition of the films. The position of the Ar 2p peak that appeared after sputtering the surface was used to correct any eventual shift due to charge effects. The *Multipak*, *IGOR pro* from *Wavemetrics, Inc* and *Origin 8.0* softwares were used to treat the resulting data.

### 2.3.4 Optical characterization

#### 2.3.4.1 Spectrophotometer

The optical properties of the samples such as total transmittance ( $T$ ), diffused transmittance ( $T_d$ ) and total reflectance ( $R$ ) were measured with a *PerkinElmer Lambda 950* spectrophotometer equipped with a 150 mm



## 2 Experimental details

integrating sphere. The system used a double illumination source consisting of a deuterium lamp for the UV interval and a halogen lamp for the VIS/IR region. For  $T$  measurements, the sample was placed in front of the integrating sphere and a *Spectralon*® white diffuse reflectance standard (99%) was set on the opposite side of the sphere in order to reflect the direct transmitted beam and accounted in the  $T$  measurement. For  $T_d$  measurements, the sample was also placed in front of the integrating sphere but instead of a reflector, a black absorber was used to exclude the directly transmitted beam. For reflection measurements, the sample was placed at the rear side of the integrating sphere, hence, only light reflected back from the sample was counted. Depending on the role of the thin film within a solar cell, the samples were oriented with the incident light facing the glass side or facing the film: for front TCOs the light entered through the glass but for rear TCOs the light passed first through the thin film side. The system was able to measure the transmitted or reflected light within the range 250 and 2500 nm.

The absorbance ( $A$ ) is deduced by using the  $T$  and  $R$  spectra according to equation:

$$A(\lambda) = 1 - T(\lambda) - R(\lambda) \quad (2.9)$$

and the haze ( $H$ ), that is often used to characterize light scattering properties of the TCOs, is defined as the quotient between  $T_d$  and  $T$ :

$$H = \frac{T_d(\lambda)}{T(\lambda)} \quad (2.10)$$

### 2.3.4.2 Photoluminescence (PL)

PL makes reference to any emission of light that results from optical stimulation. In PL technique, light is directed onto a sample, where it is absorbed by atoms or molecules imparting excess energy in a process called photo-excitation. This excitation causes electrons within the material to move into permissible excited states: a transition from the ground state to an excited state of an atom or molecule, or from the valence band to the conduction band in semiconductor crystals. When these electrons return to their equilibrium states, the excess energy is released through non-radiative (phonons) and/or radiative processes (light). This emitted

light is detected as photoluminescence, and the spectral dependence of its intensity is analysed to provide information about the optical and electrical properties of the material. To study the photoluminescent properties of the rare earth based films of Chapter 4, two kinds of PL measurements were performed, low temperature PL that was measured at the Scientific and Technological Centers (CCiT) and upconversion PL that was done at the home-made set-up of the Electronics Department at UB.

### Low temperature photoluminescence (LT PL)

LT PL measurements are often used to obtain a more accurate spectroscopic information thanks to the minimization of thermally activated non-radiative recombination processes and thermal line broadening. At LT carriers are effectively frozen, so it is possible to see more clearly lowest energy states. Moreover at room temperature (RT) carriers can thermally escape to higher energy levels and have enough energy to get to non-radiative recombination centres, then a reduction of the PL intensity could be expected as shown in Fig. 2.4.

Conventional photoluminescence (PL) spectra were acquired by a *LabRam* spectrometer from *Horiba Yvon* with a high sensitive Charge Coupled Device (CCD). An UV objective of 15 $\times$  magnification and long working distance (15 $\times$  NUV-LWD) was used to focus the film surface. A 325 nm line of a He-Cd laser (*Kimmon IK Series*) was used to excite the sample which was kept inside a *Linkam* cryostat chamber at -196 $^{\circ}$ C. Fig. 2.5 shows the schematic of the set-up used to measure conventional LT PL. For short wavelengths detection ( $\lambda < 700$  nm) the Beam Splitter UV (BSUV) filter and the Colour filter were removed and replaced by the long pass filter. The position of the filters is also shown in Fig. 2.5.

### Upconversion photoluminescence (UC PL)

The UC PL measurements were performed using an *EKSPLA PG122* optic parametric oscillator (OPO) with an output range of 420-2300 nm, and was pumped by the third harmonic of a Brilliant 5-ns-pulsed Nd:YAG laser (the peak power density was  $\sim 109$  W/cm $^2$  for a spot diameter onto the sample of 100  $\mu$ m). The OPO output was selected as 980 nm in order

## 2 Experimental details

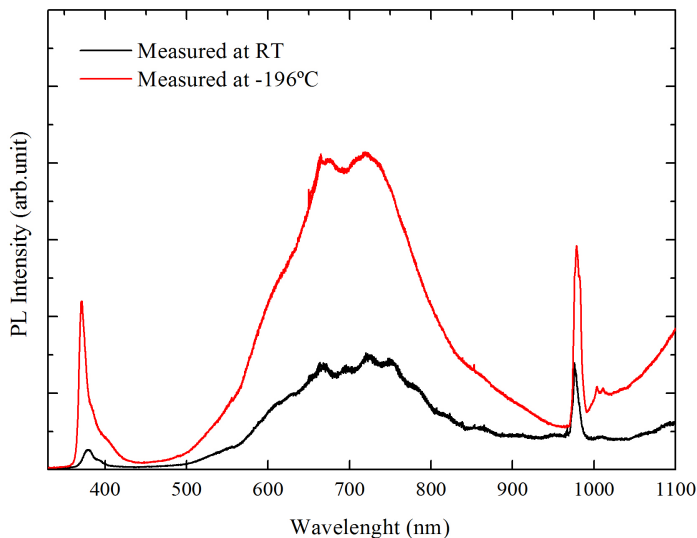


Figure 2.4: Comparison in photoluminescence of ZnO:Er:Yb measured at RT and at LT (-196°C). Excitation source: 325 nm.

to excite the  $4I_{11/2}$  and  $2F_{5/2}$  levels of  $Er^{3+}$  and  $Yb^{3+}$  ions. The resulting luminescence spectra obtained in the visible range were acquired using a GaAs photomultiplier Tube (PMT). The excited PL study was carried out tuning the OPO output in the range from 950 to 1200 nm, while monitoring the 660 nm emission line of Er with a monochromator, corresponding to the transition of the upconverted energy level. The schematic of the home-made set-up is shown in Fig. 2.6.

### 2.3.5 Electrical characterization

#### 2.3.5.1 Four point probe

The resistivity of the films was obtained by using a four point probe system *JANDEL RM3*. The system consisted of four equally spaced tungsten carbide tips, and passing a current ( $I$ ) through the two outer probes and

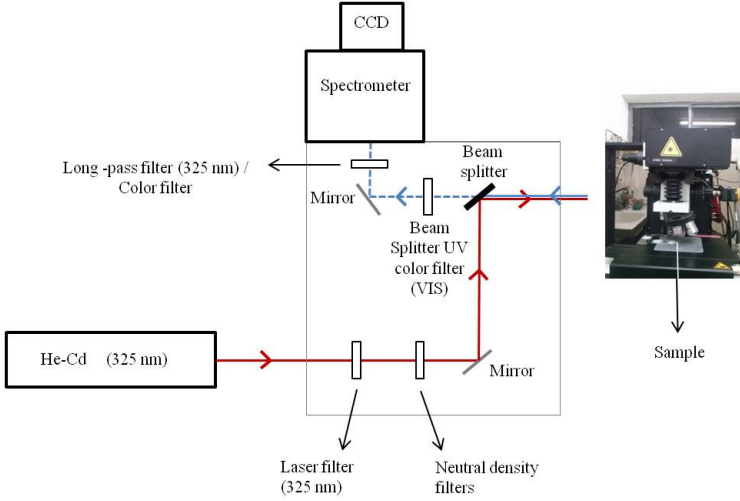


Figure 2.5: Schematic of the set-up used to measure the LT PL of the samples, excitation source: 325 nm. For short wavelengths detection ( $\lambda < 700$  nm) the BSUV filter and the Color filter were replaced by the long pass filter.

measuring the voltage ( $V$ ) through the inner probes permit the measurement of the film resistivity. The current could be modulated between 10 mA and  $1 \mu\text{A}$  that allowed to measure samples with sheet resistances ( $R_s$ ) between 1 and  $10^7 \Omega/\text{sq}$ .

From the applied current and measured voltage, the sheet resistance can be calculated following Eq. 2.11 [67]:

$$R_s = \frac{V}{I} \frac{\pi}{\ln 2} \quad (2.11)$$

And the resistivity is obtained from the product between the sheet resistance and the film thickness:

$$\rho = R_s \times d \quad (2.12)$$

To assess the quality of the transparent and conducting films, several figures of merit combining optical transparency and electrical performance can be used. In this work the figures of merit ( $\Phi$ ) has been calculated according to G. Haacke [68] using:

## 2 Experimental details

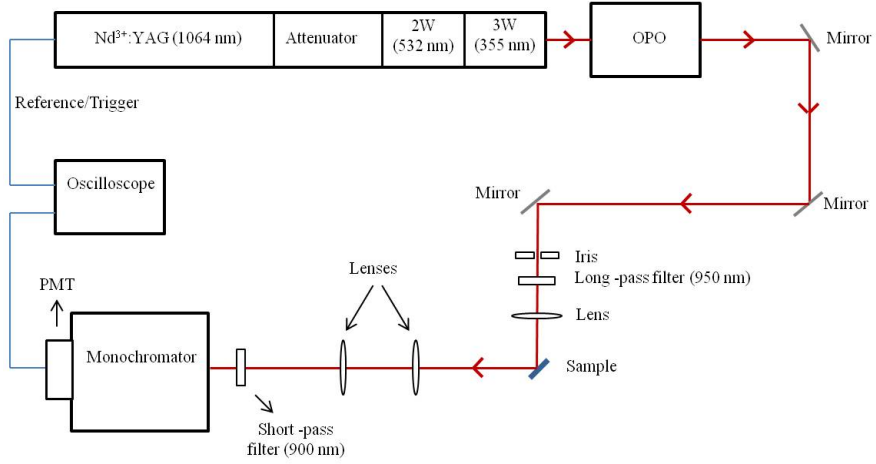


Figure 2.6: Schematic of the set-up used to measure the UC PL of the samples. Excitation source: 980 nm.

$$\Phi = \frac{T^{10}}{Rs} \quad (2.13)$$

where here  $T$  is the integrated optical transmittance in a specific range. Higher values of  $\Phi$  means better performance.

### 2.3.5.2 Hall effect and Van der Paw method

The measurement of the Hall effect in a semiconductor material permits to have additional information about its electrical properties. It permits to determine whether the conduction in the material is due to  $n$ - or  $p$ -type carriers, apart from the mobility ( $\mu$ ), carrier concentration ( $n$ ) and the resistivity ( $\rho$ ) values. The Hall effect consists in the appearance of a voltage difference when a magnetic field ( $B$ ) is applied perpendicular to the electrical current that flows in a conductor. This magnetic field induces the Lorentz force that acts on the charge carriers deviating their trajectory and thus creating an electric field that leads to a voltage difference, the Hall voltage ( $V_H$ ):

$$V_H = \frac{IB}{nq_e d} \quad (2.14)$$

where  $I$  denotes the current through the sample,  $B$  the magnetic field to which the sample is exposed,  $n$  the free carrier concentration,  $q_e$  the elementary charge and  $d$  the thickness of the layer.

The Van der Paw configuration enables to measure the Hall effect of a sample of any arbitrary shape [69], it consists of 4 small electrodes placed symmetrically in the perimeter of a thin sample with uniform thickness  $d$ . By using this configuration it is possible to determine the resistivity as explained in [69] as well as the free carrier concentration from Eq. 2.14, and the mobility from Eq. 2.15.

$$\mu = \frac{1}{q_e n \rho} \quad (2.15)$$

In this work the samples were cut into  $0.5 \times 0.5$  cm<sup>2</sup> sizes and small electrical contacts of *Cerasolzer 186* alloy were soldered at the edges by means of an ultrasonic soldering system (*MBR Electronics USS-9210*). The samples were placed in a magnetic field of 0.3 T generated by parallel coils and the selected current intensity was always the lowest one which ensured measuring the Hall voltage difference with three significant digits.

### 2.3.6 Device characterization

#### 2.3.6.1 Current-voltage characteristics

Solar cells were characterized by means of  $J$ - $V$  measurements where the current density ( $J$ ) was measured as a function of the applied voltage ( $V$ ) while the cell was kept under illumination at a known power density ( $P_0$ ). A typical  $J$ - $V$  curve of a solar cell is shown in Fig. 2.7.

From the measured  $J$ - $V$  curve, other values that are used to characterize the cells can be deduced: the short circuit current density ( $J_{sc}$ ) is the current density across the device when the voltage is zero, the open circuit voltage ( $V_{oc}$ ) is the potential difference when no current is drawn between the terminals, the fill factor ( $FF$ ) is the ratio between the maximum power that a cell can generate to the product of  $V_{oc}$  and  $J_{sc}$ .

## 2 Experimental details

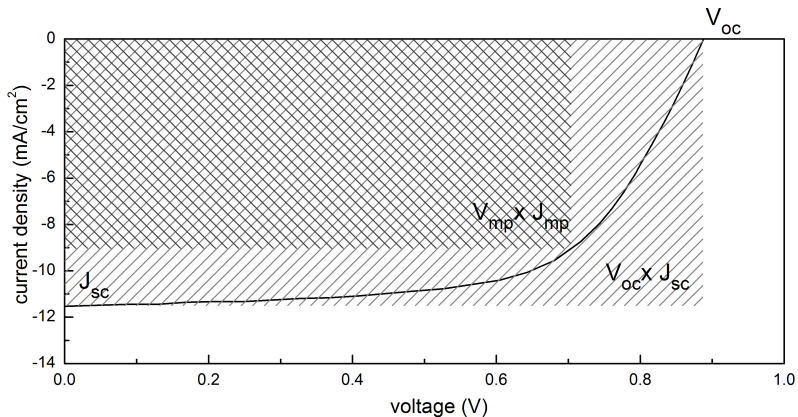


Figure 2.7: Typical  $J$ - $V$  curve of solar cell under illumination [70].

$$FF = \frac{V_{mp} \times J_{mp}}{V_{oc} \times J_{sc}} \quad (2.16)$$

and the conversion efficiency ( $\eta$ ) which is the ratio of the maximum converted power ( $V_{mp} \times J_{mp}$ ) to the power density of the incident light ( $P_0$ ),

$$\eta = \frac{V_{mp} \times J_{mp}}{P_0} = \frac{FF(V_{oc} \times J_{sc})}{P_0}. \quad (2.17)$$

The  $J$ - $V$  curve of solar cells based on a-Si:H or  $\mu$ c-Si:H can be usually described by means of an equivalent circuit (Eq. 2.18) which consists of a parallel circuit of a single diode and a voltage dependent current generator  $J_{ph}(V)$ , plus parallel and series resistance,  $R_{OC}$  and  $R_{SC}$  respectively [71].

$$J = -J_{ph}(V) + J_0 \left( \exp \left( \frac{q_e(V - JR_{SC})}{n_i k_B T} \right) - 1 \right) + \frac{V - JR_{SC}}{R_{OC}} \quad (2.18)$$

where  $J_0$  is the saturation current density,  $q_e$  is the elementary charge of electron,  $n_i$  is the ideality factor,  $k_B$  is the Boltzman constant and  $T$  is the absolute temperature.

Two different equipments have been employed for the measurement of solar cell characteristics. When the cells were characterized at the research center CIEMAT, the devices of  $0.1 \text{ cm}^2$  were illuminated under 100

mW/cm<sup>2</sup> solar spectrum at an air mass of 1.5 (AM1.5G) by using a *ThermoOriel Class A* solar simulator. Details on the illumination measurement system and procedure are explained elsewhere [72].

When the characterization was carried out at UB, the *J-V* curves were measured on 1 cm<sup>2</sup> solar cells illuminated by a *NewPort 67005* xenon lamp provided with a global air mass (AM 1.5) filter. The beam was focused towards the entrance of an optical fibre that addressed the light to the measuring stage. Before each measurement, a well known standard cell was characterized in order to control the incident power of the light source. The measurements were performed at a temperature of 25°C.

### 2.3.6.2 Spectral response (SR) and external quantum efficiency (EQE)

The spectral response is defined as the ratio of the generated photocurrent to the power incident to the solar cell. The spectral response measurements were performed at UB and also at CIEMAT, in both laboratories home-made experimental setups were employed. An *Spex 1680* monochromator in the range 350-800 nm with a step of 10 nm was used at UB and a *Triax 550* monochromator between 300 nm and 800 nm was employed at CIEMAT. The EQE can be calculated from the spectral response of the device and is defined as the fraction of incident photons at a wavelength  $\lambda$  transformed into electron-hole pairs collected at the contacts of the device. The relation between SR and EQE is given by:

$$SR(\lambda) = EQE(\lambda) \frac{\lambda q_e}{hc} \quad (2.19)$$

where  $q_e$  is the electron charge,  $\lambda$  the incident light wavelength,  $h$  Planck's constant and  $c$  the speed of light in vacuum.





# 3 Novel texturing methods for light confinement

## 3.1 Introduction

For thin film silicon solar cells light trapping plays a crucial role to improve device performance. Scattering at the interfaces between the layers that form the cell increases the path length of incident light. This fact might result in higher absorption in the active layer and hence, higher conversion efficiency (see light paths in Fig. 3.1). As mentioned in Chapter 1, the absorption is mainly limited by the band gap of the material (1.1 eV for  $\mu\text{c-Si:H}$  and 1.7-1.8 eV for a-Si:H).  $\mu\text{c-Si:H}$  is able to absorb light in a wider range of wavelengths, up to the NIR, but it has an indirect band gap that results in a low absorption coefficient. That means that in a  $\mu\text{c-Si}$  film of some microns thick, incident light will be hardly absorbed if it makes a single pass through the thin film. In the case of a-Si:H, to reduce processing costs and light induced degradation problems, the absorber layer should be as thin as possible. In both cases it is necessary to enhance the optical absorption by increasing the optical path of the solar light. In thin film silicon solar cells, light scattering is usually achieved by texturing the front TCO, the back reflector, or even the substrate with either random or periodic textures with roughness comprised between 30 to 150 nm [49]. For efficient light scattering, these textures should be in the dimension range of the incoming light wavelength [73].

For randomly textured surfaces, the incident light will be scattered randomly increasing the path length of light within the material (a schematic light path is given in the right image of Fig. 3.1). The theoretical maximum path length is given by the famous Yablonovitch limit [74] which states that the intensity within a textured and inhomogeneous medium of

### 3 Novel texturing methods for light confinement

local refractive index  $n$  will tend to be  $n^2$  times greater than the incident light intensity, this enhancement can be further multiplied by 2 if a reflector is placed behind the medium ( $2n^2$ ) and can be again multiplied by 2, in the effective absorption of indirect band gap semiconductors.

$$\alpha = 4n^2, \quad (3.1)$$

The limit assumes weak light absorption, perfect diffuse reflection at both interfaces (Lambertian surfaces whose radiance is constant at every observation angle) and that the material thickness is much larger than the wavelength of the visible light. For a solar cell made of silicon ( $n=3.5$ ) the enhancement will be  $\alpha \sim 50$  which means that a light ray in silicon may be expected to make 50 passes on average before escaping [74, 75].

The most typical TCO structures that are used for Si thin film solar cells are random textures like, the commercially available Asahi-U substrates ( $\text{SnO}_2:\text{F}$  grown by APCVD shown in Fig. 3.2 a)) and boron doped zinc oxide ( $\text{ZnO}:\text{B}$ ) grown by LPCVD. Also the chemically-etched sputtered  $\text{ZnO}:\text{Al}$  (See Fig. 3.2 b)) has been widely investigated. Even though each of these structures present very different feature sizes, all of them are suitable for thin film silicon solar cells. For example, Asahi-U glass possess features with lateral sizes of 200 nm and  $\sigma_{rms}$  values around 30 nm, on the other hand, sputtered and etched  $\text{ZnO}:\text{Al}$  has larger lateral sizes of 300 nm and greater roughness values around 100 nm. These two textures have shown to yield nearly the same efficiencies in a-Si [76] whereas textured  $\text{ZnO}$  seems to perform better in tandem and  $\mu\text{c-Si}$  solar cells. This is because larger feature sizes are more appropriate in scattering longer wavelengths [49].

In the case of  $\text{ZnO}:\text{B}$  grown by LPCVD the layers are polycrystalline and are constituted of grains whose extremities appear at the growing surface as pyramids, and yield a random pyramidal texture that efficiently scatters the light. It has been demonstrated that larger grains lead to higher scattering efficiency. Characteristic features of this textures are roughness of 60 nm, haze factor of 22% at 600 nm and lateral feature sizes between 300-500 nm [77]. Sometimes an Ar plasma treatment is performed to smoothen the pyramidal surface to avoid shunting in the cell [78]. Pyramidal  $\text{ZnO}:\text{B}$  has shown very good results in a-Si:H solar cells,

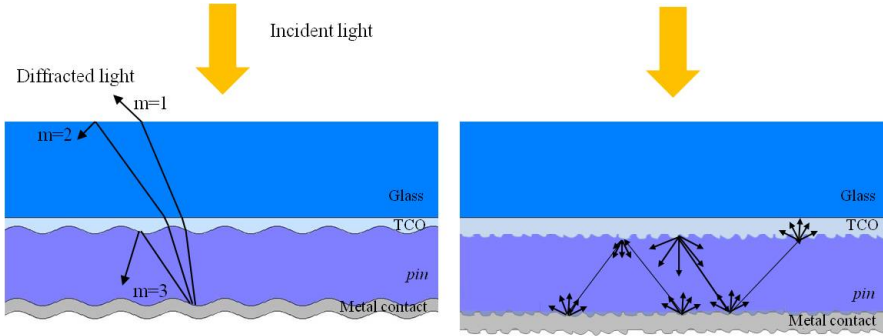


Figure 3.1: Schematic light path in a silicon thin film deposited on a periodic (left) and random (right) textured TCO surface.

with efficient light trapping [79].

In *nip* configuration solar cells, where the substrate transparency is not mandatory, it is common to texture the metal reflector. Usually Ag is grown by sputtering onto a hot substrate ( $400^{\circ}\text{C}$ ) and a texture is formed because of the partial recrystallization during growth. By varying the layer thickness and the deposition temperature, roughness values between 40 and 100 nm can be obtained [52, 80].

Besides these traditional light trapping schemes, other nanoscale approaches are currently under investigation including photonic crystals [81], nanowires [82], and periodic nanostructures. These structures include nano-domes [83], nano-cavities [84] or linear gratings [85] and can be dielectric [86], metallic [87] or be part of the semiconductor itself [88] and can be placed either on top or bottom of the photovoltaic device. a-Si:H solar cells in *nip* configuration have been fabricated on periodically textured PET (polyethylene terephthalate) substrates [89], and *pin*  $\mu\text{-Si}$  solar cells have been fabricated on 1D gratings on glass [90]. But it is still not clear whether periodic or random textures provide the best light trapping in solar cells. The most common is to study their feasibility by optical modelling and simulations. Haase *et al.* demonstrated that for the maximum light confinement the ideal period for a linear grating was 750 nm with a feature height between 200 and 300 nm. In the case of linear gratings,

### 3 Novel texturing methods for light confinement

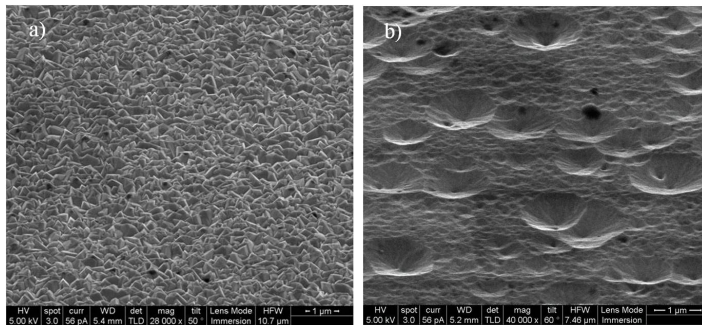


Figure 3.2: SEM images of two typical TCO structures a) APCVD grown  $\text{SnO}_2:\text{F}$  (Asahi-U) and b) sputtered and etched  $\text{ZnO}$

diffraction effects are used to guide the light into the thin absorber layers [84, 91] and enable to select the light scattering angle. Thus, by controlling the grating geometrical features, it is possible to control the scattering properties [92, 93].

Assuming normal incidence, the diffraction angle in transmission and reflection is given by:

$$d \sin \theta_m = m\lambda \quad (3.2)$$

where  $m$  is the diffraction order,  $d$  the period size and  $\lambda$  the incident wavelength. A schematic light path is given in the left image of Fig. 3.1.

This chapter deals with two different routes to enhance the efficiency of solar cells through different light trapping mechanisms. The first route is based on periodically textured  $\text{ZnO}:\text{Al}$  by means of laser ablation. Different periodic structures have been tried and the morphological, optical and electrical analysis is explained in Sec. 3.2. The second route (Sec. 3.3) consists of texturing the glass substrate by means of the Aluminium Induced Texturing method (AIT). The section starts with the AIT explanation followed by the optimization of the process. Then,  $\text{ZnO}:\text{Al}$  is grown over some of the optimized textures and a detailed characterization is presented. Also some trials have been performed to texture  $\text{ZnO}:\text{Al}$  grown over AIT glass substrates by HCl chemical etching, the objective

was not to optimize the HCl etching but to prove a double scattering at the glass/ZnO interface and ZnO/Si interface. Finally a-Si:H, and a-Si:H/pm-Si:H tandem solar cells have been deposited on the AIT substrates and the optical and electrical properties are presented.

## 3.2 Laser texturing of front contacts

Laser technology has been widely employed in the manufacturing process of photovoltaic devices. Lasers have been used in different stages of the crystalline silicon solar cell production, such as the edge isolation after the diffusion process, laser fired contacts or laser contact openings in the back surface passivated cells, etc. [94, 95]. Amongst the technologies based on thin film (CdTe, CIGS or a-Si:H), laser techniques are acquiring a more relevant and clearly strategic role. More specifically, laser ablation techniques in thin film modules (laser scribing) have proven to be the most effective, and most industrially favourable for the monolithic interconnection processing of these devices [96, 97]. As mentioned in the introduction of this chapter, in thin film technology light management is mainly developed at the substrate or at the front contact TCO that collects the light that is led to the absorbing layer. Different texturing methods commonly used to increase the light trapping in thin film silicon solar cells have been discussed in the last section. In this section, a novel method to texture the front TCO by laser ablation is presented. The advantage of this method is, one can create the desired textures with high precision on a film surface by laser processing.

Laser texturing has the ability to design customized patterns in a cost effective way introducing periodic patterns that can act as diffraction gratings. Heine *et al.* [98], Senoussaoui *et al.* [99] and Eisele *et al.* [100] have discussed the effect of gratings in solar cells. For instance, Eisele *et al.* have used laser interference lithography technique to create a periodic line pattern in AZO thin films and have demonstrated that the lowest reflectance for an a-Si solar cell deposited on this pattern was achieved for a period of 980 nm and a groove depth ( $h$ ) of 160 nm.

The objective of this work was to evaluate the feasibility of laser technology to create a transparent and conducting textured AZO. AZO samples were laser processed using fully commercial fast and ultrafast solid state

### 3 Novel texturing methods for light confinement

laser sources and the resultant surfaces were evaluated by measuring the haze factor, roughness and the sheet resistance and were compared to the commercially available Asahi-U glass. The laser processing was performed at the *Centro Láser* UPM.

An optimisation process was first performed in which an AZO film of 500 nm thick was laser processed with different patterns, rhombic, lineal, triangular or parallel combined (see Fig. 3.3) and also the processing parameters such as the laser power and speed were varied (Sec. 3.2.1). Based on the best results obtained from this initial optimisation, another set of samples with linear patterns was fabricated on a thicker AZO (1000 nm) and the results are presented in Sec. 3.2.2.

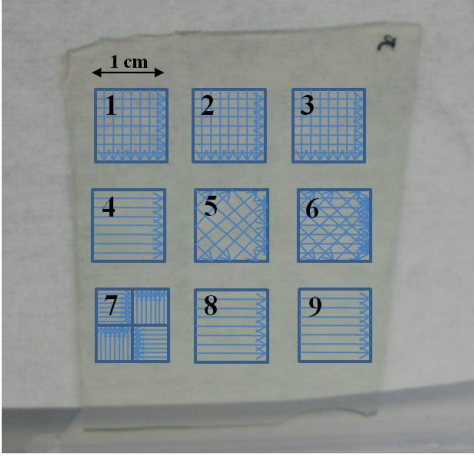
#### 3.2.1 Laser texturing: Optimization

ZnO:Al (2%) of 500 nm thickness has been grown over a  $10 \times 10$  cm<sup>2</sup> Corning 1737F glass substrate by means of dc magnetron sputtering at a power of 200 W and at a working pressure of 0.4 Pa (Ar). The substrate was kept at 300°C during deposition. The transmittance and reflectance of the AZO before laser processing are shown in Fig. 3.4. The integrated transmittance between 400 and 800 nm was  $\sim 83.8\%$  and the  $R_s$  measured with the four point probe was 9  $\Omega/\text{sq}$ .

For the laser texturing, a diode pumped Q-switched laser with Nd:YVO<sub>4</sub> (Vanadate) lasing media crystal (*Spectra Physics* HIPPO) working at its third harmonic (355 nm of wavelength) was employed. The beam was delivered to the working area via steering mirrors, which direct the beam to a scanner head (Hurricane II 14 SCANLAB) via the power attenuator AT4040. Before the entrance to the scanner head an iris was placed in order to remove the diffraction and aberration defects of the laser beam. The scanner head directs and focuses the beam onto the target via a lens with a focal length of 250 mm. The laser system specifications are described in Sec. 2.2.3 of Chapter 2.

Nine samples, each of  $1 \times 1$  cm<sup>2</sup> in area were laser processed under different conditions. The samples were named from 1 to 9 and the process parameters and patterns are depicted in Fig. 3.3. The parameters were chosen according the know-how presented in previous publications [101]. Laser processing was carried out with 355 nm, 50 kHz, and the beam size

### 3.2 Laser texturing of front contacts



Sample	Power (mW)	Peak fluence (J/cm <sup>2</sup> )	Speed (mm/s)	Pitch (μm)
1	89	0.39	170	12
2	105	0.46	170	20
3	93	0.41	500	3.4
4	105	0.46	170	20
5	105	0.46	170	20
6	105	0.46	170	20
7	105	0.46	170	13.6
8	105	0.46	85	20
9	140	0.62	170	20

Figure 3.3: Laser processed patterns (left) and the processing parameters used (right) for the 9 samples.

on the sample was  $23 \mu\text{m}$  in diameter. In the first 3 samples the pattern was in the form of a rectangular grid and just the laser power and speed of the process were varied. For samples 4, 5, 6 and 7, just the pattern was varied while the speed process, power and peak fluence was constant at  $170 \text{ mm/s}$ ,  $105 \text{ mW}$ , and  $0.46 \text{ J/cm}^2$ , respectively. And samples 8 and 9 present the same pattern while the speed process and power were varied.

Morphological characterization of the samples was performed using a confocal microscope. Two different images were taken for every sample, a 3D confocal image from which the  $\sigma_{rms}$  values and the groove depth ( $h$ ) were extracted and a 2D real image that was basically used to evaluate possible cracks on the surface.

The haze values were calculated from the transmittance and diffused transmittance recorded using a spectrophotometer and the  $Rs$  was measured with a four point probe system in two perpendicular directions (one measure placing the 4 probes parallel to the sample and another measure after rotating the probes  $90^\circ$ ). Table 3.1 presents the  $\sigma_{rms}$ , the groove depth  $h$ , the integrated transmittance in the range 400-800 nm, the haze at 600 and two values of  $Rs$ , called horizontal ( $Rsh$ ) and vertical ( $Rsv$ ) sheet resistance. The groove depth was deduced from the microscope im-



### 3 Novel texturing methods for light confinement

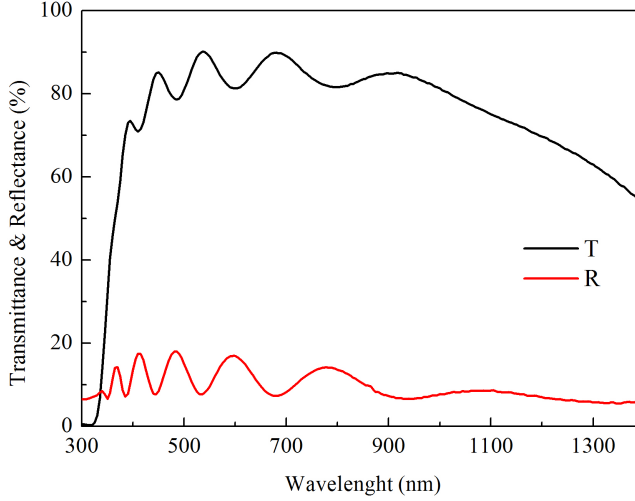


Figure 3.4: Transmittance and reflectance of the as-deposited AZO (500 nm) film.

age profile of  $120\ \mu\text{m}$  lateral size, an example of a smaller profile ( $80\ \mu\text{m}$ ) is shown for sample 9 in Fig. 3.6. The  $\sigma_{rms}$  values were calculated using the *Sensofar* software by analysing an area of  $120 \times 90\ \mu\text{m}^2$ . It was difficult to correlate the  $\sigma_{rms}$  with the groove depth because of the irregularity of the patterns. The groove depth was very high and it was deduced from a single profile while the  $\sigma_{rms}$  was extracted from a larger area. Aside from the 9 samples, the values corresponding to Asahi-U glass are also presented.

As deduced from Table 3.1, it was not easy to find an optimum film having a good haze (i.e. higher than 8.4% at 600 nm) and a good sheet resistance (i.e. lower than  $9.2\ \Omega/\text{sq}$ ). Although the integrated  $T$  of all the patterned samples was higher than that of Asahi-U substrate and similar to the as-deposited sample, the  $R_s$  values were worsened, probably because there was a loss of material. As a general tendency, the highest haze values were achieved in the most damaged films that were also the roughest and the least conductive. A special case was observed for the linear patterned textures of sample 8 and 9 with  $h$  values 500 nm and 300 nm respectively,

### 3.2 Laser texturing of front contacts

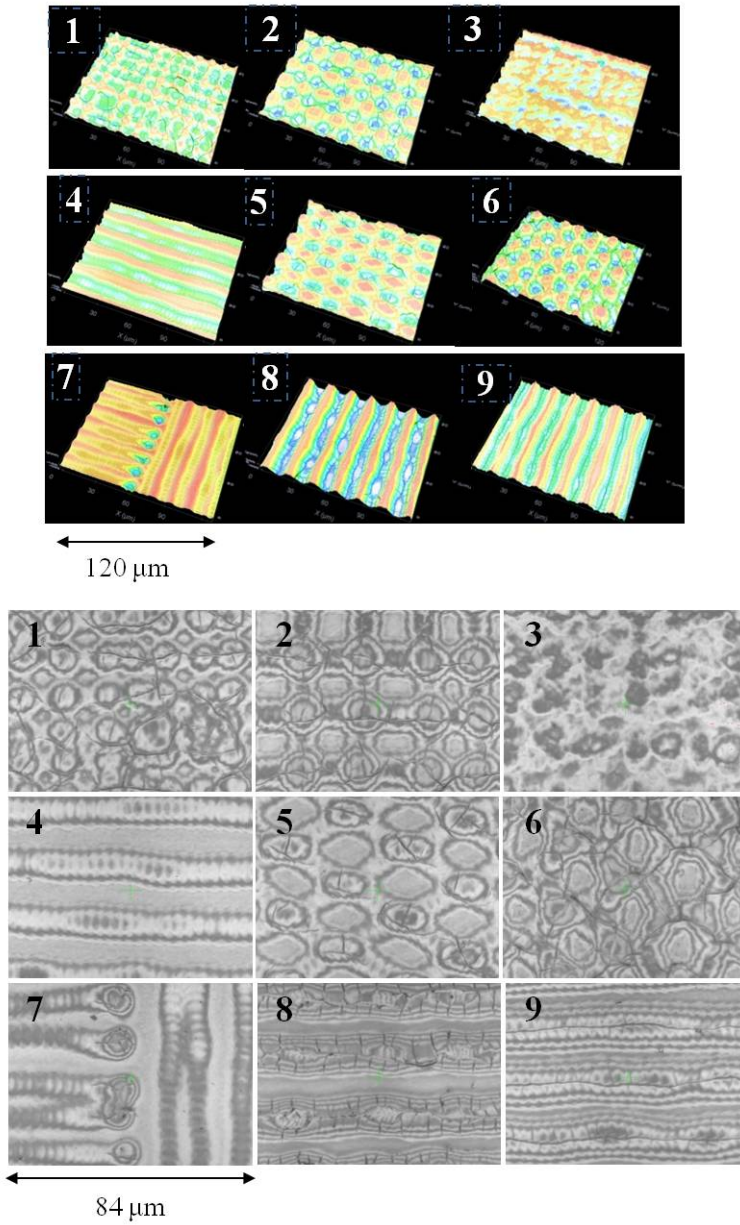


Figure 3.5: Confocal microscope images of the 9 laser textured AZO samples. On the top, 3D confocal images and on the bottom real 2D image.

### 3 Novel texturing methods for light confinement

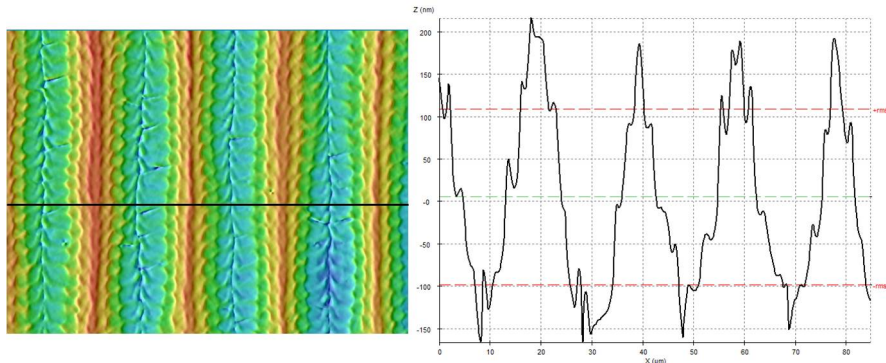


Figure 3.6: Confocal microscope image with an overlapped line (left) which indicates the extracted profile (right) of sample 9.

Table 3.1: Roughness  $\sigma_{rms}$ , groove depth ( $h$ ), integrated transmittance ( $T$ ) in the range 400-800 nm, haze at 600 nm, horizontal sheet resistance ( $Rsh$ ) and vertical sheet resistance ( $Rsv$ ) of the 9 laser textured samples with that of Asahi-U glass.

Sample	$\sigma_{rms}$ (nm)	$h$ (nm)	$T$ (400-800 nm)	Haze (%)	$Rsh$ ( $\Omega/sq$ )	$Rsv$ ( $\Omega/sq$ )
1	77	240	84.2	10.5	7k	4.3k
2	138	450	83.5	10.3	9.5k	2.6k
3	59	170	81.9	3.2	313	217
4	53	170	81.9	2.8	30	30
5	146	370	83.9	6.7	438	284
6	94	132	80.5	12.7	8.4k	8.3k
7	55	85	84.2	2.6	22	20
8	191	500	83.9	19	3k	9.4
9	102	300	83.1	8.7	2.8k	9.7
Asahi-U	31	-	78.3	8.4	9.2	9.2

which presented very different horizontal and vertical sheet resistance values (placing the 4 probes parallel or perpendicular to the laser scanning direction, respectively). They gave a vertical  $R_s$  almost equal to that given by the as-deposited film, whereas their horizontal  $R_s$  values were really high. The highest haze was also achieved by the linear patterned sample 8, that experienced also a high ablation as demonstrated with the

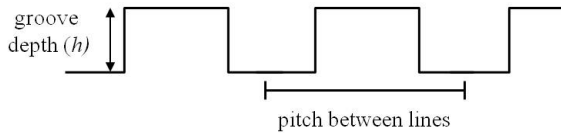


Figure 3.7: Schematic of the cross section of the lineal patterned AZO indicating the groove depth ( $h$ ) and the pitch between lines (period).

groove depth which was 500 nm (see Fig. 3.6). Sample 4 and sample 8 were processed with the same power and pitch, but with different scanning speed. The slower scan speed used for sample 8 has caused higher ablation of the material resulting in higher groove depth. Given the high haze achieved for this linearly patterned sample and that the vertical  $R_s$  was almost unchangeable, a new batch of experiments with parallel patterns was designed for a thicker film and are presented in the next section.

### 3.2.2 Laser-textured transparent and conducting AZO

As explained by other authors [99, 100], the period and the groove depth of the AZO linear grating has a critical influence on the optical behaviour of the complete device. Usually, for high light scattering in silicon thin film solar cells, periods of 1  $\mu\text{m}$  and groove depths of 200-500 nm are required. This kind of structures are normally achieved by interference lithography in which two laser beams from the same source interfere to create patterns in the sub-micrometer regime on a photoresist, then the illuminated photoresist is removed and the remaining one is used as an etching mask for HCl. In this work, the aim was to demonstrate the proof of concept to create a pattern by directly scribing on the AZO by laser ablation in a simple single step. To do that, a single laser beam scanned an AZO surface with sufficient energy to ablate part of the sample. The diameter of the laser spot (23  $\mu\text{m}$ ) was the factor that limited the minimum period, hence, periods smaller than the ones presented here were not feasible. Even though, some trials were performed and the resultant samples were characterized.

For a better understanding on the meaning of period and groove depth, a schematic cross section of a lineal pattern is depicted in Fig. 3.7.

### 3 Novel texturing methods for light confinement

A thick AZO of 1000 nm was deposited under the same conditions used in the first trial, by increasing the deposition time. The integrated transmittance in the range 400-800 nm was 82.8% and the  $R_s$  was 8  $\Omega$ /sq.

Laser processing was performed with the same laser (at 355 nm), with a process speed of 85 mm/s, at 50 kHz, at different powers and by varying the pitch between the lines (period). Table 3.2 gives all the laser parameters used. The samples were 1×1 cm<sup>2</sup> in size.

Table 3.2: Sample names with the corresponding power, peak fluence and period used to create the lineal patterns on AZO (1000 nm) film.

Sample	Power (mW)	Peak fluence (J/m <sup>2</sup> )	Period ( $\mu$ m)
L1	50	0.22	3
L2	50	0.22	6
L3	50	0.22	10
L4	50	0.22	15
L5	75	0.36	3
L6	75	0.36	10
L7	75	0.36	15
L8	75	0.36	20
L9	100	0.48	3
L10	100	0.48	10
L11	100	0.48	15
L12	100	0.48	20
L13	135	0.63	3
L14	135	0.63	10
L15	135	0.63	15
L16	135	0.63	20

At 0.22 J/m<sup>2</sup> the samples were not textured, at 0.36 J/m<sup>2</sup> the AZO got textured just for small pitch distances (3 and 10  $\mu$ m) but was too much damaged for a pitch of 3  $\mu$ m. In the case of 0.48 J/m<sup>2</sup>, all the samples got textured but again, a pitch of 3  $\mu$ m led to a damaged surface with very low conductivity. At 0.63 J/m<sup>2</sup> the samples were textured but 3, 10 and 15  $\mu$ m of pitch between lines yielded to spoiled surfaces.

Among all the laser parameters employed, just 5 samples have been chosen to show the results. As explained before, the other ones were either too much ablated (very high  $R_s$  in horizontal or vertical direction) or on the contrary almost not textured (very low haze). A summary with the

### 3.2 Laser texturing of front contacts

Table 3.3: Roughness  $\sigma_{rms}$ , groove depth ( $h$ ), integrated transmittance ( $T$ ) in the range 400-800 nm, haze at 600 and sheet resistance ( $Rs$ ) of the 5 samples and Asahi-U glass.

Sample	$\sigma_{rms}$ (nm)	$h$ (nm)	$T(400-800 \text{ nm})$	Haze at 600 nm (%)	$Rs$ ( $\Omega/\text{sq}$ )
L6	76	360	77.76	12.7	11
L10	151	680	81.87	18.6	60
L11	192	710	79.08	20.1	16.5
L12	183	730	78.51	11.7	11.7
L16	284	708	81.54	37.1	110
Asahi-U	31	-	78.26	8.4	9.2

laser parameters of these 5 samples and the resultant morphology evaluated by confocal microscopy is shown in Fig. 3.8. The diffused transmittance is also presented in Fig. 3.9 and the morphological, electrical and optical properties are summarized in Table 3.3.

Results shown in Table 3.3 and Fig. 3.9 demonstrated that with a lineal pattern it was possible to preserve a good conductivity while improving the scattering properties of the film. The  $Rs$  was almost identical placing the probes parallel or perpendicular to the scanning direction, thus, just one value is shown in the table. Haze values up to almost 40% at 600 nm and transmittance higher than 81.5% could be achieved employing a pitch distance of 20  $\mu\text{m}$  and a peak fluence of 0.63  $\text{J}/\text{cm}^2$ . In all shown samples the haze at 600 nm was higher than that of Asahi-U and in L10 and L16 the transmittance was even better. The  $Rs$  was the most difficult parameter to preserve but still, L6, L11 and L12 presented acceptable values. In order to probe the effect of this patterned textures on the optical properties of Si solar cells, a-Si:H solar cells were grown on L6, L10, L11, L12, L16, over non-textured glass and over Asahi-U. A conventional RF-PECVD (13.56 MHz) multi-chamber reactor was used to deposit the  $p$ -,  $i$ - and  $n$ -type a-Si layers of  $\sim 15$ ,  $\sim 200$  and  $\sim 15$  nm thick, respectively. The solar cells of 1  $\text{cm}^2$  area were completed by evaporating silver back contacts. Further information on the experimental details is given in Chapter 2, Sec. 2.1.4. The recorded total reflectance of the complete devices is depicted in Fig. 3.10. As deduced from the spectra no substantial improvement is achieved in any of the patterns in comparison to the smooth glass confirming that

### 3 Novel texturing methods for light confinement

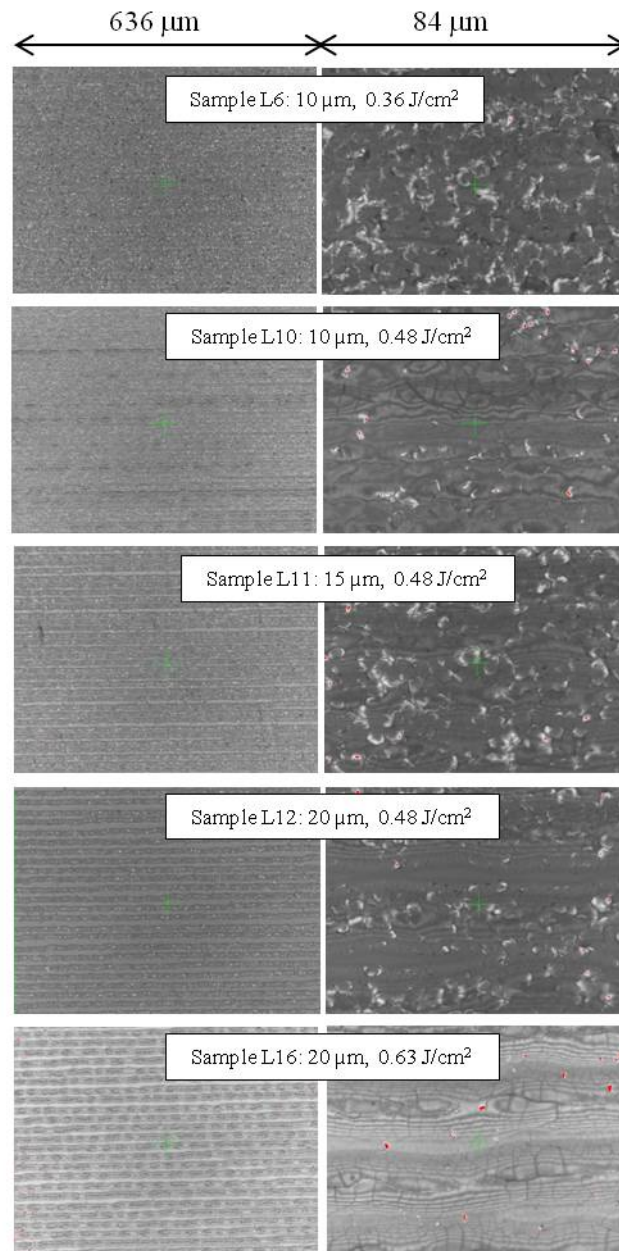


Figure 3.8: Confocal microscope images of the laser textured samples seen through the  $20\times$  objective (left) and through the  $150\times$  objective (right). The white labels contain the sample name, the pitch between lines (period) and the peak fluence.

### 3.3 Nano-textured glass substrates

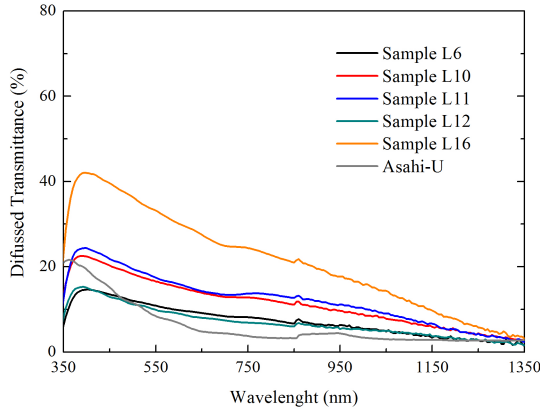


Figure 3.9: Diffused transmittance of the 5 linear patterned samples L6, L10, L11, L12, L16 and of Asahi-U.

the pattern spacing is not suitable to scatter the visible light.

In this section we have demonstrated the methodology to texture AZO by direct laser processing. The major challenge in doing laser texturing of TCO is to maintain the conductivity and at the same time to ablate the material to create textured patterns. We have shown that linear pattern seemed to be the most adequate in preserving the conductivity. The methodology opens up the possibility to create scattering textures for solar cells. It is obvious that direct single beam texturing can not produce the desired periodic spacing which is limited by the laser beam spot. Therefore, the period could not be in the sub-micrometer range which is the adequate value for Si thin film solar cells.

### 3.3 Nano-textured glass substrates

Texturing the substrate is a good alternative instead of texturing the TCO or the back reflector. An optimized textured glass surface will provide the application of a wider range of TCOs suitable for thin film solar cells, for example non-texturable TCOs or alternative front contacts, such as carbon



### 3 Novel texturing methods for light confinement

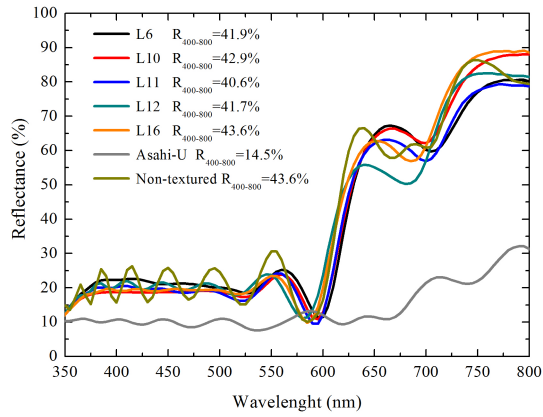


Figure 3.10: Total reflectance of a-Si solar cells deposited on L6, L10, L11, L12, L16, over non-textured glass and over Asahi-U.

nanotubes [102]. Moreover texturing the glass gives the possibility for two fold light scattering at two interfaces (glass/TCO and TCO/silicon) as exhibited in Fig. 3.11.

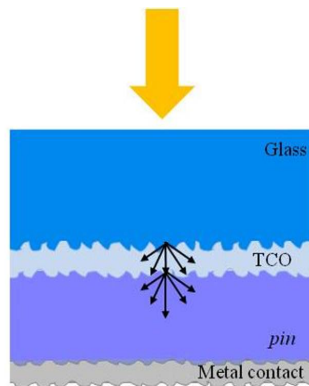


Figure 3.11: Schematic light path in a silicon thin film deposited on a textured glass surface.

### 3.3 Nano-textured glass substrates

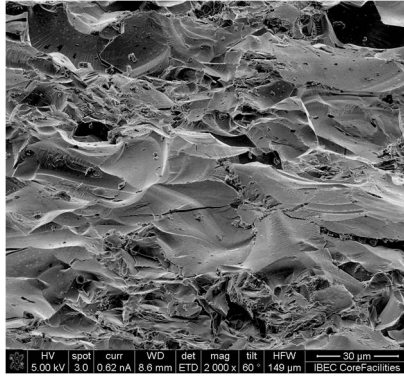


Figure 3.12: SEM image recorded at a tilted angle of  $60^\circ$  of Soda-Lime glass surface after sand blasting at an air pressure of  $6 \times 10^5$  Pa.

The first attempt to texture the glass surface was done by means of sand blasting.  $\text{Al}_2\text{O}_3$  99% pure with grains between 0.09 and 0.125 mm was blasted towards a Soda-Lime glass at an air pressure of  $6 \times 10^5$  Pa. The process was found to be highly destructive and the surface became too much damaged as exhibited in Fig. 3.12, and hence this method was discarded.

The second attempt was done with the Aluminium Induced Texturing method. It is a method that was first patented in 2004 by Aberle *et al.* [103] and permits to have roughness values suitable for thin film silicon solar cells. In the next section, the process is explained and studied in detail.

#### 3.3.1 Aluminum Induced Texturing (AIT)

The section is divided into four main parts. The first one briefly describes what is the AIT process, the second part, presents a comparison between the three glass substrates that have been used to apply the method and the third one consists in a detailed explanation on the experimental process. Finally the last subsection presents the results on the process optimization.

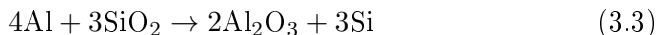
### 3 Novel texturing methods for light confinement



Figure 3.13: AIT process scheme: a) as-deposited Al on glass, b) same sample after annealing and c) resultant glass after etching.

#### 3.3.1.1 Description of the process

The AIT is a method to texture the glass surface which is based on a thermally activated chemical reaction between the glass and a thin Al layer deposited either by sputtering or evaporation method [104]. The high temperature during the thermal annealing of the Al coated glass favours a spatially non-uniform redox reaction where oxygen in the glass, mainly present in the  $\text{SiO}_2$  form, is transferred to the Al according to



After this thermal annealing, the reaction products are removed by wet chemical etching, usually hot  $\text{H}_3\text{PO}_4$  followed by a fast dip in a  $\text{HF}:\text{HNO}_3$  mixture is used and the result is a rough and uniform texture over the glass surface.

In Fig. 3.13 the main steps of the process are presented. Fig. 3.13 a) represents the glass with the as-deposited Al thin film. Fig. 3.13 b) makes reference to the post-annealed sample and Fig. 3.13 c) exhibits the resultant glass surface after removing the reaction products.

#### 3.3.1.2 Choice of glass substrates

Schott Borofloat 33 [105] is a smooth borosilicate float glass that has been chosen for almost all the experiments within this chapter. Some of its properties together with the properties of Soda-Lime microscope slides [106] and Corning 1737F [107] are presented in Table 3.4. Some trials were performed to texture Corning 1737F and Soda-Lime glasses. Corning 1737F needs a higher temperature ( $>700^\circ\text{C}$ ) than Borofloat to induce the reaction and it has less  $\text{SiO}_2$  content (55%) which hinders the texturing

### 3.3 Nano-textured glass substrates

Table 3.4: Schott Borofloat 33, Corning 1737F, and Soda-Lime glass properties (1 mm thick).

Property	Schott Borofloat 33	Corning 1737F	Soda-Lime
Softening point	820°C	975°C	720°C
Annealing point	560°C	721°C	546°C
Strain point	518°C	666°C	513°C
Density (g/cm <sup>3</sup> )	2.2	2.54	2.44
$T$ (300-1100 nm)	91.9%	89.13%	90.69%
Thermal Expansion (0/300°C)(K <sup>-1</sup> )	$32.5 \times 10^{-7}$	$37.6 \times 10^{-7}$	$90 \times 10^{-7}$
SiO <sub>2</sub> content	81%	55%	72%

process. Soda-Lime is the lowest-cost substrate and needs similar temperature than Borofloat to react with the Al layer ( $\sim 580^\circ\text{C}$ ) but it has lower silica content (72%) than Borofloat, and it contains Fe which absorbs solar radiation in the red and near infrared region. This fact makes Soda-Lime glass not adequate for  $\mu\text{c-Si}$  or tandem solar cells [108].

Borofloat 33 presents a high chemical and thermal resistance, low density and has the highest optical transmission and SiO<sub>2</sub> content (81%) [105]. These glasses (as well as Soda-Lime glasses) are produced using the float method which means that one side of the molten glass comes into contact with a bath of molten tin. Thus, when the glass is removed from the bath, some traces of tin will remain on one of the sides. Tin has a higher UV reflectance than glass so it is possible to identify the tin side by measuring the reflectance between 200 and 300 nm by means of a spectrophotometer (see Fig. 3.14). Trials to texture both glass sides under the same conditions were performed and the resultant roughness was exactly the same indicating that the tin content was not affecting the AIT process.

#### 3.3.1.3 Preparation of the textured substrates

Borofloat 33 glass substrates of 2 mm thick were cautiously cleaned in an ISO 7 (10000 type) clean room. The cleaning process of the substrate was found to be a very critical step in the resulting uniformity and texture of the glass surface. The glass substrates were initially cleaned with detergent solution (Decon 90) followed by the ultrasonic cleaning for 15 min each in

### 3 Novel texturing methods for light confinement

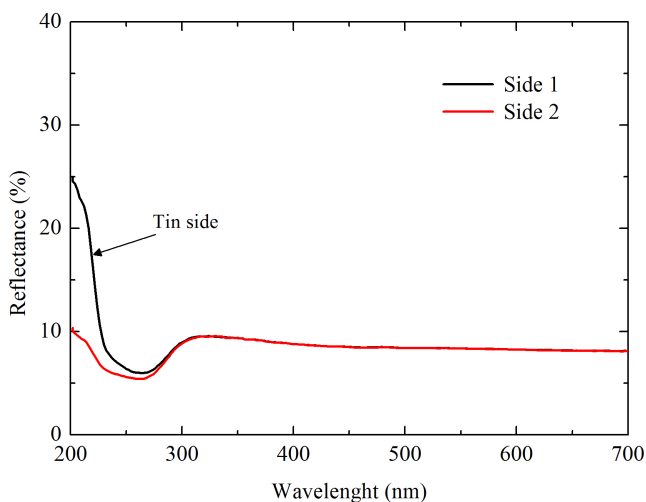


Figure 3.14: Reflectance of the Borofloat 33 glass measured on both sides. Higher UV reflectance is seen on the tin side.

deionised water, isopropanol and again in deionised water, and then dried in nitrogen. To remove the humidity at the surface, the cleaned glasses were kept in a hot air oven at 120°C for 30 min.

By means of resistive thermal evaporation, sputtering and e-beam evaporation, Al films with thickness between 30 nm and 250 nm were deposited over the cleaned substrates.

The samples were then annealed in air atmosphere in a quartz tubular furnace between 550 to 600°C and between 10 to 90 min, allowing a chemical reaction between the glass substrate and the Al layer. The samples were introduced directly at the desired temperature and were removed after they were cooled down.

Removal of the Al layer and the reaction products was realized by immersing in hot concentrated (85%) orthophosphoric acid ( $\text{H}_3\text{PO}_4$ ) followed by a fast dip in a  $\text{HF}:\text{HNO}_3$  mixture or using just hot  $\text{H}_3\text{PO}_4$ . The immersion time was varied from the minimum time needed for

the complete removal of the resultant layer (as determined from visual inspection) to a maximum of 90 min, and the  $\text{H}_3\text{PO}_4$  solution temperature was also varied from 160 to 210°C. The temperature of the acid solution was controlled with a contact electronic thermometer ETS-D6 and an RCT basic IKAMAG® safety control hot plate from IKA.

#### 3.3.1.4 Process optimization

In this subsection a detailed optimization of the process is explained. The resultant glass roughness is discussed depending on the AIT process parameters: i) the thermal reaction parameters, ii) the etching process and iii) the deposition method.

##### i) The thermal reaction and annealing temperature

To study the effect of annealing time and Al thickness on the glass texturisation process, Al layers of different thickness were thermally evaporated at 3 Å/s in a vacuum of  $5 \times 10^{-3}$  Pa on Borofloat 33 glass substrates ( $\sim 2 \times 5$  cm<sup>2</sup>). The deposition rate was controlled by a quartz crystal thickness monitor. The as-deposited films were post-annealed in air atmosphere varying the time and temperature.

Independently of the thickness or the evaporation conditions, the minimum temperature to allow the reaction process between Borofloat glass and the evaporated Al layer was  $\sim 600^\circ\text{C}$ . The reaction usually started from the edges of the samples and propagated to the centre till the whole surface changed its aspect and became dark like shown in the inset of Fig. 3.15 c). Fig. 3.15 contains three images taken by means of a confocal microscope, and two inset images taken with a conventional camera. Fig. 3.15 a) corresponds to as-deposited Al on a piece of Borofloat glass, Fig. 3.15 b) shows the aspect of the Al on glass after annealing during 20 min and Fig. 3.15 c) after annealing it for 30 min (time needed for this specific sample to complete the chemical reaction).

The time needed for the complete reaction depends on the Al layer thickness and the area of the sample. For example, 10 min were enough for 30 nm thick Al film on a  $2 \times 5$  cm<sup>2</sup> area substrate. To study the final glass roughness depending on the annealing time, the furnace temperature

### 3 Novel texturing methods for light confinement

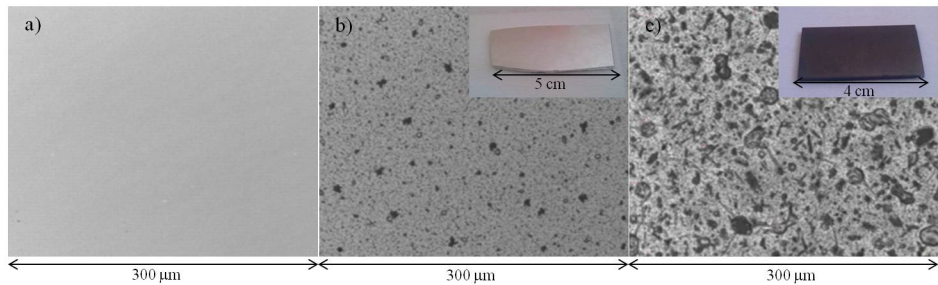


Figure 3.15: Confocal microscope images of 250 nm evaporated Al on glass a) as-deposited, b) after annealing 20 min and c) after annealing 30 min (time needed for the reaction to occur). The two insets correspond to the samples photographs.

was kept at 600°C and after the annealing process the reaction products were etched with hot  $\text{H}_3\text{PO}_4$  until they were completely removed. Then, from AFM images in  $15 \times 15 \mu\text{m}^2$  areas the  $\sigma_{rms}$  values were estimated. Fig. 3.16 presents the  $\sigma_{rms}$  values depending on the annealing time and the initial Al thickness. The first point in the plot for each sample represents the minimum annealing time required to produce the reaction.

As seen in Fig. 3.16, once the reaction has occurred no difference in the  $\sigma_{rms}$  was observed by increasing the time of annealing. This behaviour was also observed for the haze values of the samples (Fig. 3.17) where the difference was minimal between annealing the samples for 30 or 90 min. In addition, it was seen that soft textures were formed ( $\sigma_{rms} \sim 15 \text{ nm}$ ) for thicknesses  $< 50 \text{ nm}$  due to the limited Al used, whereas for thicknesses  $> 50 \text{ nm}$ , textures with higher roughness could be achieved.

To conclude, the annealing of the as-deposited Al films was optimized to be at 600°C until the samples became dark.

#### ii) The etching process

When the Al deposited Borofloat glass substrates are annealed at 600°C, a redox chemical reaction takes place at the interface according to the equation Eq. 3.3 resulting in a dark surface.

### 3.3 Nano-textured glass substrates

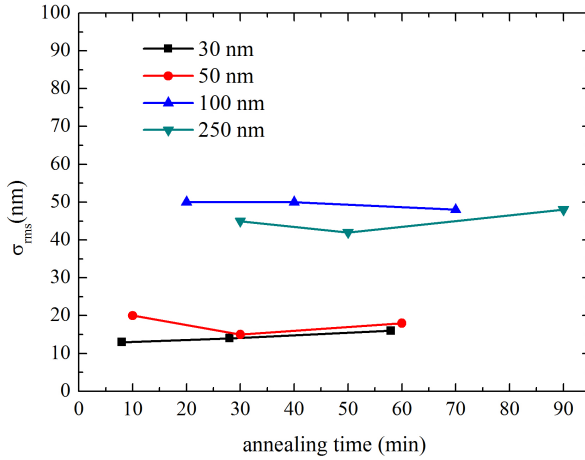


Figure 3.16:  $\sigma_{rms}$  values estimated from AFM over  $15 \times 15 \mu\text{m}^2$  images for different annealing time and Al thickness.

On this dark surface (Fig. 3.15 c)) an XPS scan was performed and the resultant spectrum is shown in Fig. 3.18. Carbon, silicon, oxygen, sodium and aluminum were detected from the peaks position through the Multipak software. According to literature [66], Si 2p (peak position of 102.1 eV) was found in the form of  $\text{SiO}_4$ , and the small amount of remaining Al in the form of  $\text{Al}_2\text{O}_3$ . Moreover due to the high temperature, Na diffused from the glass into the reacted film. This indicates that besides the reaction 3.3, other elements also take part in the annealing process.

Following previous bibliography [109] it is known that a typical Si etchant based on  $\text{HF}:\text{HNO}_3$  mixtures will perform a two step etching process including first, the oxidation of silicon by nitric acid and second, the subsequent dissolution of formed  $\text{SiO}_2$  by HF.

In this work the first trials to etch the reaction products were done with different  $\text{HF}:\text{HNO}_3$  ratios by varying the dipping time. the result was that even at high HF concentration and dipping for 12 hours the reaction products were not completely removed, as determined from visual inspection.



### 3 Novel texturing methods for light confinement

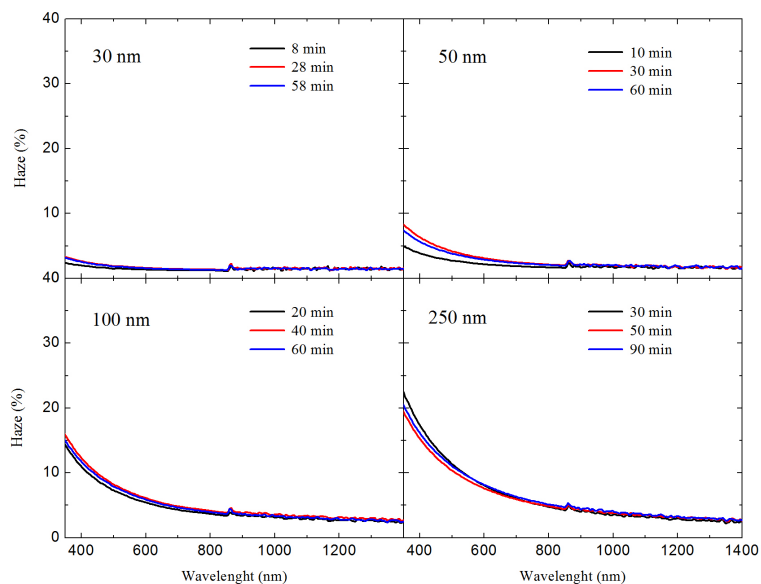


Figure 3.17: Haze factor of the resultant glass substrates after applying the AIT method varying the Al thickness and the time of annealing.

Next trials were done with hot concentrated (85%)  $\text{H}_3\text{PO}_4$  that is also known as an etchant for  $\text{Si}_3\text{N}_4$ ,  $\text{SiO}_2$  and  $\text{Si}$  at a temperature of  $\sim 160^\circ$  [110]. The post-annealed samples were dipped in concentrated (85%)  $\text{H}_3\text{PO}_4$  at temperatures between  $160^\circ\text{C}$  and  $210^\circ\text{C}$ . It was observed that the minimum temperature required to etch the reaction products was  $185^\circ\text{C}$ , and that the etching time depended on the initial Al thickness. Thus, thicker layers required more time in the etchant, approximately 15 min were required for 250 nm. Furthermore, the etching process above  $210^\circ\text{C}$ , led to the reaction of the solution with the glass, forming silicon phosphate spots (Fig. 3.19) and reduced the texture [111]. Another fact to take into account is that water evaporates from the solution at these temperatures, so the solution gets more concentrated and the etching rate increases and becomes difficult to control [110], hence, new  $\text{H}_3\text{PO}_4$  had to be used always.

### 3.3 Nano-textured glass substrates

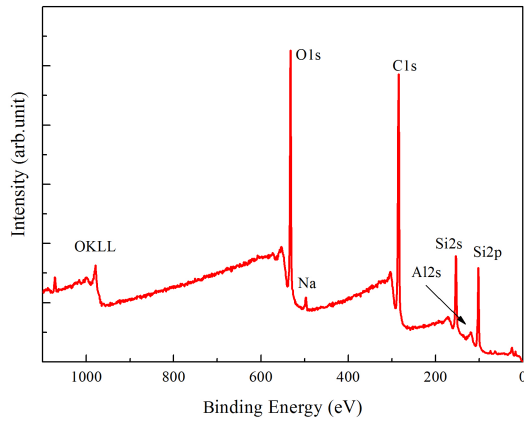


Figure 3.18: XPS spectrum of the reacted film after the annealing.

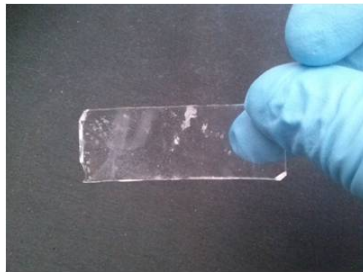


Figure 3.19: Silicon phosphate spots (whitish colour) formed on the Borofloat 33 glass substrate after etching the reaction products with  $\text{H}_3\text{PO}_4$  at  $210^\circ\text{C}$ .

According to other authors [104, 112, 113], a second step etch using  $\text{HF}:\text{HNO}_3$  is usually needed. In this thesis, after verifying through XPS measurements that the remaining products were completely removed just with hot  $\text{H}_3\text{PO}_4$ , no other acid treatments were employed. Fig. 3.20 shows the XPS spectra of untreated Borofloat 33 glass, the reacted film, the resultant glass surface after etching with hot  $\text{H}_3\text{PO}_4$  and after etching first with hot  $\text{H}_3\text{PO}_4$  and then dipped in  $\text{HF}:\text{HNO}_3$  (1:1). As evident from the

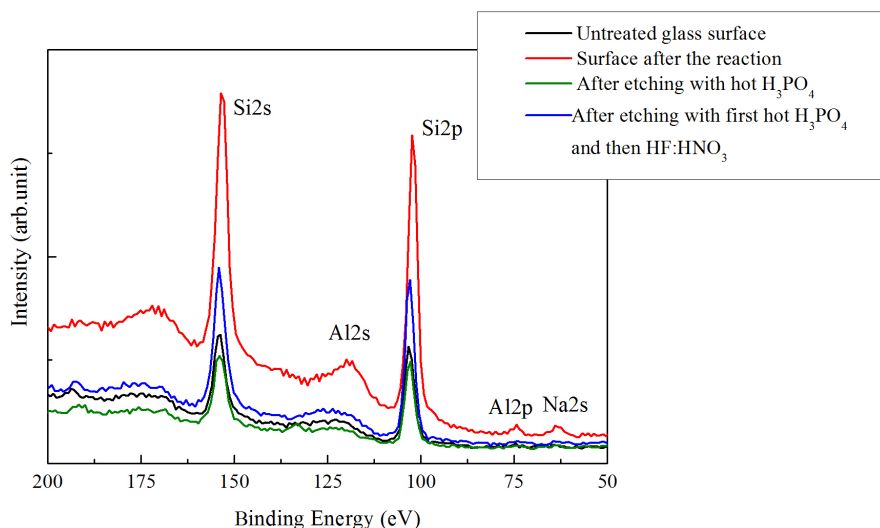


Figure 3.20: XPS spectra of Borofloat 33 glass, the Al film after the reaction, the glass surface after etching with hot  $\text{H}_3\text{PO}_4$  and after etching first with hot  $\text{H}_3\text{PO}_4$  and then with  $\text{HF}:\text{HNO}_3$ .

spectra, the amount of Si and Al present after the reaction is removed either by using just hot  $\text{H}_3\text{PO}_4$  or using first hot  $\text{H}_3\text{PO}_4$  and then  $\text{HF}:\text{HNO}_3$ .

In conclusion, in this work we have optimized the etching process to use only  $\text{H}_3\text{PO}_4$  at  $185^\circ\text{C}$  until the reaction products are completely removed as determined from visual inspection.

### iii) The influence of Al deposition method on AIT

A magnetron sputtering system and an e-beam evaporator were also employed for the deposition of the Al film in order to compare the effect of different deposition methods. It was found that the energy at which the Al particles reach the glass surface is the main important dependence parameter, and, by controlling it, it is possible to have very extremely

different textures.

In a physical vapour deposition process, material is vaporized from a solid or liquid source in the form of atoms or molecules and transported through a vacuum or plasma environment to the substrate, where it condenses.

In a thermal evaporation process (either resistive or e-beam evaporation) the vacuum pressure should be as low as  $1 \times 10^{-3}$  Pa to achieve reasonable evaporation rates, and the evaporation material may reach temperatures of (1000°C-2500°C) to evaporate [114]. The average energy of vapour atoms reaching the substrate surface is generally low, and this affects seriously the morphology of the films, often resulting in a porous and poor adherent film. The kinetic energy of the evaporated molecules can be deduced from the following equation:

$$KE = 3k_B T/2 \longrightarrow 0.16 - 0.35 \text{ eV}(1000^\circ\text{C} - 2500^\circ\text{C}) \quad (3.4)$$

where  $k_B = 8.617385 \times 10^{-5}$  eV/K is the Boltzmann's constant and  $T$  the temperature in Kelvin. In the case of Al the minimum temperature to evaporate is  $T \sim 1010^\circ\text{C}$  at 0.013 Pa [115].

In kinetic theory, the average distance a particle or molecule can travel between collisions with other moving particles is called the mean free path and can be calculated from:

$$\lambda = k_B T / \sqrt{2} \pi \sigma^2 p \quad (3.5)$$

where  $\sigma$  is the diameter of the particle,  $\pi \sigma^2$  the collision cross-section and  $p$  the pressure in Pa [115].

As seen from such expression, the average mean free path is proportional to the temperature and inversely proportional to the pressure which indicates that at lower pressures, less collisions and thus, higher energetic molecules will reach the substrate.

An important disadvantage of the thermal evaporation is the strong directionality of the process which leads to small area uniformity and poor step coverage of the films (shadowing). Usually heating and rotating the substrate can help to overcome this problem [115].

Other disadvantages include contamination by crucibles, filaments or support materials and the limitation of low input powers, thus, it is more

### 3 Novel texturing methods for light confinement

difficult to deposit pure films. E-beam evaporation, instead, can add a larger amount of energy into the source material which leads to more compact films and better adhesion to the substrate. Moreover the focused beam only heats the source material and not the crucible, hence, there is a lower degree of contamination from the crucible. In contrast, it uses high voltage ( $\sim 10$  kV) that may produce X-rays, which can damage the film [116].

In a sputtering process, the kinetic energies of the sputtered particles that reach the substrate are much higher than the evaporated ones, between 2-30 eV. As a result, the quality of the films is better. The energy of the sputtered species depends mainly on the working pressure, the power and the excitation mode (rf or dc) [41]. The resultant roughness that can be achieved by depositing the Al through sputtering are much higher because the adhesion, density, and uniformity are greater. The main disadvantage is that the deposition rate is lower, the sputtering velocity is  $5 \times 10^{-4}$  g/cm<sup>2</sup>s for ion incident energies of 1-3 kV whereas it is  $10^{-2}$  g/cm<sup>2</sup>s in the case of thermal evaporation [115].

In the first AIT experiments, all the Al films were deposited through resistive thermal evaporation with the same initial vacuum level of 0.001 Pa, and trying to maintain the deposition rate at 3 Å/s. The equipment was not provided with a substrate heater so just the deposition rate and thickness could be controlled. The biggest issue was the lack of reproducibility of the layers. Even after repeating exactly the same process conditions, the properties of the Al layers obtained were not always the same. An example is exhibited in Fig. 3.21, where 3 different textures were achieved by repeating the same AIT conditions. Probably other non controlled parameters were affecting the deposition such as the heat distribution in the filament, the exact position of the Al bars, the contamination degree inside the vacuum chamber or maybe the contamination from the filament itself. Moreover, the process was not as controlled as the sputtering. The samples shown in Fig. 3.21 are the result of evaporating 250 nm of Al, post-annealing the samples at 600°C during 1 hour followed by the etching with H<sub>3</sub>PO<sub>4</sub> at 185°C.

As seen in Fig. 3.21 a), it is possible to obtain a texture based on U-shaped craters, with crater size varying between 500 nm to 1.5 μm and  $\sigma_{rms}=56$  nm or higher roughness of 70 nm and 90 nm for Fig. 3.21 b)

### 3.3 Nano-textured glass substrates

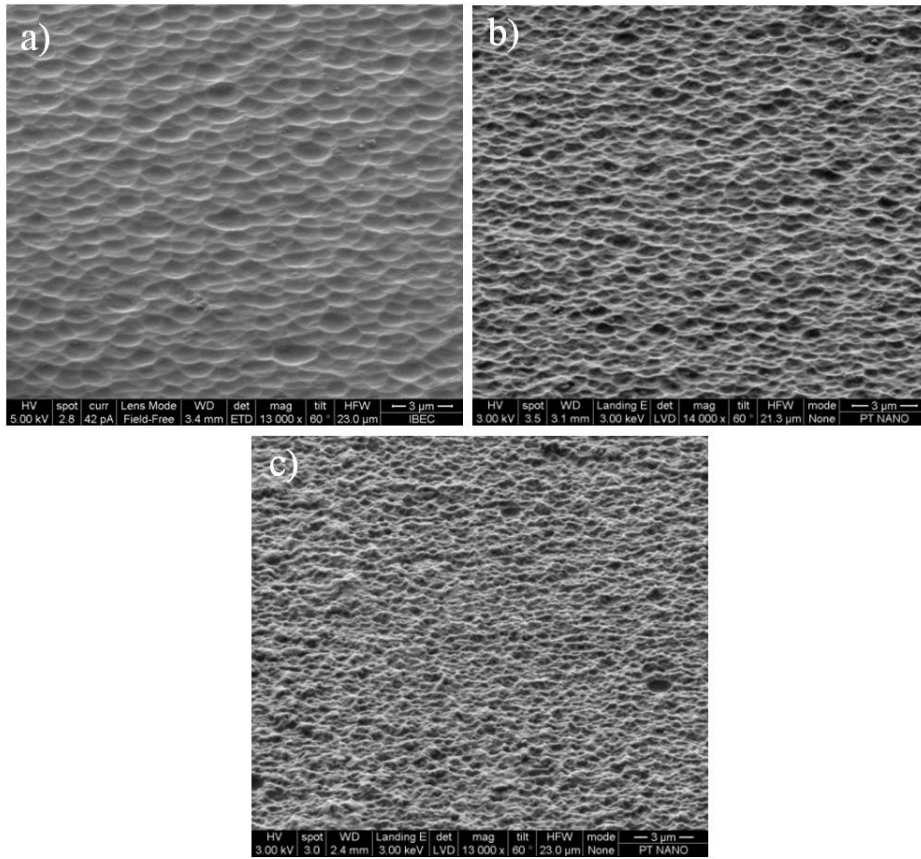


Figure 3.21: SEM images recorded at a tilt angle of  $60^\circ$  of the different textures achieved by depositing the Al by resistive thermal evaporation. a) Texture E,  $\sigma_{rms}=56$  nm, b) Texture E1,  $\sigma_{rms}=70$  nm and c) Texture E2,  $\sigma_{rms}=90$  nm

and Fig. 3.21 c) respectively. This U-shape crater morphology can also be achieved by evaporating a very thin Al layer. A maximum roughness of 90 nm has been achieved through resistive evaporation.

Also one trial was performed by means of e-beam evaporation to deposit 200 nm of Al over a Borofloat glass substrate. The resultant texture was very similar to that provided with the resistive evaporation, probably be-

### 3 Novel texturing methods for light confinement

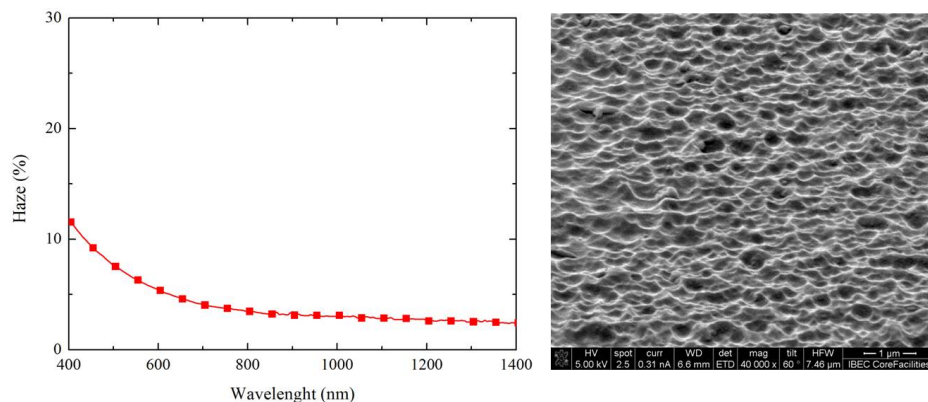


Figure 3.22: Haze factor (left) and SEM image (right), of the resultant texture after applying the AIT method on the samples with Al deposited by e-beam evaporation.

cause the e-beam evaporated particles possess kinetic energies the same order than that of resistive evaporation (0.1-0.3 eV). The haze and the SEM image recorded at a tilt angle of  $60^\circ$  are displayed in Fig. 3.22.

The sputtering method was found to be more reliable. The samples were easy to reproduce and the texture could be controlled precisely thanks to all the parameters that could be controlled during the Al growth. The textures shown in Fig. 3.23 have been achieved by sputtering 200 nm of Al over Borofloat glass while it was rotating at 20 rpm at a working pressure of 0.13 Pa and at 14 cm from the target. The sputtering dc power was varied at 60 W, 100 W, 150 W and 200 W. The samples were post-annealed at  $600^\circ\text{C}$  during 1h and etched with  $185^\circ\text{C}$   $\text{H}_3\text{PO}_4$ .

By increasing the dc power, the Al particles reached the glass with higher energy and the resultant roughness was found to increase. It was observed that at powers as high as 200 W, the surface became too damaged affecting the uniformity (Fig. 3.23 d)). Fig. 3.23 and Fig. 3.24 exhibit the SEM micrographs and the haze values of the resultant textures after depositing 200 nm of sputtered Al by changing the dc sputtering power.

From other trials it was found that, like in the resistive thermal evaporation, very soft textures can be obtained by depositing very thin Al layers

### 3.3 Nano-textured glass substrates

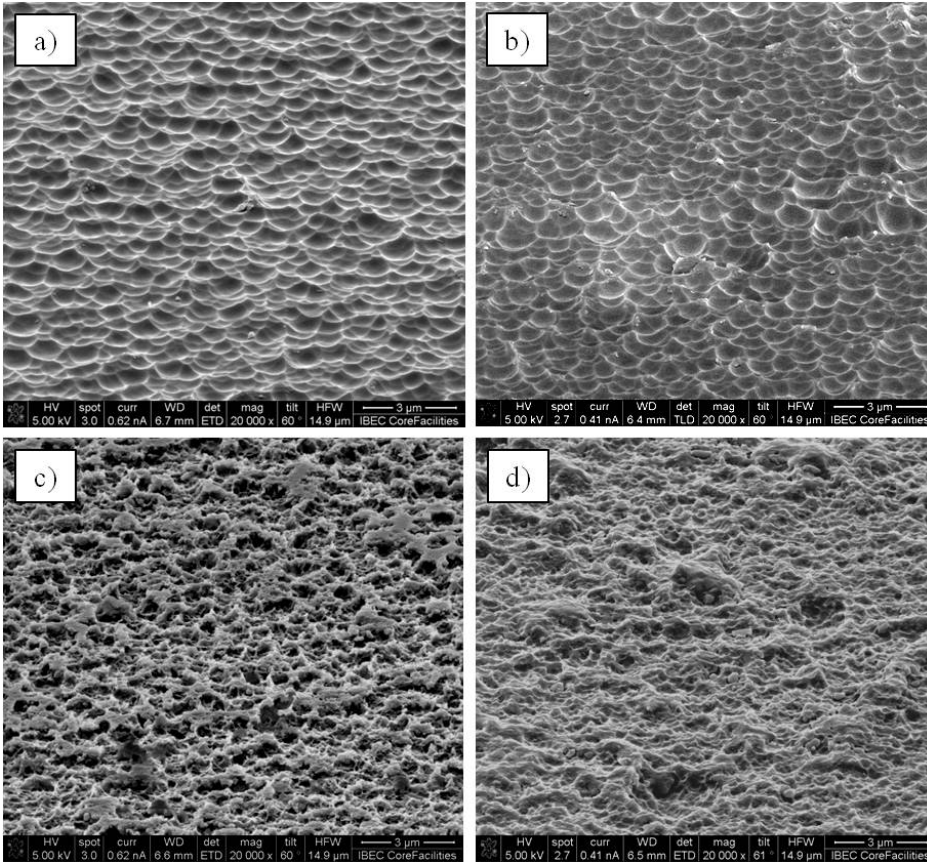


Figure 3.23: SEM images recorded at a tilt angle of  $60^\circ$  of the textured glass substrates achieved by sputtering the Al at different powers: a) Texture S1, 60 W. b) Texture S2, 100 W c) Texture S3, 150 W and d) Texture S4, 200 W.

$d < 50$  nm, and no higher roughness values were achieved albeit increasing the thickness.

One trial was performed using the rf power source. 200 nm of Al were deposited at an rf power of 150 W, at a working pressure of 0.13 Pa and without intentional heating of the substrate. The sample was post-annealed at  $600^\circ\text{C}$  during 1 hour and etched with  $185^\circ\text{C}$   $\text{H}_3\text{PO}_4$ . The texture achieved with the rf source at 150 W was very similar to the one achieved by sputter-



### 3 Novel texturing methods for light confinement

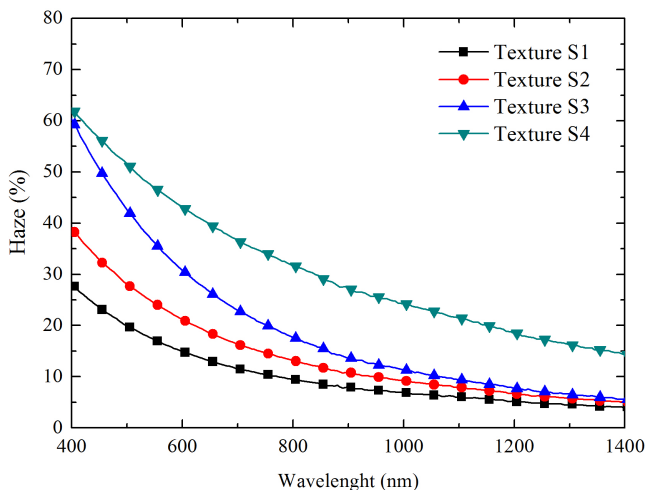


Figure 3.24: Haze values of textured glass substrates achieved by sputtering the Al at different dc powers. S1 at 60 W, S2 at 100 W, S3 at 150 W and S4 at 200 W.

ing the Al at a dc power of 150 W (shown in Fig. 3.23 c)). The roughness value extracted from the AFM image was also around  $\sigma_{rms}=145$  nm. A SEM image is shown in Fig. 3.25.

In order to intend a cost-reduction, few unsuccessful attempts were done to further optimize the AIT process. For instance, it was tried to induce the reaction in situ by sputtering the Al while maintaining the glass at 600°C. But, the result was that the Al grew forming nano islands as shown in the SEM image in Fig. 3.26 and did not react with the glass. To confirm that the glass was not textured, the Al nano islands were etched with  $H_3PO_4$  and the resultant glass surface was evaluated with a confocal microscope. This behaviour is similar to that observed when silver is sputtered on hot substrates which is commonly used as textured back reflectors in *nip* solar cells [52].

Other trial was done by depositing the Al film with a commercial Al

### 3.3 Nano-textured glass substrates

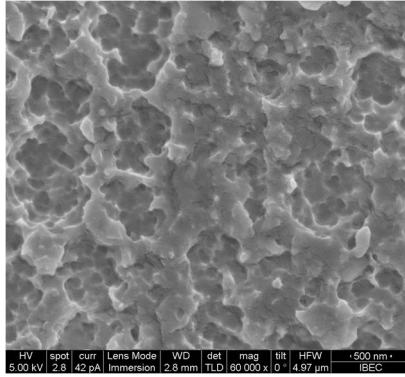


Figure 3.25: SEM image of textured glass achieved by sputtering the Al at 150 W of rf power. Texture S ( $\sigma_{rms}=145$  nm).

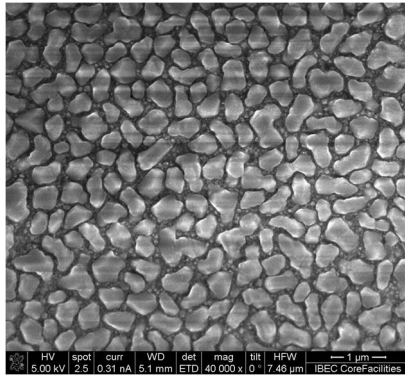


Figure 3.26: SEM image of sputtered Al on 600°C substrate.

spray of 99.5% purity bought from the company *Alumabe Castellanos*. The objective was to avoid the costly use of employing vacuum technology to deposit the Al. But the time needed to induce the reaction was about 10 times higher than the time needed when the layers were sputtered or evaporated and the glass always bent. Moreover the roughness was not uniform and formed very big craters. A SEM image of the surface after removing the reaction products is shown in Fig. 3.27.

### 3 Novel texturing methods for light confinement

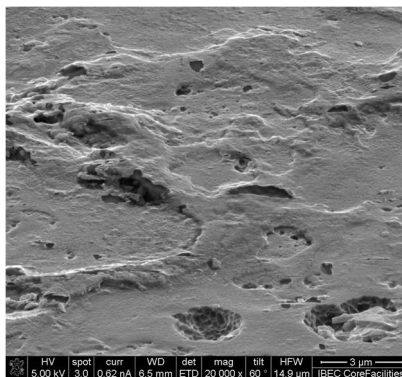


Figure 3.27: SEM image recorded at a tilt angle of  $60^\circ$  of the resultant texture after applying the AIT on the samples with spray deposited Al.

In conclusion, the deposition method and the deposition parameters are critical for the resultant roughness. In the case of sputtering, the energy at which the Al particles reach the glass substrate is higher than with evaporation. As a consequence, the Al films possess better adhesion, grow more compact and even might diffuse into the substrate [115, 117]. Moreover, since it is an interface reaction, the cleanliness of the surface is also extremely important.

#### 3.3.2 Growth of AZO on AIT substrates

From all the samples presented in the previous section, two extremely different textures were chosen to grow an AZO. A very soft texture achieved by resistive evaporation (texture E as shown in Fig. 3.21 a)) and a very rough texture achieved through the sputtering (texture S as shown in Fig. 3.25). The experimental details are given in Sec. 3.3.1.4. Some of the results presented in this section have been published in [118].

Fig. 3.28 and Fig. 3.29 show the morphology of textures E and S, respectively, and Fig. 3.30 shows the haze values. It is seen that the haze value at  $\lambda=600$  nm reaches 35% for texture S and 15% for texture E. Moreover the integrated transmittance of these samples in the range 400-800 nm is above 91%.

To study the influence of the glass texture on the growth of AZO, three

### 3.3 Nano-textured glass substrates

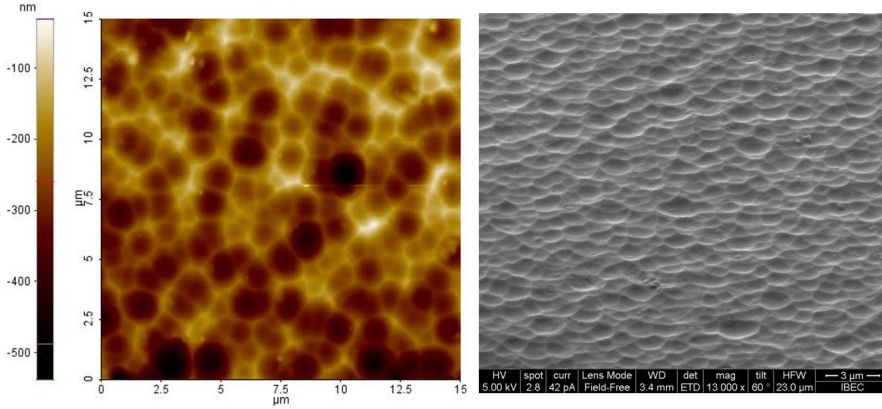


Figure 3.28: The AFM image (left) and the SEM micrograph (right) of texture E,  $\sigma_{rms}=56$  nm.

Table 3.5: Sample names, type of substrate and AZO thickness of the samples studied in this section (Sec. 3.3.2). Texture E was obtained from evaporated Al and texture S from the sputtered Al.

Sample name	Substrate	AZO thickness
AZO1	smooth glass	500 nm
AZO2	smooth glass	700 nm
AZO3	smooth glass	1000 nm
E+AZO1	texture E	500 nm
E+AZO2	texture E	700 nm
E+AZO3	texture E	1000 nm
S+AZO1	texture S	500 nm
S+AZO2	texture S	700 nm
S+AZO3	texture S	1000 nm

different thicknesses of AZO, 500 nm (AZO1), 700 nm (AZO2), and 1000 nm (AZO3) were deposited via dc magnetron sputtering onto a smooth glass surface, and on textures E and S. For clarity, a summary of the samples is provided in Table 3.5.

### 3 Novel texturing methods for light confinement

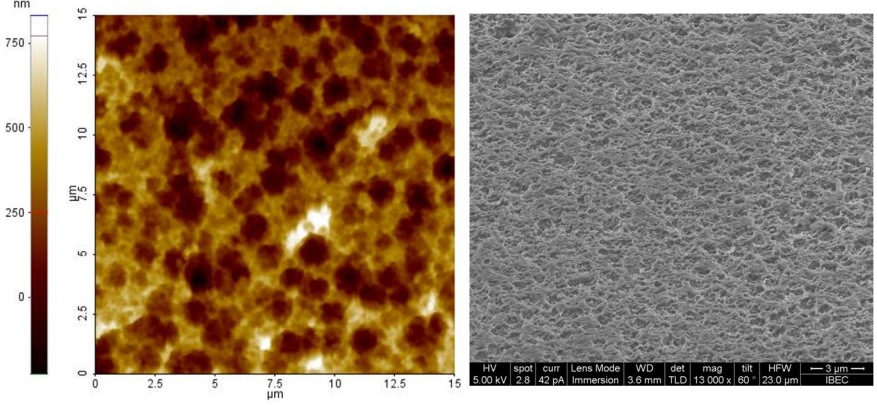


Figure 3.29: The AFM image (left) and the SEM image (right) of texture S,  $\sigma_{rms}=145$  nm.

The films were deposited at a working pressure of 0.4 Pa, using a dc power of 200 W and keeping the substrate at a temperature of 300°C. The target was ZnO/Al<sub>2</sub>O<sub>3</sub> (98/2 wt%) of 3 inch diameter and 99.99% purity. The base pressure in the chamber was always below  $7 \times 10^{-4}$  Pa.

The characteristic texture of the sputtered AZO depends on the deposition conditions [42] and thickness [119]. According to the Thornton model, at higher deposition pressures and lower temperatures, higher roughness and less compact layers are formed [42]. Since, in this work it was prioritized to get better conductivity, transparency and compactness than higher roughness values for the TCO, sputtering conditions of high substrate temperature and low working pressure were used to yield films having soft textures of  $\sigma_{rms} \sim 5-9$  nm on smooth substrates. AZO3 (1000 nm) on flat glass is shown in the SEM tilted image of Fig. 3.31. Fig. 3.32 shows the SEM image of texture E and its combination with 500 nm, 700 nm and 1000 nm of AZO. It can be seen that the samples with AZO over texture E show a double texture based on U shaped interconnected craters of about  $1 \mu\text{m}$  in size with nano scale pattern spread over the surface (Fig. 3.32 b), c) and d)).

The nano scale pattern that is observed over the craters could be due to

### 3.3 Nano-textured glass substrates

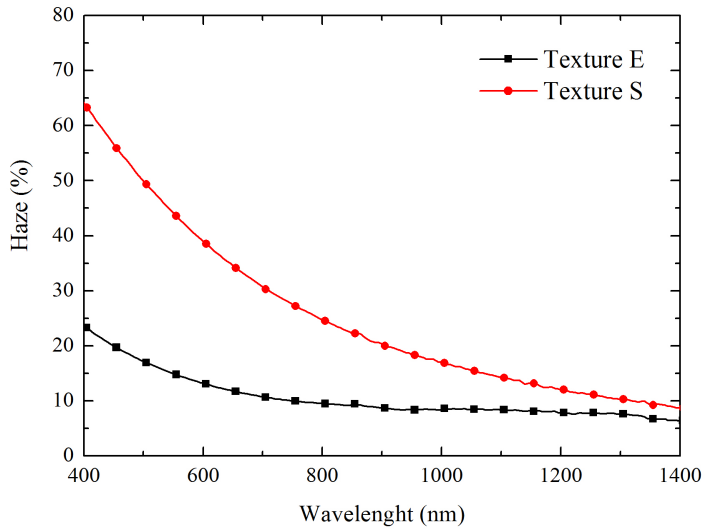


Figure 3.30: Haze of texture E and texture S.

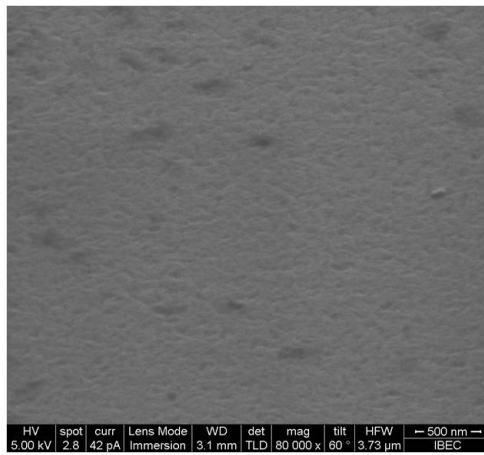


Figure 3.31: SEM (tilted at 60°) image of AZO3 (1000 nm).

### 3 Novel texturing methods for light confinement

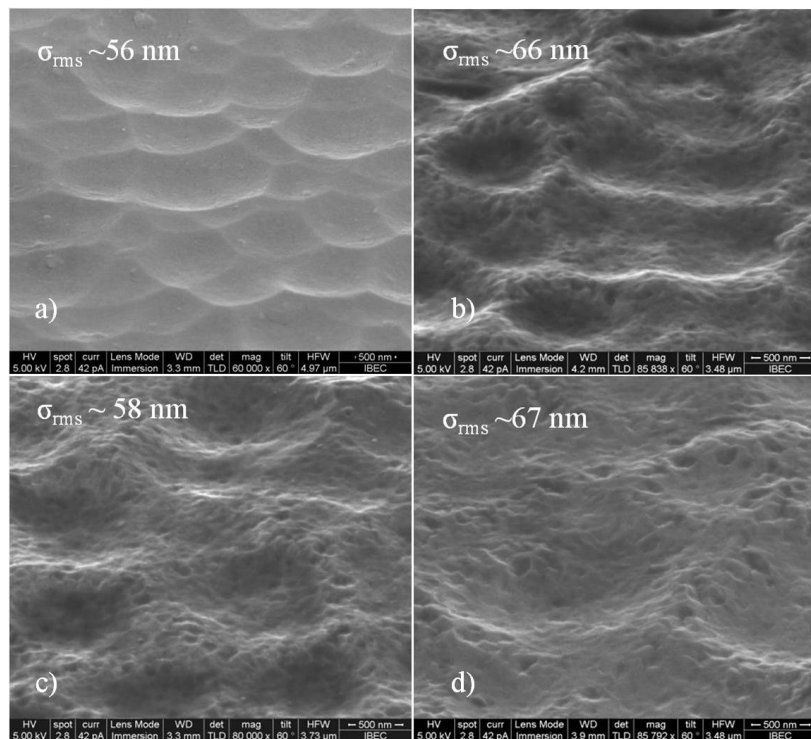


Figure 3.32: SEM (tilted at  $60^\circ$ ) micrographs of a) texture E, b) E+AZO1 (500 nm), c) E+AZO2 (700 nm), d) E+AZO3 (1000 nm). The  $\sigma_{rms}$  values were obtained from AFM.

the presence of a minor roughness that might have formed during the AIT process (not appreciable in SEM micrograph of texture E, Fig. 3.32 a)) and became pronounced with the growth of AZO deposition and/or due to the columnar growth over tilted substrate surfaces. Such nano dimensional etching patterns have been observed for the wet chemical etching of sputtered AZO films when HF is also used as an etchant along with HCl [120].

The roughness values were estimated from AFM images. Depending on the chosen area to take the image, the roughness values could differ  $\pm 10$  nm. It was found that, the  $\sigma_{rms}$  of texture E ( $\sim 56$  nm) had a slight

### 3.3 Nano-textured glass substrates

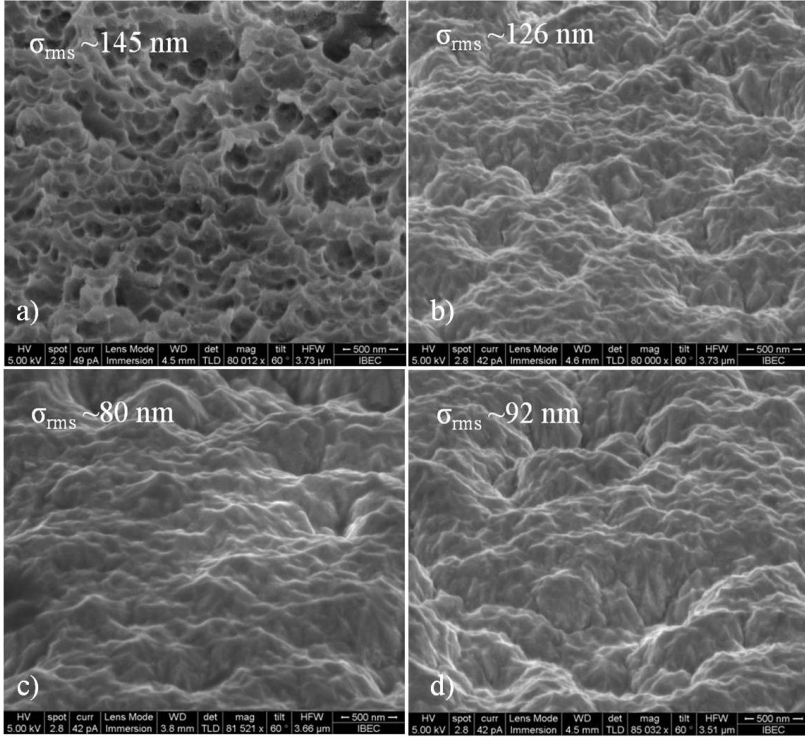


Figure 3.33: SEM (tilted at 60°) images of a) texture S, b) S+AZO1 (500 nm), c) S+AZO2 (700 nm), d) S+AZO3 (1000 nm). The  $\sigma_{rms}$  values were obtained from AFM images.

tendency to increase with the addition of 500 nm, 700 or 1000 nm of AZO and seemed to result in a suitable morphology for the growth of thin film Si solar cells as it did not exhibit peaks or deep valleys that could create cracks, in particular to  $\mu c$ -Si films. Moreover, the craters diameter laid between 500 nm and 1  $\mu m$  and had large opening angles that have been reported to be adequate for thin film silicon solar cells [121, 122].

Texture S, with a high substrate roughness of  $\sigma_{rms} \sim 145$  nm, was found to be porous and randomly etched (Fig. 3.33a)). The deposition of AZO over texture S resulted in a cauliflower-like morphology with smooth valleys and free from sharp peaks or edges. The high surface porosity of texture



### 3 Novel texturing methods for light confinement

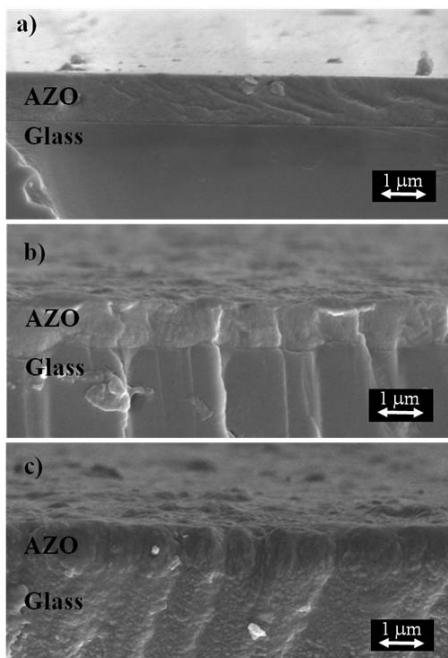


Figure 3.34: Cross sectional SEM images of AZO3 (1000 nm) deposited on a) smooth glass, b) texture E and c) texture S.

S should have significantly controlled the initial phase of the AZO growth over this texture.

The nucleation of the AZO films might have started by filling the highly porous surface and then continued to grow into the bulk columnar phase. This might be the reason for the smooth and continuous transition of texture S/AZO interface as shown in the cross sections SEM images of Fig. 3.34. This also explains the decrease in surface roughness from 145 nm for texture S to 126 nm, 80 nm or 92 nm when different AZO thicknesses (500, 700 or 1000 nm) are deposited above.

For further details on the growth interface between the textures and the TCO, cross sectional TEM images were taken for the AZO2 (700 nm) samples deposited over smooth glass and textures E and S.

It is known that TCOs sputtered on amorphous substrates such as Bo-

rofloat glass tend to follow a growth pattern that consists of an initial stage between 0 to 100 nm called incubation stage in which the film starts growing in an amorphous structure, which becomes polycrystalline after 5-10 nm. Above this incubation zone, a preferentially oriented polycrystalline stage is normally formed and is named the growth or bulk zone [65]. This growth procedure has been observed in TCOs such as  $\text{TiO}_2$ ,  $\text{SnO:F}$ ,  $\text{ZnO}$ ,  $\text{ZnO:Al}$ , and ZITO, etc. [17].

In the case of sputtered  $\text{ZnO}$  on an amorphous substrate, this growth process is fulfilled, the film starts growing in an amorphous structure, continues growing in a randomly oriented polycrystalline phase and ends with most of the  $\text{ZnO}$  columns (crystallites) oriented perpendicular to the substrate with a preferential orientation (002) and  $c$ -parameter of 0.5208 nm [123].

The TEM images exhibited in Fig. 3.35, Fig. 3.36 and Fig. 3.37, permit to identify these different stages of  $\text{ZnO:Al}$  grown on non-textured glass, texture E and texture S, respectively.

In every micrograph, diffraction patterns were taken from the incubation and the bulk zones. In the incubation zone the patterns were measured at two different points, at the amorphous zone and at the polycrystalline area. It was observed that AZO2 grown on non-textured glass, presented the typical AZO growth structure, 5 nm belonging to a- $\text{ZnO}$  followed by 20 nm of randomly oriented crystals and then the higher crystalline stage. Some of the crystallites can be identified in the form of columns, that is the typical morphology of sputtered  $\text{ZnO:Al}$  grown on hot substrate. The electron diffraction confirms the degree of crystallinity at every stage as seen in Fig. 3.35. Furthermore, at higher magnifications it is possible to identify the crystalline lattice planes from which the lattice spacing can be deduced.

In the case of texture E (Fig. 3.36), the sputtered film presents a similar behaviour, with also three differentiable areas. The amorphous area covers also around 5 nm, the randomly oriented crystals of the incubation zone account for  $\sim 100$  nm, and, then the preferentially oriented stage comprises the rest. It is seen here that due to the textured surface, the columns tend to grow perpendicular to the surface colliding between them and creating an additional texture. Therefore, the resultant AZO grows with the superposition of the replica of texture E and the resultant texture created due to the strained overlapped columns.

### 3 Novel texturing methods for light confinement

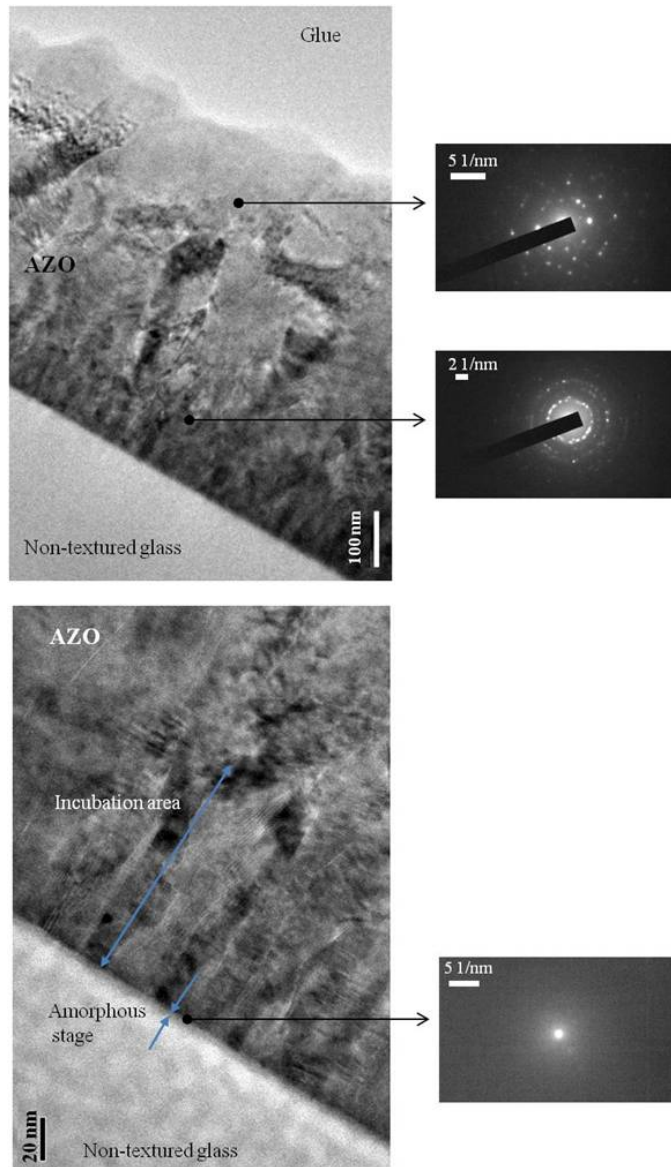


Figure 3.35: Cross sectional TEM images of AZO<sub>2</sub> (700 nm) deposited on smooth glass and electron diffraction patterns at three different zones.

### 3.3 Nano-textured glass substrates

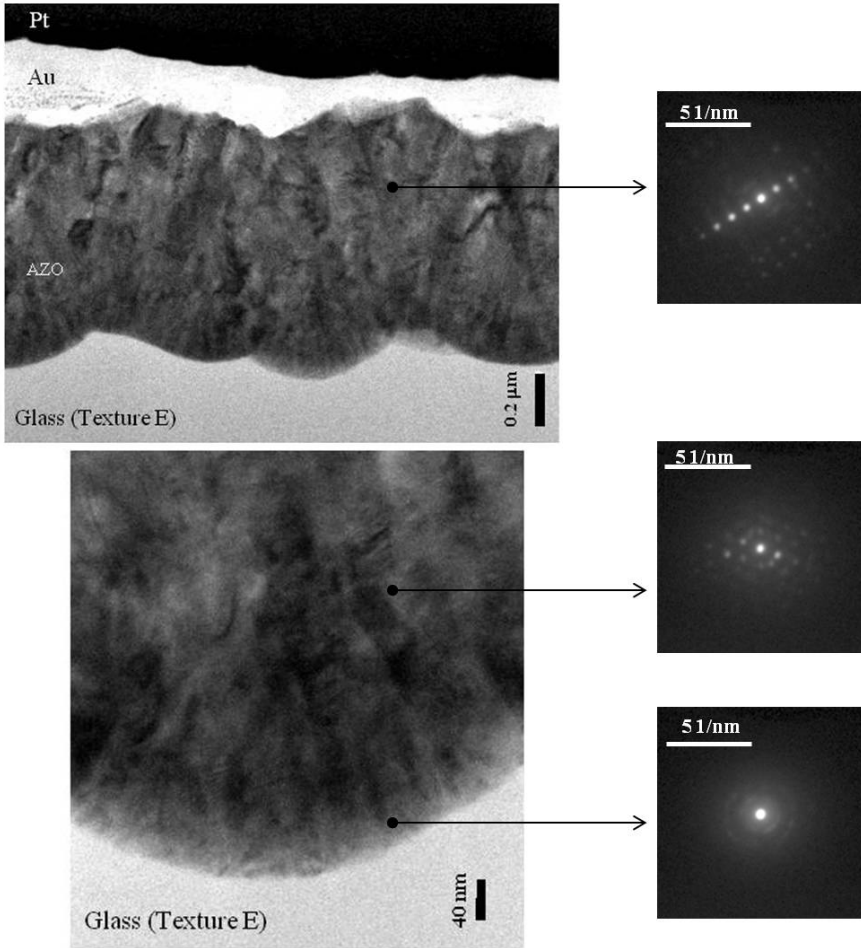


Figure 3.36: Cross sectional TEM images of AZO<sub>2</sub> (700 nm) deposited on texture E and electron diffraction patterns at three different zones.

In texture S, the amorphous stage is inappreciable, it seems that the AZO starts growing directly in a polycrystalline structure. This suggests that maybe remaining Al on the glass surface could be the responsible of inducing directly a polycrystalline growth. Moreover, in the bulk region, the diffraction pattern shows lower preferential orientation than the AZO

### 3 Novel texturing methods for light confinement

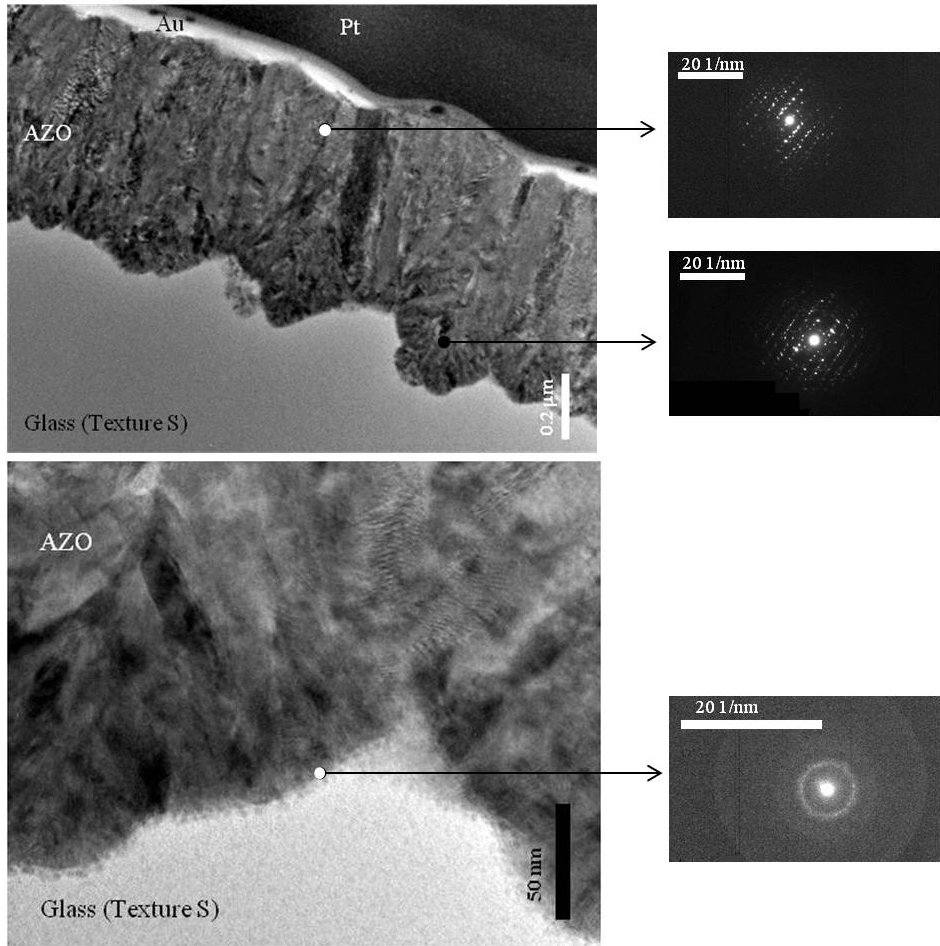


Figure 3.37: Cross sectional TEM images of AZO<sub>2</sub> (700 nm) deposited on texture S and electron diffraction patterns at three different zones.

grown on texture E which is in good agreement with the XRD pattern shown.

The structure of the AZO samples was also analysed by means of XRD measurements. Fig. 3.38 shows the XRD patterns in logarithmic scale to emphasize the low intensity features of the different AZO layers deposited

### 3.3 Nano-textured glass substrates

on smooth substrates and on both textures E and S. All samples were found to be polycrystalline and presented the most intense diffraction peak at around  $2\theta=34.4^\circ$ , indicating a hexagonal wurtzite structure of ZnO with the  $c$ -axis perpendicular to the substrate and oriented preferentially along the [001] direction. Comparing the XRD pattern of three different thicknesses of AZO grown on smooth surfaces, only (002) and its second order reflection (004) were observed. In the case of AZO films over textured substrates, a decrease in the intensity of (002) peak was observed with increase in roughness along with the appearance of other crystallographic peaks corresponding to (100), (102) and (101), probably due to the fact that the grains were turned as the substrate was not smooth, revealing other ZnO wurtzite orientations.

The lattice parameter  $c$  was estimated from the position of the (002) peak according to Eq. 2.4, and all the films showed  $c$  parameter values very similar to that of undoped ZnO ( $c=0.521$  nm). The average crystallite sizes (Eq. 2.6) in the direction normal to the reflecting planes of AZO films over the smooth substrates showed values  $\sim 60$  nm, and this was because these films were deposited under identical conditions which differ only in thickness. The average crystallite size of the films deposited on textured substrates was  $38\pm 5$  nm. This difference in the crystallite size and the appearance of the additional crystallographic peaks for the textured substrates indicate that, the growth of AZO over randomly nano-textured substrates is quite different than on the smooth substrates.

The surface roughness values, electrical and optical properties of the AZO deposited samples are summarised in Table 3.6. The resistivity of the AZO samples with different thickness (average  $\rho=5.6\times 10^{-4}$   $\Omega$  cm) over smooth substrates did not show any significant difference since they were deposited under the same conditions, moreover the average crystallite size values were also the same ( $\sim 60$  nm). AZO deposited over texture E showed resistivity values ( $7\times 10^{-4}$   $\Omega$  cm) slightly higher than that on smooth samples. Texture E presented very smooth craters and its texture might not have critically influenced the AZO growth. The resistivity of the AZO films on texture S showed higher values of  $10^{-3}$   $\Omega$  cm. One of the limiting mechanisms for electrical transport is the grain boundary potential barrier, and less grain boundaries means better conductivity. The presence of different crystal planes in the AZO films over texture S

### 3 Novel texturing methods for light confinement

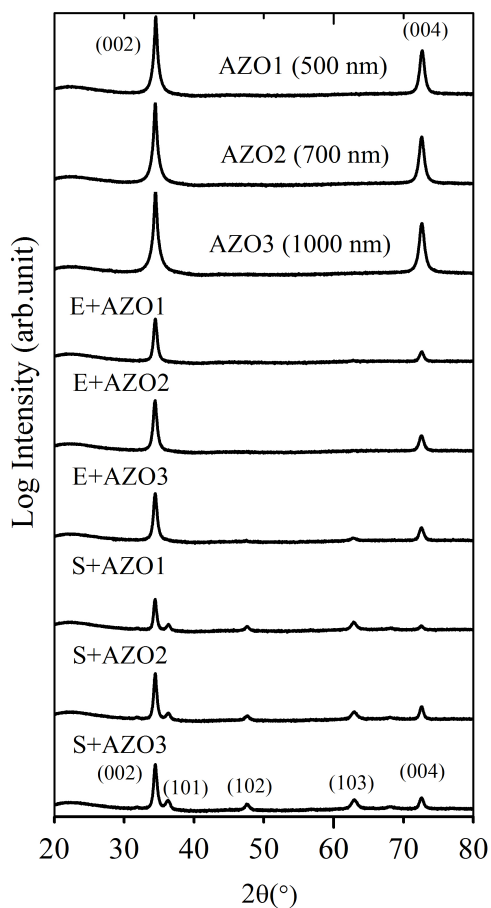


Figure 3.38: XRD patterns of the AZO films deposited over smooth and textured glasses.

compared to the other samples suggests the existence of larger number of grain boundaries, and this might have resulted in the higher resistivity of these samples. The results from the TEM analysis also support this argument since the crystallinity and grain sizes of the bulk growth were lower compared to those on smooth or texture E substrates.

### 3.3 Nano-textured glass substrates

Table 3.6: Surface roughness ( $\sigma_{rms}$ ), resistivity ( $\rho$ ), sheet resistance ( $Rs$ ), integrated transmittance ( $T$ ) in the range 400-800 nm, haze at 600 nm, and figure of merit values ( $\Phi$ ) of the AZO layers deposited on smooth and textured glass along with that of Asahi-U substrate.

Sample name	$\sigma_{rms}$ (nm)	$\rho$ ( $\Omega$ cm)	$Rs$ ( $\Omega$ /sq)	$T$ (400-800 nm) (%)	Haze at 600 nm (%)	$\Phi$ (400-800 nm) ( $10^{-3}\Omega^{-1}$ )
AZO1 (500 nm)	5	$5.6 \times 10^{-4}$	11.2	84.5	-	16.5
AZO2 (700 nm)	7	$5.9 \times 10^{-4}$	8.4	84.5	-	22.1
AZO3 (1000 nm)	9	$5.3 \times 10^{-4}$	5.3	81.8	-	25.4
E+AZO1	66	$7.1 \times 10^{-4}$	14.2	84.5	13.7	13
E+AZO2	58	$6.9 \times 10^{-4}$	9.8	84.5	10.7	19
E+AZO3	67	$7.0 \times 10^{-4}$	7	81.6	14.1	18.8
S+AZO1	126	$1.2 \times 10^{-3}$	23	75.5	43.7	2.6
S+AZO2	80	$1.2 \times 10^{-3}$	16.5	75.9	32.5	3.8
S+AZO3	92	$9.5 \times 10^{-4}$	9.5	73.5	33.1	4.9
Asahi-U	31	-	9.2	78.3	8.3	9.4

The haze ratios of the AZO coated substrates are plotted in Fig. 3.39 a) and b) for texture E and texture S respectively along with that of Asahi-U. The integrated transmittance in the wavelength 400 to 800 nm and the calculated haze values at 600 nm of the AZO coated samples are given in Table 3.6. The haze at 600 nm showed a similar trend to that of the roughness, where the samples with 700 nm of AZO showed the lowest values for both textures E and S. Even though, texture S+AZO2 had a high haze at 600 nm of 33%. The elevated haze in the wavelength range 600 to 1200 nm given in all the AIT coated samples is highly beneficial for light trapping in a-Si/ $\mu$ c-Si solar cells.

More detailed understanding of the surface roughness can be extracted using the frequency distribution analysis of the roughness obtained by the Fourier transform of the AFM images. The power spectral density (PSD) function is the frequency spectrum of the surface roughness measured in inverse length and gives information about the periodicity and amplitude of the roughness. The PSD functions were extracted from AFM images of  $15 \times 15 \mu\text{m}^2$  through the *XEI 1.7.3* software and are plotted in Fig. 3.40. The PSD at low spatial frequencies reflects the large lateral feature sizes that will contribute to lower-angle scattering and the PSD at high spatial frequencies is the result of a surface with small feature sizes which



### 3 Novel texturing methods for light confinement

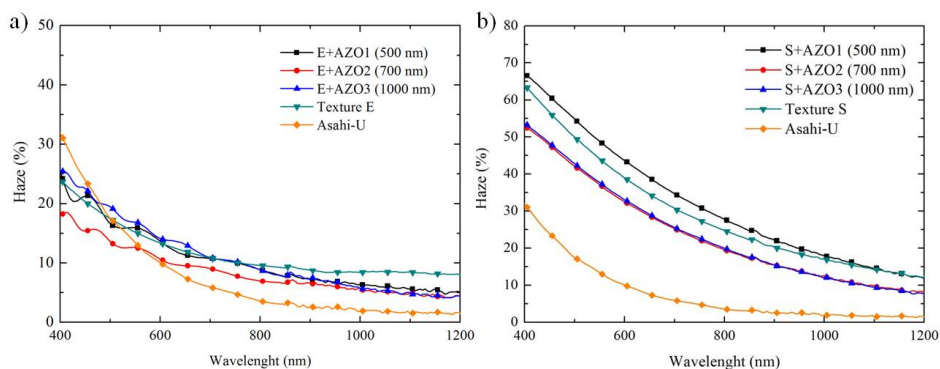


Figure 3.39: Haze values of the samples a) Texture E, texture E + three different AZO thicknesses and Asahi-U substrate. b) Texture S + three different AZO thicknesses and Asahi-U substrate.

gives the large-angle light scattering [124]. AZO grown on texture E and S exhibited higher PSD values than Asahi-U, especially in the low spatial frequency range. This fact indicated their superior light scattering capability and also meant that these textures posed both small and larger feature sizes which could be confirmed by looking at the SEM images (Fig. 3.32 and 3.33), where in all cases a superposition of a micro and a nano-texture was observed.

The desired sheet resistance value of the TCO for the application as front contact in thin film silicon solar cells is  $\sim 10 \Omega/\text{sq}$ . Among the different samples reported here, the sheet resistance showed a tendency to increase with the surface roughness of the glass. Considering the samples coated with the same thickness of AZO, texture S showed sheet resistance values nearly double than the corresponding on smooth substrate and an AZO thickness of nearly 1000 nm was necessary to get a sheet resistance lower than  $10 \Omega/\text{sq}$ . Even the high haze values at 600 nm for AZOs on texture S, the transmittance was too low. Commercially available Asahi-U substrate showed a sheet resistance of  $9.2 \Omega/\text{sq}$ , integrated transmittance of 78.3% in the range 400-800 nm and a haze value of 8.3% at 600 nm. Though texture S with 1000 nm AZO shows very high haze and good sheet

### 3.3 Nano-textured glass substrates

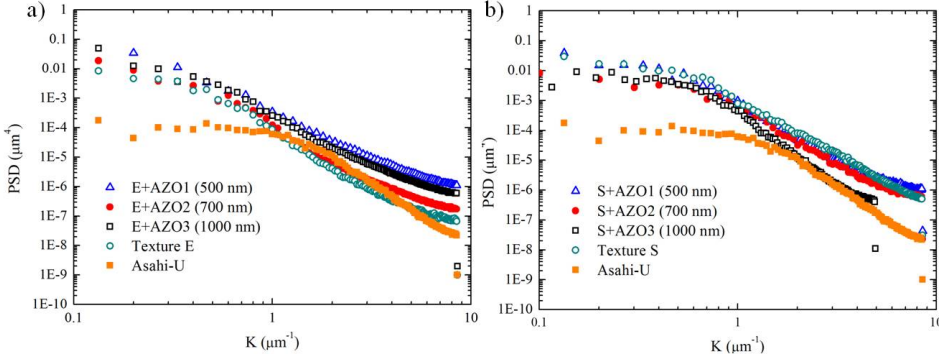


Figure 3.40: PSD plots for a) Texture E, E + AZO1, E + AZO2, E + AZO3, and Asahi-U. b) Texture S, S + AZO1, S + AZO2, S + AZO3, and Asahi-U.

resistance compared to Asahi-U, their transmittance is nearly 5% lower. Texture E with 700 nm AZO showed high transmittance of 84.5%, haze value of 10.7% and a low sheet resistance of  $9.8 \Omega/\text{sq}$ , which is comparable to that of Asahi-U. Texture E with 1000 nm of AZO exhibited 81.5% transmittance with a high haze  $\sim 14\%$  and a very low sheet resistance of  $7 \Omega/\text{sq}$ .

In order to probe the effectiveness of the glass texture on the optical absorption in an a-Si solar cell, 200 nm of a-Si:H were deposited over AZO3 coated texture E, texture S and on smooth glass; followed by 300 nm of Ag. The absorption spectra ( $1-R$ ) of these samples (textured glass/AZO/a-Si:H/Ag) in the wavelength range 350 to 800 nm are compared in Fig. 3.41. The high absorption region below 800 nm was due to the optical band gap absorption of a-Si which has a band gap energy of 1.74 eV. Moreover the oscillations due to thin film interferences disappeared for the textured surfaces and the absorbance in this range (350-800 nm) was highly improved in comparison to the smooth glass.

The calculated figure of merit ( $\Phi$ ) values for TCOs on the smooth and textured glass are also given in Table 3.6. The  $\Phi$  used in this work is an estimation of the quality of the TCO based on the transmittance and sheet resistance but does not take into account the scattering properties. The higher the  $\Phi$ , the better is the TCO. The  $\Phi$  values were calculated

### 3 Novel texturing methods for light confinement

according to Eq. 2.13 given in Chapter 2, Sec. 2.3.5.1. AZO deposited on smooth glass substrates showed the highest  $\Phi$  values, whereas AZO on texture S showed the lowest ones. But, according to the absorption of the device (see Fig. 3.41), texture S showed the highest values. Hence, it can be concluded that this particular  $\Phi$ , is not a qualifying property to be addressed for the light scattering efficiency of a TCO in a solar cell; whereas the haze value plays the decisive role. Other figure of merit considering the scattering properties as well as the transparency and conductivity might have been more appropriate to evaluate rough TCOs. The samples on texture E and texture S showed an increase in absorption (increase in absorption for textured device /absorption for smooth one) of 35% and 53% respectively, compared to those on the smooth glass. The texturing at the glass/TCO in combination with the modulated texture at AZO/a-Si interfaces results in an improved optical scattering yielding a higher absorption.

#### 3.3.3 HCl texturing of AZO grown on AIT substrates

For magnetron sputtered AZO films, wet-chemical etching based on diluted HCl is usually employed to texture the surface. The crater-like feature surface (see Fig. 3.2 b)) that results from the etching has proved to be suitable for thin film silicon solar cells. The biggest issue of this method was to control the homogeneity and the appearance of deep holes on the surface [120, 125]. The morphology of the AZO after the wet etching is highly related to the initial film properties. Up to now there is no theoretical model to predict the etching behaviour depending on the sputtering conditions but many empirical relationships have been done after many years of experiments. For instance, Kluth *et al.* that adapted the Thornton model [43] to magnetron sputtered ZnO films included a study on the HCl etching behaviour depending on the pressure and substrate temperature during sputter deposition of ZnO:Al. More details are explained in Sec. 1.4.1 of Chapter 1.

In this work, the objective was to have the superposition of two textures on the same device, hence, AZO grown on AIT substrates was chemically etched by diluted HCl. The idea was not to optimize the etching procedure but to probe that a double texture (i.e. superposition of two textures) will increase the scattering properties of the sample. The etching parameters

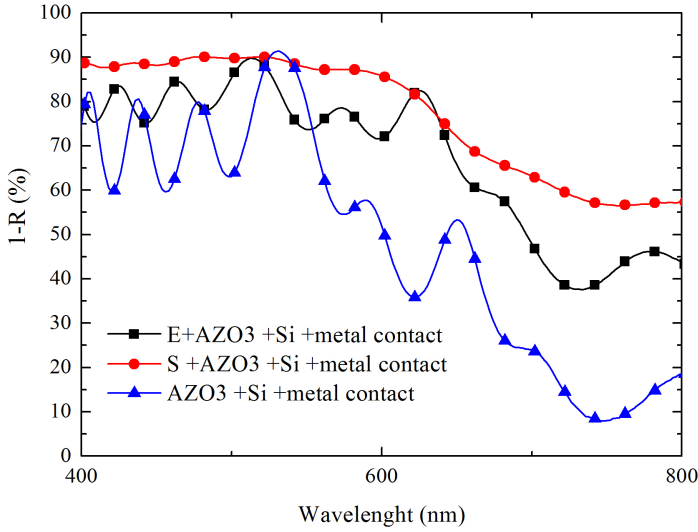


Figure 3.41: (1-R) spectra for smooth glass, texture E and texture S with AZO3/a-Si:H (200 nm)/Ag (300 nm).

were chosen according to previous bibliography [10, 15, 126], and after some previous trials in which the priority was to maintain the  $R_s$  of the AZO lower than  $15 \Omega/\text{sq}$ . The sample chosen for the etching study was texture S2 (Fig. 3.23 b)) with 800 nm of AZO (Fig. 3.42). The AZO thin film was the same that have been studied along this chapter, with the only difference on the deposition time to adjust the thickness. The same AZO deposited on smooth glass was also etched for comparison.

Three etching solutions were prepared with 0.5%, 1% and 2% HCl concentration and the dipping durations were 2 and 10 seconds. The samples were dipped horizontally, i.e. parallel to the solution surface with a slow stirring of the etching solution. After dipping, the samples were rinsed in deionised water and dried with nitrogen. All this process was done at room temperature.

The morphology was studied with SEM, the  $R_s$  with a four point probe

### 3 Novel texturing methods for light confinement

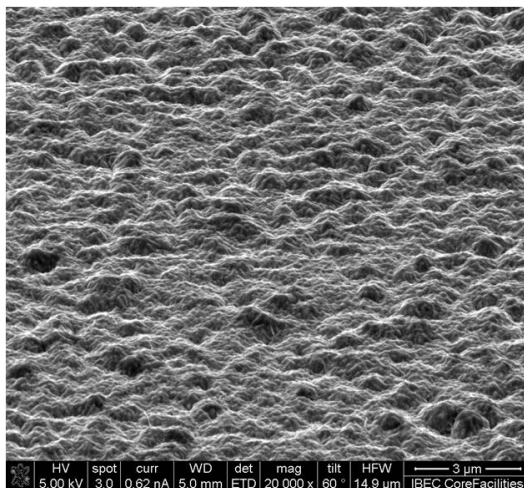


Figure 3.42: SEM image of AZO (800 nm) deposited on texture S2.

system and the scattering properties were evaluated by measuring the haze factor using a spectrophotometer.

Fig. 3.43 and Fig. 3.44 present the the SEM micrographs and haze values of the samples after the etching procedure. It is observed that for the lower etchant concentration, no substantial change was appreciable on the AZO surface, as deduced from the haze values, it seemed that the surface was even smoothed. Therefore, 0.5% HCl concentration was not enough to create a texture on AZO grown on AIT glass, even after dipping for 10 s. However, HCl (2%) formed deep holes even for a dipping duration of 2 s, as a consequence, the haze factor was improved to higher values but probably the cells will grow shunted on such surfaces with large number of pin holes. The  $R_s$  of the as-deposited AZO on S2 was  $11 \Omega/\text{sq}$  and just increased up to  $12 \Omega/\text{sq}$  with the etching in 0.5% HCl solution for 2 and 10 s. For 1% and for 2% the  $R_s$  increased until  $12 \Omega/\text{sq}$  for 2 s and up to  $14 \Omega/\text{sq}$  for 10 s.

To check whether the etching solution has the same effect on AZO grown on smooth glass, AZO (800 nm) was etched during 10 s by HCl 0.5% and 2%. But as shown in the SEM images and haze factor of Fig. 3.45 the etching behaviour was very different to that on AIT glass.

### 3.3 Nano-textured glass substrates

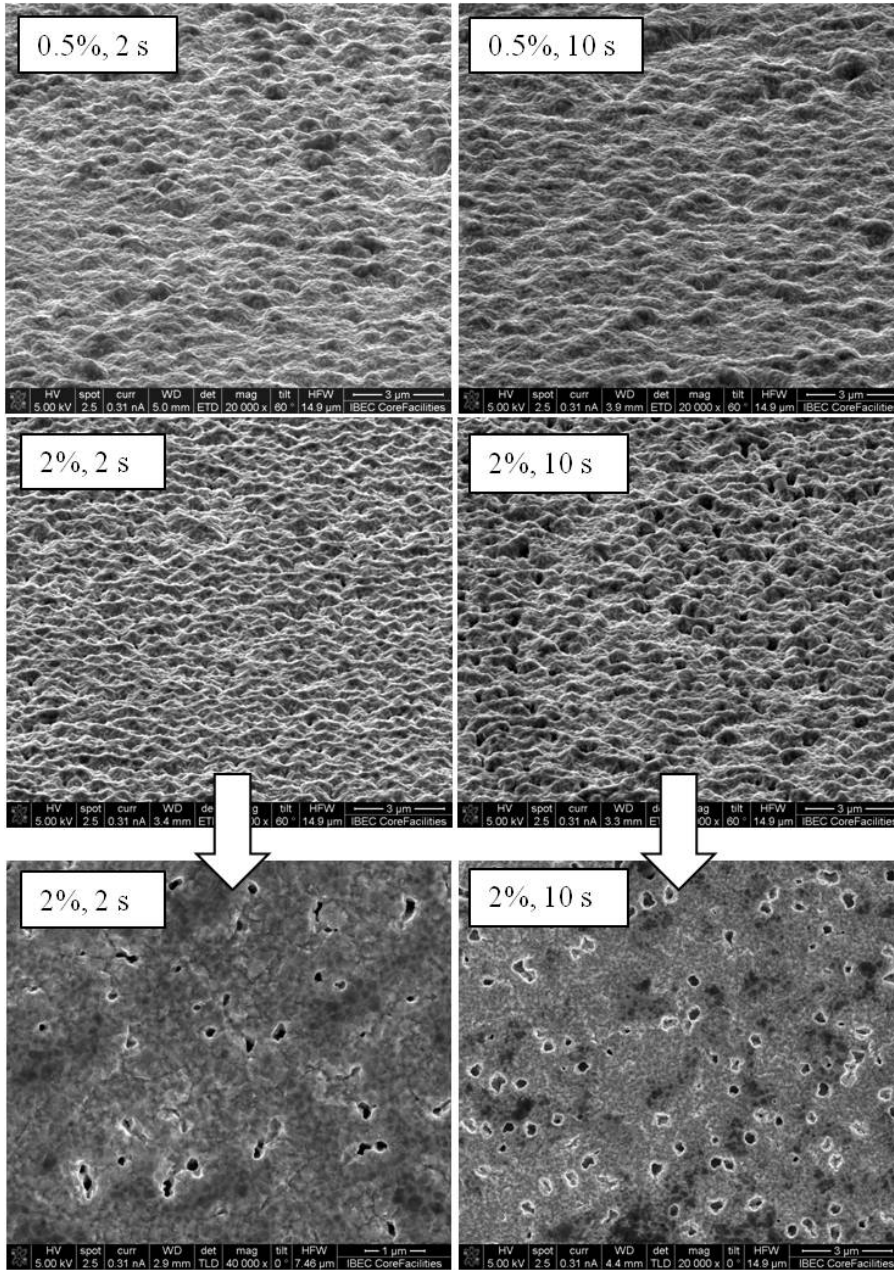


Figure 3.43: SEM images of etched AZO on AIT glass dipping in HCl (0.5% and 2%) solution for 2 and 10 seconds. The two bottom images are non-tilted micrographs.

### 3 Novel texturing methods for light confinement

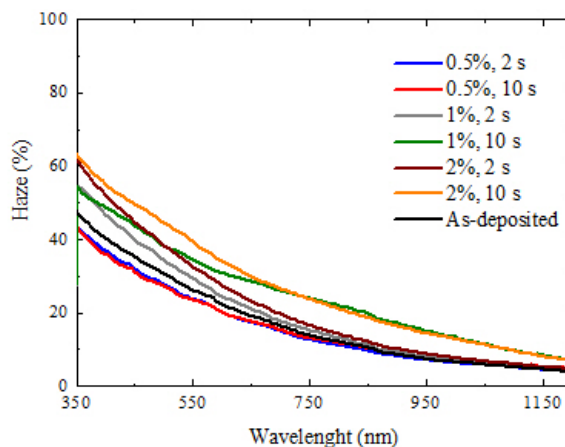


Figure 3.44: Haze values of as-deposited AZO on AIT glass and of the same sample after dipping in HCl (0.5%, 1% and 2%) solution during 2 and 10 seconds.

These results implied that, creating superposition of textures with AIT glass and wet etching of AZO is a very difficult process and hence was discarded from studying further. It is already very difficult to control the etching behaviour in sputtered AZO thin films on smooth substrates as many studies have demonstrated [120, 125], hence, to control the etching process on textured AZO films deserves much time, effort, and a deep understanding of the process. What we have observed is that the same etching conditions led to very different textures if the substrate is rough or smooth so the etching parameters used in smooth substrates will not work on AIT glasses. What we have concluded is that low concentrations do not seem to affect the surface, whereas higher concentrations form deep holes instead of creating a typical sputtered-etched AZO surface.

#### 3.3.4 Thin film silicon solar cells on AIT substrates

In order to prove the suitability of the AIT glasses on solar cells, different trials with thin film silicon solar cells have been realized.

The first trial was performed on textures E1 and E2 achieved by evap-

### 3.3 Nano-textured glass substrates

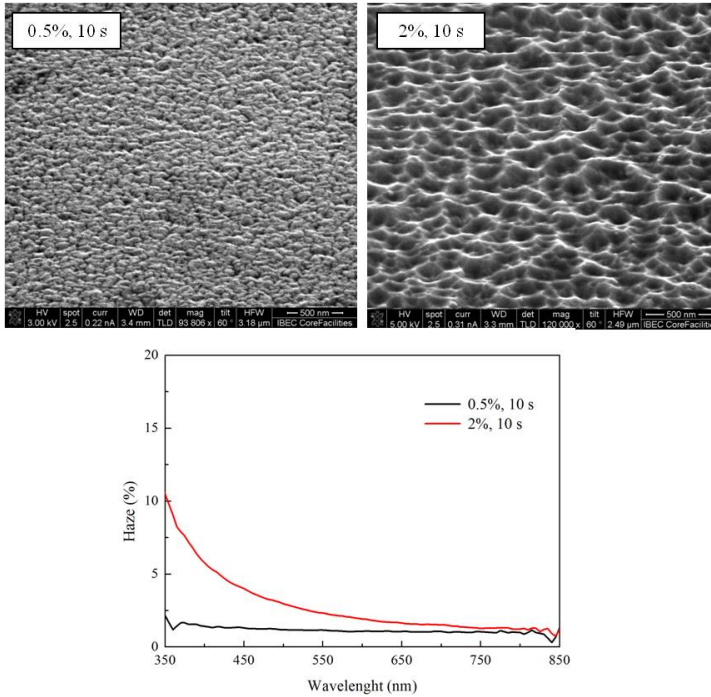


Figure 3.45: SEM images and haze factor of etched AZO on smooth glass dipping in HCl (0.5% and 2%) solution during 10 seconds.

orating the Al in the AIT process (Fig. 3.21 b) and c) in Sec. 3.3.1.4), and a-Si:H solar cells were deposited at the research centre CIEMAT of Madrid. The second trial was done also with a-Si:H solar cells, but were fabricated at UB and the substrates were the two extremely different textures E and S as shown in Fig. 3.28 and Fig. 3.29, respectively. Some of the results have been published in [127] and [128].

Furthermore, tandem solar cells (formed with an a-Si:H and a pm-Si:H solar cell) were fabricated at the *Laboratoire de Physique des Interfaces et des Couches Minces* in Palaiseau, France. In this case the AIT substrates used were texture S1 and S2 as shown in Fig. 3.23 a) and b).



### 3.3.4.1 a-Si:H solar cells fabricated at CIEMAT

Identical a-Si:H *pin* structures have been deposited over E1 ( $\sigma_{rms} \sim 70$  nm) and E2 ( $\sigma_{rms} \sim 90$  nm), and over non-textured glass covered with 400 nm of AZO, and over the commercial Asahi-U type substrates as the reference. The experimental details as well as the optical and morphological analyses were explained in Sec. 3.3.1.4.

Thin AZO layers of 400 nm and  $6.7 \Omega/\text{sq}$  have been deposited at CIEMAT on both textures E1 and E2. The morphology of the samples was very similar to that of Fig. 3.46, presenting a  $\sigma_{rms} \sim 57$  nm for E1+AZO and  $\sigma_{rms} \sim 68$  nm for E2+AZO. The image is the result of 800 nm of AZO on textures E1 and E2, but for the solar cells a more optimized AZO of 400 nm was used. The haze factor values at 600 nm were 7% for E1+AZO and 15% for E2+AZO. The  $R_s$  was also measured and gave values of  $R_s \sim 13 \Omega/\text{sq}$  and  $R_s \sim 14 \Omega/\text{sq}$  for E1+AZO and E2+AZO, respectively.

Amorphous silicon solar cells in the *pin* configuration were deposited using RF-PECVD. The a-Si:H structure consisted of 7.5 nm thick *p*-type a-Si:H layer, 5 nm thick carbon-graded buffer layer, 400 nm thick absorber and 30 nm thick *n*-type a-Si:H layer. Further details are explained in the experimental chapter in Sec. 2.1.4. Solar cells with an area of the order of  $0.1 \text{ cm}^2$  were prepared by evaporating Al back contacts.

As seen in Fig. 3.47, the solar cells deposited on E1+AZO and E2+AZO showed a total reflectance ( $R$ ) significantly lower than that obtained in the case of smooth Borofloat glass, whose average value was  $R_{400-800} = 31.8\%$ . The increase in the roughness at the modulated texture interface of AZO/a-Si:H resulted in an improved optical coupling because the refractive index varies progressively from glass to the silicon layer, and hence the reflected light component was decreased. Higher surface roughness means better optical coupling and lower optical losses, which explains that texture E2+AZO was found to be the most appropriate for the fabrication of the cells, presenting an average reflectance of  $R_{400-800} = 14.6\%$ . This value was very close to that recorded for the cells fabricated over the commercial Asahi-U substrate ( $R_{400-800} = 13.7\%$ ). By comparing these two curves, a slightly better behaviour was observed for E2+AZO at short wavelengths whereas the Asahi-U substrate behaved softer and was more efficient in

### 3.3 Nano-textured glass substrates

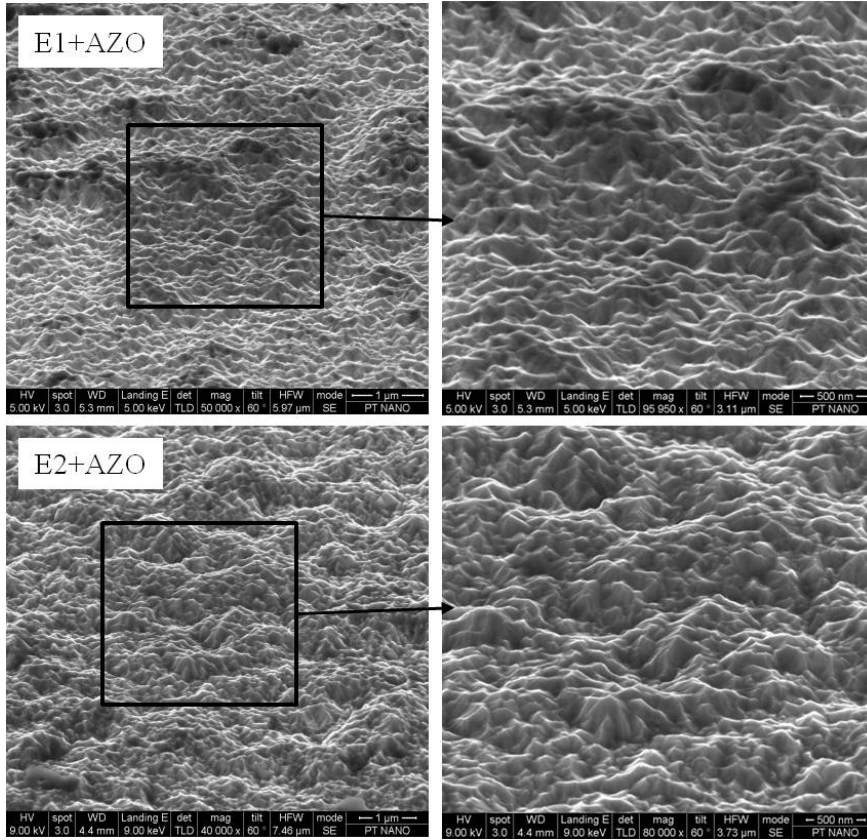


Figure 3.46: SEM tilted micrographs of texture E1 and E2 with 800 nm thick AZO.

minimizing losses in the vicinity of the absorption edge of a-Si:H ( $\lambda \sim 750$  nm).

The surface reflectance of the solar cell has a direct influence on the external quantum efficiency (EQE) of the device. As can be seen in Fig. 3.48, the EQE curve of the device on the flat substrate has the typical maximum and minimum peaks which arise from the optical interferences between the incident and reflected light at the interfaces glass/AZO and AZO/a-Si:H. The improvement of the optical coupling associated with the increase of the surface roughness results in a progressive increase of the EQE through-

### 3 Novel texturing methods for light confinement

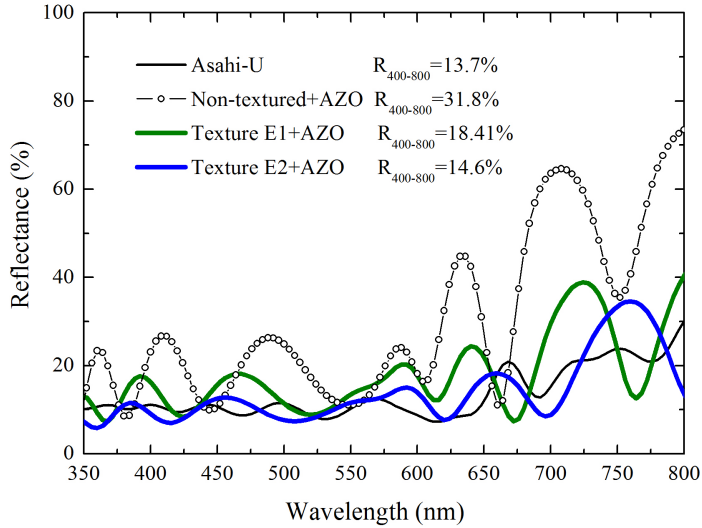


Figure 3.47: Comparative reflectance curves of the devices deposited on E1, E2, non-textured Borofloat glass and Asahi-U substrate.

out all the wavelength range, being more evident for E2+AZO. Moreover, the textured surface also leads to a curve with a softer and smoother EQE profile and therefore, more homogeneous. Comparing the device grown on the commercial substrate Asahi-U, and that grown on the E2+AZO, the EQE shows a very similar curve in almost all the range of response. It is worth noticing that in the range of longer wavelengths,  $\lambda > 700$  nm, the EQE obtained with E2+AZO is slightly higher than that obtained for the Asahi-U. In terms of generated photocurrent, it seems evident that the main disadvantage of the E2+AZO is not associated to the texture of the glass, but to the higher optical absorption of the AZO in comparison to the  $\text{SnO}_2:\text{F}$  for  $\lambda \leq 375$  nm.

Considering the electrical characteristics of these solar cells under illumination (see Table 3.7 and Fig. 3.49), it can be observed that the parameter that better shows the substrate effect is the short circuit

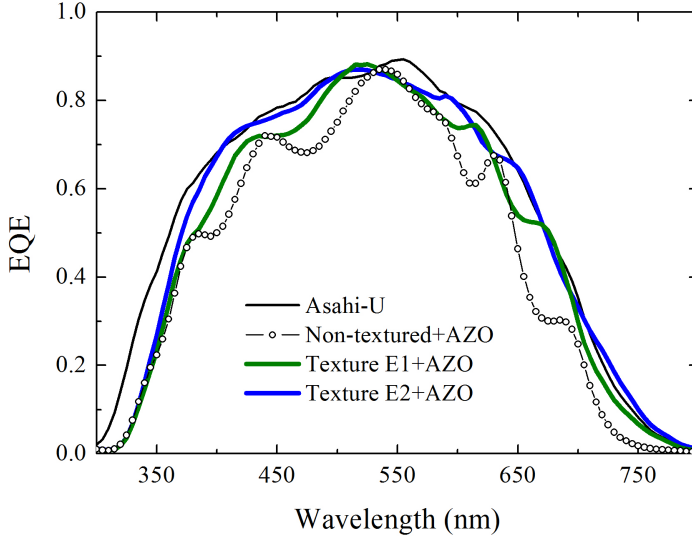


Figure 3.48: Comparison between the external quantum efficiency curves obtained for the devices on each of the substrates tested.

current. The solar cells deposited over E1+AZO showed an increase  $\Delta J_{SC} \sim 1.5 \text{ mA/cm}^2$  in short circuit current density compared to the ones deposited over non-textured+AZO substrate. In the case of E2+AZO, this increase is found to be much higher, reaching values in the order of  $\Delta J_{SC} \sim 2.3 \text{ mA/cm}^2$ . The use of Borofloat/AZO introduces an optical absorption loss due to the band edge absorption differences between AZO and  $\text{SnO}_2\text{:F}$  (FTO) of Asahi-U. This is evident in the EQE as shown in Fig. 3.48. But the short circuit current for the solar cells deposited over E2+AZO is only  $0.33 \text{ mA/cm}^2$  less than that for Asahi-U substrate. It should be noted that an excellent  $J_{SC}$  is obtained even with the existence of the slightly rectifying contact at the interface AZO/(p)a-SiC:H which weakens the driving electric field in the absorber, reducing the collection of photo-generated holes. This potential barrier appears because of the band gap differences between the ZnO:Al and

### 3 Novel texturing methods for light confinement

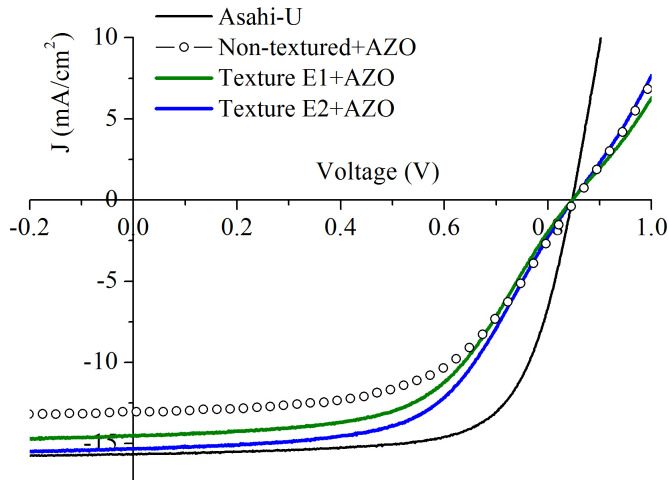


Figure 3.49:  $J$ - $V$  curves under AM1.5G illumination for the solar cells deposited on different substrates.

Table 3.7: Average solar cell parameters values under AM1.5G illumination for the cells on different substrates.

Parameters	Asahi-U	E1+AZO	E2+AZO	Non-textured+AZO
$J_{SC}$ (mA/cm <sup>2</sup> )	15.70	14.57	15.37	13.09
$V_{OC}$ (V)	0.850	0.843	0.845	0.851
$FF$ (%)	69.2	55.4	56.8	54.8
$Eff$ (%)	9.23	6.81	7.35	6.10
$R_{SC}$ (k $\Omega$ cm <sup>2</sup> )	1.5	1.0	1.0	1.0
$R_{OC}$ ( $\Omega$ cm <sup>2</sup> )	6.2	24.1	16.8	24.0

the a-Si  $p$ -type film and yields to an S-shaped  $J$ - $V$  characteristics [129]. The main consequence of this non-ohmic contact is a loss of almost 2% of efficiency in comparison to the cells over Asahi-U, which is reflected through the high open circuit resistance and the low fill factor (FF).

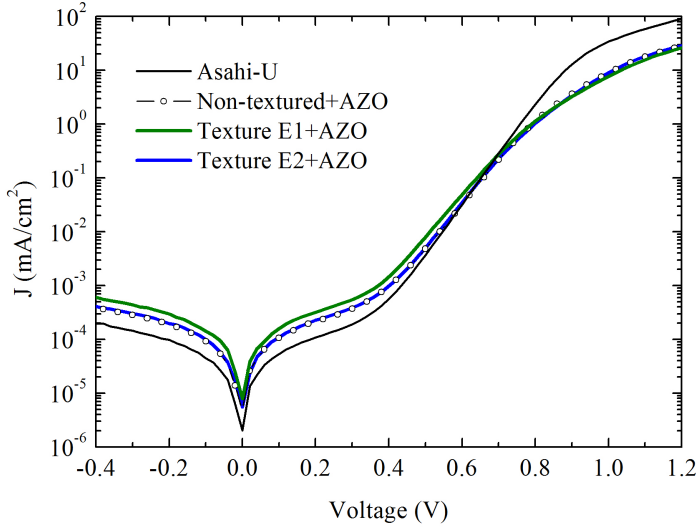


Figure 3.50: Comparison between dark  $J$ - $V$  curves for a-Si:H solar cells deposited on different substrates.

The dark  $J$ - $V$  curves (Fig. 3.50) obtained for the different variants of Borofloat/AZO are practically identical, suggesting that the texture of the substrate has no effect on the dark current behaviour of the deposited amorphous silicon  $pin$  diode.

On the other hand, some differences arise when these cells are compared with the solar cell grown on Asahi-U. Visual analysis of the curve obtained on the commercial substrate presents a lower current in the range  $-0.4$ ,  $+0.4$  V, which suggests a slightly higher parallel resistance ( $R_{OC}$ ). Finally for voltages  $>+0.8$  V, larger current values indicate lower series resistance values. All these differences can be assigned to the differences between the AZO and the  $SnO_2:F$ . The existence of the rectifying contact explains the higher series resistance ( $R_{SC}$ ) on Borofloat/AZO samples. It has been demonstrated that ZnO under hydrogen exposure induces an electron accumulation layer on the ZnO:Al/ $p$  interface (caused during the  $p$  layer growth in the PECVD system) which is the responsible for the decrease in

the FF of *pin* a-Si:H solar cells [129, 130].

#### 3.3.4.2 a-Si:H solar cells fabricated at UB

a-Si:H solar cells were deposited at UB over AZO3 (1000 nm) coated textures E and S (Fig. 3.32 d) and Fig.3.33 d)), smooth Borofloat glass and also over Asahi-U substrate coated with a very thin AZO film (40 nm). The electrical, morphological and optical properties of the substrates are already analysed in Sec. 3.3.2.

In order to correct the potential barrier that was seen in the first trial (a-Si:H solar cells deposited at the research centre CIEMAT) now, a thin *p*-type  $\mu\text{c-Si}$  layer of  $\sim 25$  nm was deposited between the front AZO and the a-Si *p*-type layer. It is well known that an  $\text{SnO}_2$  exposed to atomic hydrogen (needed for  $\mu\text{c-Si}$  growth) is easily reduced to metallic Sn which yields to a decrease in the  $\text{SnO}_2$  transmittance [131]. For this reason 40 nm of AZO were deposited over Asahi-U. A conventional RF-PECVD (13.56 MHz) multi-chamber reactor was used for the deposition of thin film silicon layers, the thicknesses of *p*-, *i*- and *n*-type a-Si layers were  $\sim 15$ ,  $\sim 200$  and  $\sim 15$  nm respectively. The solar cells of  $1 \text{ cm}^2$  area were completed by evaporating silver back contacts. Further information on the experimental details is given in Chapter 2, Sec. 2.1.4.

The reflectance spectra of the solar cells fabricated over different substrates are shown in Fig. 3.51. The solar cells deposited over the texture E and texture S show an integrated reflectance ( $R_{400-800}$ ) (21% and 18% respectively) significantly lower than that obtained for the non-textured Borofloat glass ( $R_{400-800}=34\%$ ) in the wavelength range 400-800 nm. The  $R_{400-800}$  value for the cells on the rougher surface was 3% lower than those on the soft texture. Even though the reflectance losses are reduced using these textured surfaces, their  $R_{400-800}$  values were still far from the value given by the commercial Asahi-U substrate ( $R_{400-800}=14.4\%$ ).

This difference might be due to the differences in thickness and optical properties of the glasses used, differences in optical absorption of  $\text{SnO}_2\text{:F}$  and AZO, and also in the type of roughness. When comparing the two textured substrates, very similar behaviour is observed for both soft and rough textures at short wavelengths, whereas the rougher texture is more efficient in minimizing losses in the range 650-750 nm. The re-

### 3.3 Nano-textured glass substrates

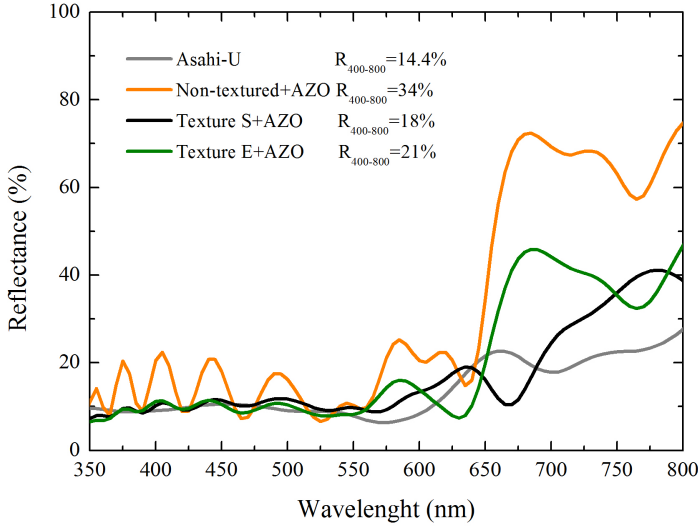


Figure 3.51: Comparative reflectance curves of solar cells fabricated on texture E and texture S, non-textured Borofloat glass and Asahi-U substrate.

reflectance of the solar cell has a direct influence on the external quantum efficiency (Fig. 3.52). The non-textured sample presents slight interference fringes that arise from the optical interferences of the incident and reflected light at the device interfaces (glass/AZO, AZO/Si). These fringes become smoother for the textured substrates but the softest EQE profile is given by the Asahi-U glass. Although AIT textures present  $\sigma_{rms}$  values higher than that of Asahi-U, they present larger lateral feature sizes ( $\sim 1 \mu\text{m}$ ) in comparison to the Asahi-U surface. This could be the reason why the highest roughness (which is estimated from the  $15 \times 15 \mu\text{m}^2$  AFM images) does not completely suppress interferences in EQE. It is worth noting that the cells have two *p*-type layers with a total thickness of 40 nm and is responsible of the high absorption at short wavelengths. This has significantly influenced in reducing the cell efficiency. The EQE of the cells on textured surfaces present a notable improvement at longer wave-



### 3 Novel texturing methods for light confinement

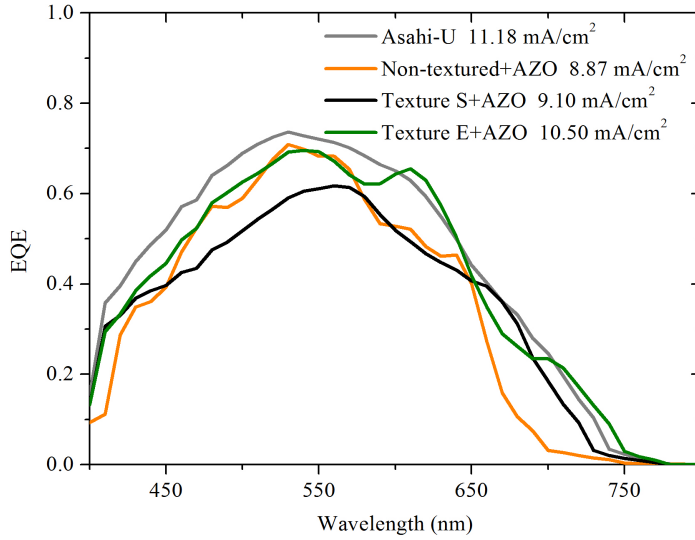


Figure 3.52: Comparison between the external quantum efficiency curves obtained for the devices on each of the substrates tested.

lengths (650-750 nm) in comparison to the smooth glass which resulted in achieving higher short circuit current values confirming the effectiveness of the light trapping by these textures.

Considering the electrical characteristics of these solar cells under illumination (see Table 3.8 and Fig. 3.53), it can be observed that the devices have grown successfully over both extremely different textures. Moreover, the S-shape problem that appeared in Fig. 3.49 has been solved. The parameter that better shows the substrate effect is the short circuit current. The solar cells deposited over the soft texture showed an increase of  $\Delta J_{SC} \sim 1.63 \text{ mA/cm}^2$  in short circuit current density compared to the ones deposited over non-textured+AZO substrate. In the case of the texture S+AZO, this increase was found to be lower,  $\Delta J_{SC} \sim 0.23 \text{ mA/cm}^2$ . It is possible that the substrate roughness for texture S was too high and developed some defects during the Si growth, especially during the growth

### 3.3 Nano-textured glass substrates

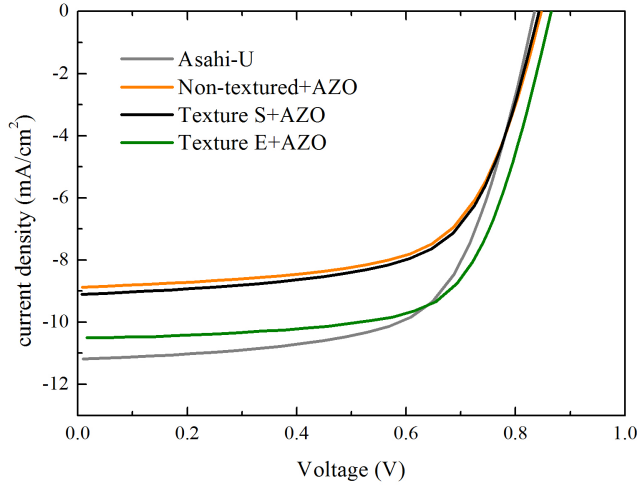


Figure 3.53:  $J$ - $V$  curves under AM1.5G illumination for the a-Si:H solar cells deposited on different substrates.

of microcrystalline  $p$ -type silicon layer. Comparing both textures it seems that texture E is more suitable for a-Si solar cells, however, the roughness morphology needs to be further optimized as well as the Si thin film device.

Table 3.8: Average solar cell parameters values under AM1.5G illumination for the cells on different substrates.

Parameters	Asahi-U	E+AZO	S+AZO	Non-textured+AZO
$J_{SC}$ (mA/cm <sup>2</sup> )	11.18	10.50	9.10	8.87
$V_{OC}$ (V)	0.84	0.84	0.85	0.86
$FF$ (%)	65	68	64	59
$Eff$ (%)	6.1	6.0	4.9	4.5

### 3 Novel texturing methods for light confinement

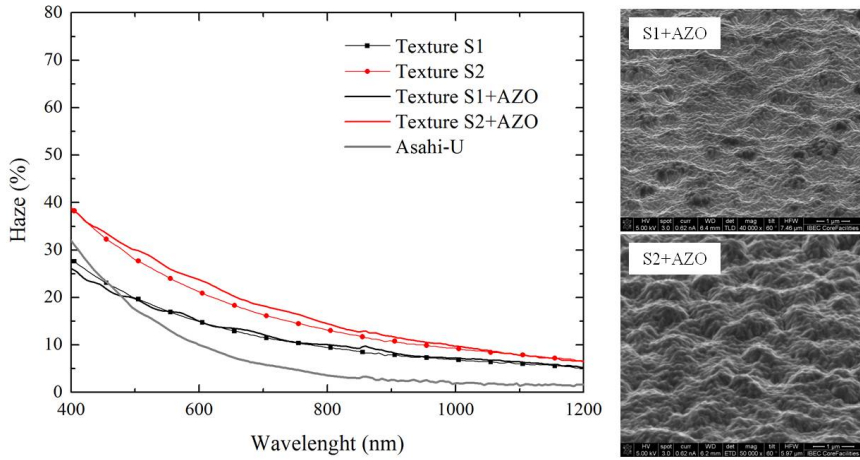


Figure 3.54: Left graph corresponds to the haze values of textures S1, S2, S1+AZO, S2+AZO and Asahi-U. The right images correspond to the SEM images of S1+AZO and S2+AZO surfaces.

#### 3.3.4.3 a-Si:H/pm-Si:H tandem solar cells on AIT substrate

Tandem silicon thin film solar cells with a-Si:H/pm-Si:H structure were fabricated over AIT substrates at the *Laboratoire de Physique des Interfaces et des Couches Minces* from the *École Polytechnique* in Palaiseau, France.

The chosen AIT substrates were S1 and S2 (Fig. 3.23 a) and b) in Sec. 3.3.1.4) with roughness values of 80 nm and 90 nm, respectively. Details on the preparation of the substrates and its characterization are already explained in Sec. 3.3.1.4.

Over these substrates (S1 and S2) and over non-textured glass, 900 nm of ZnO:Al<sub>2</sub>O<sub>3</sub> (2%) were deposited through dc magnetron sputtering. The parameters of the deposition process are those described in Sec. 3.3.2.

The haze factors of S1 and S2 and of S1+AZO and S2+AZO are plotted in Fig. 3.54 together with that of Asahi-U. Also the morphology of S1+AZO and S2+AZO is shown in Fig. 3.54, and Table 3.9 shows the integrated transmittance in the range 400-800 nm, the sheet resistance, the haze at 600 nm and the  $\sigma_{rms}$  of the samples.

### 3.3 Nano-textured glass substrates

Table 3.9: Surface roughness ( $\sigma_{rms}$ ), Sheet resistance ( $Rs$ ), Integrated transmittance  $T$  (400-800 nm), Haze at 600 nm of the AZO layers deposited on smooth and textured glass along with that of Asahi-U substrate.

Sample	$\sigma_{rms}$ (nm)	$Rs$ ( $\Omega$ /sq)	$T$ (400-800 nm) (%)	Haze at 600 nm (%)
AZO (900 nm)	5	8	80.63	-
S1+AZO	80-90	12	81.28	15
S2+AZO	90-100	12	77.07	23.7
Asahi-U	31	9.2	78.3	8.3

The cells were deposited in a home-made RF-PECVD reactor with mono-chamber cluster configuration [58]. The structure of the tandem cells was with a top cell of a-Si:H having a thin active layer of 65 nm and a bottom cell of pm-Si:H with 500 nm thick intrinsic layer. The tandem solar cell was optimized for a maximum current of 7 mA/cm<sup>2</sup> with the aim of matching it with the next stacked solar cells. Further details on the solar cell preparation are explained in the experimental chapter in Sec. 2.1.4. The cells were finished with a back contact of 0.126 cm<sup>2</sup> that consist of 80 nm of AZO and sputtered Ag.

According to the recorded spectra, the total reflectance is highly minimized when the substrate is textured and as explained in the case of a-Si solar cells on AIT substrates, the refractive index varies progressively at the interface AZO/Si. Then, the interference fringes are smoothed and the reflectance is decreased. Higher roughness leads to a lower integrated reflectance in the range 400-800 nm. The device deposited on texture S1 ( $\sigma_{rms} \sim 80$  nm) resulted in an integrated reflectance of 19.7% and on texture S2 was 17.9%, just 3.2% higher than that given by Asahi-U glass. Both textures have reduced the total reflectance which was 30.7% when the cells were deposited on non-textured substrate.

The four cells were deposited at the same time but the cell deposited over non-textured glass appeared to be shunted, probably because it was placed at the border during deposition and grew with poor homogeneity. As the doped layers are very thin, the lack of homogeneity can strongly affect the device performance. In the  $J-V$  plot in Fig.3.56 the short-circuited cell is not shown. Table 3.10 contains the solar cell parameters data of the tandem solar cells grown on texture S1+AZO, S2+AZO and Asahi-

### 3 Novel texturing methods for light confinement

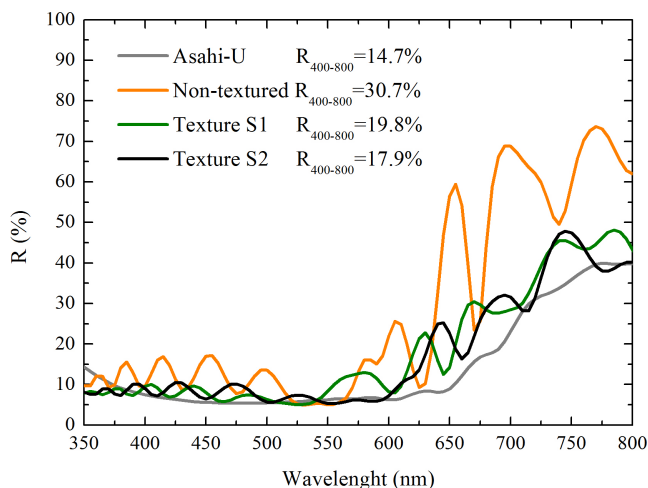


Figure 3.55: Comparative reflectance curves of tandem solar cells fabricated on texture S1 and S2, non-textured Borofloat glass and Asahi-U substrate.

U glass. The results show that the cells have grown without shunting albeit the high roughness of their surface. S2 that is the roughest texture gives better values than S1 and gives a higher voltage value than the one achieved with Asahi-U. The current density, which was optimized to be  $7 \text{ mA/cm}^2$ , was almost reached for the Asahi-U and was not far for texture S2.

In conclusion, AIT method performs suitable textures for pm-Si based solar cells. The cells grow without shunting and gave always greater short circuit current values than the cells grown on smooth substrates. The integrated reflectance in the range 400-800 nm of the whole device has always lower values in comparison to the smooth glass. The EQE is softened and is improved at longer wavelengths (650-750 nm). Nevertheless, Asahi-U glass exhibits always the best solar cell properties.

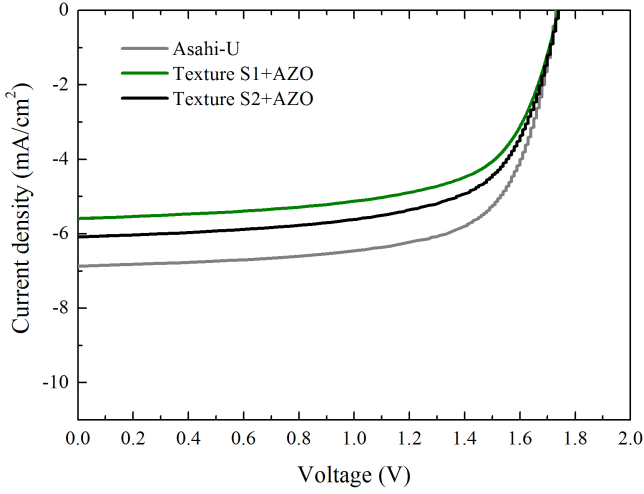


Figure 3.56:  $J$ - $V$  curves under AM1.5G illumination for the tandem solar cells deposited on different substrates.

Table 3.10: Average solar cell parameters values under AM1.5G illumination for the cells on different substrates.

Parameters	Asahi-U	S1+AZO	S2+AZO
$J_{SC}$ (mA/cm <sup>2</sup> )	6.86	5.6	6.13
$V_{OC}$ (V)	1.73	1.74	1.75
$FF$ (%)	68.2	64.4	65.8
$Eff$ (%)	8.1	6.27	7.1
$R_{SC}$ (k $\Omega$ cm <sup>2</sup> )	6.1	5.7	6.2
$R_{OC}$ ( $\Omega$ cm <sup>2</sup> )	20.1	27.9	23.4

### 3.4 Conclusions

This chapter is focused on improving the light trapping properties of Si solar cells by manipulating the light path. Two different approaches have been studied, the first one was to create a periodic pattern on the front

### 3 Novel texturing methods for light confinement

AZO by means of direct laser ablation and the second, was to randomly texture the glass substrate through the Aluminium Induced Texturing method.

It has been demonstrated that laser technology is able to create different patterns on AZO samples increasing the haze factor and keeping a good  $R_s$  and transmittance values. The structure with the best equilibrium between haze and conductivity was the linear pattern with a pitch and groove depth of 10  $\mu\text{m}$  and 360 nm, respectively, which yielded to an  $R_s$  of 11  $\Omega/\text{sq}$  and a haze of 12.7% at 600 nm. However, as the intention was to avoid using laser interferences, the minimum period was limited by the laser spot and it was not possible to create patterns in the sub-micron range that are the optimum for Si thin film solar cells.

The second approach was to texture the glass surface by means of the AIT. The process parameters such as the Al deposition method, the annealing time and temperature, the Al thickness and the etching conditions have been varied in order to control the resultant glass roughness. Among all the varied parameters, the most critical were the Al deposition method and the glass cleanness, as it is an interface reaction. The energy at which the Al particles reach the glass determines the adhesion and the compactness of the film which will define the degree of resultant glass roughness. By using evaporation (Al particles reaching the glass at 0.1-0.2 eV) it was possible to create morphologies based on smooth U-shaped craters (0.5 to 1  $\mu\text{m}$ ) and roughness ranging from 50 nm to 90 nm, whereas the sputtered films (Al particles 2-30 eV) resulted in very rough and porous textures with  $\sigma_{rms}$  values upto 145 nm. With the sputtering, the roughness could be easily tuned, for instance, by changing the power, while it was difficult to control through evaporation.

AZO grown over the smooth U-shape crater morphology lead to a double texture with haze values above 10% at 600 nm, transparency above 84%, and  $R_s \sim 7 \Omega/\text{sq}$  whereas AZO on very rough glass result in cauliflower-like surface with haze values  $>32\%$  at 600 nm,  $R_s$  around 9.5  $\Omega/\text{sq}$  and transmittance of 74%. Single junction a-Si:H and tandem solar cells with a-Si:H/pm-Si:H structure were deposited on some different AIT textures and it was demonstrated an improvement of the short circuit current in comparison to the cells deposited on smooth glass as well as a reduction of the device reflectivity.

# 4 Transparent conducting upconverters

In this chapter, upconversion mechanism is used to exploit part of the solar spectrum that is normally not absorbed by most of the solar cells. A transparent and conducting upconverter is optimized for the use in thin film Si solar cells. The chapter is structured into 3 sections, the first one explains the main theoretical concepts related to upconversion, the second presents all the experiments and results drawn out of it and the last section includes the conclusions.

## 4.1 Fundamentals

### 4.1.1 Spectral conversion

To reduce spectral mismatch losses in solar cells, spectral conversion of sunlight is a potential promising route. As mentioned in the introductory chapter, silicon-based single junction solar cells are transparent to photons with energies below the band gap energy, and also suffer from thermalization losses induced by higher energy (UV) photons. These two loss mechanisms (processes 1 and 2 in Fig.1.6) account for 33% and 23%, respectively [108]. Fig. 4.1 schematizes this picture: the black area represents the AM1.5G solar spectrum and the grey area the fraction effectively utilised by Si, if all other losses are neglected.

One way to increase solar cell efficiency is to adapt the solar spectrum so that it matches better the Si absorption spectrum and this could be done by means of upconversion (UC), downconversion (DC) and downshifting (DS) mechanisms.

The UC effect is a process where two or more incoming low energy photons are converted into a single high-energy photon, thus, sub-band gap photons can be converted into supra-band gap ones. The maximum quan-



#### 4 Transparent conducting upconverters

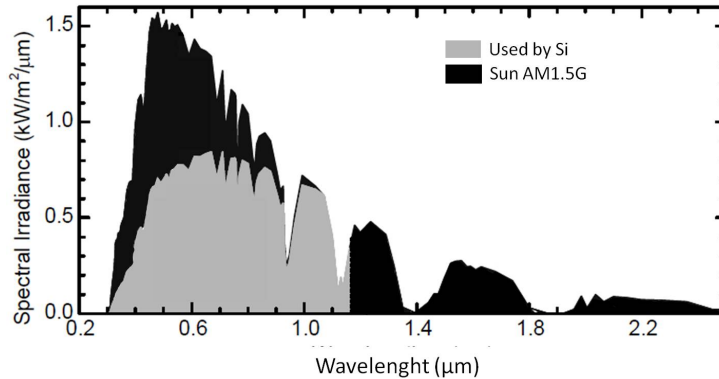


Figure 4.1: Fraction of the solar spectrum effectively available for current generation in a crystalline silicon absorber after the two main optical losses, namely thermalization and transmission [45].

tum yield is 0.5 and is potentially useful to recover the transparency loss. DC, also called quantum cutting, is the opposite process, one high energy photon is converted into two or more lower energy photons, the ideal quantum yield, i.e. the number of outgoing photons per incident photon, is 2 [132]. And DS consists in decreasing the photon energy without changing the photon number [133]. DS may rise the efficiency of the solar cell by converting one high energy photon into one low energy photon which will be more efficiently absorbed (for instance, it would be useful in solar cells whose spectral response is low in the blue part of the spectrum) but would never exceed the S-Q limit [46]. The three processes are depicted in Fig. 4.2.

Assuming that all converted photons are absorbed by the active layer of the solar cell, the maximum energy fraction that can be recovered by DC and UC processes is represented by the grated area in Fig. 4.3 and is 32% for DC and 35% for UC (air mass coefficient 1.5G) [46]. Assuming maximum yields for both DC or UC processes, the theoretical photovoltaic conversion efficiency for a single-band gap (1.1 eV) solar cell could reach 40% [5].

Up and downconverters or downshifters can be studied in layers which are independent of the photovoltaic cell because they only influence the

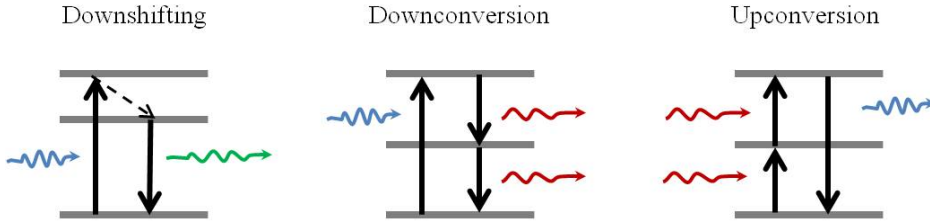


Figure 4.2: Schematic energy diagrams showing photon adsorption and subsequent downshifting, downconversion and upconversion [45].

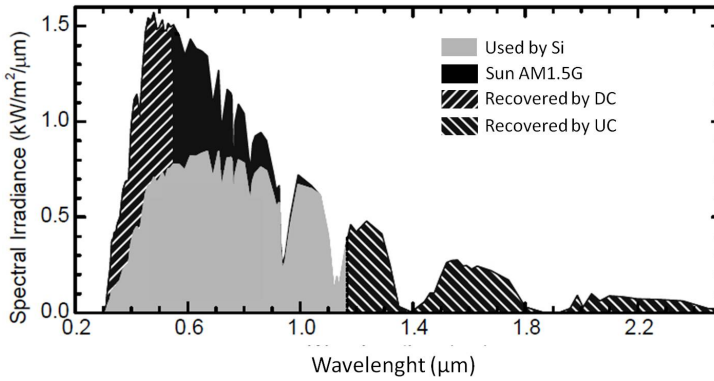


Figure 4.3: Fraction of sunlight effectively absorbed by a crystalline silicon device and fraction of the lost energy potentially recovered by UC and DC mechanisms [45].

solar cell performance optically, hence, the optimised electrical properties of the cell can be maintained. As DC and DS both involve one incoming photon per conversion, the intensity of converted or shifted emitted photons is linear with the incident light intensity. In contrast, the intensity of converted light in an UC process, which involves two photons, scales quadratically with the incident light intensity [133].

Normally, the upconversion layer is placed between the photovoltaic material and the back reflector, whereas the downconversion or downshifting

material is located on top. Research on spectral conversion is mainly focused on organic dyes and quantum dots for downshifting and rare earth or transition metal ions for up and downconversion [46, 134, 135]. In particular upconversion attracts a lot of attention in the solar energy field because low energy photons that are normally transmitted through the cell can be converted into higher energy ones that can be absorbed. In this thesis we focus on upconverters which are suitable for thin film silicon solar cells.

### 4.1.2 Upconversion: Principles

As mentioned above, the basic principle of an upconverter consists in two incoming low energy photons that excite an electron to a higher energy level, and then, a single photon is emitted when the electron relaxes to the ground state [136]. Upconversion was first suggested by Bloembergen [137] and was initially related to the development of infrared detectors. Following this, upconversion was demonstrated in several materials which most of them consists in rare earth or transition metal ions embedded in a host material. Auzel *et al.* [138] studied the possible UC mechanisms and calculated the theoretical efficiency of each mechanism through the Einstein coefficients as reported in Fig. 4.4. The most efficient mechanism is named APTE (*Addition de Photon par Transferts d'Énergie*) or GSA/ETU (Ground State Absorption followed by Energy Transfer Upconversion). In this process three ions are involved, two of them are excited from the ground state and upconversion takes place by transferring their energy stepwise to a third ion. The next most efficient process is a two step absorption of a single ion, it can also be described with the words GSA/ESA that mean Ground State Absorption followed by an Excited Step Absorption. These two mechanisms involve real intermediate states whereas the other ones involve one or more virtual energy levels which imply lower efficiencies. Virtual energy levels mean that the emission and absorption takes place without the existence of the electronic levels [136] and in this case, upconversion requires very high excitation intensities ( $10^{13}$  W/m<sup>2</sup>) [136]. Therefore upconverters considered for application to solar cells are based on process APTE and GSA/ESA.

Among all types of energy transfer between ions (i.e. in ETU), resonant non-radiative transfer and phonon-assisted non-radiative transfer are the most common. When the excited energies of two ions named sensitizer

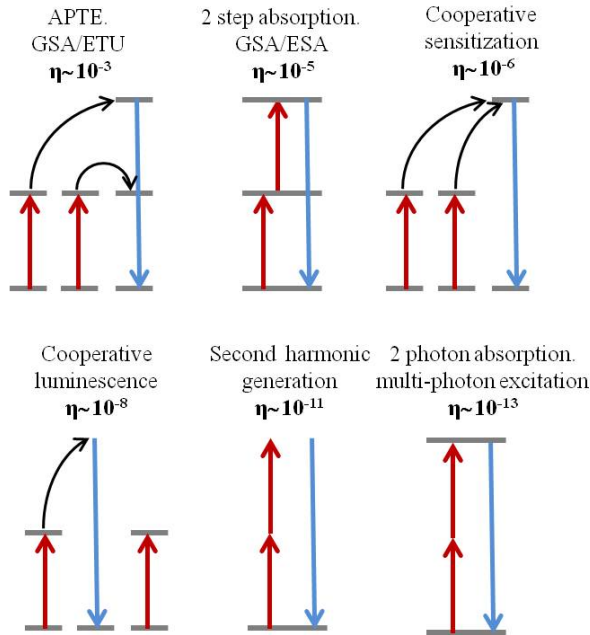


Figure 4.4: UC mechanisms and their relative efficiencies following Auzel [138]. Excitation or de-excitation are indicated by vertical arrows (red and blue, respectively). Curved black arrows indicate energy transfer and horizontal grey lines are real existing energy levels.

(S) and activator (A) are nearly equal and the distance between them is close enough, energy can be transferred from S to A. A is excited from its ground state to an excited state before S emits photons. In phonon-assisted non-radiative transfer, there is an energy mismatch between S and A ions, hence, phonon assistance is necessary to have the energy transfer process. In Fig. 4.5 both energy transfer processes are schematised. Efficient energy transfer requires the ions to be nearby [139].

Since upconversion was first discovered in 1959, it has been widely applied for example to infrared indicator cards, bio-labels, 3D displays or upconversion lasers and it is not until 1996 that Gibart *et al.* [140] applied an upconverter to a solar cell.

## 4 Transparent conducting upconverters

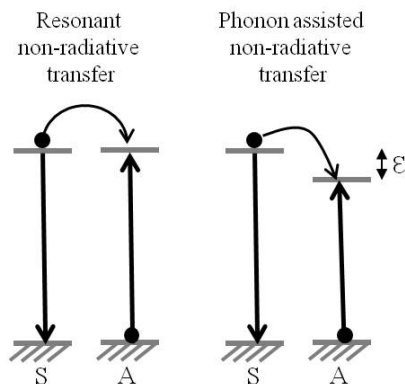


Figure 4.5: Scheme of the different energy transfer mechanisms between two ions. S is the sensitizer (the ion donating energy) and A is the activator (the ion accepting energy) [138].

### 4.1.3 Rare earth ions

Rare earth (RE) ions have been widely studied concerning their photoluminescence properties for use in lasers, phosphors, amplifiers, plasma displays and solar cells among others [141–143]. The unique spectral properties due to their electronic configuration occur as a result of their intra 4f-4f shell transitions [46].

RE ions are defined as lanthanides (elements with atomic number between 57 to 71) together with scandium and yttrium elements [144]. What all them have in common is that their 4f inner shell is partially filled and is spatially located within the energetic lower lying fully filled 5s and 5p shells. As a consequence, the 4f subshell is shielded and their electrons (responsible of the optical transitions) are barely affected by the surrounding [145]. RE incorporated in host materials occur typically in trivalent state ( $\text{RE}^{3+}$ ) and their electronic configuration can be written as  $4f^n 5s^2 5p^6$  where  $n$  is the number of electrons in the 4f shell and increases from  $n=1$  for  $\text{Ce}^{3+}$  to  $n=13$  for  $\text{Yb}^{3+}$ . Because the electrons of the 4f subshell are weakly affected by the host material, Dieke [146] could report a universal map with discrete energy levels for trivalent lanthanides and is shown in Fig. 4.6.



#### 4 Transparent conducting upconverters

The energy levels in the Dieke diagram are described by the Russell-Saunders notation  $(2S+1)L_J$  (also called spectroscopic notation) where  $S$  is the total spin angular momentum,  $J$  the total angular momentum and  $L$  is the total orbital angular momentum. The spin orbit coupling effect causes the  $4f^n$  to split in sublevels and a further splitting occurs due to the influence of the electrostatic field of the neighbouring ions of the crystal lattice (Stark levels). In the case of lanthanides this Stark splitting is two orders of magnitude lower than the spin orbit interaction, hence, their optical spectra is almost unaffected by the host material [136].

RE ions have been used as dopant in a wide variety of materials such as crystals, glass or fibers, the best UC luminescence has been achieved in host materials with low phonon energy (to avoid non-radiative relaxation) such as fluorides, chlorides, iodides or bromides and higher phonon energy hosts are for examples, the oxides [139]. A detailed review on RE ions embedded in different matrix can be found elsewhere [136].

When a RE ion is embedded into a host matrix, it has to enter the lattice with a specific structure. In the case of ZnO, the lattice site involves divalent bonding and if the RE is stable in trivalent form, the crystal structure will be locally unstable [147]. For this reason, the formation of charge compensating defects such as interstitial oxygen is often required to have  $3^+$  ions. It will be demonstrated in this chapter that adding more oxygen during deposition or post-annealing the as-deposited films will allow better atomic organization, which is highly beneficial for trivalent ion formation in ZnO.

REs in their trivalent form are ideally surrounded by six oxygen atoms but this is not enough to achieve an optically active center, the simplest six fold configuration is a central Er and 6 surrounding equally spaced oxygens ( $O_h$  symmetry), but it has been demonstrated by Ishii *et al.* [148, 149] that this arrangement will not allow the 4f transitions to occur due to the high order symmetry in the crystal field surrounding of the  $Er^{3+}$  ions, the most suitable configuration is a pseudo-octahedron structure with a  $C_{4v}$  symmetry that means an Er atom placed at the centre of an oxygen octahedron with unequal edge lengths (Fig. 4.7) [150].

In the bulk wurtzite structure, the site symmetry of any atom of the lattice is  $C_{3v}$  and the coordination is only tetrahedral. This means that a RE ion replacing Zn in the ZnO lattice does not act as an optically active centre (there is not enough oxygen to create the  $3^+$  state), unless

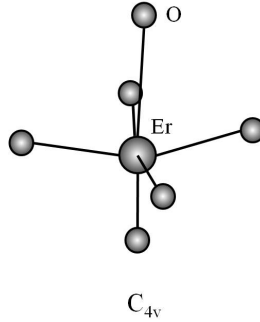


Figure 4.7:  $C_{4v}$  point symmetry of six-fold coordinated  $Er^{3+}$  ion [150].

the local structure is changed by interstitial oxygen or zinc vacancies [148, 149, 151]. Non-stoichiometric growth, high deposition temperatures or annealing treatments are often needed in order to activate the rare earth ion.

#### 4.1.4 Rare earth based upconverters for solar cells

RE-based upconverters have been tried on amorphous [152] and crystalline [153] Si solar cells, on GaAs [140] and also on dye sensitized solar cells [154] and efficiency improvements have been demonstrated in all of them. The first application of an upconverter to a solar cell was reported by Gibart *et al.* in 1996 [140], and it was a gallium arsenide solar cell on top of a vitroc ceramic containing Er and Yb ions, they demonstrated an improvement of 2.5%. The first upconverter applied to a Si solar cell was in 2003 by Shalav *et al.* [155] and was based on  $NaYF_4:Er^{3+}$ .

To apply an upconverter to a silicon solar cell, some requirements must be fulfilled, in the case of c-Si the excitation range should be at wavelengths longer than 1100 nm ( $E < 1.1$  eV) and the emitted photons should have wavelengths shorter than 1100 nm, the upconverter must respond at low excitation intensities (range of  $W/cm^2$ ), must have a high conversion efficiency and should be transparent to the upconverted light.

For application to Si solar cells, Er based upconverters are the most promising since Er excitation takes places at 1500 nm and 980 nm and the upconverted photons are emitted within the Si absorption range. Er, with



## 4 Transparent conducting upconverters

11 electrons in the 4f inner shell, has equally spaced energy levels which match the excitation wavelength of the ground state. As seen in Fig. 4.8 Er can emit at wavelengths of 410, 520, 550, 660 or 810 nm with an error of  $\pm 10$  depending on the host material [136].

Upconversion systems are usually doped with two RE materials, one ion acting as the sensitizer, characterized by a long life time and a broad absorption spectrum, and the other ion, called the activator, acting as the emitter. It is common to use the Er and Yb couple where, Yb is the sensitizer and Er the activator. They cooperate together because of the matching of their energy levels for  $\lambda=980$  nm (see Fig. 4.8) and Er state ( $^4I_{11/2}$ ) can be populated by energy transfer from Yb and enhance the Er visible emission [156]. The most efficient upconversion system that has been reported is for Er and Yb doped  $\text{NaYF}_4$  where it was demonstrated that almost 50% of the absorbed NIR photons were converted into visible light [157].

The objective of this study was to create a transparent and conducting upconverter to be used as the TCO of the rear reflector of a thin film Si solar cell. This TCO is normally used to improve the back reflector optical properties and acts as a diffusion barrier, but in this work will also act as an upconverter. Therefore, ZnO has been chosen to host Er and Yb ions, and rf magnetron sputtering has been used to grow the films. Similar systems have been reported elsewhere [158–161].

## 4.2 Results and discussion

This section is structured into 5 parts, the first one, explains all the initial experiments that were done in order to have a transparent and conducting upconverter, the second section presents the results on thick ZnO:RE films before and after an annealing treatment, the third one is a comparison between different annealing methods performed on a thick ZnO:Er:Yb film, and the last two sections consists of ZnO:Er:Yb thick film annealed using laser technology. The UC PL and RT conventional PL have been measured with the set up provided by the group of Electro-Photonics Division of the Micro- and Nanoscopies and Nanotechnologies for Electronic and Photonic Devices of the Electronics Department of the UB and the low temperature conventional PL have been measured at the facilities of the

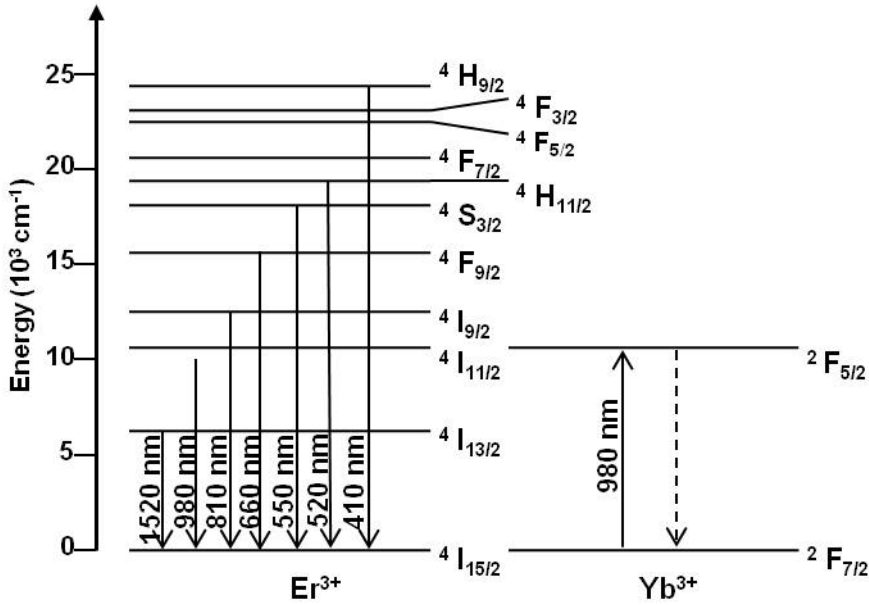


Figure 4.8: Generic scheme of Er/Yb energy transfer; full vertical arrows represent the radiative decay, the dashed ones depict upconversion processes and the curly lines indicate multi-phonon relaxation. Energy transfer processes are sketched by Yb-to-Er solid arrows. Russel-Saunders  $(^{2S+1}L_J)$  notation was employed to refer to the f states: spin ( $S$ ), orbital ( $L$ ) and angular momentum ( $J$ ) quantum numbers.

*Centres Científics i tecnològics (CCiT) of the UB.*

### 4.2.1 Initial trials

As the objective was to dope ZnO with Er,  $\text{Er}_2\text{O}_3$  pellets were made with a pelletizer. Details on the procedure are explained in the experimental chapter. The idea was to place these pellets on the erosion area of the ZnO sputtering target.

Prior to any trials to grow ZnO:Er films,  $\text{Er}_2\text{O}_3$  pellets were optically characterized. UC PL measurements were performed at room temperature. Fig. 4.9 exhibits the visible emission at 480 nm, 540 and 660 nm

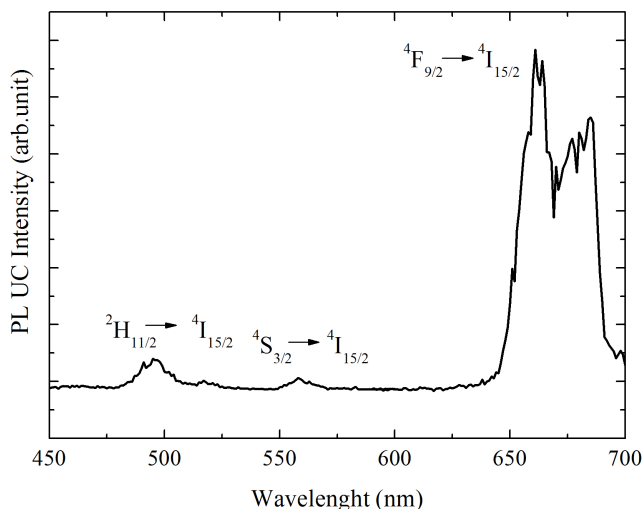


Figure 4.9: Upconversion spectra of the  $\text{Er}_2\text{O}_3$  pellet under 980 nm laser illumination.

corresponding to the erbium electronic transitions under 980 nm laser illumination.  $\text{Er}_2\text{O}_3$  has a cubic-rare-earth structure with a distorted octahedron, in which Er is surrounded by six O acting as optically active centers [148].

Once the UC was confirmed in  $\text{Er}_2\text{O}_3$  pellets, the next step was to characterize Er doped ZnO. Hence, Er doped ZnO thin films, 200 nm thick, were prepared by rf magnetron sputtering over Corning 1737F glass substrates at a power of 120 W. The doping of Er was achieved by placing the pellets on the eroded area of the ZnO target as shown in Fig. 2.3. The ZnO:Er films were deposited with three different doping levels (1, 2 or 3 pellets) without intentional heating, and at substrate temperatures of 160°C and 320°C.

In order to verify that Er was successfully incorporated in the ZnO thin films, XPS measurements were performed in all the samples. The spectra were recorded after cleaning the surface with an Ar sputtering during 3

min. The atomic content was calculated from the integrated peak areas after a Shirley background subtraction. The results showed that  $\sim 0.5\%$  Er atomic content was obtained for doping with one pellet,  $\sim 1.5\%$  with two pellets and  $\sim 3\%$  with 3 pellets.

Then, X-ray diffraction was also performed (Fig. 4.10) to analyse the structural properties of the films. All the samples showed a diffraction peak at around  $2\theta=34.2^\circ$  and an additional second peak of lower intensity at  $72.2^\circ$ . The first peak at  $34.2^\circ$  corresponds to the (002) wurtzite hexagonal plane of ZnO and the second one at  $72.2^\circ$  corresponds to its second order diffraction (004). This implied a hexagonal wurtzite structure having a strong preferred orientation along the [001] direction with the  $c$ -axis perpendicular to the substrate surface. No  $\text{Er}_2\text{O}_3$  related phases could be detected in the XRD patterns suggesting that Er substitutionally replaced zinc in the hexagonal lattice or segregated to the non-crystalline region in grain boundaries.

In the case of the samples with the same doping level, the intensity of the (002) peak was found to decrease with increase in substrate temperature. This behaviour did not strictly mean that the samples became less crystalline with the temperature, because XRD technique only detects the planes that are parallel to the substrate surface and it could be possible that the grains were slightly turned respect to the surface. The average size of the crystallites or grain size  $D$  was calculated by using Eq. 2.6 and the resultant values have been plotted as a function of the Er content. The size of the crystallites increased with the deposition temperature and presented a highest value around 31 nm for the highest temperature and regardless of the doping level. Assuming the hexagonal structure for the ZnO:Er films, the lattice parameter  $c$  was calculated and plotted against the Er content. Even though all the  $c$  values were slightly higher than the standard value (0.521 nm), no appreciable changes were observed with the deposition temperature nor with the doping level. This small discrepancy respect to the standard value could be assigned either to substitutional Er ions in Zn sites, that were distorting the lattice because of their higher ionic radii than Zn or due to the intrinsic stress caused by the ions bombardment during the sputtering.

The transmittance of the films was also evaluated, and showed integrated values above 84% in the range 400-1100 nm. The absorption coefficient was determined from the transmittance and reflectance according to Eq.

#### 4 Transparent conducting upconverters

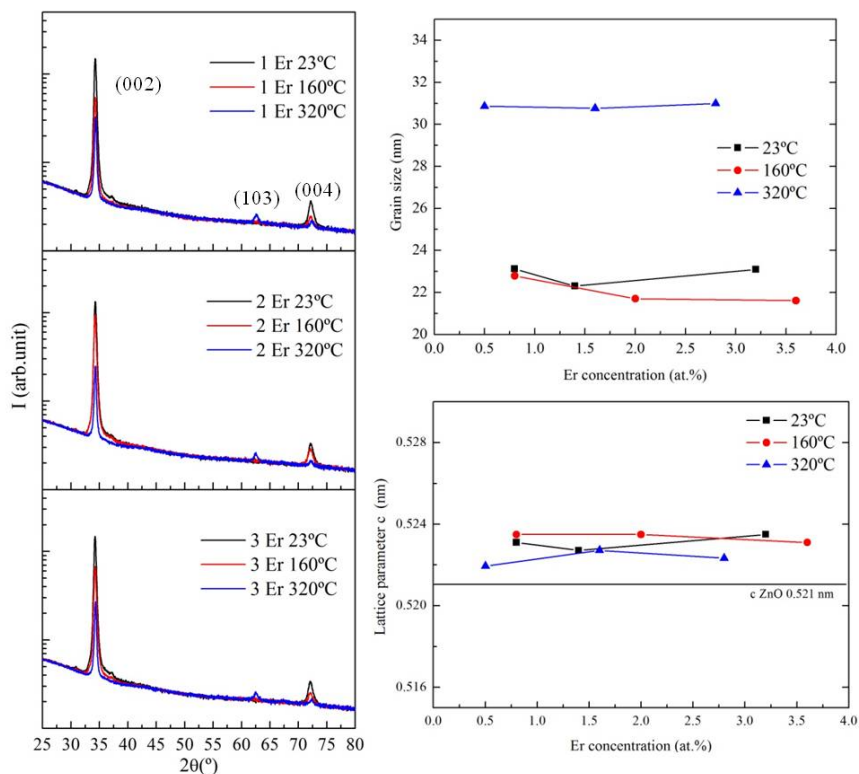


Figure 4.10: XRD patterns and average grain size and  $c$ -parameter values of 200 nm of ZnO:Er thin films with different Er content and deposited at different substrate temperatures.

1.2 and considering ZnO:Er as a direct band gap material, the absorption coefficient was also calculated from Eq. 1.3. The band gap values were estimated from the Tauc plot of  $(\alpha h\nu)^2$  against  $h\nu$  and are depicted in Fig. 4.11.

The band gap values showed an increase with increase in Er doping and also with substrate temperature. They changed from 3.27 eV for 0.8 at.% doping at RT to 3.39 eV for the films deposited at 320°C with 2.8 at.% Er content. This shift to higher energies with increase in doping concentration

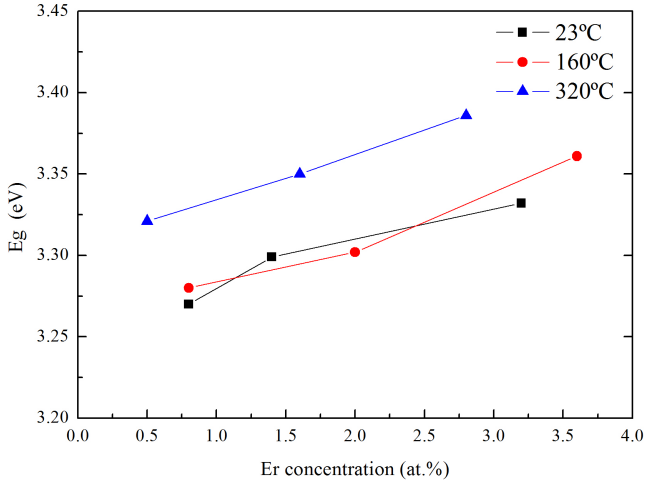


Figure 4.11: Optical band gap energies deduced from the plot of  $(\alpha h\nu)^2$  against  $h\nu$ .

might be due to the Burstein-Moss effect that is explained in Sec. 1.4.1.

Besides exploring the composition, structure and transmittance of the samples, two other important parameters were crucial to determine if a transparent and conducting upconverter was achieved, and these were the conductivity and the upconversion photoluminescence.

With a four point probe system, the  $R_s$  of the samples was measured, and the resistivity was calculated from the product between the  $R_s$  and the film thickness. See Table 4.1.

The resistivity of the films deposited at RT was not measurable for 1 and 2 pellets, but achieved a value of  $7.90 \times 10^{-1} \Omega \text{ cm}$  with the highest Er content. In general terms, the conductivity tended to increase with the Er content and with the deposition temperature. But the most conductive sample was found to be the one doped with one pellet and deposited at 320°C. As explained in the Introduction chapter, the conductivity of doped ZnO can be either due to substitutional Er or oxygen vacancies. The sheet resistance values appear to fluctuate at the four point probe system reading so the table values might have an error of 10%.

#### 4 Transparent conducting upconverters

Table 4.1: Electrical resistivity of the films.

	Resistivity ( $\Omega$ cm)		
N <sup>o</sup> of pellets	23°C	160°C	320°C
1	-	$3.7 \times 10^{-1}$	$1.1 \times 10^{-2}$
2	-	$8.2 \times 10^{-1}$	$1.9 \times 10^{-2}$
3	$7.9 \times 10^{-1}$	$1.5 \times 10^{-1}$	$1.9 \times 10^{-2}$

Until this point, the samples were all transparent and some of them were also conducting. The next step was to check the luminescence properties. The UC PL (laser source 980 nm) and the conventional PL (laser source 325 nm) were measured in all the samples but neither Er or ZnO related emissions were detected even in the films doped with the highest content.

In order to achieve photoluminescence in the samples, and as reported in the literature [149, 162] some of the films were post-annealed at 800°C in air atmosphere and were characterized again. In particular, ZnO:Er deposited at 23°C, at 160°C and at 320°C, doped with 1 pellet and doped with 3 pellets were post-annealed at 800°C during 1 hour.

The composition analysis showed that the content of Er in each sample was invariable. The structure was again analysed by X-ray diffraction and the patterns as well as the  $c$ -parameter values and the estimated average grain size are provided in Fig. 4.12.

After the post-annealing the preferential orientation (002) increased in all the samples and the average grain size became much bigger, specially for the films grown at 320°C. The peaks were shifted to higher diffraction angles suggesting that the compressive stress was decreasing, and no Er<sub>2</sub>O<sub>3</sub> related peaks were observed. The integrated transmittance increased in all the samples and was higher than 86% in the range 400-1100 nm. But the samples became insulating after annealing even for the film with the highest Er content.

At the facilities of *Centres Científics i tecnològics* (CCiT), conventional PL measurement was performed by irradiating with 325 nm laser source while the sample was kept at -196°C. The resultant spectra is shown in

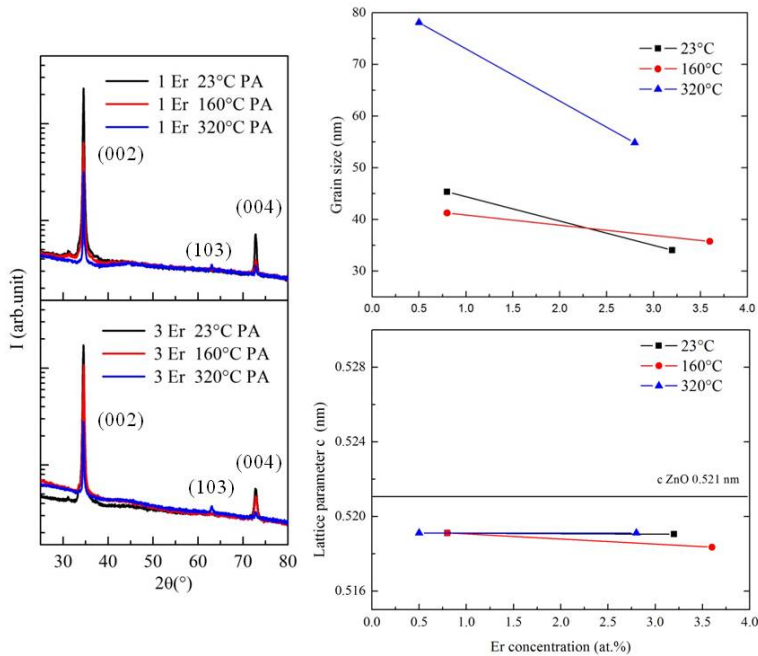


Figure 4.12: XRD patterns and average grain size and  $c$ -parameter values of 200 nm of post-annealed (PA) ZnO:Er thin films deposited with 1 and 3 Er pellets and at different substrate temperatures.

Fig. 4.13 and exhibits different peak emissions coming from Er electronic transitions as well as from ZnO confirming the need of a post-annealing to optically activate either the rare earth species or the ZnO matrix. As-deposited ZnO:Er with 3 pellets and at RT is also shown for comparison.

Annealing the films was necessary to activate the Er ions, as stated in the Fundamentals Section of this chapter. Er needs to be surrounded by O to act as an optically active center. PL emission at 660 nm coming from an Er energy level raised in the samples with higher Er content. The ZnO matrix was also active after the post-annealing and provided the typical PL spectra of annealed ZnO films: an intense UV peak followed by a visible broadband luminescence [26–30]. The UV peak is assigned to the band-to-band excitonic recombination and the visible wide band is related



#### 4 Transparent conducting upconverters

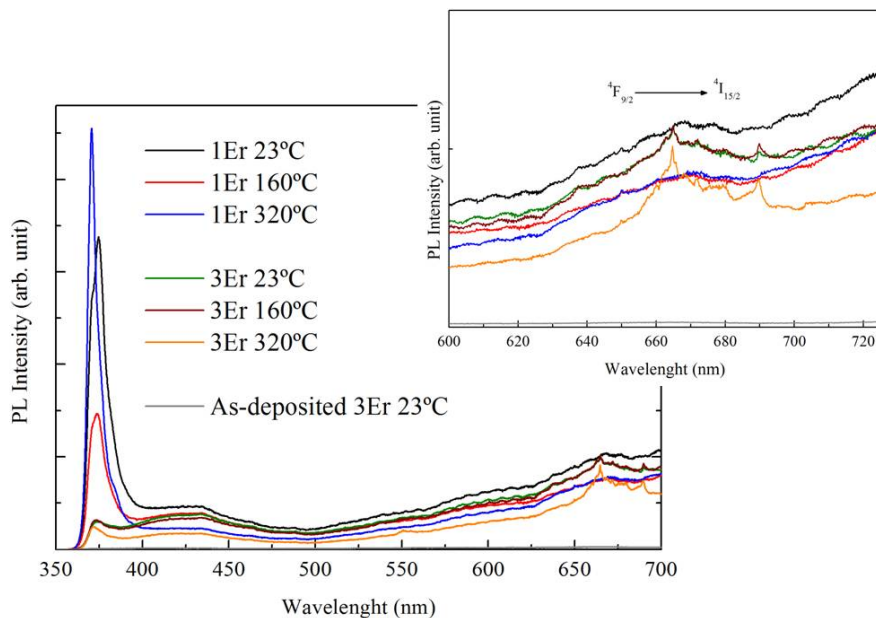


Figure 4.13: Low temperature PL intensity of post-annealed ZnO:Er thin films deposited with 1 and 3 Er pellets at different substrate temperatures. Excitation source: 325-nm line from a He-Cd laser.

to defects within the band gap [26–33]. Moreover, there was an energy transfer from the ZnO matrix to the RE species where ZnO acted as the sensitizer and Er as the emitter. ZnO absorbed the laser radiation (325 nm), transferred its energy to Er ions and when this excited ions relaxed, they emitted photons at their transition wavelength (660 nm).

After verifying the efficiency of the air annealing in activating the Er ions, UC measurements were performed with the set up provided by the Electronics Department of UB but none of the samples showed UC PL emission. The problem was that the samples were too thin (200 nm) to be precisely focused with that set up. To deal with this issue, thicker layers had to be grown. Hence, 800 nm of ZnO:Er was deposited at RT, using 3 pellets and under the same sputtering conditions (rf, 120 W, 0.4 Pa).



## 4 Transparent conducting upconverters

annealing is explained in the following section. Some of those results have already been published in [156].

### 4.2.2 Er- and Yb-doped ZnO thin films

Three different ZnO-based thin films were deposited at a working pressure of 0.4 Pa in Ar gas, while the substrate rotation was kept at 10 rpm and the target to substrate distance was 12 cm. The first two samples, EZO (ZnO doped with Er) and EYZO (ZnO doped with Er and Yb) were deposited at RT without any intentional heating of the substrate at an rf power of 120 W. The deposition rate for these samples was 2.4 nm/min and the thickness of the samples was 800 nm. The third sample, OEYZO, was doped with Er and Yb but deposited at a lower rf power (60 W) and at a substrate temperature of 350°C in oxygen presence (oxygen-to-argon ratio of 1:4), with the aim to favour the incorporation of oxygen into the growing film. A lower rf power was used to have a slow growth rate to enhance oxygen incorporation and to yield better stoichiometric film. This sample had a thickness of 450 nm and the deposition rate was 0.8 nm/min. The three samples EZO, EYZO and OEYZO have been annealed at 800°C for one hour in a quartz tubular furnace, and are labelled as EZOA, EYZOA and OEYZOA, respectively. Also ZnO without doping has been used for comparison before and after the same post-annealing treatment (ZO and ZOA). For better clarity, Table 4.2 has been used to summarize all the studied samples.

Table 4.2: Sample names with the corresponding description: material of the film, thickness, sputtering conditions and post-annealing treatment.

Sample name	Material	Thickness (nm)	Sputtering conditions	Post-annealing
ZO	ZnO	800	rf, 120 W, RT	×
ZOA	ZnO	800	rf, 120 W, RT	✓
EZO	ZnO:Er	800	rf, 120 W, RT	×
EZOA	ZnO:Er	800	rf, 120 W, RT	✓
EYZO	ZnO:Er:Yb	800	rf, 120 W, RT	×
EYZOA	ZnO:Er:Yb	800	rf, 120 W, RT	✓
OEYZO	ZnO:Er:Yb	450	rf, 60 W, 350°C, O <sub>2</sub>	×
OEYZOA	ZnO:Er:Yb	450	rf, 60 W, 350°C, O <sub>2</sub>	✓

#### 4.2.2.1 Structure and composition

Fig. 4.15 shows the XRD patterns of the three samples, before and after the annealing step. The patterns were similar to those shown in the previous section with the highest intensity diffraction peak at around  $2\theta=34.4^\circ$ , indicating a hexagonal wurtzite structure with a strong preferred orientation along the [001] direction with the  $c$ -axis perpendicular to the substrate. In addition, a weak peak from the wurtzite structure was also observed at  $2\theta=47.67^\circ$ , corresponding to the reflection of (102) plane. In the case of EZOA, a peak of low intensity was observed at  $2\theta=29.31^\circ$  that corresponded to the (222) reflection of  $\text{Er}_2\text{O}_3$  cubic structure, and EYZOA showed a peak at  $2\theta=29.62^\circ$ , attributed to the (222) reflection of  $\text{Yb}_2\text{O}_3$ . On the other hand, when the samples were annealed, the microstructure of the films was changed by the plausible oxidation of Er and/or Yb and presented  $\text{Er}_2\text{O}_3$  or  $\text{Yb}_2\text{O}_3$  related peaks. The presence of those phases was not observed in the sample deposited under oxygen, neither after post-annealing it, probably associated to the relatively small amount of Er and/or Yb atoms incorporated into the film (low doping level) or due to the employed deposition conditions. In fact, XPS analysis (see results and comments below) indicates RE concentration of  $<1\%$  in OEYZOA (below the detection limit of our instrument). It is worth noticing that the peaks that were observed in all samples at  $2\theta=31.05^\circ$  and  $2\theta=37.42^\circ$  corresponded to instrumental artifacts.

The lattice parameter of each sample as well as that of undoped ZnO (ZO), have been estimated from the diffraction peak (002) (see Table 4.3). ZO, EZO and EYZO showed  $c$ -parameter values slightly higher than that of stress-free ZnO powder specimen ( $c=0.521$  nm,  $a=0.325$  nm), indicating that the unit cells were elongated along the  $c$ -axis and the compressive forces were predominant as usual in rf sputtered ZnO thin films [163–165]. The internal compressive stress in the as-deposited films is assigned to the bombardment of energetic particles during deposition and not to the thermal stress originating from the difference between the thermal expansion coefficients of the film and the substrate. Even though, this thermal stress effect is slightly appreciable in the case of OEYZO. The film was deposited at  $350^\circ\text{C}$  and the Corning glass gave a tensile stress to the film when it cooled down [166] compensating the compressive stress and giving a  $c$  value closer to the ideal (ZnO powder) and even lower.

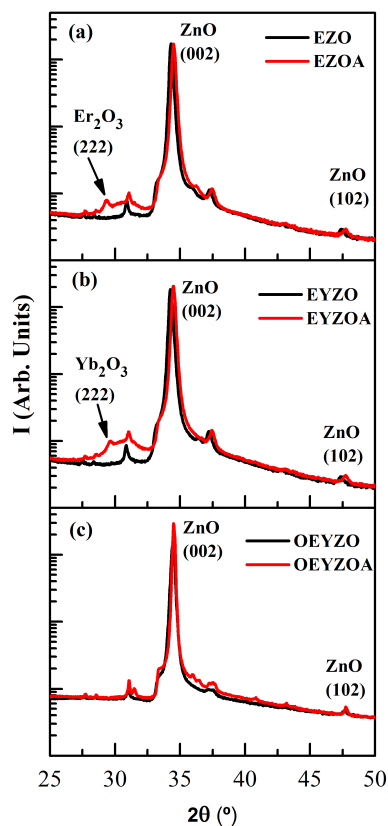


Figure 4.15: XRD patterns plotted on a logarithmic scale of the as-deposited and annealed films: (a) EZO and EZOA, (b) EYZO and EYZOA, and (c) OEYZO and OEYZOA. The peaks that appear in all samples at  $2\theta=31.05^\circ$  and  $2\theta=37.42^\circ$  correspond to instrumental artifacts.

After the annealing, the peaks were shifted to higher diffraction angles and all the films showed lattice parameters ( $a$  and  $c$ ) slightly lower than the ideal values for undoped ZnO powder. This suggested that the stress was changing from compressive to tensile. Although the post-annealing has been reported to contribute to the relaxation of rf sputtered ZnO films [167], it is possible that such high temperature of  $800^\circ\text{C}$  produced tensile

Table 4.3: Average crystallite size and lattice parameter values obtained from XRD measurements. \*The peak corresponding to the (102) planes reflection did not appear in the ZO diffraction pattern.

Sample name	Grain size (nm)	$c$ (nm)	$a$ (nm)
ZO	21	0.523	*
ZOA	50	0.519	0.32
EZO	35	0.522	0.326
EZOA	34	0.519	0.323
EYZO	31	0.522	0.326
EYZOA	32	0.519	0.323
OEYZO	36	0.520	0.323
OEYZOA	54	0.519	0.322

stress due to the mismatch between thermal energy coefficients when the films cooled down.

The average crystallite size in the direction normal to the reflecting planes was not affected by the heat treatment except in the case of OEYZO and ZO, where it increased significantly after the annealing process. Actually, both films with almost no doping (OEYZO) or undoped (ZO) could present fewer grain boundaries due to the absence of RE ions and the annealing might have helped the grains to grow much bigger.

The composition of the films before and after the annealing was estimated from the XPS spectra and appeared to be invariable after the heat treatment (within the resolution provided by the system for such low concentrations). Table 4.4 presents the atomic concentration of Er and/or Yb incorporated to the films depending on the sputtering conditions and the number of pellets. Fig. 4.16 shows the XPS spectra of O 1s core level in the films, before and after annealing. To further study the bonding state of Zn, O and the doping elements in the ZnO films, a high resolution scan of O 1s peak was performed. From previous reports [168], O 1s state can be fitted into three Gaussian functions centered at  $\sim 529.9$  eV,  $\sim 531.4$  eV and  $\sim 532$  eV. The peak at the lowest binding energy (BE) is associated with the  $O^{2-}$  ions at the intrinsic sites in the wurtzite structure; in other words, it indicates the presence of O bonds to Zn atoms or to substitutional  $Er^{3+}$  or  $Yb^{3+}$  ions in the ZnO matrix. The medium centered peak is attributed to the  $O^{2-}$  ions in the oxygen-deficient regions and the change

#### 4 Transparent conducting upconverters

Table 4.4: Atomic concentration of Er and Yb in the as-deposited EZO, EYZO and OEYZO films, estimated from the XPS data analysis.

Sample name	No of Er <sub>2</sub> O <sub>3</sub> pellets	No of Yb <sub>2</sub> O <sub>3</sub> pellets	Atomic concentration
EZO	3	-	Er ~3%
EYZO	1	3	Er ~1%, Yb ~3%
OEYZO	1	3	Er <1%, Yb <1%

in its intensity may be related to the variation of the concentration of oxygen vacancies. The peak at the highest BE position is usually attributed to chemisorbed oxygen species (that appears also in ZnO-based thin films without Er or Yb) [169, 170] and/or to the formation of Er or Yb oxide [171, 172]. Although the film surface was previously sputtered for 3 min, it does not strictly mean that the contamination component was completely removed [169, 173].

As seen in Fig. 4.16, the intensity of the medium BE peak is always higher than the other peaks, indicating a large concentration of oxygen vacancies in the surface layers. The medium BE peak intensity at  $\sim 531.4$  eV was found to decrease after the post-annealing process in the case of EZO and EYZO samples. This is reasonable due to the fact that EZO and EYZO films were deposited at room temperature with a lower oxygen concentration. For EZO and EYZO samples, the post-annealing process caused a slight increase of the higher BE peak, suggesting the formation of Er and Yb oxides and/or an increase of the surface contamination (chemisorbed oxygen species). To sum up, observing Er 4d peak in EZO (not shown here) a small change in the peak shape was detected after annealing, presenting an increase in the contribution of Er<sub>2</sub>O<sub>3</sub> on the area of the peak. This behaviour is consistent with XRD results, where an Er<sub>2</sub>O<sub>3</sub> phase was seen after annealing the sample. On the other hand, Yb<sub>2</sub>O<sub>3</sub> contribution was not observed in Yb 4d peak of EYZO. In contrast, for OEYZO, the highest BE peak decreased after the annealing. Finally, and according to XRD results, the crystalline arrangement was enhanced by the annealing for EYZO and OEYZO samples. This result agrees with the behaviour of the low BE peak, which also increased, indicating the formation of a larger number of bonds between Zn or the substitutional RE ions to O within

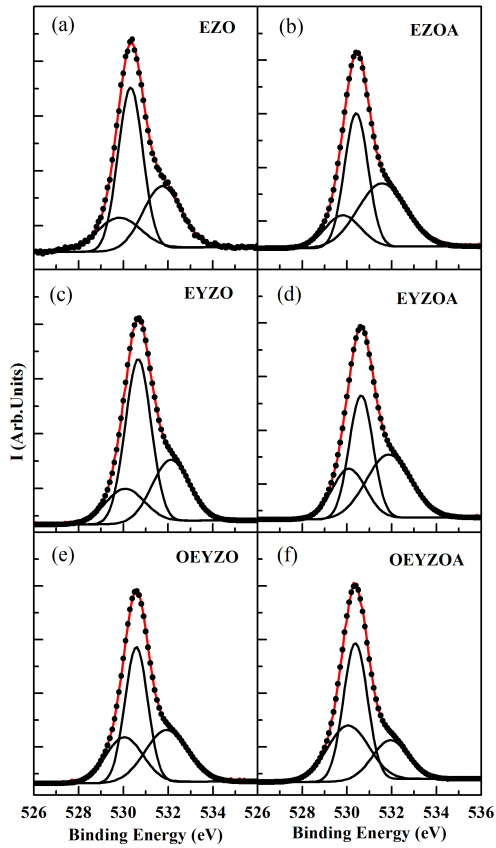


Figure 4.16: XPS O 1s peak Gaussian deconvolution for (a) EZO, (b) EZOA, (c) EYZO, (d) EYZOA, (e) OEYZO and (f) OEYZOA. Black points indicate XPS spectra and red line represents the fitted function.

the ZnO matrix.

#### 4.2.2.2 Optical and electrical properties

All films were found to be transparent and showed integrated transmittance values above 80% within the range 400-1100 nm. Fig. 4.17 exhibits the



#### 4 Transparent conducting upconverters

Table 4.5: Resistivity ( $\rho$ ), carrier concentration ( $n$ ), mobility ( $\mu$ ) and optical band gap ( $E_g$ ) of the as-deposited and annealed films.

Sample name	$\rho$ ( $\Omega$ cm)	$n$ ( $\text{cm}^{-3}$ )	$\mu$ ( $\text{cm}^2\text{V}^{-1}\text{s}^{-1}$ )	Egap (eV)
EZO	3.60E-02	2.88E+19	6.03	3.32
EZOA	1.06E-01	2.35E+19	2.52	3.30
EYZO	1.32E-01	1.38E+19	5.16	3.34
EYZOA	1.89E-01	9.15E+18	2.4	3.30
OEYZO	-	-	-	3.28
OEYZOA	-	-	-	3.31

transmittance spectra of the as-deposited and post-annealed films. It can be observed that the post-annealing treatment favours the transparency of the samples and leads to integrated values of 85%. The calculated optical band gap together with the electrical properties are exposed in Table 4.5. The most conductive sample was EZO with  $\rho=3.6\times 10^{-2}$   $\Omega$  cm followed by EYZO with  $\rho=1.32\times 10^{-1}$   $\Omega$  cm. After annealing the resistivity increased almost one order of magnitude probably due to the incorporation of oxygen at the grain boundaries, the filling of the oxygen vacancies or the migration of the substitutional RE to form RE oxide. OEYZO was totally insulating before and after the annealing treatment. Carrier concentration and mobility were determined from Hall effect measurements. The carrier concentration of all the samples was one or two orders of magnitude lower than the typical concentration given by ZnO:Al thin films [70]. As explained in [18] for carrier concentrations below  $3\times 10^{20}\text{cm}^{-3}$ , grain boundary is one of the main mechanisms that limit the electrical transport, thus, the lateral grain size, the trap density at the boundaries and the carrier concentration play a crucial role in the mobility. The mobility, that was already low for the as-deposited films, decreased to almost its halve after the annealing.

The absorption coefficient and the optical band gap were deduced from Eq. 1.3 and 1.2. The band gap energy variation was consistent with the variation of the carrier concentration: after the annealing, lower carrier concentration and smaller optical band gap values were observed. This was attributed to the Burstein-Moss effect [23].

In Fig. 4.18, the RT PL spectra obtained from the samples under study are displayed. The first main observation is the fact that as-deposited sam-

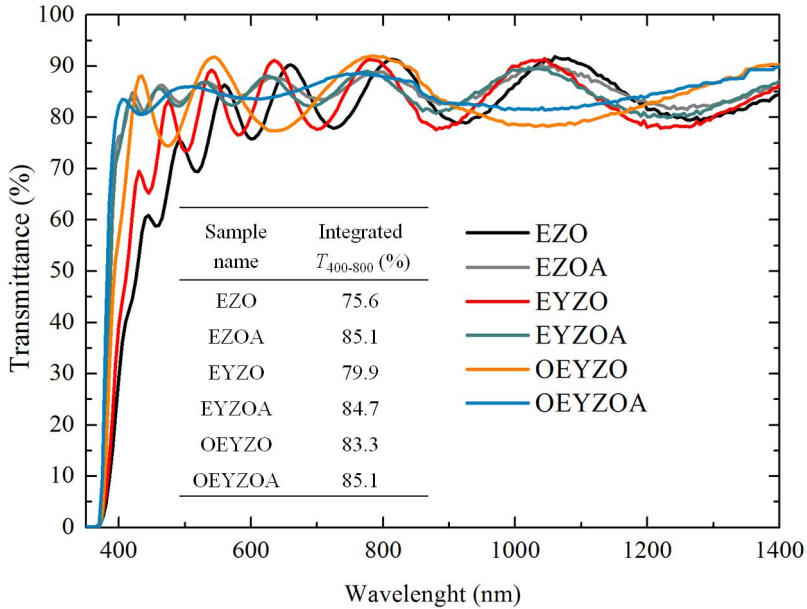


Figure 4.17: Transmittance of EZO, EZOA, EYZO, EYZOA, OEYZO and OEYZOA. The inset table contains the integrated transmittance values in the range 400-800 nm.

ples presented a broad band peak around 450-500 nm, whereas annealed samples presented a spectrum typical from ZnO: a sharp emission around 375 nm and a broad band centred at 600-660 nm. The emission observed in the case of the as-deposited samples is attributed to the combination of emissions coming from highly defective ZnO and the defects present in the Corning glass substrate (low intensity emission in the blue range).

As far as the annealed samples are concerned, the intensity of the emission at 375 nm, related to the excitonic band-to-band recombination (BBR) of ZnO (usually observed in the nanostructured material) [174], increased with the crystalline domain size, obtaining higher intensity for the sample deposited under  $O_2$  atmosphere (see experimental results of XRD data). On the other hand, the broad visible emission (BVE) that these samples presented is due to the radiative recombination in deep-level defects such

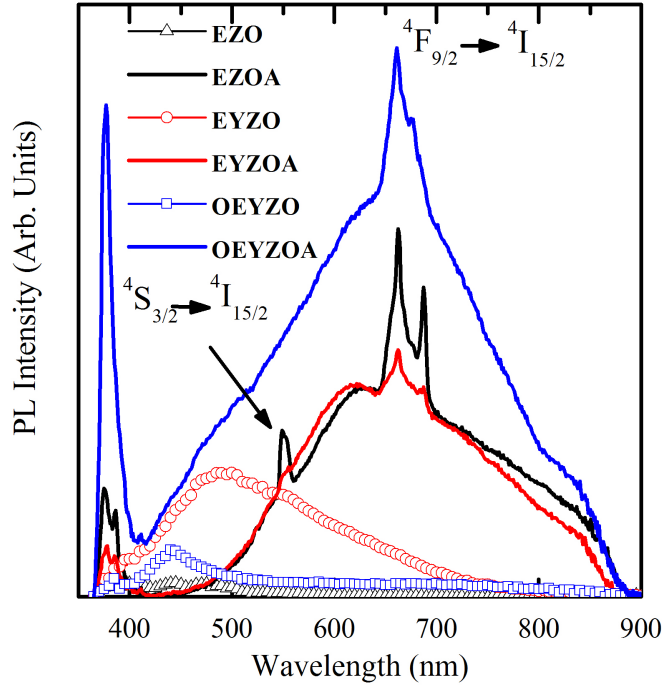


Figure 4.18: RT PL spectra of the different samples considered for the present study. The 325-nm line from a He-Cd laser was employed to excite the samples, being the PL emission acquired in the near-UV and visible ranges. Open symbols indicate as-deposited samples, whereas continuous lines account for the annealed ones.

as oxygen vacancies and/or Zn atoms in interstitial position inside the ZnO lattice [175]. Considering the ratio between the maximum PL intensity of the BBR ( $\lambda=375$  nm) and BVE ( $\lambda=600$ - $660$  nm, depending on the spectrum) bands,  $r=I(\lambda_{BBR})/I(\lambda_{BVE})$ , we obtained a value of  $r=1.2$  for the annealed OEYZOA sample, that clearly overcomes those for EZOA and EYZOA samples ( $r=0.52$  and  $0.22$ , respectively). One possible explanation is the higher stoichiometry and crystalline arrangement that this sample presents, as the deposition parameters and annealing process in-

produced a higher amount of O atoms to the ZnO matrix that contribute to reduce structural defects, reducing non-radiative paths and, in turn, enhancing the PL emission of ZnO. In addition, the three annealed samples presented peak-like emissions around 550 nm and 660-680 nm [176], related to radiative transitions between different electronic levels of  $\text{Er}^{3+}$  ions (see Fig. 4.8). This fact indicates that the  $\text{Er}^{3+}$  ions occupy optically active centres, either in the ZnO host ( $\text{Er}^{3+}$  ions are excited through the ZnO host matrix) or in grain boundaries [177]. Considering now the intensity dependence of the Er emission in annealed samples with and without  $\text{Yb}^{3+}$  ions (red and black lines, respectively), a clear intensity reduction was observed for the samples containing  $\text{Yb}^{3+}$ . This fact could be associated with the lower Er content present in these samples (see Table 4.4). Therefore, this RE-related emission is comparable for all the annealed samples when using the host ZnO material to excite them, suggesting that the RE ions are well integrated inside the ZnO matrix. The active movements of  $\text{O}_2$  during the annealing process result in an adequate environment of Er atoms forming an appropriate crystal configuration for the intra-4f shell transition where Er atoms are surrounded by O forming  $\text{ErO}_6$  clusters [148, 149, 177, 178].

The UC PL spectra were obtained by exciting the samples using single excitation wavelength in the range from 900 to 1300 nm and acquiring the emission in the range from 400 to 850 nm, i.e. at higher energies. We found that the excitation at 980 nm induced the optimum upconversion emission at 660 nm; therefore, this wavelength was selected for exciting the samples in upconversion experiments. The resulting UC PL spectra are shown in Fig. 4.19 a). An intense emission can be appreciated around 660 nm that is composed of two different contributions, one centred at 655 and another at 675 nm [179] that we assign tentatively to a level splitting of the  $^4\text{F}_{9/2}$  energy state of  $\text{Er}^{3+}$  ions. Both emissions present an energy value higher than the energy of the excitation photons, which clearly demonstrates that an upconversion process is taking place in the  $\text{Er}^{3+}$  ions. Actually, the 980 nm excitation coincides in energy with the  $^4\text{I}_{15/2} \rightarrow ^4\text{I}_{11/2}$  transition, so that electrons initially in the ground state populate the excited  $^4\text{I}_{11/2}$  level. The further absorption of photons from the excitation source may promote electrons in the latter state to higher energy ones, being  $^4\text{F}_{7/2}$  the most probable one. In this case, the GSA/ESA UC mechanism is taking place (see Fig. 4.4). In this two-photon absorption process, the time interval between the arrivals of the involved photons has to be lower than

#### 4 Transparent conducting upconverters

the relaxation time of the intermediate energy level ( ${}^4I_{11/2}$ ). The relaxation of the final high energy levels populates the  ${}^4F_{9/2}$  electronic state, whose radiative decay towards the ground state originates the observed PL emission around 660 nm. Upconversion emission corresponding to the  ${}^4S_{3/2}$  decay has been observed by many other authors in similar material systems [180, 181]; however, the lower Er concentration employed in our work, as well as the quality of the matrix surrounding the RE ions, may influence the transition probability between further separated energy states. As can be observed in Fig. 4.19 (a), the as-deposited samples, either Er doped or Er-Yb co-doped did not show upconversion emission, in agreement with the absence of RE-emission in conventional PL. On the other hand, if we compare the emission of these two samples after the annealing process, we observe an increase in the UC PL due to the presence of Yb in the samples. Actually, the  $\text{Er}^{3+} {}^4I_{15/2} \rightarrow {}^4I_{11/2}$  transition (980 nm) presents exactly the same energy than that of (i.e. it is resonant with) the  ${}^2F_{5/2} \rightarrow {}^2F_{7/2}$  one in  $\text{Yb}^{3+}$ . Consequently, the laser excitation of the sample not only populates the Er  ${}^4I_{11/2}$  level but also the analogous one in Yb. Then, by means of direct transfer involving those states from different ionic species, the Er excited level substantially increases its population density. In addition, the relaxation of  $\text{Yb}^{3+}$  ions releases photons with the same energy than the incoming radiation, which in turn can activate the  ${}^4I_{11/2} \rightarrow {}^4F_{7/2}$  transition in Er [182, 183]. The sum of both possible pictures results in an enhancement of the upconversion probability in  $\text{Er}^{3+}$  ions, as demonstrated by the increase of about one order of magnitude in the UC PL of the sample containing  $\text{Yb}^{3+}$  ions. In this case GSA/ESA or/and GSA/ETU are taking place.

To have an idea of the efficiency of the UC process, Eq. 4.1 was used to estimate the quantum yield (QY). Considering the incident intensity at 980 nm ( $P_{out660}$ ) and the detected intensity at 660 nm ( $P_{in980}$ ), the film thickness ( $d$ ) and the absorption coefficient ( $\alpha$ ) of the film, the result for EYZOA was approximately  $10^{-5}\%$  that is the same order as the GSA/ETU UC mechanism shown in Fig. 4.4.

$$QY = \frac{P_{out660}}{P_{in980} \times e^{-\alpha d}} \quad (4.1)$$

The UC PL emission of the samples deposited under an  $\text{O}_2$  atmosphere presented a different behaviour: both the as-deposited (OEYZO) and

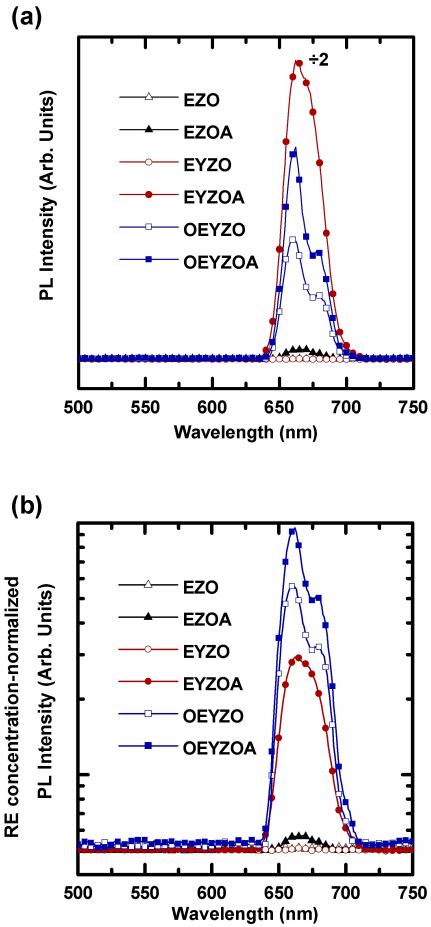


Figure 4.19: (a) Upconversion PL spectra of the samples under study. 980 nm was selected as the excitation wavelength, and resulting PL spectra were acquired through the visible range. The observed peaks belong to the  ${}^4F_9/2 \rightarrow {}^4I_{15/2}$  Er transition. (b) Upconversion spectra displayed in (a), corrected taking into account the total rare-earth (Er and Yb) atomic concentration for each sample. Open symbols indicate as-deposited samples, whereas full symbols account for the annealed ones.

annealed (OEYZOA) samples displayed a strong emission, but lower than the EYZOA sample. The fact that as-deposited samples present UC PL signal may account for the oxygen-rich atmosphere and substrate temperature employed during deposition ( $350^{\circ}\text{C}$ ); this temperature seems high enough for activating the RE ions but not the ZnO matrix, as no conventional PL signal was observed (see Fig. 4.18). In order to compare the emission of these samples to the previous ones, we have normalized the spectra to the concentration of the different involved RE atoms (Er and Yb). Although the emission only comes from Er, the normalization also took into account the Yb concentration, as both species are excited with the incoming radiation at 980 nm. The normalized spectra are displayed in Fig. 4.19(b). It is clearly observed that, under equivalent ion concentration conditions, samples that were deposited under  $\text{O}_2$  flow show a stronger emission, even in the as-deposited case. As mentioned in the conventional PL analysis, the extra O atoms occupy O vacancies within the lattice, thus increasing the crystalline domain size. With these facts, we assume that the confinement of the RE ions within the matrix, and thus their localization, is strongly increased; therefore, the probability of the resonant transfer mechanism to occur (from  $\text{Yb}^{3+}$  to  $\text{Er}^{3+}$  ions) is enhanced. In conclusion, these results indicate that Er-Yb co-doped ZnO deposited in O-rich atmosphere and at high temperatures can be used as upconversion system to take profit of the near infrared light. Probably  $\text{ErO}_6$  clusters are formed either at the grain boundaries or within the ZnO matrix.

Although visible upconversion has been achieved in a transparent thin film, further improvement on the electrical properties was required. For this reason, other annealing methods were investigated such as laser annealing or vacuum annealing and the results are presented in the following section.

#### 4.2.3 Annealing methods on Er- and Yb-doped ZnO thin films

This section presents an evaluation of different post-annealing treatments in order to get a transparent and conducting upconverter. Laser annealing, vacuum annealing and air annealing are compared and contrasted. The laser annealing parameters shown in this section were chosen after

many trials with pulsed and continuous lasers, changing the laser's power, wavelength and scan speed. From the initial trials, just the samples irradiated with CW (continuous wave) 532 nm at powers of 0.05, 0.1 and 0.2 W and scan speed of 400 mm/s showed PL and are the ones presented in this section.

ZnO:Er:Yb thin films of 800 nm thickness were deposited by rf magnetron sputtering onto a  $10 \times 10$  cm<sup>2</sup> Corning 1737F glass substrate. The deposition parameters were exactly the same used to deposit sample EYZO from the previous section. In order to analyse the influence of the annealing methods, 6 identical pieces of  $1 \times 1$  cm<sup>2</sup> were cut from the as-deposited ZnO:Er:Yb film and were subjected to different annealing treatments. Among the six samples, one piece was kept without any annealing treatment (AS DEP) for comparison purposes; a second sample was annealed in air atmosphere (AIR) at 800°C during 1 h in a conventional quartz tubular furnace; the third piece was annealed at 800°C in vacuum (VAC) for 1 hour at a pressure of  $2.1 \times 10^{-4}$  Pa; and the three remaining samples were subjected to laser annealing with a CW, diode-pumped and frequency-doubled Nd:YVO<sub>4</sub> (Vanadate) laser system (MILLENNIA PRO SPECTRA-PHYSICS) yielding an emission wavelength of 532 nm. The beam was delivered to the working area via steering mirrors, which directed the beam to a scanner head (Hurricane II 14 SCANLAB) via the power attenuator AT4040. Before the entrance of the scanner head an iris is placed in order to remove the diffraction and aberration defects of the laser beam. The scanner head directs and focuses the beam onto the target via a lens with a focal length of 250 mm. The beam size on the sample was 29  $\mu$ m in diameter. The laser annealing process was performed by scanning  $10 \times 10$  mm<sup>2</sup> areas with parallel lines without any gap between them. The scanning speed used was 400 mm/s and the irradiation conditions for the three laser annealed samples were as follows; LAS1: P=0.05 W, peak fluence= 0.37 J/cm<sup>2</sup>, LAS2: P=0.1 W, peak fluence= 0.74 J/cm<sup>2</sup>, LAS3: P=0.2 W, peak fluence= 1.48 J/cm<sup>2</sup>. A summary with the sample names and its description is given in Table 4.6.



## 4 Transparent conducting upconverters

Table 4.6: Samples name with the post-annealing description.

Sample name	Post-annealing
AS DEP	As-deposited
AIR	Air, 800°C, 1 h
VAC	Vacuum ( $2.1 \times 10^{-4}$ Pa), 800°C, 1 h
LAS1	P=0.05 W, peak fluence= 0.37 J/cm <sup>2</sup> , 400 mm/s
LAS2	P=0.1 W, peak fluence= 0.74 J/cm <sup>2</sup> , 400 mm/s
LAS3	P=0.2 W, peak fluence= 1.48 J/cm <sup>2</sup> , 400 mm/s

### 4.2.3.1 Structure and composition

XPS analysis revealed that the composition of the films in terms of Er and Yb atomic contents remained invariant at 0.5 at.% and 2.5 at.%, respectively, regardless of the annealing method. Fig. 4.20 presents the XRD patterns of the as-deposited and the annealed ZnO:Er:Yb samples.

The ZnO:Er:Yb films showed the strong *c*-axis orientation of (002) plane and its second order reflection (004) of the hexagonal ZnO wurtzite structure. In the case of the as-deposited ZnO:Er:Yb film, no Er<sub>2</sub>O<sub>3</sub> or Yb<sub>2</sub>O<sub>3</sub> related phases were observed, suggesting that the RE ions are either substitutionally replacing Zn in the ZnO lattice or segregated to the grain boundaries. The annealing process, however, induced the appearance of different phases within the XRD patterns. The peak at  $2\theta=29.62^\circ$  that appeared in both air and vacuum annealed films corresponds to the (222) reflection of Yb<sub>2</sub>O<sub>3</sub> cubic structure. The Er<sub>2</sub>O<sub>3</sub> related peaks were not shown by any film, probably due to the rather small amount of Er content in the films. In the laser annealed samples, only the peaks related to ZnO wurtzite reflections were observed. Assuming hexagonal structure, the lattice parameter value *c* was calculated from the (002) peaks, and the values are tabulated in Table 4.7.

The lattice parameter calculated for the as-deposited film was slightly larger than that of undoped polycrystalline ZnO ( $c=0.521$  nm) [10], indicating a higher compressive stress, caused mainly by the ion bombardment during the sputtering process [163] or due to the substitutional REs in zinc positions. The thermal annealing in air and in vacuum contributed to the lattice relaxation, and the *c*-parameter values became closer to that of

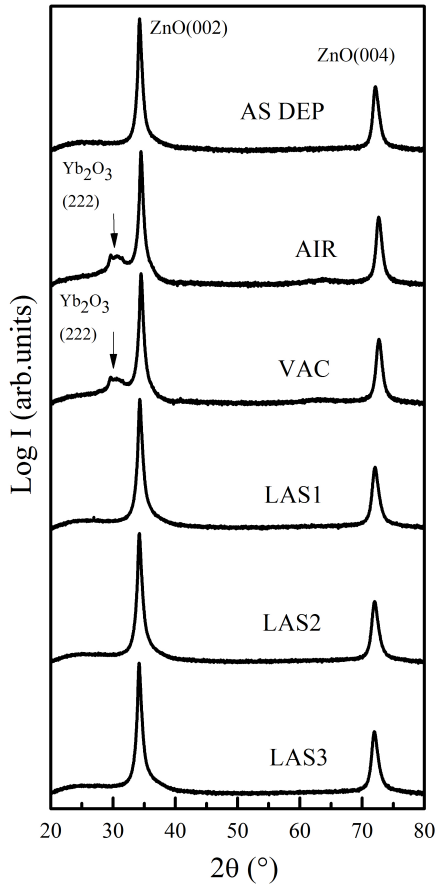


Figure 4.20: X-ray diffraction patterns of as-deposited (AS DEP) ZnO:Er:Yb and that of films annealed in air (AIR), vacuum (VAC) and laser-annealed at three different laser powers (LAS1, LAS2, LAS3).

undoped ZnO. Even though, a slight tensile stress appeared, due to the mismatch between the thermal energy coefficients of the Corning 1737F glass substrate and the film when the samples cooled down [166]. In the case of laser annealed samples, LAS1 did not show any change in the XRD peak implying that the laser fluence employed for the annealing (0.37

## 4 Transparent conducting upconverters

Table 4.7: Values of the  $c$ -parameter for the as-deposited, air annealed, vacuum annealed films and the films irradiated with three different laser powers.

Sample name	$c$ (nm)
AS DEP	$0.523 \pm 0.002$
AIR	$0.520 \pm 0.002$
VAC	$0.520 \pm 0.002$
LAS1	$0.523 \pm 0.002$
LAS2	$0.524 \pm 0.002$
LAS3	$0.524 \pm 0.002$

$\text{J}/\text{cm}^2$ ) was not affecting the film stress; whereas, when the laser fluence was increased ( $0.74 \text{ J}/\text{cm}^2$  and  $1.48 \text{ J}/\text{cm}^2$ , for samples LAS2 and LAS3, respectively) the (002) peak shifted to lower diffraction angles, indicating the predominance of compressive forces. This is in contrast to the thermal annealing effect.

### 4.2.3.2 Optical and electrical properties

Fig. 4.21 shows the transmission spectra of the thermal- and laser-annealed samples, compared to the as-deposited one. The inset table presents the integrated  $T$  values within the range 400-800 nm. All these samples were transparent enough to be used as TCO for the back reflector in a thin film Si solar cell. Moreover, the transparency notably increased beyond 84% when the samples were thermally annealed, due to the enhancement of the stoichiometry rather than the crystallinity of the films, as described in [184].

The electrical properties of bulk ZnO are, as in any other solid material, tightly related to its crystalline structure. In particular, the conduction mechanism of ZnO films is mainly due to the electrons supplied from the donor sites associated with oxygen vacancies and zinc interstitials. The ZnO films doped with metallic Er and Yb species showed higher electrical conductivity than pure ZnO films due to the contribution of  $\text{Er}^{3+}$  and  $\text{Yb}^{3+}$  ions placed at the substitutional sites of  $\text{Zn}^{2+}$  ions, as well as due to presence of the aforementioned oxygen vacancies and zinc interstitials [185]. The resistivity values of the as-deposited and of the samples sub-

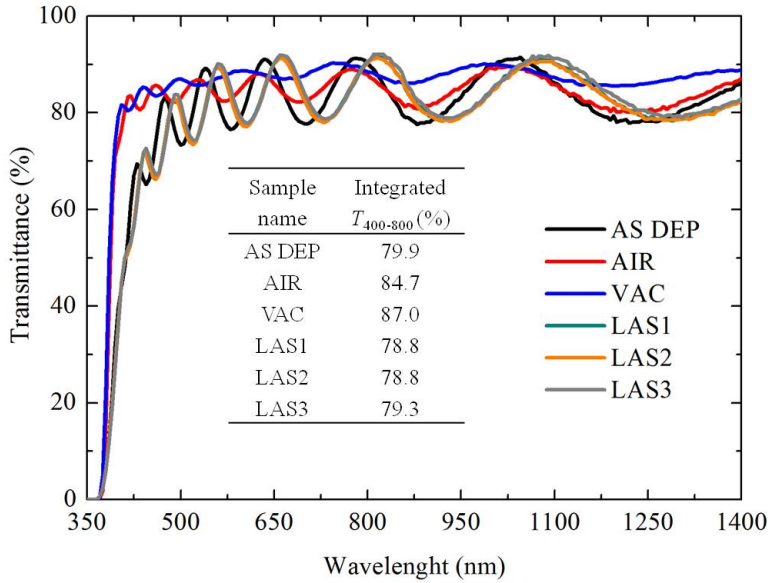


Figure 4.21: Transmittance spectra for the as-deposited ZnO:Er:Yb, the air- and vacuum-annealed samples and the three laser-annealed ones. The inset table contains the integrated transmittance values in the range 400-800 nm.

jected to different annealing methods were estimated from the electrical  $R_s$  measurements. The as-deposited ZnO:Er:Yb showed a resistivity of  $5 \times 10^{-2} \Omega \text{ cm}$  which increased to  $1 \times 10^4 \Omega \text{ cm}$  due to the thermal annealing in air, and  $4 \times 10^{-1} \Omega \text{ cm}$  upon vacuum annealing. This increase in resistivity can be ascribed to either a decrease of the oxygen vacancies, oxygen chemisorption at the grain boundaries or to the migration of substitutional REs to form RE oxide. All cases would reduce the density of donor sites and/or the RE interstitial atoms, resulting in the decrease of the carrier concentration and a rise of the potential barrier, which would consequently reduce the mobility of the films [185–187]. The increase in resistivity of only one order of magnitude for the sample annealed in vacuum conditions gives evidence to this argument, as the oxygen content is far reduced. In the case of the laser-annealed films, the conductivity

does not change, irrespective of the laser power, which implies that air molecules do not take part in the local structure modification carried out by the surface-concentrated radiation annealing.

The effect of the different annealing treatments on the luminescence properties of the ZnO:Er:Yb films was also investigated by means of PL. The films were excited using 325 nm, and the temperature of the samples was kept constant at  $-196^{\circ}\text{C}$  during the measurements. Fig. 4.22 shows the PL emission spectra of each of these samples acquired in the range 330-850 nm, whereas the inset presents their emission around  $\lambda=980$  nm indicating the effect of each annealing treatment on the  $\text{Er}^{3+}$  and  $\text{Yb}^{3+}$  common electronic transition. The first observation is that the non-treated ZnO:Er:Yb sample did not show any PL emission, implying the need of a post-deposition annealing to optically activate the matrix. The air- and vacuum-annealed samples exhibit the maximum emission intensity along the whole spectral range (350-1020 nm).

The UV emission peak for the air- and vacuum-annealed samples at 372-375 nm corresponds to the band-to-band excitonic recombination, and the broad band centered around 660 nm is attributed to deep intra-band gap energy states generated by defects within the ZnO matrix [174]. The ratio of the intensities for visible defects-related band to the UV band-to-band recombination is much larger for the air annealed sample. Since the Er and Yb doping concentration is the same for air and vacuum annealed samples, oxygen and nitrogen incorporation during the air-annealing may be playing an important role in their photoluminescence properties. The enhancement in the UV emission is related to a higher stoichiometry of the films, and can be improved by oxygen incorporation through a post-deposition annealing process [186, 188, 189]. The PL emission observed from the laser-annealed samples, much lower in intensity than the former ones, suggests that the film stoichiometry does not vary with respect to the as-deposited film. This observation agrees with the XRD results, where almost no variation of the lattice parameter occurred with laser annealing (see Table 4.7). Therefore, we can conclude that laser annealing prevents the uncontrolled insertion of oxygen within the ZnO matrix, probably due to the very short exposure times for the laser heating in each point (some tens of milliseconds).

Apart from the matrix (ZnO)-related PL, Fig. 4.22 also shows a peak at 750 nm for the air annealed sample, attributed to the second order of the

excitonic recombination-related emission. And the emission around 660 nm corresponds to an  $\text{Er}^{3+}$  relaxation ought to the  ${}^4\text{F}_{9/2} \rightarrow {}^4\text{I}_{15/2}$  transition. The near infrared part of the spectra (inset of Fig. 4.22) presents an emission peak, centered at 980 nm, corresponding to either the  $\text{Er}^{3+} {}^4\text{I}_{11/2} \rightarrow {}^4\text{I}_{15/2}$  or  $\text{Yb}^{3+} {}^2\text{F}_{5/2} \rightarrow {}^2\text{F}_{7/2}$  electronic transitions (or to a combination of both). The clear observation of this intra 4f-shell transition is a strong evidence for the optical activation of the RE ions introduced inside the ZnO matrix. To directly excite the RE ions and induce inter-level transitions, the incident photons need to have an energy resonant with one of their electronic levels. Therefore, the 325-nm laser excitation should not be able to produce such effects. Nevertheless, a possible energy transfer can take place from the host matrix to the integrated ions, which is translated into their excitation [156, 190]. As observed in Fig. 4.22, this energy transfer occurs in all annealed samples, where the ZnO matrix is optically active.  $\text{Er}^{3+}$  and  $\text{Yb}^{3+}$  ions might occupy optically active sites either in the host matrix lattice or in the grain boundaries.

In the case of laser annealing, the spectra display a low PL efficiency at 980 nm with respect to other annealing treatments. This could be due to the lack of incorporation of oxygen atoms into the lattice during laser annealing, which strongly decreases the ZnO excitation, quenches the PL emission, and consequently the energy transfer to RE ions. In addition, when locally studying the different laser annealing processes, LAS3 presents a higher PL emission at 980 nm than LAS1 and LAS2, the latter ones exhibiting a nearly flat spectrum. The employed laser power is notably affecting the local arrangement of RE ions within the ZnO lattice, allowing their optical activation. In particular, a higher laser power seems to improve the local environment of  $\text{Er}^{3+}$  and  $\text{Yb}^{3+}$  ions, which is translated into more stable levels within the ZnO band gap. Contrary to what was expected, LAS2 shows lower emission at 980 nm than LAS1, but the difference is almost negligible and might be related to the non-uniform film or to the manually chosen focus point during the PL measurement.

To further understand the annealing effect on the RE ions incorporated inside the host matrix, room temperature upconversion experiments were performed. Provided that PL emission was observed at 980 nm (see Fig. 4.22), indicating the activation of  $\text{Er}^{3+} {}^4\text{I}_{11/2} \rightarrow {}^4\text{I}_{15/2}$  and  $\text{Yb}^{3+} {}^2\text{F}_{5/2} \rightarrow {}^2\text{F}_{7/2}$  transitions, the samples were excited at this particular wavelength by means of a ns-pulsed Nd:YAG laser coupled to an OPO. The

#### 4 Transparent conducting upconverters

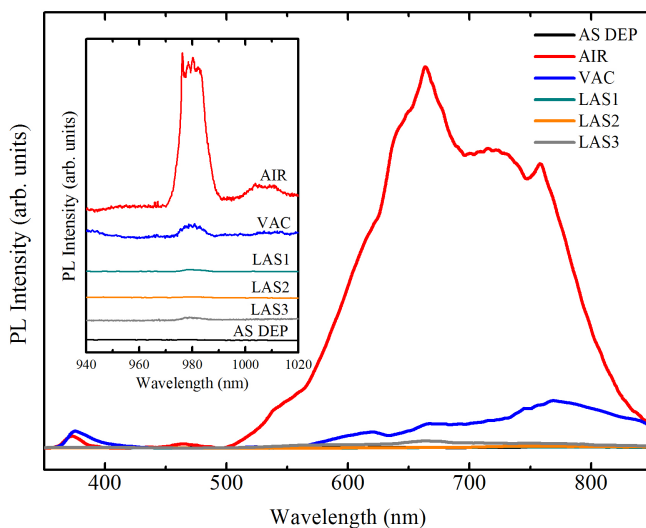


Figure 4.22: Photoluminescence spectra corresponding to the as-deposited sample as well as the vacuum-, air- and laser-annealed ones, under 325-nm laser excitation. The spectra were acquired at  $-196^{\circ}\text{C}$ . The inset displays the 980 nm PL emission.

acquired UC PL spectra (under 980-nm laser excitation) are displayed in Fig. 4.23.

No emission was observed from the untreated sample which is in good accordance with the PL results, and may be due to the fact that the surrounding of RE is not adequate to realize upconversion, and consequently a post-deposition annealing process is necessary. In the case of the annealed samples, the emission intensity of the air and vacuum treatments is in agreement with the one observed in conventional PL spectra: the presence of oxygen enhances RE-related emission/absorption, probably by propitiating the generation of  $\text{ErO}_6$  complex [149]. The laser annealed samples show, a very poor upconversion emission for LAS1 and LAS2, whereas an intense emission is displayed by LAS3, owing to the higher laser power employed. This latter fact establishes a minimum laser power requisite for

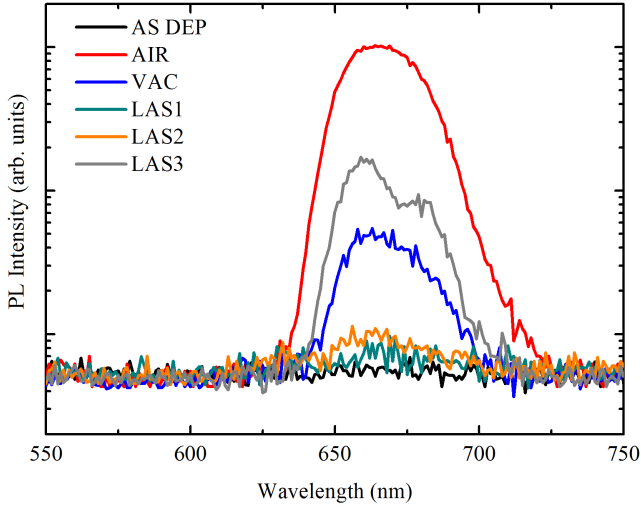


Figure 4.23: Upconversion PL spectra in logarithmic scale of the as-deposited sample, the air-annealed, the vacuum-annealed and the three laser-annealed samples. 980 nm was used as the excitation wavelength.

the proper ordering of the RE atomic environment.

The integration of RE ions within the ZnO matrix has been proved to generate optically active centers able to provide high-energy photons out of the absorbed low-energy ones by means of the upconversion process. The results shown here establish laser annealing as an alternative to conventional thermal annealing (under air or in vacuum) to obtain upconversion properties with an added advantage of preserving the film conductivity and transparency. Besides, it has been shown that a minimum laser power is required for the correct structural modification of the RE environment, which is essential for the good optical performance of  $\text{Er}^{3+}$  and  $\text{Yb}^{3+}$  ions to produce upconversion. According to these results, next section presents ZnO:Er:Yb thin film treated with more optimized laser parameters.



## 4 Transparent conducting upconverters

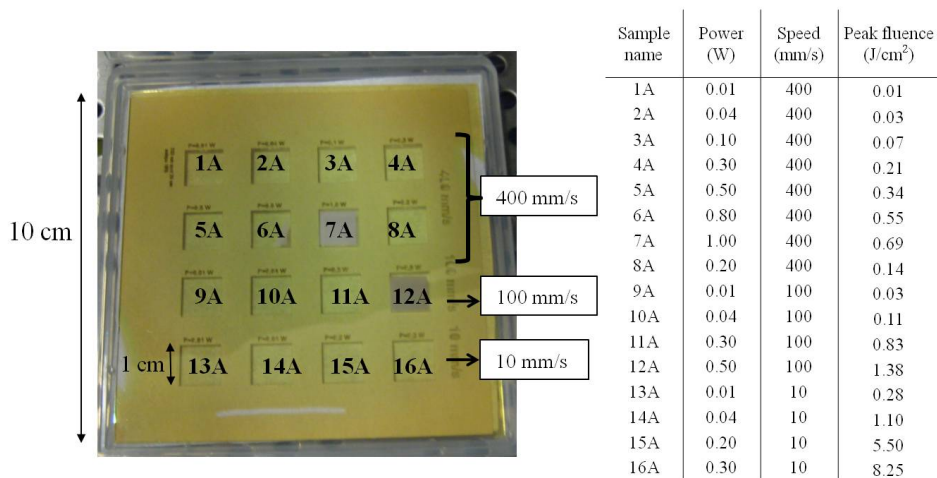


Figure 4.24: On the left, image of the laser treated  $10 \times 10$  cm<sup>2</sup> ZnO:Er:Yb sample and the right table contains a summary with the name of the samples and the process parameters for the laser annealing.

### 4.2.4 Laser annealing of Er- and Yb-doped ZnO thin films: Optimization

After proving that laser annealing was able to preserve the electrical properties and at the same time activate Er ions, another set of ZnO:Er:Yb samples was laser annealed. The laser was the same used in Sec. 4.2.3, a diode pump solid state Nd:YVO<sub>4</sub> laser system emitting at 532 nm. The laser power was varied between 0.01-1.0 W and the process speed from 10 mm/s to 400 mm/s. In this section, the electrical, optical and morphological properties of the laser annealed ZnO:Er:Yb samples are presented.

For a better understanding on the experimental process, a picture of ZnO:Er:Yb thin film overlapped with the laser annealed areas and a table that summarizes the laser parameters are shown in Fig. 4.24.

For the laser annealing tests, a ZnO:Er:Yb thin film of 800 nm thick, was deposited onto a  $10 \times 10$  cm<sup>2</sup> Corning 1737F glass substrate by means of rf magnetron sputtering.

In contrast to all the previous trials, where the doping content was achieved with pellets, now a single target of ZnO:Er<sub>2</sub>O<sub>3</sub>:Yb<sub>2</sub>O<sub>3</sub> (89:1.2:9.8

wt%) with 99.99% purity and a diameter of 3 inches was used for the deposition. The deposition conditions were again the same as EYZO from Sec. 4.2.2. Nevertheless, at that point of time, the sputtering system suffered from a leakage and the minimum pressure that was able to reach was  $1 \times 10^{-3}$  Pa. This fact could be related with the low transparency of this film.

As seen in Fig. 4.24 sixteen pieces of  $10 \times 10 \text{ mm}^2$  were irradiated with 532 nm at different powers and process speeds, a small piece without treatment was annealed in air during 1 hour at  $800^\circ\text{C}$  and another piece was kept without any annealing for comparison purposes.

In the left side of Fig. 4.24, it is possible to perceive a change in the morphology of samples 7A and 12A and slightly for sample 6A. The laser radiation gave too much energy to those films and resulted in a damaged surface from which part of the material ablated away. A confocal microscope images of samples 5A, 6A, 7A and 12A are presented in Fig. 4.25. Sample 5A did not suffer any appreciable change in its morphology and had the same aspect as all the other samples that are not shown here. Instead, the laser's path is easily detectable on samples 6A, 7A and 12A, being more evident for the two last ones. At a scanning speed of 400 mm/s, 0.8 W seems to be the maximum power allowed to avoid damaging the sample, in the case of 100 mm/s the maximum power was  $\sim 0.3$  W and no damage was seen at 10 mm/s even at 0.3 W.

A depth profile was taken for sample 7A (Fig. 4.26) revealing that the ablation of the material had even reached up to the glass. Assuming that the film thickness was 800 nm, it is appreciable that in some areas the profile reaches lower values.

XPS was used to analyse the chemical composition of all the films and revealed that before and after any annealing treatment, the composition was invariable and was 0.5 at.% for Er and 3 at.% for Yb even in the ablated samples. Moreover, Si content appeared in the spectra of samples 7A and 12A confirming that the laser ablation had reached the glass.

The conductivity and the upconversion photoluminescence were the next parameters to measure. The  $R_s$  was measured with the four point probe technique before and after the laser treatment. The top image shown in Fig. 4.27 presents the  $R_s$  map of the  $10 \times 10 \text{ cm}^2$  sample surface before the laser annealing. On the bottom there is a plot of  $\Delta R_s/R_s$

#### 4 Transparent conducting upconverters

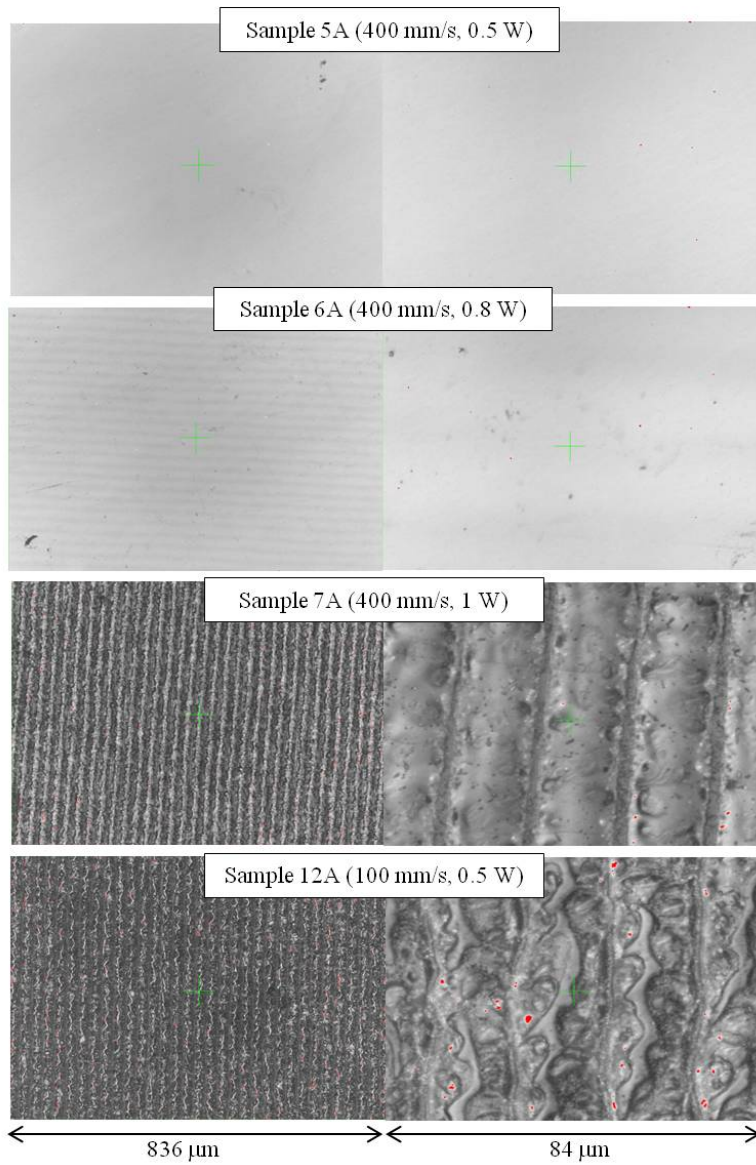


Figure 4.25: Confocal microscope images of samples 5A, 6A, 7A and 12A taken with an objective 20 $\times$  (left images) and 150 $\times$  (right images).

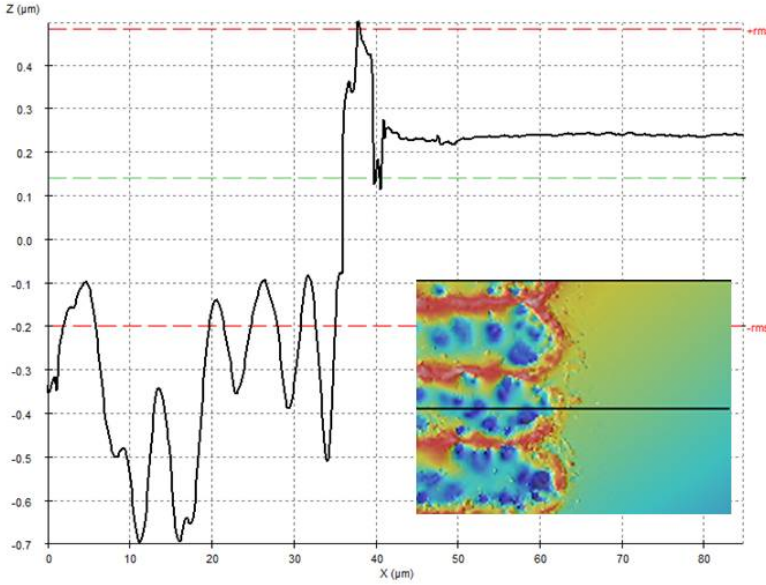


Figure 4.26: Profile taken from the confocal image of sample 7A with  $150\times$  objective. The inset is the confocal image and the black line indicates the profile.

against the laser power where  $\Delta R_s = R_s$  before  $-R_s$  after the laser annealing. The  $R_s$  map of the as-deposited sample presented lack of homogeneity and the best values were obtained in the central part where the  $R_s$  was around  $500 \Omega/\text{sq}$ . As deduced from the bottom graph, when the power was so high that spoiled the film surface, the  $R_s$  drastically increased. This was observed in the case of samples 7A and 12A. In all the other samples the laser treatment did not influence the conductivity and  $\Delta R_s/R_s$  was always  $<0.4$ .

The UC PL was measured for all the laser annealed samples and also for the as-deposited and the air annealed samples. The UC PL in logarithmic scale is depicted in Fig. 4.28. For a better clarity, the samples that did not show upconversion PL (like the spectra of the as-deposited film or sample 16A) are not represented. As shown in the graph, visible upconversion was achieved in the samples annealed with the highest energy, including

#### 4 Transparent conducting upconverters

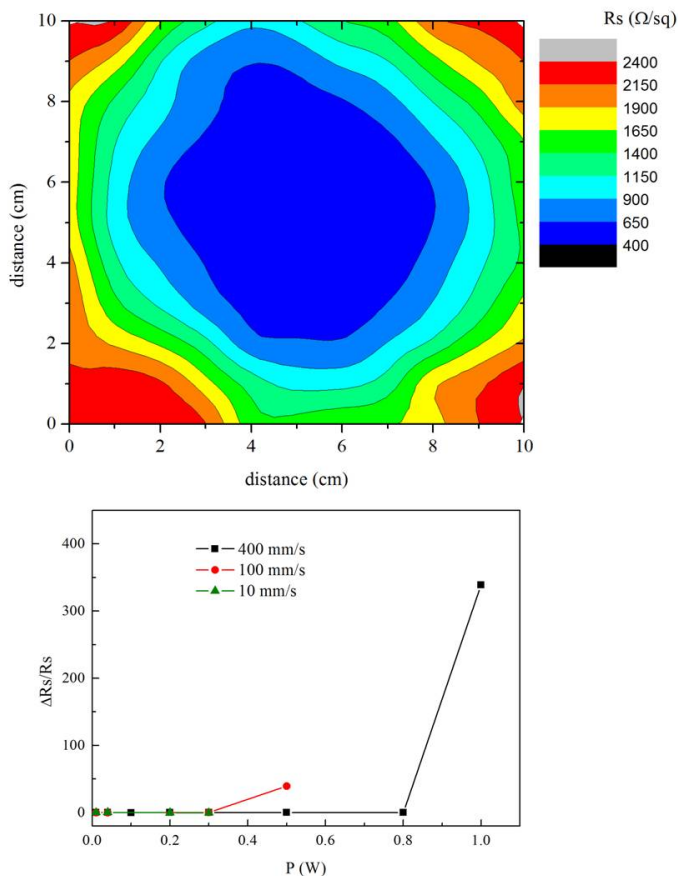


Figure 4.27: The top image contains a  $R_s$  map of the  $10 \times 10 \text{ cm}^2$  as-deposited samples. The bottom graph is the plot of  $\Delta R_s/R_s$  where  $\Delta R_s = R_s$  before  $- R_s$  after the laser annealing.

those that had been ablated. Only samples 5A, 6A, 7A and 12A had the suitable Er environment that allow Er radiative transitions to occur like in the case of the air annealed sample. Furthermore, other visible photons were emitted from the laser treated surfaces that had never appeared before when the samples were annealed in air. This spectra demonstrates that Er is optically active when the laser treatment gives enough energy to the

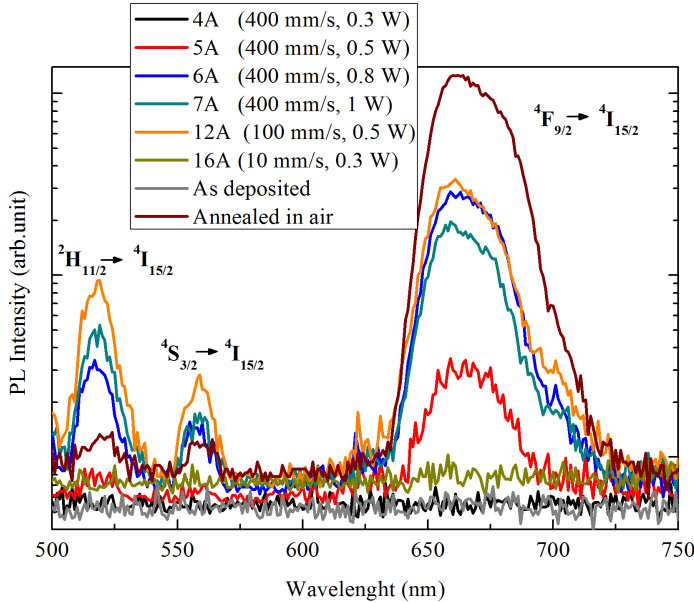


Figure 4.28: UC PL in logarithmic scale of the as-deposited, air annealed and laser annealed samples 5A, 6A, 7A, 12A and 16A. Laser excitation at 980 nm.

sample and enables to change the Er local structure. Moreover, as seen for samples 5A and 6A, it is completely feasible to get visible upconversion in a transparent and conducting film without ablating the material.

Care must be taken to avoid damaging the surface while activating the Er ions, thus, next experiments were done just around the damage threshold of the film. Since the as-deposited film was grown with a relatively high base pressure, a new ZnO:Er:Yb was grown again under the same conditions but at a vacuum pressure of  $1 \times 10^{-4}$  Pa. The as-deposited film was now 6% more transparent than the previous sample.

In the next section a detailed study is given on laser treated ZnO:Er:Yb where the chosen laser parameters were those that gave very high energy without ablating the films.

### 4.2.5 Upconversion from transparent and conducting laser annealed ZnO:Er:Yb

The preparation of the sample was the same as given in Sec. 4.2.4 with the unique difference on the base pressure of the sputtering system. Now a base vacuum of  $1 \times 10^{-4}$  Pa was achieved before the sputtering process.

Sixteen pieces of  $10 \times 10$  mm<sup>2</sup> were cut from the central part of the sample, sample 4 was kept without any annealing treatment, another small piece taken also from the centre was annealed in air atmosphere at 800°C during 1 hour, and the fifteen remaining samples were irradiated with a 532 nm CW laser.

Laser annealing experiments were carried out working just around the damage threshold of the film in order to avoid as much as possible the ablation and loss of material but giving enough energy to achieve upconversion. The processes were performed by scanning  $10 \times 10$  mm<sup>2</sup> areas with parallel lines and varying the gap between them. The beam size on the sample was 29 μm in diameter. The laser parameters are presented together with an image of the irradiated sample in Fig. 4.29. The sample seems dark because it is placed over a black surface but the integrated transmittance in the range 400-1100 nm was ~84%.

Samples 1B, 2B, 3B and 12B have been laser processed below the damage limit of the material, samples 4B, 5B, 6B and 7B have been annealed at the minimum energy able to ablate the film. In the case of samples 9B, 10B, and 11B the processing conditions were kept below the damage limit but the laser scan have been repeated over the same surface 2, 3, and 4 times. Samples 13B, 14B, 15B and 16B have been irradiated by varying the pitch between lines to 20, 40, 50 and 60 μm.

#### 4.2.5.1 Morphology

The probability to damage the film was very high as the aim of the experiments was to be around the ablation limit of the material. Thus, half of the samples suffered from material losses. A confocal microscope have been used to observe the morphology of the treated samples, and the results are shown in Fig. 4.30.

Evaluating the resultant morphology it was possible to observe that samples 1B, 5B, 6B, 7B, 12B, 13B and 14B were almost ablated completely.

## 4.2 Results and discussion

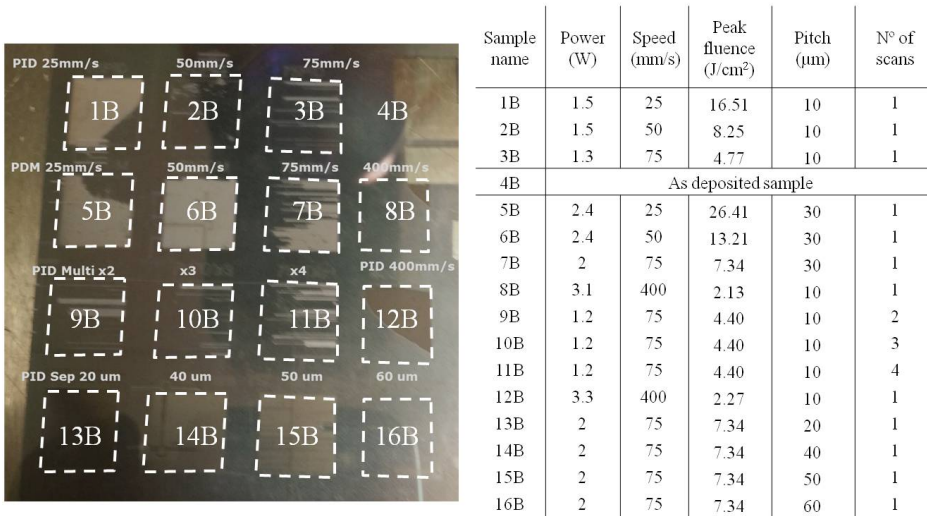


Figure 4.29: Image of the sample with the corresponding irradiated areas. The right table contains a summary with the name of the samples and the process parameters for the laser annealing.

In contrast, samples 2B, 3B, 8B, 9B, 10B and 11B remained unaffected except in very small areas, and in samples 13B, 14B, 15B and 16B where the pitch between lines was varied it could be appreciable that when larger was the pitch lower was the damage. Since the laser spot was around  $29 \mu\text{m}$ , when the pitch was  $40$  (14B),  $50$  (15B) or  $60$  (16B)  $\mu\text{m}$ , some areas between lines remained untreated. When the pitch was  $60 \mu\text{m}$ , the totality of the film seemed completely undamaged. Fig. 4.31 shows an SEM micrograph of samples 13B, 14B and 15B. In sample 14B and 15B it is possible to appreciate these untreated areas between laser scans.

### 4.2.5.2 Structure

XRD was performed on all the laser treated samples, the air annealed and in the as-deposited one. Fig. 4.32 presents all the patterns obtained.

In general, all samples presented the most intense diffraction peak at around  $2\theta=33.5-34.5^\circ$ , suggesting the typical ZnO hexagonal wurtzite



#### 4 Transparent conducting upconverters

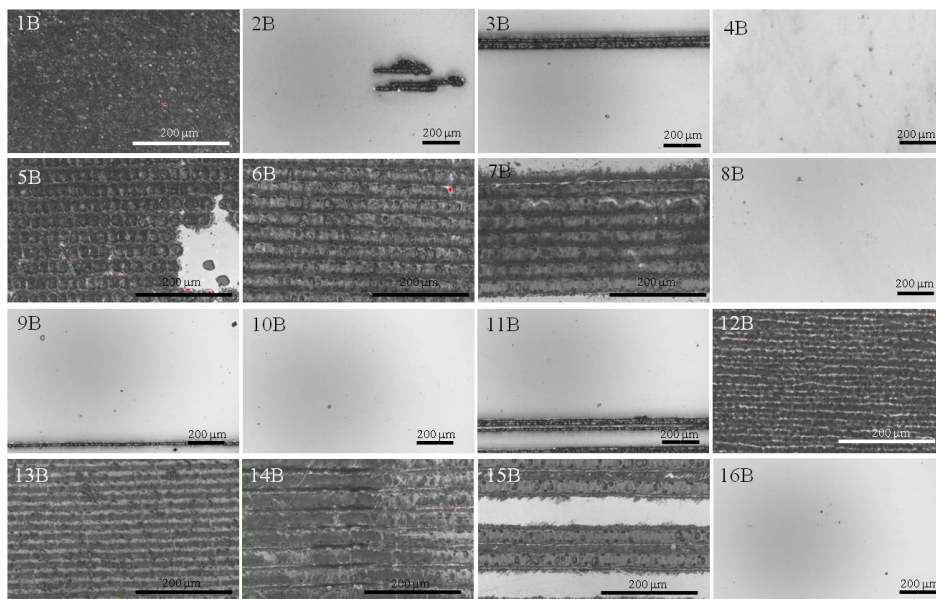


Figure 4.30: Confocal microscope images from all the laser treated ZnO:Er:Yb samples and the as-deposited one.

structure with the  $c$ -axis perpendicular to the substrate. But as observed in the as-deposited sample, the peak was not symmetric indicating that a second peak was also involved. Moreover, when this sample was laser treated and the energy was high enough, a peak splitting was clearly observed confirming the coexistence of two different wurtzite structures in the same sample. In addition, also in the highest energy treated samples a peak raised at  $2\theta=29.62^\circ$  corresponding to the (222) reflection of  $\text{Yb}_2\text{O}_3$  cubic structure. It seemed that Yb, that was initially substituting Zn in the ZnO lattice or at the grain boundaries, migrates to form  $\text{Yb}_2\text{O}_3$  due to the high amount of energy received. As usual in our ZnO:Er:Yb films, no  $\text{Er}_2\text{O}_3$  related peaks were seen due to the small amount of Er content.

For a better understanding on the ZnO:Er:Yb structural changes, first, a comparison between the as-deposited sample, the air annealed and sample 6B is presented (Fig. 4.33). The as-deposited sample reveals just two

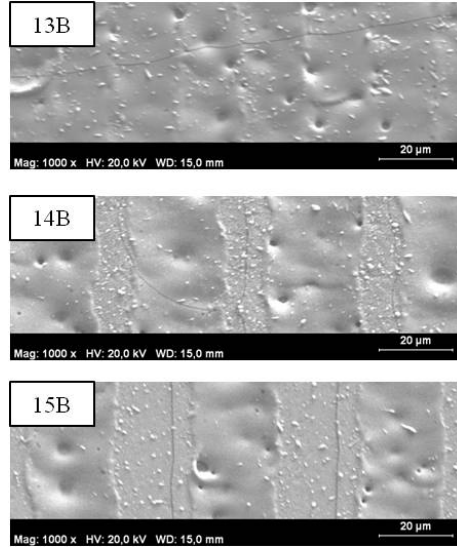


Figure 4.31: SEM images of samples 13B, 14B and 15B.

peaks that correspond to the first and second order diffraction of a typical wurtzite structure, (002) and (004). Due to the clear asymmetry in both peaks, a deconvolution in two Pseudo-Voigt functions has been performed to identify the exact peaks positions (See Fig. 4.33 right). The first peak was centred at  $33.53^\circ$  ( $c_1=0.534$  nm) and the second at  $34.11^\circ$  ( $c_2=0.525$ ), suggesting that two different wurtzite structures were involved, each of them with different lattice parameters. These two structures have been referred as wurtzite 1 (W1) and wurzite 2 (W2). When the sample was air annealed,  $\text{Yb}_2\text{O}_3$  was formed in its cubic structure with preferential orientation (222). Furthermore, it seemed that instead of two wurtzite structures just W2 was observed in the sample. When the sample was laser annealed at high energy like in the case of sample 6A, then the (002) peak, experienced a splitting in two peaks that we identified as W1 and W2, in addition, other orientations belonging also to W2 appeared in the sample. A peak corresponding to  $\text{Yb}_2\text{O}_3$  was also observed at  $31.86^\circ$ . This substantial difference on the lattice structure between the as-deposited sample and the laser annealed suggested that the laser melted the film

#### 4 Transparent conducting upconverters

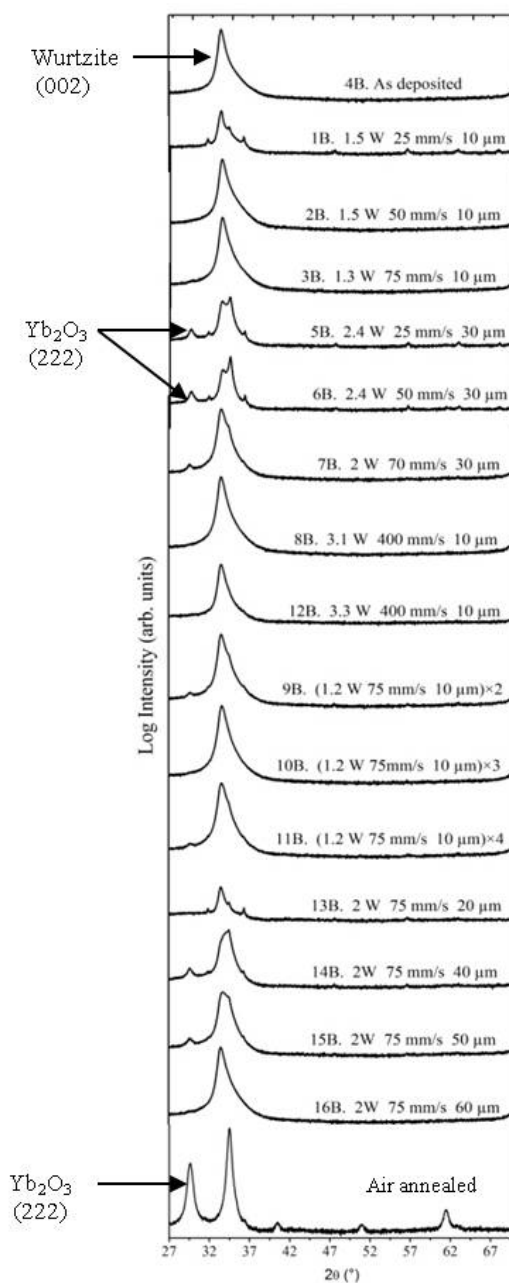


Figure 4.32: X-ray diffraction patterns in logarithmic scale of all the laser treated samples along with the as-deposited (4B) and the air annealed sample.

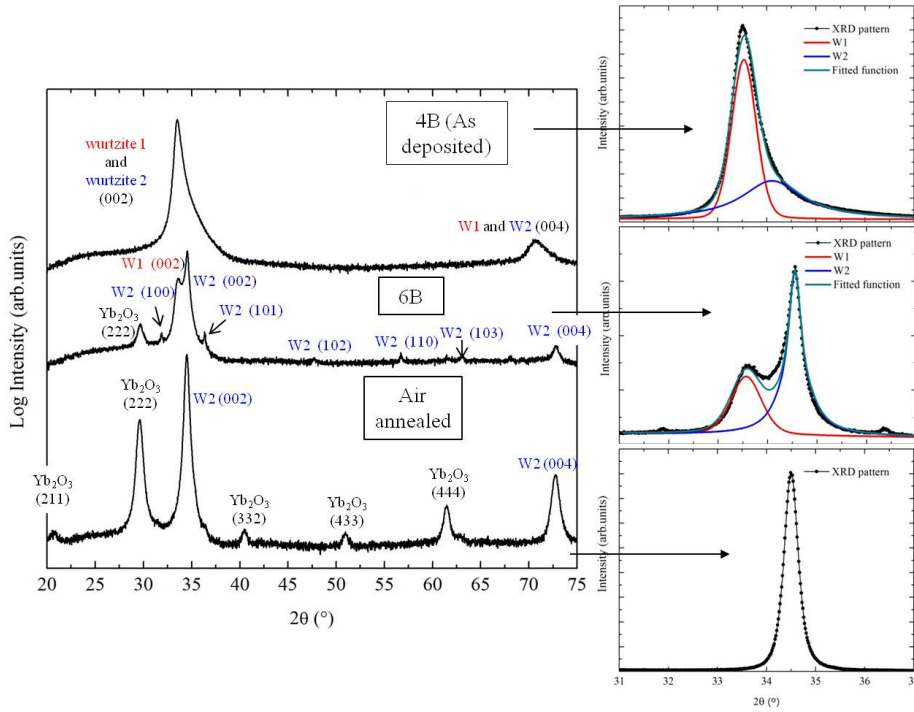


Figure 4.33: X-ray diffraction patterns in logarithmic scale of the as-deposited sample, the air annealed sample and the laser annealed 6B, with the  $2\theta$  values from  $20.75^\circ$  on the left and from  $31^\circ$  to  $37^\circ$  on the right.

and when it cooled down it recrystallized with a different structure that in this case was the coexistence of two wurtzite structures rich in ZnO and a cubic structure of  $\text{Yb}_2\text{O}_3$ .

The  $c$ -parameter was calculated for W1 and W2 in all the samples and the lattice parameter  $a$  could be calculated in samples 1B, 5B, 6B, 13B, 14B and 15B from the (102) peak position. A Pseudo-Voigt deconvolution has been done when the two peaks involved in the (002) peak were not clearly identified. Table 4.8 presents all the calculated lattice parameters.

W1 had lattice parameters values much higher than the standard ZnO value ( $c=0.521$  nm) and also than sputtered and undoped ZnO ( $c=0.523$  nm, calculated in Sec. 4.2.2.1) indicating a very high compressive stress

#### 4 Transparent conducting upconverters

Table 4.8: Values of lattice parameters for the as-deposited, air annealed, vacuum annealed films and the 15 samples irradiated with at different laser parameters.

Sample name	Wurtzite 1		Wurtzite 2	
	$c_1$ (nm)	$c_2$ (nm)	$a_2$ (nm)	
1B	0.534	0.519	0.314	
2B	0.535	0.528	-	
3B	0.534	0.525	-	
4B (As-deposited)	0.534	0.525	-	
5B	0.535	0.519	0.313	
6B	0.534	0.519	0.313	
7B	0.534	0.519	-	
8B	0.534	0.525	-	
9B	0.535	0.519	-	
10B	0.533	0.524	-	
11B	0.536	0.519	-	
12B	0.534	0.526	-	
13B	0.536	0.519	0.313	
14B	0.528	0.513	0.318	
15B	0.531	0.520	0.316	
16B	0.535	0.526	-	
Air annealed	-	0.520	-	

caused mainly by the large ionic radius of the REs species that in substitutional Zn sites are distorting the lattice. Instead, W2 presented closer values to the standard suggesting that the RE ions migrated from these substitutional positions into other sites in or outside the lattice, yielding to a more stress free film.

By grouping the samples according to the laser parameters and plotting the patterns within the range 27-40° (see Fig. 4.34) it was easier to see that the lowest laser energies maintain the patterns unchanged, nevertheless, when increasing the energy (i.e. increasing the power, lowering the speed or decreasing the pitch) the (002) peak started to split and Yb started to oxidise. When the energy was very high like in samples 1B and 13B, and the surface was highly damaged, the peaks intensity decreased and even the Yb<sub>2</sub>O<sub>3</sub> phases disappeared.

## 4.2 Results and discussion

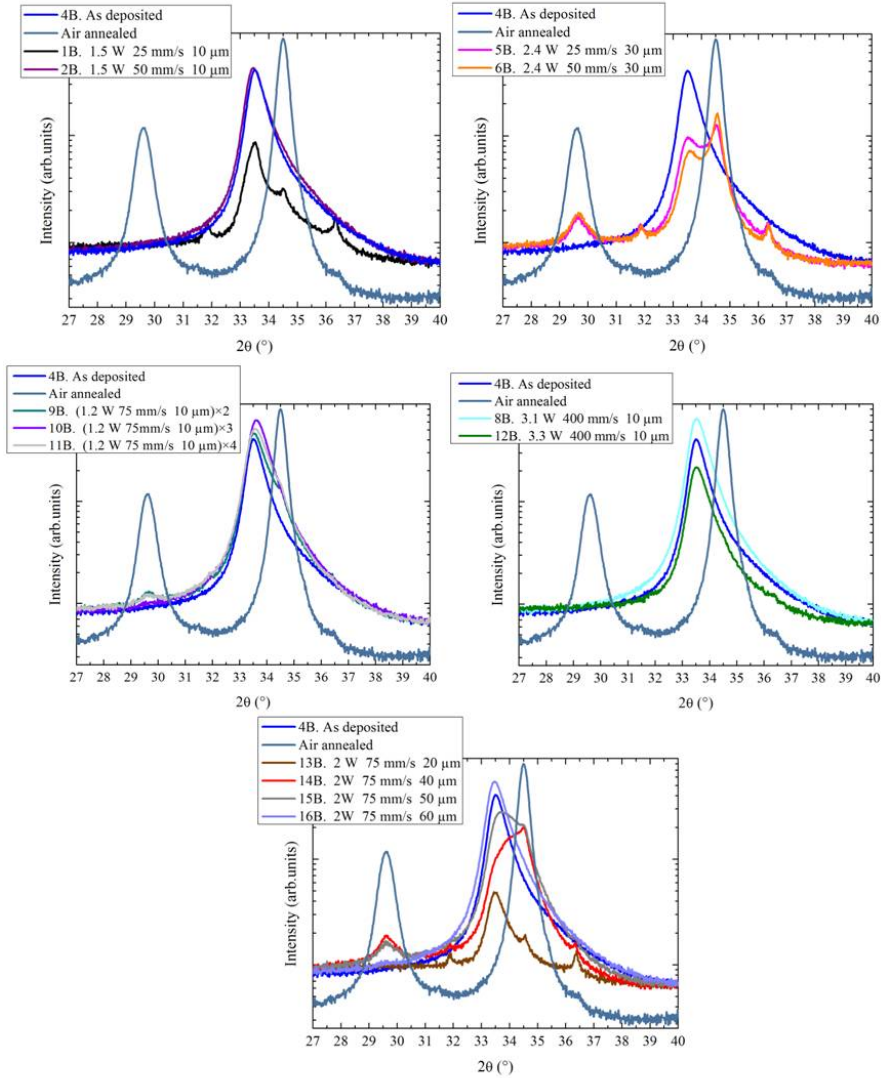


Figure 4.34: X-ray diffraction patterns grouped according to the laser parameters and plotted together with the as-deposited sample and the air annealed sample.

## 4 Transparent conducting upconverters

Table 4.9: Values of the  $R_s$  and the integrated  $T$  in the range 400-1100 nm of the sixteen samples.

Sample name	$R_s$ ( $\Omega/\text{sq}$ )	$T$ (400-1100 nm)	Sample name	$R_s$ ( $\Omega/\text{sq}$ )	$T$ (400-1100 nm)
1B	100-130k	63.10	9B	1.7k	85.06
2B	45k	83.55	10B	1.7k	85.06
3B	3M	69.38	11B	2.6k	84.35
4B	2-10k	83.85	12B	2.3M	85.83
5B	2M	78.72	13B	10M	79.93
6B	13k	81.58	14B	-	81.51
7B	2k	85.24	15B	-	81.04
8B	10k	83.74	16B	2.6k	83.79

### 4.2.5.3 Electrical and optical properties

To evaluate the feasibility as a transparent and conducting film, the  $R_s$  and the transmittance were measured. The  $R_s$  behaved according to the morphology of the samples, a higher ablation corresponded to a higher  $R_s$  due to the non-uniform loss of material. When the samples did not present a damaged surface, the  $R_s$  kept invariable. The same happened with the transmittance of the films, just the damaged films yield to lower transmittance values while they look changeless if the morphology seemed unaltered as deduced from the confocal microscope images. A summary of the  $R_s$  values is shown in Table 4.9 along with the integrated transmittance values in the range 400-1100 nm. In accordance with this results, only samples 2B, 6B, 7B, 8B, 9B, 10B, 11B and 16B could be used as the transparent and conducting oxide that that can be applied as the back reflector of a *pin* Si thin film solar cell.

Conventional PL at low temperature was measured in some of the samples. The excitation was performed at 325 nm and the detection was recorded between 340 and 1100 nm. For a clearer understanding the PL resultant spectra has been shown in different graphs, Fig. 4.35 a) contains the spectra in the range 340-480 nm, Fig. 4.35 b) in the range 600-700 nm (left) and its enlargement (right) and in Fig. 4.35 c) the range is 800-1100 nm in the left graph and the right one presents its zoomed area.

The conventional PL spectra is similar to that seen in Figures 4.18, 4.22 and 4.13: In general terms, it presents a UV emission that corresponds to

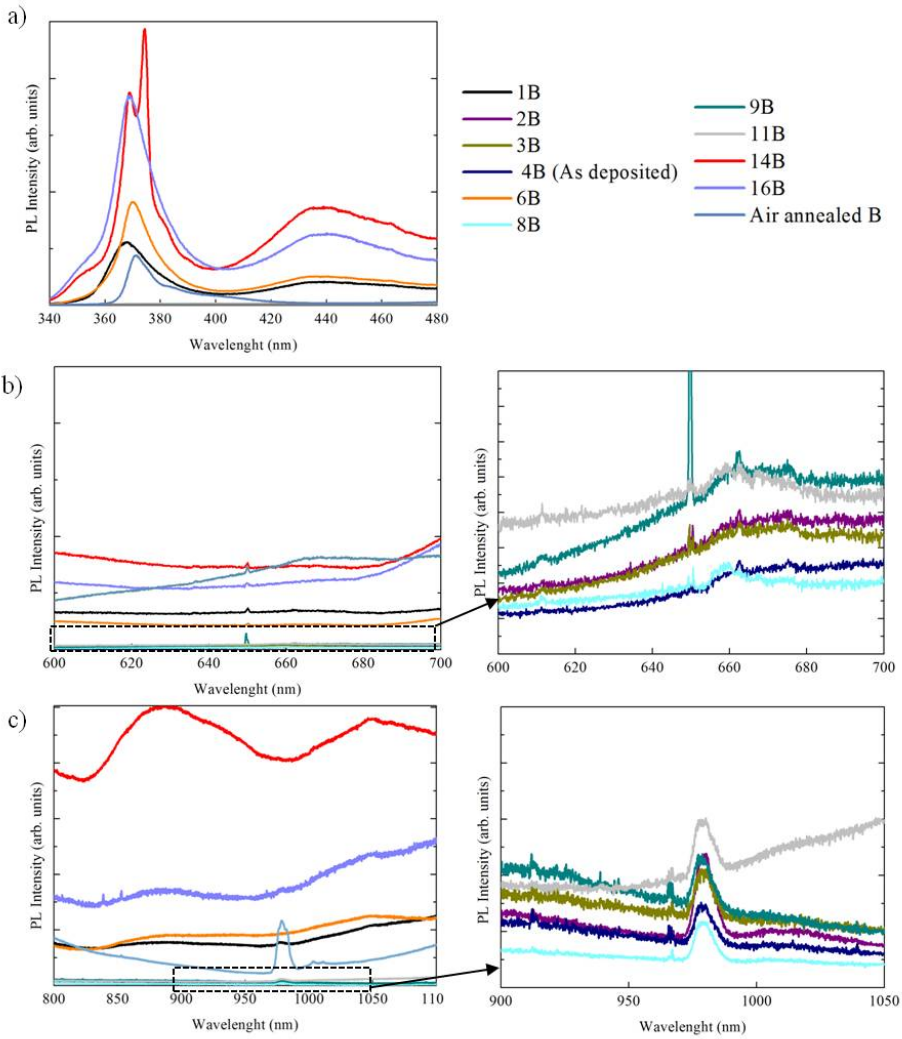


Figure 4.35: Conventional PL recorded at  $-196^{\circ}\text{C}$  of the laser treated ZnO:Er:Yb samples, the air annealed sample and the as-deposited one in the range a) 340-480 nm, b) 600-700 nm in the left graph and its zoomed portion in the right graph and c) 800-1100 nm in the left graph and its zoomed portion in the right graph. Laser source: 325 nm.



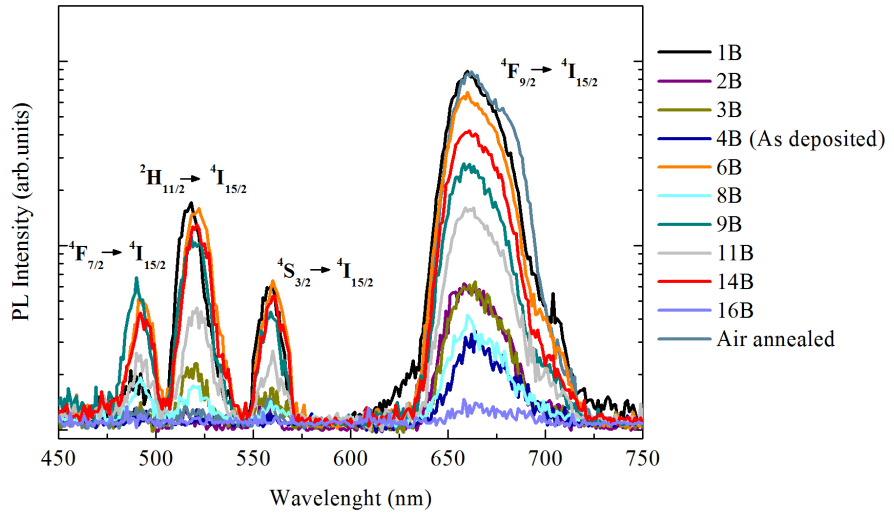


Figure 4.36: Upconversion PL of the laser treated ZnO:Er:Yb samples, the air annealed sample and the as-deposited one. Laser source: 980 nm.

the band-to-band excitonic recombination, a visible emission at 660 nm ought to an Er electronic transition and another peak at 980 nm corresponding to Er or Yb emissions. UV emission only raises from the sample annealed in air and from the ablated samples, and as higher was the ablation, higher was the UV emission. The films that kept the same surface morphology before and after the laser treatment do not present this band to band excitonic emission.

If Er and Yb emissions are taking place (660 or 980 nm), it is because ZnO is absorbing the laser radiation and transferring its energy to the rare earth species. At 660 nm just sample 9B seems to show a very small peak that can be negligible if taking into account the ratio to the UV peak.

UC PL was measured on the same samples and is presented in Fig. 4.36. The laser source was 980 nm and the detection was performed in the range 450-750 nm. In contrast to the as-deposited film shown in Sec. 4.2.4 where

the base pressure before deposition was one order of magnitude higher, the as-deposited ZnO:Er:Yb presented UC emission at 660 nm without the need of any annealing treatment. As expected, after the air annealing this UC PL was drastically increased. Most of the laser treated samples presented other visible UC emissions in addition to the one at 660 nm which implies a higher quantum yield, hence, a greater number of visible photons are emitted (480, 520, 550 and 660 nm). In general, when higher was the ablation, higher was the UC PL. For example samples 1B, 6B and 14B presented very high UC intensities and, as seen in Fig. 4.30, correspond to the highest ablated surfaces. A direct comparison between samples intensity can not be done because of the lack of homogeneity in the  $10 \times 10 \text{ cm}^2$  thin film surface. Some previous characterization was performed comparing two as-deposited pieces taken from a lateral and from the centre of the whole  $10 \times 10 \text{ cm}^2$  sample and the optical, structural and electrical characterization on those pieces indicated that the surface was not homogeneous. Moreover as the measurement was performed manually, some small variations can also be added between one measurement to another. For instance, sample 16B that was close to the lateral, did not show any emission. When comparing the UC PL to the conductivity and transparency of the samples, it could be demonstrated that it is possible to achieve a transparent and conducting upconverter. As shown by samples 9B and 11B, the  $R_s$  was lower than  $3 \text{ k}\Omega/\text{sq}$ , the integrated transmittance in the range 400-1100 nm was higher than 84% and visible UC emission was achieved at 480, 520, 550 and 660 nm.

Comparing the structural patterns to the PL results, the first observation was that the highest upconversion was given by the sample annealed in air that was the one that contained the highest amount of  $\text{Yb}_2\text{O}_3$  crystals and in which just the W2 structure was seen. As shown in the introduction of this chapter the rare earth oxides posses the adequate configuration to allow the optical transitions to occur, hence, higher  $\text{Yb}_2\text{O}_3$  means higher UC efficiency. Moreover the RE ions forming  $\text{RE}_2\text{O}_6$  complexes inside or outside the ZnO matrix will also lead to UC emissions. Hence, the total UC luminescence will be the contribution of the  $\text{RE}_2\text{O}_3$  and  $\text{RE}_2\text{O}_6$  complexes. Although those complexes could not be detected through XRD, it was probable that the RE in substitutional sites formed W1 and the RE in non-substitutional sites formed W2. Then, the probability to have  $\text{Er}_2\text{O}_6$  complexes was higher if the RE were not substituting zinc and the

contribution of W2 was higher. The coexistence of W1 and W2 could be the reason why the conductivity remained in the non-ablated samples after laser annealing. As mentioned before, the conductivity in ZnO:Er:Yb films can be either due to substitutional RE in the ZnO lattice or to oxygen vacancies, therefore W1 seemed to be the structure responsible of the electrical conduction. It was also observed that as higher was the ablation, more evident was the (002) peak splitting and higher was the UC emission. In conclusion, the UC seemed to be related to the appearance of W2 and Yb<sub>2</sub>O<sub>3</sub> phases and the conductivity seemed to be related to W1. The coexistence of W1, W2 and Yb<sub>2</sub>O<sub>3</sub> may result in a conducting upconverter.

### 4.3 Conclusions

The aim of this chapter was to create a transparent and conducting upconverter to be used as the rear reflector for a thin film Si solar cell. ZnO has been doped with Er and Yb and has been post-annealed under different treatments in order to optically activate the RE ions. To be an optically active centre, the RE ion needs to be surrounded by 6 oxygen in a distorted octahedron. As-deposited ZnO:Er:Yb is transparent and conducting but does not show any photoluminescence because Er replacing zinc in the ZnO lattice is not surrounded by 6 oxygen atoms. Hence, a post-deposition treatment is needed. When the films are annealed in air, visible UC emissions are produced at 660 nm under 980 nm laser excitation but the films become almost insulating. When the films are annealed in vacuum then also UC luminescence at 660 nm is achieved but lower than that achieved for annealing in air ambient, and the resistivity increases just 1 order of magnitude. By using CW laser to anneal the samples just before the ablation limit of the material, the electrical properties are completely maintained and high UC is also achieved at 660, 560, 520 and 480 nm. The structural and PL characterization of all the samples have demonstrated that UC comes from clusters of REO<sub>6</sub> as well as from RE<sub>2</sub>O<sub>3</sub> inside or outside the matrix, the as-deposited films have a lack of oxygen which yields to non luminescent samples. When they are annealed in air, the oxygen from the air binds to the RE species that migrate from substitutional sites and from the grain boundaries to form RE oxides or REO<sub>6</sub>

complexes. The same happens when the samples are annealed in vacuum, but the lower oxygen content in the vacuum atmosphere leads to less optically active centres and better conductivity. The laser annealing seems to be able to preserve the electrical properties while producing optically active centres. Probably the laser energy is melting part of the material which recrystallizes creating RE oxides, and two wurtzite structures, one that has substitutional rare earths and oxygen vacancies (i.e. responsible of the conductivity) and the other without substitutional REs (responsible of UC emissions).



## 5 Conclusions

The objective of this work was to study two different light management approaches to enhance the efficiency of thin film Si solar cells and these were the manipulation of the light path (e.g. light trapping) and changing the incoming photon energy (e.g. upconversion).

In the first approach the path length of light was increased by creating either periodic or random textured interfaces to increase the light trapping by scattering. Periodic patterns were created at the front AZO by means of direct laser ablation and random textures were performed on the glass substrate by means of the Aluminium Induced Texturing method (AIT).

Laser ablation of AZO was performed at 355 nm and 50 kHz. The process speed, the power, the pitch between lines and the pattern were varied. After evaluating the electrical and optical properties of the resultant structures it can be concluded that:

- The best equilibrium between haze and conductivity was achieved with a linear pattern of 10  $\mu\text{m}$  of pitch and 360 nm of groove depth, that yielded to an  $R_s$  of 11  $\Omega/\text{sq}$  and a haze of 12.7%.
- The use of a single laser beam could not create pattern structures in the sub-micrometer range which is the most adequate to scatter light in thin film silicon solar cells. The minimum period that could be created was limited by the laser spot size (23  $\mu\text{m}$ ).

In the AIT method a thin Al film is deposited onto a glass substrate and a redox reaction between the Al and the  $\text{SiO}_2$  of the glass is induced by high temperature annealing. The reaction products are wet-etched and the result is a uniform and nanotextured glass surface. The process parameters such as the Al deposition method, the annealing time and temperature, the Al thickness and the etching conditions were varied in order to control the resultant glass roughness and the conclusions are:

## 5 Conclusions

- The minimum temperature to allow the reaction process between Borofloat glass and the Al layer was  $\sim 600^\circ\text{C}$  and the time needed for the complete reaction depended on the Al layer thickness and area of the sample (for example, 10 min were enough for 30 nm thick Al film on a  $2 \times 5 \text{ cm}^2$  area substrate). Once the reaction had occurred, no difference in the roughness was observed by increasing further the time of annealing.
- The final texture did not depend on the Al film thickness albeit for small thickness in which the final glass roughness was very soft.
- The etching process was done with  $\text{H}_3\text{PO}_4$  at  $185^\circ\text{C}$  until the reaction products were completely removed, the etching time depended on the Al thickness (for example, 15 min were required when the initial Al film was 250 nm).
- As it was an interface reaction, the most critical parameters were the deposition method and the glass cleanness. The energy at which the Al particles reach the glass determined the adhesion and compactness of the film which defined the degree of glass roughness. By using evaporation (Al particles reaching the glass at 0.1-0.2 eV) it was possible to create morphologies based on smooth U-shaped craters (0.5 to 1  $\mu\text{m}$ ), roughness between 50 to 90 nm and haze up to 15% at 600 nm (Fig. 5.1 left), whereas the sputtered films (Al particles 2-30 eV) resulted in very rough and porous textures with  $\sigma_{rms}$  values upto 145 nm and haze values up to 45% at 600 nm (Fig. 5.1 right). By using e-beam evaporation to deposit the Al, the resultant glass roughness was very similar to that achieved by using resistive evaporation, in both methods the Al particles reached the glass with similar kinetic energy.
- The resultant roughness was difficult to control by depositing the Al through evaporation while with the sputtering, could be easily tunable. By varying the dc sputtering power at 60 W, 100 W or 150 W, the resultant glass surface yielded haze values of 15%, 22% and 32% at 600 nm, respectively. At powers higher than 200 W the surface got too much damaged affecting the uniformity.

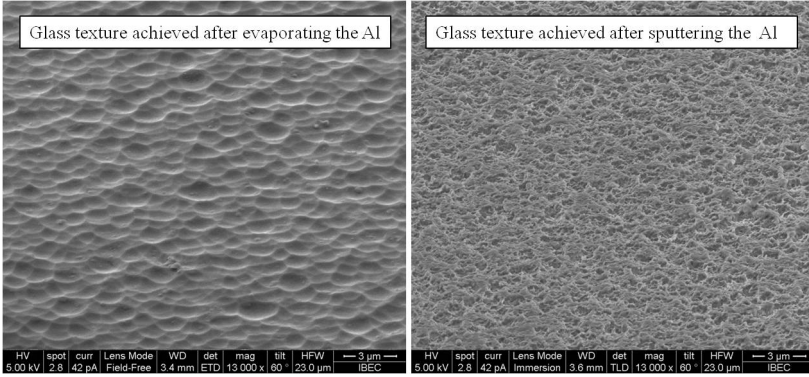


Figure 5.1: SEM micrographs of two textured glass surfaces. Left: texture achieved by depositing the Al by evaporation. Right: texture achieved by depositing the Al by sputtering.

Once the AIT process was controlled and optimized, sputtered AZO of different thickness (500, 700, 1000 nm) was deposited on two different textures, one very soft ( $\sigma_{rms}=56$  nm) and one very rough ( $\sigma_{rms}=145$  nm). The objective was to achieve a transparent and conducting front contact with high haze values. The main conclusions after morphological, optical and electrical characterization are the following:

- The best result for the smooth U-shape crater morphology was for the AZO of 700 nm which led to haze values above 10% at 600 nm, transparency above 84.5%, and  $Rs \sim 7 \Omega/\text{sq}$ .
- The best result for the roughest surface was for the AZO of 1000 nm that yielded to haze value  $>33\%$  at 600 nm,  $Rs$  around  $9.5 \Omega/\text{sq}$  and transmittance of 73.5%.
- XRD results of AZO grown over textured glass presented a hexagonal wurtzite structure with the  $c$ -axis perpendicular to the substrate. AZO on highly textured surfaces showed a decrease in the (002) peak intensity together with the appearance of other wurtzite structure orientations (100), (102), and (101).

To prove the suitability of these morphologies in improving the light



## 5 Conclusions

trapping, a-Si:H solar cells were fabricated on different AIT textures.

In the first trial a-Si:H *pin* solar cells were deposited over AIT substrates ( $\sigma_{rms} \sim 70$  nm and  $\sigma_{rms} \sim 90$  nm) and flat Borofloat glass covered with an AZO of 400 nm and also over Asahi-U. The device characterisation resulted in:

- A reduction of the device reflectivity was observed for both textures, being higher for  $\sigma_{rms} \sim 90$  nm.
- 17% improvement in short-circuit current value for the cells deposited on the rougher texture with respect to the flat one, achieving similar value to the reference cells over Asahi-U. In contrast, a rectifying junction was formed at the ZnO/p-type a-Si:H interface, which resulted in low FF values.

In order to correct the potential barrier that was seen in the first trial a second trial was performed: a thin *p*-type  $\mu$ c-Si layer of  $\sim 25$  nm was deposited between the front AZO and the a-Si *p*-type layer. The AIT substrates used were a very soft ( $\sigma_{rms} \sim 56$  nm) and a very rough ( $\sigma_{rms} \sim 145$  nm) texture.

- The integrated reflectance in the range 400-800 nm of the whole device decreased from 34% (cell on smooth glass) to 18% for the rougher substrate and to 21% for the softer texture.
- The *J-V* curves showed an increase in the short circuit current for both textures compared to the smooth substrate,  $\Delta J_{sc} \sim 0.23$  mA/cm<sup>2</sup> for the rough and  $\Delta J_{sc} \sim 1.63$  mA/cm<sup>2</sup> for the soft. The lower current density of the cell fabricated on the roughest texture can be assigned to the development of some defects during the microcrystalline *p*-type Si growth.
- The AIT method provides suitable textures for Si-based solar cells, the cells were fabricated without shunting and gave always greater short circuit current values than the cells grown on smooth substrates.
- Textured glass substrates can find application in different thin film based solar cells where light scattering is needed for achieving higher photon absorption.

The second approach was to convert the incoming photons to photons that match better the Si absorption spectrum and this was done using upconversion mechanisms. The aim was to create a transparent and conducting upconverter to be used as the TCO of the back reflector of a Si thin film solar cell. For that purpose, ZnO was doped with Er or codoped with Er and Yb ions and was post-annealed under different conditions to activate the upconversion. The equilibrium between the transparency, the conductivity and the photoluminescence of the samples was investigated. The main conclusions are:

- Er<sub>2</sub>O<sub>3</sub> powder showed visible upconversion under 980 nm laser excitation.
- As-deposited ZnO doped with rare earths (RE) was transparent (>80% in the range 400-1100 nm) and conducting ( $\rho \sim 10^{-2} \Omega \text{ cm}$ ) but not luminescent.
- The conduction in ZnO:REs was mainly due to substitutinal RE in Zn sites, oxygen vacancies or the contribution of both.
- The structure of as-deposited ZnO:REs indicate a hexagonal wurtzite structure with preferential orientation along (002) plane with the *c*-axis perpendicular to the sample surface. The lattice experienced a compressive stress due to the substitutinal REs in Zn sites and due to the bombardment during the sputtering.
- RE ions needed to be surrounded by 6 oxygen ions in a distorted octahedron to be optically active and REs replacing zinc in the ZnO lattice do not present this symmetry, hence, a post-deposition treatment was needed.
- Codoping the films with Er and Yb enhanced the upconversion efficiency. The optimum composition was found to be 1% at. Er and 3% at. Yb.
- When the films were post-annealed in air:
  - RE oxides phases appeared in the XRD patterns. The lattice stress was now slightly tensile.

## 5 Conclusions

- The films became almost insulating due to the migration of the RE ions from Zn sites to other positions and/or due to the filling up of oxygen vacancies.
- The transparency increased up to 85%.
- Visible upconversion was seen at 660 nm under 980 nm laser excitation.
- When the films were annealed in vacuum:
  - RE oxides phases appeared in the XRD patterns.
  - The resistivity increased only 1 order of magnitude.
  - The transparency increased up to 87%.
  - UC luminescence was achieved, but lower than in the air annealed samples.
- When the films were annealed using CW laser radiation just before the ablation point of the material:
  - The laser energy recrystallized the material mixing crystallites of RE oxides, and two wurtzite structures, the one that had substitutional rare earths and oxygen vacancies and the one without substitutional REs.
  - The electrical properties were conserved.
  - The transparency was invariable.
  - Visible UC was observed at 660, 560, 520 and 480 nm under 980 nm laser excitation and was just slightly lower than the UC achieved when the samples were annealing in air.
- UC luminescence came from clusters of  $\text{REO}_6$  as well as from  $\text{RE}_2\text{O}_3$  inside or outside the matrix. The as-deposited films had a lack of oxygen which yielded to non luminescent samples. When the samples were annealed in air, vacuum or by laser radiation, oxygen from the atmosphere bonded to the RE species which migrated from substitutional sites or from the grain boundaries to form RE oxides and/or  $\text{REO}_6$  complexes.
- The atomic composition was invariable after any annealing treatment.

- Among all the post-annealing treatments assessed, laser annealing was the only annealing method able to preserve the conductivity, transparency and achieve visible upconversion.
- The upconverting transparent conducting oxide material (ZnO:Er:Yb) can be applied to most of the solar cells where the NIR wavelength of light is not used.



# Bibliography

- [1] “Renewables 2014 Global Status Report, (Paris: REN21 Secretariat),” *REN21*, 2014.
- [2] A. Jäger-Waldau, *PV status report 2013*. Joint Research Centre, 2013.
- [3] M. A. Green, K. Emery, Y. Hishikawa, W. Warta, and E. D. Dunlop, “Solar cell efficiency tables (version 44),” *Progress in Photovoltaics: Research and Applications*, vol. 22, p. 1, 2014.
- [4] M. A. Green, “Third generation photovoltaics: Ultra-high conversion efficiency at low cost,” *Progress in Photovoltaics: Research and Applications*, vol. 9, no. 2, p. 123, 2001.
- [5] T. Trupke, M. Green, and P. Würfel, “Improving solar cell efficiencies by up-conversion of sub-band-gap light,” *Journal of Applied Physics*, vol. 92, no. 7, p. 4117, 2002.
- [6] T. Trupke, M. Green, and P. Würfel, “Improving solar cell efficiencies by down-conversion of high-energy photons,” *Journal of Applied Physics*, vol. 92, no. 3, p. 1668, 2002.
- [7] D. Staebler and C. Wronski, “Reversible conductivity changes in discharge produced amorphous Si,” *Applied Physics Letters*, vol. 31, no. 4, p. 292, 1977.
- [8] J. Meier, S. Dubail, S. Golay, U. Kroll, and S. Fa, “Microcrystalline silicon and the impact on micromorph tandem solar cells,” *Solar Energy Materials and Solar Cells*, vol. 74, p. 457, 2002.
- [9] K. Sato, Y. Gotoh, Y. Wakayama, Y. Hayashi, K. Adachi, and H. Nishimura, “Highly textured SnO<sub>2</sub>:F TCO films for a-Si solar cells,” *Report of Research Laboratory. Asahi Glass Company Ltd.*, vol. 42, p. 129, 1992.
- [10] O. Kluth, B. Rech, L. Houben, S. Wieder, G. Schoepe, C. Beneking, H. Wagner, A. Loeffl, and H. W. Schock, “Texture etched ZnO: Al coated glass substrates for silicon based thin film solar cells,” *Thin Solid Films*, vol. 351, p. 247, 1999.
- [11] J. Steinhauser, S. Fay, N. Oliveira, E. Vallat-Sauvain, and C. Ballif, “Transition between grain boundary and intragrain scattering transport mechanisms in boron-doped zinc oxide thin films,” *Applied Physics Letters*, vol. 90, no. 14, p. 142107, 2007.

## Bibliography

- [12] J. Wager, D. Keszler, and R. Presley, *Transparent electronics*. USA: Springer, 2008.
- [13] R. Schropp and M. Zeman, *Amorphous and microcrystalline silicon solar cells: modelling, materials and device technology*. USA: Kluwer academic, 1998.
- [14] J. Morris, R. R. Arya, J. G. O'Dowd, and S. Wiedeman, "Absorption enhancement in hydrogenated amorphous silicon based solar cells," *Journal of Applied Physics*, vol. 47, no. 1079, p. 4086, 1990.
- [15] K. Ellmer, A. Klein, and B. Rech, *Transparent conductive zinc oxide. Basics and application in thin film solar cells*. Germany: Springer, 2008.
- [16] H. McMurdie, M. Morris, E. Evans, B. Paretzkin, W. Wong-Ng, L. Ettliger, and C. Hubbart, "ZnO reference for bragg peak position and net constants," *Powder Diffraction*, vol. 1, no. 2, p. 76, 1986.
- [17] D. S. Ginley, H. Hosono, and D. C. Paine, *Handbook of transparent conductors*. USA: Springer, 2010.
- [18] K. Ellmer and R. Mientus, "Carrier transport in polycrystalline transparent conductive oxides: A comparative study of zinc oxide and indium oxide," *Thin Solid Films*, vol. 516, no. 14, p. 4620, 2008.
- [19] S. Takata, T. Minami, and H. Nanto, "The stability of aluminium-doped ZnO transparent electrodes fabricated by sputtering," *Thin Solid Films*, vol. 135, p. 183, 1986.
- [20] T. Minami, H. Sato, H. Nanto, and S. Takata, "Group III impurity doped zinc oxide thin films prepared by RF magnetron sputtering," *Japanese Journal of Applied Physics*, vol. 24, no. 10, p. L781, 1985.
- [21] J. Seto, "The electrical properties of polycrystalline silicon films," *Journal of Applied Physics*, vol. 46, no. 12, p. 5247, 1975.
- [22] J. I. Pankove, *Optical processes in semiconductors*. USA: Dover Publications, 1971.
- [23] E. Burstein, "Anomalous optical absorption limit in InSb," *Physical Review Letters*, vol. 93, p. 632, 1954.
- [24] T. Moss, "The interpretation of the properties of indium antimonide," *Proceedings of the Physical Society. Section B*, vol. 67, p. 775, 1954.
- [25] P. Drude, "Zur elektronentheorie der metalle," *Annalen der Physik*, vol. 306, p. 566, 1900.

- [26] B. Lin, Z. Fu, and Y. Jia, "Green luminescent center in undoped zinc oxide films deposited on silicon substrates," *Applied Physics Letters*, vol. 79, no. 7, p. 943, 2001.
- [27] Y. Wang, S. Lau, X. Zhang, H. Hng, H. Lee, S. Yu, and B. Tay, "Enhancement of near-band-edge photoluminescence from ZnO films by face-to-face annealing," *Journal of Crystal Growth*, vol. 259, no. 4, p. 335, 2003.
- [28] K. Bouzid, A. Djelloul, N. Bouzid, and J. Bougdira, "Electrical resistivity and photoluminescence of zinc oxide films prepared by ultrasonic spray pyrolysis," *Physica Status Solidi (a)*, vol. 206, no. 1, p. 106, 2009.
- [29] A. B. Djuricic, Y. H. Leung, K. H. Tam, L. Ding, W. K. Ge, H. Y. Chen, and S. Gwo, "Green, yellow, and orange defect emission from ZnO nanostructures: Influence of excitation wavelength," *Applied Physics Letters*, vol. 88, no. 10, p. 3107, 2006.
- [30] S. A. Studenikin, M. Cocivera, W. Kellner, and H. Pascher, "Band-edge photoluminescence in polycrystalline ZnO films at 1.7 K," *Journal of Luminescence*, vol. 91, p. 223, 2000.
- [31] I. Soumahoro, G. Schmerber, a. Douayar, S. Colis, M. Abd-Lefdil, N. Hassanain, a. Berrada, D. Muller, a. Slaoui, H. Rinnert, and a. Dinia, "Structural, optical, and electrical properties of Yb-doped ZnO thin films prepared by spray pyrolysis method," *Journal of Applied Physics*, vol. 109, no. 3, p. 033708, 2011.
- [32] Y. C. Kong, D. P. Yu, B. Zhang, W. Fang, and S. Q. Feng, "Ultraviolet-emitting ZnO nanowires synthesized by a physical vapor deposition approach," *Applied Physics Letters*, vol. 78, no. 4, p. 407, 2001.
- [33] X. M. Teng, H. T. Fan, S. S. Pan, C. Ye, and G. H. Li, "Photoluminescence of ZnO thin films on Si substrate with and without ITO buffer layer," *Journal of Physics D: Applied Physics*, vol. 39, no. 3, p. 471, 2006.
- [34] J. S. Kang, H. S. Kang, S. S. Pang, E. S. Shim, and S. Y. Lee, "Investigation on the origin of green luminescence from laser-ablated ZnO thin films," *Thin Solid Films*, vol. 443, no. 1-2, p. 5, 2003.
- [35] R. Va, M. J. Bushiri, and V. Vaidyan, "Visible Luminescence Centers in Zinc Oxide Films Deposited by Spray Pyrolysis," *Journal of Optoelectronics and Advanced Materials*, vol. 9, no. 12, p. 3740, 2007.
- [36] M. Liu, A. H. Kitai, and P. Mascher, "Point defects and luminescence centres in zinc oxide and zinc oxide doped with manganese," *Journal of Luminescence*, vol. 54, p. 35, 1992.



## Bibliography

- [37] Q. Luo, X. Qiao, X. Fan, and X. Zhang, "Near-infrared emission of Yb<sup>3+</sup> through energytransfer from ZnO to Yb<sup>3+</sup> in glass ceramic containing ZnO nanocrystals," *Optics letters*, vol. 36, no. 15, p. 2767, 2011.
- [38] X. L. Wu, G. G. Siu, C. L. Fu, and H. C. Ong, "Photoluminescence and cathodoluminescence studies of stoichiometric and oxygen-deficient ZnO films," *Applied Physics Letters*, vol. 78, no. 16, p. 2285, 2001.
- [39] C. Ja, Z. Feng, P. Ying, M. Li, B. Han, and C. Li, "The visible luminescent characteristics of ZnO supported on SiO<sub>2</sub> powder," *Physical Chemistry Chemical Physics*, vol. 6, no. 18, p. 4473, 2004.
- [40] Y. Igasaki and H. Saito, "Substrate temperature dependence of electrical properties of ZnO:Al epitaxial films on sapphire (1210)," *Journal of Applied Physics*, vol. 69, no. 4, p. 2190, 1991.
- [41] K. Ellmer, "Magnetron sputtering of transparent conductive zinc oxide: relation between the sputtering parameters and the electronic properties," *Journal of Physics D: Applied Physics*, vol. 33, p. R17, 2000.
- [42] O. Kluth, G. Schöpe, J. Hüpkens, C. Agashe, J. Müller, and B. Rech, "Modified Thornton model for magnetron sputtered zinc oxide: film structure and etching behaviour," *Thin Solid Films*, vol. 442, no. 1-2, p. 80, 2003.
- [43] J. A. Thornton, "High rate thick film growth," *Annual Review of Material Science*, vol. 7, p. 239, 1977.
- [44] W. Shockley and H. J. Queisser, "Detailed Balance Limit of Efficiency of p-n Junction Solar Cells," *Journal of Applied Physics*, vol. 32, no. 3, p. 510, 1961.
- [45] B. Richards, "Enhancing the performance of silicon solar cells via the application of passive luminescence conversion layers," *Solar Energy Materials and Solar Cells*, vol. 90, no. 15, p. 2329, 2006.
- [46] B. M. van der Ende, L. Aarts, and A. Meijerink, "Lanthanide ions as spectral converters for solar cells," *Physical chemistry chemical physics*, vol. 11, no. 47, p. 81, 2009.
- [47] J. Nelson, *The physics of solar cells*. UK: Imperial College Press, 2003.
- [48] D. C. Law, R. King, H. Yoon, M. Archer, a. Boca, C. Fetzer, S. Mesropian, T. Ishiki, M. Haddad, and K. Edmondson, "Future technology pathways of terrestrial III-V multijunction solar cells for concentrator photovoltaic systems," *Solar Energy Materials and Solar Cells*, vol. 94, no. 8, p. 1314, 2010.
- [49] J. Müller, B. Rech, J. Springer, and M. Vanecek, "TCO and light trapping in silicon thin film solar cells," *Solar Energy*, vol. 77, no. 6, p. 917, 2004.

- [50] L. Feitknecht, O. Kluth, Y. Ziegler, X. Niquille, P. Torres, J. Meier, N. Wyrsh, and A. Shah, "Microcrystalline n-i-p solar cells deposited at 10 A/ss by VHF-GD," *Solar Energy Materials and Solar Cells*, vol. 66, p. 397, 2001.
- [51] T. Brammer, W. Reetz, N. Senoussaoui, O. Vetterl, O. Kluth, B. Rech, H. Stiebig, and H. Wagner, "Optical properties of silicon-based thin-film solar cells in substrate and superstrate configuration," *Solar Energy Materials and Solar Cells*, vol. 74, p. 469, 2002.
- [52] V. T. Daudrix, J. Guillet, F. Freitas, A. Shah, C. Ballif, P. Winkler, M. Ferrelloc, S. Benagli, X. Niquille, D. Fischer, and R. Morf, "Characterisation of Rough Reflecting Substrates Incorporated Into Thin-film Silicon Solar Cells," *Progress in Photovoltaics: Research and Applications*, p. 485, 2006.
- [53] P. Campbell and M. Keevers, "Light trapping and reflection control for silicon thin films deposited on glass substrates textured by embossing," in *Proceedings of the 28th IEEE Photovoltaics Specialists Conference*, (Alaska), 2000.
- [54] A. V. Shah, M. Vaněček, J. Meier, F. Meillaud, J. Guillet, D. Fischer, C. Droz, X. Niquille, S. Faÿ, E. Vallat-Sauvain, V. Terrazzoni-Daudrix, and J. Bailat, "Basic efficiency limits, recent experimental results and novel light-trapping schemes in a-Si:H,  $\mu$ c-Si:H and 'micromorph tandem' solar cells," *Journal of Non-Crystalline Solids*, vol. 338-340, p. 639, 2004.
- [55] J. Escarré, *Tècniques de confinament òptic en cèl·lules solars sobre substrat plàstic*. PhD thesis, Universitat de Barcelona, 2008.
- [56] M. Ohring, *The materials science of thin films*. USA: Academic Press, 1992.
- [57] J. D. Santos, *Desarrollo y caracterización de dispositivos fotovoltaicos p-i-n de silicio amorfo depositados por PECVD*. PhD thesis, Universidad Complutense de Madrid, 2013.
- [58] P. R. Cabarrocas, J. B. Chevrier, J. Hue, A. Lloret, J. Y. Parey, and J. P. M. Sehmw, "A fully automated hot-wall multiplasma-monochamber reactor for thin film deposition," *Journal of Vacuum Science and Technology A*, vol. 9, p. 2331, 1991.
- [59] S. Guha, J. Yang, A. Banerjee, B. Yan, and K. Lord, "High quality amorphous silicon materials and cells grown with hydrogen dilution," *Solar Energy Materials and Solar Cells*, vol. 78, no. 1-4, p. 329, 2003.
- [60] F. J. Giessibl, "AFM's path to atomic resolution," *Materials Today*, vol. 8, no. 5, p. 32, 2005.
- [61] C. R. Brundle, C. A. Evans, and S. Wilson, *Encyclopedia of materials characterization: surfaces, interfaces, thin films*. USA: Butterworth-Heinemann, 1992.

## Bibliography

- [62] E. J. Mittemeijer and U. Welzel, "The state of the art of the diffraction analysis of crystallite size and lattice strain," *Zeitschrift für Kristallographie*, vol. 223, no. 9, p. 552, 2008.
- [63] T. Roisnel and J. Rodríguez-Carvajal, "WinPLOTR: A windows tool for powder diffraction pattern analysis," in *Materials Science Forum, Proceedings of the Seventh European Powder Diffraction Conference (EPDIC 7)*, p. 118, 2000.
- [64] R. F. Egerton, *Physical principles of electron microscopy*. USA: Springer, 2005.
- [65] F. Rojas, *Análisis microestructural de materiales fotovoltaicos mediante métodos ópticos y microscopia electrónica*. PhD thesis, Universitat de Barcelona, 2014.
- [66] J. F. Moulder, W. F. Stickle, P. E. Sobol, and K. D. Bomben, *Handbook of X-ray photoelectron spectroscopy*. Minnesota: Physical Electronics, Inc., 1992.
- [67] B. F. M. Smits, "Measurement of Sheet Resistivities with the Four-Point Probe," *Bell System Technical Journal*, vol. 37, no. 3, p. 711, 1958.
- [68] G. Haacke, "New figure of merit for transparent conductors," *Journal of Applied Physics*, vol. 47, no. 9, p. 4086, 1976.
- [69] L. Van der Pauw, "A method of measuring the resistivity and hall coefficient on lamellae of arbitrary shape," *Philips Technical Review*, vol. 26, p. 220, 1958.
- [70] P. Carreras, *Doped and multi-compound ZnO-based transparent conducting oxides for silicon thin film solar cells*. PhD thesis, Universitat de Barcelona, 2013.
- [71] J. Loeffler, *Transparent conductive oxides for thin-film silicon solar cells*. PhD thesis, Utrecht University, 2005.
- [72] J. L. Balenzategui, J. Cuenca, I. R. Outon, and F. Chenlo, "Intercomparison and validation of solar cell I-V characteristic measurement procedures," in *Proceedings of the 27th European Photovoltaic Solar Energy Conference and Exhibition*, p. 1471, 2012.
- [73] T. Soderstrom, F. J. Haug, X. Niquille, and C. Ballif, "TCOs for Nip Thin Film Silicon Solar Cells," *Progress in Photovoltaics: Research and Applications*, vol. 17, no. 3, p. 165, 2008.
- [74] E. Yablonovitch and G. D. Cody, "Intensity Enhancement in Textured Optical Sheets for Solar Cells," *Transactions on electron devices*, vol. 29, no. 2, p. 300, 1982.
- [75] E. Yablonovitch, "Statistical ray optics," *Journal of Optical Society of America*, vol. 72, no. 7, p. 899, 1982.
- [76] B. Rech and H. Wagner, "Potential of amorphous silicon for solar cells," *Applied Physics A*, vol. 69, p. 155, 1999.

- [77] M. Despeisse, C. Ballif, a. Feltrin, F. Meillaud, S. Fay, F. Haug, D. Dominé, M. Python, T. Soderstrom, P. Buehlmann, and G. Bugnon, "Research and developments in thin-film silicon photovoltaics," in *Proc. of SPIE*, p. 7409, 2009.
- [78] J. Bailat, R. Domine, D. Schluchter, J. Steinhauser, S. Fay, F. Freitas, C. Bucher, L. Feitknecht, X. Niquille, T. Tschärner, A. Shah, and C. Ballif, "High efficiency p-i-n microcrystalline and micromorph thin film silicon solar cells deposited on LPCVD ZnO coated glass substrates," in *Proceedings of the 24th World Conference on European Photovoltaic Solar Energy Conference on Photovoltaic energy conversion*, p. 1533, 2006.
- [79] S. Benagli, D. Borrello, E. Vallat-Sauvain, J. Meier, U. Kroll, J. Hötzel, J. Bailat, J. Steinhauser, M. Marmelo, G. Monteduro, and L. Castens, "High-efficiency amorphous silicon devices on LPCVD-ZnO TCO prepared in industrial KAI TM-M R&D reactor," *Proceedings of the 24th European Photovoltaic Solar Energy Conference*, p. 2293, 2009.
- [80] R. Franken, *Transparent conducting oxide contacts and textured metal back reflectors for thin film silicon solar cells*. PhD thesis, Utrecht University, 2006.
- [81] P. Bermel, C. Luo, L. Zeng, L. C. Kimerling, and J. D. Joannopoulos, "Improving thin-film crystalline silicon solar cell efficiencies with photonic crystals Abstract ;," *Optics Express*, vol. 15, no. 25, p. 16986, 2007.
- [82] B. Liu and E. S. Aydil, "Growth of Oriented Single-Crystalline Rutile TiO<sub>2</sub> Nanorods on Transparent Conducting Substrates for Dye-Sensitized Solar Cells," *Journal of the American Chemical Society*, vol. 131, no. 9, p. 3985, 2009.
- [83] J. Zhu, C. M. Hsu, Z. Yu, S. Fan, and Y. Cui, "Nanodome solar cells with efficient light management and self-cleaning," *Nano Letters*, vol. 10, p. 1979, 2010.
- [84] C. Battaglia, C. Hsu, K. Soderstrom, J. Escarre, M. Haug F.J, Charriere, M. Boccard, M. Despeisse, D. T. L. Alexander, and M. Cantoni, "Light Trapping in Solar Cells : Can Periodic Beat Random ?," *Acs Nano*, vol. 6, no. 3, p. 2790, 2012.
- [85] C. Haase and H. Stiebig, "Optical properties of thin-film silicon solar cells with grating couplers," *Progress in Photovoltaics: Research and Applications*, vol. 14, no. 7, p. 629, 2006.
- [86] J. Grandidier, D. M. Callahan, J. N. Munday, and H. a. Atwater, "Light absorption enhancement in thin-film solar cells using whispering gallery modes in dielectric nanospheres," *Advanced materials (Deerfield Beach, Fla.)*, vol. 23, no. 10, p. 1272, 2011.
- [87] M. J. Naughton, K. Kempa, Z. F. Ren, Y. Gao, J. Rybczynski, N. Argenti, W. Gao, Y. Wang, Y. Peng, J. R. Naughton, G. McMahon, T. Paudel, Y. C. Lan, M. J. Burns, a. Shepard, M. Clary, C. Ballif, F.-J. Haug, T. Söderström,

## Bibliography

- O. Cubero, and C. Eminian, "Efficient nanocoax-based solar cells," *physica status solidi (RRL) - Rapid Research Letters*, vol. 4, no. 7, p. 181, 2010.
- [88] L. Cao, J. S. White, J.-S. Park, J. a. Schuller, B. M. Clemens, and M. L. Brongersma, "Engineering light absorption in semiconductor nanowire devices.," *Nature materials*, vol. 8, no. 8, p. 643, 2009.
- [89] V. Terrazzoni-daudrix, J. Guillet, X. Niquille, L. Feitknecht, F. Freitas, P. Winkler, A. Shah, R. Mor, and D. Fischer, "Enhanced light trapping in thin film silicon solar cells deposited on PET and glass Fabrication methods," in *3rd World Conference on Photovoltaic Energy Conversion*, p. 1596, 2003.
- [90] H. Stiebig, C. Haase, C. Zahren, B. Rech, and N. Senoussaoui, "Thin-film silicon solar cells with grating couplers. An experimental and numerical study," *Journal of Non-Crystalline Solids*, vol. 352, no. 9-20, p. 1949, 2006.
- [91] Z. Yu, A. Raman, and S. Fan, "Fundamental limit of light trapping in grating structures," *Optics Express*, vol. 18, no. S3, p. 366, 2010.
- [92] A. N. Sprafke and R. B. Wehrspohn, "Light Trapping Concepts for Photon Management in Solar Cells," *Green*, vol. 2, no. 4, p. 177, 2012.
- [93] O. Isabella, A. Campa, M. C. R. Heijna, W. Soppe, R. van Erven, R. H. Franken, H. Borg, and M. Zeman, "Diffraction gratings for light trapping in thin-film silicon solar cells," in *Proc. 23rd European Photovoltaic Solar Energy Conf., Valencia, Spain*,; p. 3AV.1.48., 2008.
- [94] O. Schultz and R. Russel, "Proceedings of the 21st European Photovoltaic Solar Energy Conference Dresden, Germany," in *High-efficiency solar cells with laser-grooved buried contact front and laser-fired rear for industrial production*, p. 2CV.3.17, 2006.
- [95] A. Hauser, G. Hahn, M. Spiegel, H. Feist, O. Breitenstein, J. P. Rakotoniaina, P. Fath, and E. Bucher, "17 European Photovoltaic Solar Energy Conference and Exhibition, Munich, Germany," in *Comparison of different techniques for edge isolation*, p. 1, 2001.
- [96] A. D. Compaan, I. Matulionis, and S. Nakade, "Laser scribing of polycrystalline thin films," *Optics and Lasers in Engineering*, vol. 34, p. 15, 2000.
- [97] A. V. Shah, H. Schade, M. Vanecek, J. Meier, E. Vallat-Sauvain, N. Wyrsh, U. Kroll, C. Droz, and J. Bailat, "Thin-film silicon solar cell technology," *Progress in Photovoltaics: Research and Applications*, vol. 12, no. 23, p. 113, 2004.
- [98] C. Heine and R. H. Morf, "Submicrometer gratings for solar energy applications," *Applied Optics*, vol. 34, no. 14, 1995.

- [99] N. Senoussaoui, M. Krause, J. Müller, E. Bunte, T. Brammer, and H. Stiebig, "Thin-film solar cells with periodic grating coupler," *Thin Solid Films*, vol. 451-452, p. 397, 2004.
- [100] C. Eisele, C. E. Nebel, and M. Stutzmann, "Periodic light coupler gratings in amorphous thin film solar cells," *Journal of Applied Physics*, vol. 89, no. 12, p. 7722, 2001.
- [101] D. Canteli, S. Fernández, J. D. Santos, J. P. González, C. Molpeceres, I. Torres, J. Cárabe, and J. J. Gandía, "Laser texturing of ZnO : Al front contact for efficiency enhancement in thin-film silicon solar cells," in *Poster communication at The European Conference on Lasers and Electro-Optics*, vol. 917, p. 28040, 2013.
- [102] M. A. Contreras, T. Barnes, J. V. D. Lagemaat, G. Rumbles, T. J. Coutts, C. Weeks, P. Glatkowski, I. Levitsky, J. Peltola, and D. A. Britz, "Replacement of Transparent Conductive Oxides by Single-Wall Carbon Nanotubes in Cu ( In , Ga ) Se 2 -Based Solar Cells," *The Journal of Physical Chemistry Letters C*, vol. 111, no. 38, p. 14045, 2007.
- [103] A. G. Aberle, P. I. Widenborg, and N. Chuangsuwanich, "Glass texturing, International PCT patent application WO2004/089841 A1," 2004.
- [104] P. I. Widenborg and A. G. Aberle, "Polycrystalline Silicon Thin-Film Solar Cells on AIT-Textured Glass Superstrates," *Advances in OptoElectronics*, vol. 2007, p. 1, 2007.
- [105] Schott, accessed 19 June 2013. <<http://www.schott.com/>>.
- [106] Menzel-Glaser, accessed 19 June 2013. <<http://www.menzel.de/>>.
- [107] V. Design, accessed 19 June 2013. <<http://www.valleydesign.com/>>.
- [108] C. S. Solanki, *Solar Photovoltaics. Fundamentals, Technologies and Applications*. India: PHI Learning Pvt. Ltd., 2011.
- [109] M. Steinert, J. Acker, S. Oswald, and K. Wetzig, "Study on the Mechanism of Silicon Etching in HNO<sub>3</sub>-Rich HF / HNO<sub>3</sub> Mixtures," *The Journal of Physical Chemistry C*, vol. 111, no. 2, p. 2133, 2007.
- [110] W. V. Gelder and V. E. Hauser, "The Etching of Silicon Nitride in Phosphoric Acid with Silicon Dioxide as a Mask," *Journal of Electrochemistry Society*, vol. 114, no. 8, p. 869, 1967.
- [111] N. Ray, "The action of phosphoric acid on glass," *Journal of Non-Crystalline Solids*, vol. 5, no. 2, p. 71, 1970.

## Bibliography

- [112] N. Chuangsuwanich, P. Campbell, P. Widenborg, a. Straub, and a.G. Aberle, "Light trapping properties of evaporated poly-silicon films on AIT-textured glass substrates," *Conference Record of the Thirty-first IEEE Photovoltaic Specialists Conference, 2005.*, p. 1161.
- [113] J. Wang, S. Venkataraj, C. Battaglia, P. Vayalakkara, and A. G. Aberle, "Analysis of Optical and Morphological Properties of Aluminium Induced Texture Glass Superstrates Analysis of Optical and Morphological Properties of Aluminium Induced Texture Glass Superstrates," *Japanese Journal of Applied Physics*, vol. 51, no. 10, 2012.
- [114] D. M. Mattox, *Handbook of Physical Vapor Deposition (PVD) Processing*. U.S: William Andrew, 2010.
- [115] M. Ohring, "Discharges, Plasmas, and Ion-Surface Interactions," in *Materials Science of Thin Films*, vol. 226, ch. 4, p. 794, Academic Press, Feb. 2001.
- [116] M. J. Madou, *Fundamentals of Microfabrication: The Science of Miniaturization*. U.S: CRC Press, 2002.
- [117] B. N. Chapman, "Thin-film adhesion," *Journal of Vacuum Science and Technology*, vol. 11, no. 1, p. 106, 1974.
- [118] M. Llusà, A. Antony, and J. Bertomeu, "Growth and Properties of ZnO : Al on Textured Glass for Thin Film Solar Cells," *International Journal of Photoenergy*, vol. 2014, p. 10, 2014.
- [119] A. M. Rosa, E. P. da Silva, E. Amorim, M. Chaves, a. C. Catto, P. N. Lisboa-Filho, and J. R. R. Bortoleto, "Growth evolution of ZnO thin films deposited by RF magnetron sputtering," *Journal of Physics: Conference Series*, vol. 370, p. 012020, 2012.
- [120] J. I. Owen, J. Hüpkes, H. Zhu, E. Bunte, and S. E. Pust, "Novel etch process to tune crater size on magnetron sputtered ZnO:Al," *Physica Status Solidi (a)*, vol. 208, no. 1, p. 109, 2011.
- [121] M. Berginski, J. Hüpkes, M. Schulte, G. Schöpe, H. Stiebig, B. Rech, and M. Wuttig, "The effect of front ZnO:Al surface texture and optical transparency on efficient light trapping in silicon thin-film solar cells," *Journal of Applied Physics*, vol. 101, p. 074903, 2007.
- [122] M. Python, O. Madani, D. Dominé, F. Meillaud, E. Vallat-Sauvain, and C. Ballif, "Influence of the substrate geometrical parameters on microcrystalline silicon growth for thin-film solar cells," *Solar Energy Materials and Solar Cells*, vol. 93, no. 10, p. 1714, 2009.

- [123] Y. Yoshino, K. Inoue, M. Takeuchi, K. Ohwada, and M. M. Co, "Effects of interface micro structure in crystallization of ZnO thin films prepared by radio frequency sputtering," *Vacuum*, vol. 51, no. 4, p. 601, 1998.
- [124] N. Sahraei, K. Forberich, S. Venkataraj, A. G. Aberle, and M. Peters, "Analytical solution for haze values of aluminium-induced texture ( AIT ) glass superstrates for a-Si : H solar cells," *Optics Express*, vol. 22, no. S1, p. 53, 2014.
- [125] S. Fernández, O. de Abril, F. Naranjo, and J. Gandía, "High quality textured ZnO:Al surfaces obtained by a two-step wet-chemical etching method for applications in thin film silicon solar cells," *Solar Energy Materials and Solar Cells*, vol. 95, no. 8, p. 2281, 2011.
- [126] J. I. Owen, *Growth, etching and stability of sputtered ZnO:Al for thin film silicon solar cells*. PhD thesis, Forschungszentrum Jülich, 2011.
- [127] M. Llusçà, J. D. Santos, S. Fernández, J. P. González, J. J. Gandía, J. Cárabe, A. Antony, J. M. Asensi, and J. Bertomeu, "Textured glass substrates for thin film silicon solar cells," in *28th European Photovoltaic Solar Energy Conference and Exhibition*, p. 2170, 2013.
- [128] M. Llusçà, L. Morrone, Álvaro Caballero, A. Antony, J. M. Asensi, J. Andreu, and J. Bertomeu, "Growth differences of AZO on different glass textures and their application in thin film silicon solar cells," in *29th European Photovoltaic Solar Energy Conference and Exhibition*, p. 1912, 2014.
- [129] M. Kubon, E. Boehmer, F. Siebke, B. Rech, C. Beneking, and H. Wagner, "Solution of the ZnO/p contact problem in a-Si:H solar cells," *Solar Energy Materials and Solar Cells*, vol. 41-42, p. 485, 1996.
- [130] G. Ganguly, D. E. Carlson, S. S. Hegedus, D. Ryan, R. G. Gordon, D. Pang, and R. C. Reedy, "Improved fill factors in amorphous silicon solar cells on zinc oxide by insertion of a germanium layer to block impurity incorporation," *Applied Physics Letters*, vol. 85, no. 3, p. 479, 2004.
- [131] A. Masuda, K. Imamori, and H. Matsumura, "Influence of atomic hydrogen on transparent conducting oxides during hydrogenated amorphous and microcrystalline Si preparation by catalytic chemical vapor deposition," *Thin Solid Films*, vol. 411, p. 166, 2002.
- [132] M. Balestrieri, *Transparent conductive oxides with photon converting properties in view of photovoltaic applications: the cases of rare earth doped zinc oxide and cerium oxide*. PhD thesis, Université de Strasbourg, 2014.
- [133] W. G. V. Sark, J. D. Wild, J. K. Rath, A. Meijerink, and R. E. I. Schropp, "Upconversion in solar cells," *Nanoscale research letters*, vol. 8, no. 81, p. 1, 2013.



## Bibliography

- [134] W. van Sark, A. Meijerink, R. Schropp, J. van Roosmalen, and E. Lysen, "Enhancing solar cell efficiency by using spectral converters," *Solar Energy Materials and Solar Cells*, vol. 87, no. 1-4, p. 395, 2005.
- [135] H. U. Gu, M. Pollnau, D. R. Gamelin, and S. R. Lu, "Power dependence of up-conversion luminescence in lanthanide and transition-metal-ion systems," *Physical Review B*, vol. 61, no. 5, 2000.
- [136] C. Strumbel, *Application of erbium-doped up-converters to silicon solar cells*. PhD thesis, Universitat Konstanz, 2007.
- [137] N. Bloembergen, "Solid State Infrared quantum Counters," *Physical review letters*, vol. 2, no. 3, 1959.
- [138] F. Auzel, "Upconversion and Anti-Stokes Processes with f and d Ions in Solids," *Chemical reviews*, vol. 104, p. 139, 2004.
- [139] J. de Wild, A. Meijerink, J. K. Rath, W. G. J. H. M. van Sark, and R. E. I. Schropp, "Upconverter solar cells: materials and applications," *Energy & Environmental Science*, vol. 4, no. 12, p. 4835, 2011.
- [140] J. C. G. Pierre Gibart, François Auzel and K. Zahrman, "Below Band-Gap IR Response of Substrate-Free GaAs Solar Cells Using Two-Photon Up-Conversion," *Japanese Journal of Applied Physics*, vol. 35, no. 8, p. 4401, 1996.
- [141] S. Hilderbrand, F. Shao, C. Salthouse, U. Mahmood, and R. Weissleder, "Upconverting luminescent nanomaterials: application to in vivo bioimaging," *Chemical communications (Cambridge, England)*, vol. 28, no. 28, p. 4188, 2009.
- [142] C. W. Thiel, Y. Sun, and R. L. Cone, "Progress in relating rare-earth ion 4f and 5d energy levels to host bands in optical materials for hole burning, quantum information, and phosphors," *Journal of Modern Optics*, vol. 49, no. 14-15, p. 2399, 2002.
- [143] H.-Q. Wang, M. Batentschuk, A. Osvet, L. Pinna, and C. J. Brabec, "Rare-earth ion doped up-conversion materials for photovoltaic applications," *Advanced Materials*, vol. 23, no. 22-23, p. 2675, 2011.
- [144] *International Union of Pure and Applied Chemistry (IUPAC), Nomenclature of Inorganic Chemistry*. Butterworth, London: Vol. Second Edition, 1970.
- [145] M. G. Mayer, "Rare-Earth and Transuranic Elements," *Physical review*, vol. 60, p. 1, 1941.
- [146] G. H. Dieke, "The Spectra of the Doubly and Triply Ionized Rare Earths," *Applied Optics*, vol. 2, no. 7, p. 675, 1963.

- [147] C. W. Thiel, *Energies of rare-earth ion states relative to host bands in optical materials from electron photoemission spectroscopy*. PhD thesis, Montana State University, 2003.
- [148] M. Ishii, T. Ishikawa, T. Ueki, S. Komuro, T. Morikawa, Y. Aoyagi, and H. Oyanagi, "The optically active center and its activation process in Er-doped Si thin film produced by laser ablation," *Journal of Applied Physics*, vol. 85, no. 8, p. 4024, 1999.
- [149] M. Ishii, S. Komuro, T. Morikawa, and Y. Aoyagi, "Local structure analysis of an optically active center in Er-doped ZnO thin film," *Journal of Applied Physics*, vol. 89, no. 7, p. 3679, 2001.
- [150] A. J. Kenyon, "Recent developments in rare-earth doped materials for optoelectronics," *Progress in Quantum Electronics*, vol. 26, no. 4-5, p. 225, 2002.
- [151] Z. Zhou, T. Komaki, A. Koizumi, T. Komori, M. Yoshino, M. Morinaga, Y. Fujiwara, and Y. Takeda, "Photoluminescence around 1.54  $\mu\text{m}$  from Er-containing ZnO at Room Temperature \* 1," *Materials Transactions*, vol. 45, no. 7, p. 2003, 2007.
- [152] J. de Wild, J. Rath, A. Meijerink, W. van Sark, and R. Schropp, "Enhanced near-infrared response of a-Si:H solar cells with  $\beta\text{-NaYF}_4\text{:Yb}^{3+}$  (18%),  $\text{Er}^{3+}$  (2%) upconversion phosphors," *Solar Energy Materials and Solar Cells*, vol. 94, no. 12, p. 2395, 2010.
- [153] B. S. Richards and A. Shalav, "Enhancing the Near Infrared Spectral Response of Silicon Opto-Electronic Devices," in *IEEE Transactions on Electron Devices* 2007 54 (10), vol. 54, p. 2679, 2007.
- [154] M. Liu, Y. Lu, Z. Xie, and G. Chow, "Enhancing near-infrared solar cell response using upconverting transparent ceramics," *Solar Energy Materials and Solar Cells*, vol. 95, no. 2, p. 800, 2011.
- [155] A. Shalav, B. Richards, T. Trupke, R. Corkish, K. Kramer, H. Gudel, and M. Green, "The application of up-converting phosphors for increased solar cell conversion efficiencies," in *Proceedings of the 3rd Conference on Photovoltaic Energy Conversion*, (Osaka, Japan), 2003.
- [156] M. Llusçà, J. López-Vidrier, A. Antony, S. Hernández, B. Garrido, and J. Bertomeu, "Up-conversion effect of Er- and Yb-doped ZnO thin films," *Thin Solid Films*, vol. 562, p. 456, 2014.
- [157] J. Suyver, J. Grimm, K. Krämer, and H. Güdel, "Highly efficient near-infrared to visible up-conversion process in," *Journal of Luminescence*, vol. 114, no. 1, p. 53, 2005.

## Bibliography

- [158] A. Oliveira, M. de Araujo, A. Gouveia Neto, A. Medeiros Neto, A. S. Sombra, and Y. Messaddeq, "Frequency upconversion in Er<sup>3+</sup>/Yb<sup>3+</sup> codoped chalcogenide glass," *Applied Physics Letters*, vol. 72, p. 753, 2002.
- [159] M. Wang, C.-c. Mi, W.-x. Wang, C.-h. Liu, Y.-f. Wu, Z.-r. Xu, B. Mao, and S.-k. Xu, "Immunolabeling and NIR-Excited Fluorescent Imaging of Hela Cells by Using naYf<sub>4</sub>:Yb,Er Upconversion Nanoparticles," *Acs Nano*, vol. 3, no. 6, p. 1580, 2009.
- [160] X. Meng, C. Liu, F. Wu, and J. Li, "Strong up-conversion emissions in ZnO:Er<sup>3+</sup>, ZnO:Er(3+)-Yb<sup>3+</sup> nanoparticles and their surface modified counterparts.," *Journal of colloid and interface science*, vol. 358, no. 2, p. 334, 2011.
- [161] J. F. Philipps, T. Töpfer, E.-H. H. D. Ehrt, and R. Sauerbrey, "Spectroscopic and lasing properties of Er<sup>3+</sup>:Yb<sup>3+</sup>-doped fluoride phosphate glasses," *Applied Physics B*, vol. 72, p. 399, 2001.
- [162] Y. Terai, K. Yamaoka, T. Yamaguchi, and Y. Fujiwara, "Structural and luminescent properties of Er-doped ZnO films grown by metalorganic chemical vapor deposition," *Journal of Vacuum Science & Technology B: Microelectronics and Nanometer Structures*, vol. 27, no. 5, p. 2248, 2009.
- [163] W. Dang, Y. Fu, J. Luo, a.J. Flewitt, and W. Milne, "Deposition and characterization of sputtered ZnO films," *Superlattices and Microstructures*, vol. 42, no. 1-6, p. 89, 2007.
- [164] R. Ondo-Ndong, G. Ferblantier, M. Al Kalfioui, a. Boyer, and a. Foucaran, "Properties of RF magnetron sputtered zinc oxide thin films," *Journal of Crystal Growth*, vol. 255, no. 1-2, p. 130, 2003.
- [165] J. H. Jou, M. Y. Han, and D. J. Cheng, "Substrate dependent internal stress in sputtered zinc oxide thin films," *Journal of Applied Physics*, vol. 71, no. 9, p. 4333, 1992.
- [166] S. Hu, Y. Lee, J. Lee, J. Huang, J. Shen, and W. Water, "The structural and optical properties of ZnO/Si thin films by RTA treatments," *Applied Surface Science*, vol. 254, no. 6, p. 1578, 2008.
- [167] E. M. Bachari, G. Baud, S. B. Amor, and M. Jacquet, "Structural and optical properties of sputtered ZnO films," *Thin Solid Films*, vol. 348, no. 165-172, 1999.
- [168] Y. Chen and X. Xu, "Effect of oxygen deficiency on optical band gap shift in Er-doped ZnO thin films," *Physica B: Condensed Matter*, vol. 406, no. 17, p. 3121, 2011.
- [169] M. N. Islam, T. Ghosh, K. Chopra, and H. Acharya, "XPS and X-ray diffraction studies of aluminum doped zinc oxide transparent conducting films," *Thin Solid Films*, vol. 280, no. 1-2, p. 20, 1996.

- [170] H. Cao, Z. Pei, J. Gong, C. Sun, R. Huang, and L. Wen, "Preparation and characterization of Al and Mn doped ZnO (ZnO (Al, Mn)) transparent conducting oxide films," *Journal of Solid State Chemistry*, vol. 177, no. 4-5, p. 1480, 2004.
- [171] C. Liao and L. Chao, "Growth and Characterization of Er doped ZnO prepared by reactive ion beam sputtering," in *Proceedings of the 3rd International Nanoelectronics Conference*, (Piscataway, N.J), 2010.
- [172] S. Komuro, T. Katsumata, T. Morikawa, X. Zhao, H. Isshiki, and Y. Aoyagi, "Highly erbium doped zinc oxide thin film prepared by laser ablation and its 1.54  $\mu\text{m}$  emission dynamics," *Journal of Applied Physics*, vol. 88, no. 12, p. 7129, 2000.
- [173] M. Chen, X. Wang, Y. H. Yu, Z. L. Pei, X. D. Bai, C. Sun, R. F. Huang, and L. S. Wen, "X-ray photoelectron spectroscopy and auger electron spectroscopy studies of Al-doped ZnO films," *Applied Surface Science*, vol. 158, no. 1-2, p. 134, 2000.
- [174] Y. X. Liu, Y. C. Liu, C. L. Shao, and R. Mu, "Excitonic properties of ZnO nanocrystalline films prepared by oxidation of zinc-implanted silica," *Journal of Physics D: Applied Physics*, vol. 37, no. 21, p. 3025, 2004.
- [175] Y. Chen, Y. Bagnall, H. Koh, K. Park, K. Hiraga, Z. Zhu, and T. Yao, "Plasma assisted molecular beam epitaxy of ZnO on c plane sapphire, growth and characterization," *Journal of Applied Physics*, vol. 84, no. 3912, 1998.
- [176] Z. Pan, S. H. Morgan, A. Ueda, R. Aga, A. Steigerwald, A. B. Hmelo, and R. Mu, "Er-doped ZnO films grown by pulsed e-beam deposition," *Journal of Physics: Condensed Matter*, vol. 19, no. 26, p. 266216, 2007.
- [177] Z. Zhou, T. Komaki, T. Komori, A. Koizumi, M. Yoshino, N. Matsunami, Y. Takeda, and M. Morinaga, "Effects of Nitrogen Irradiation on Photoluminescence around 1.54  $\mu\text{m}$  from Er-containing ZnO," *Materials Transactions*, vol. 45, no. 9, p. 2906, 2004.
- [178] L. Douglas, R. Mundle, R. Konda, C. E. Bonner, A. K. Pradhan, D. R. Sahu, and J.-l. Huang, "Influence of doping rate in Er<sup>3+</sup>: ZnO films on emission characteristics," *Optics letters*, vol. 33, no. 8, p. 815, 2008.
- [179] S. Hinojosa, O. Barbosa-Garcia, M. Meneses Nava, J. Maldonado, E. de la Rosa Cruz, and G. Ramos Ortiz, "Luminescent properties and energy transfer processes of codoped Yb,Er polycrystalline YAG matrix," *Optical Materials*, vol. 27, no. 12, p. 1839, 2005.
- [180] F. Vetrone, J.-C. Boyer, J. a. Capobianco, A. Speghini, and M. Bettinelli, "980 nm excited upconversion in an Er-doped ZnO-TeO<sub>2</sub> glass," *Applied Physics Letters*, vol. 80, no. 10, p. 1752, 2002.
- [181] A. Kanoun, N. Jaba, and A. Brenier, "Time-resolved up-converted luminescence in Er<sup>3+</sup>-doped TeO<sub>2</sub>-ZnO glass," *Optical Materials*, vol. 26, no. 1, p. 79, 2004.

## Bibliography

- [182] L. Yang, X. Wang, Z. Li, P. Liu, F. Liu, S. Ge, F. Song, B. Liu, Y. Shi, and R. Zhang, "(Er, Yb)-co-doped multifunctional ZnO transparent hybrid materials: fabrication, luminescent and magnetic properties," *Journal of Physics D: Applied Physics*, vol. 44, no. 15, p. 155404, 2011.
- [183] Y. Liu, Q. Yang, and C. Xu, "Single-narrow-band red upconversion fluorescence of ZnO nanocrystals codoped with Er and Yb and its achieving mechanism," *Journal of Applied Physics*, vol. 104, no. 6, p. 064701, 2008.
- [184] B. Du Ahn, S. Hoon Oh, C. Hee Lee, G. Hee Kim, H. Jae Kim, and S. Yeol Lee, "Influence of thermal annealing ambient on Ga-doped ZnO thin films," *Journal of Crystal Growth*, vol. 309, no. 2, p. 128, 2007.
- [185] H. Tong, Z. Deng, Z. Liu, C. Huang, J. Huang, H. Lan, C. Wang, and Y. Cao, "Effects of post-annealing on structural, optical and electrical properties of Al-doped ZnO thin films," *Applied Surface Science*, vol. 257, no. 11, p. 4906, 2011.
- [186] B. Zhu, X. Sun, X. Zhao, F. Su, G. Li, X. Wu, J. Wu, R. Wu, and J. Liu, "The effects of substrate temperature on the structure and properties of ZnO films prepared by pulsed laser deposition," *Vacuum*, vol. 82, no. 5, p. 495, 2008.
- [187] S. S. Lin, J. L. Huang, and P. Šajgalik, "The properties of heavily Al-doped ZnO films before and after annealing in the different atmosphere," *Surface and Coatings Technology*, vol. 185, no. 2-3, p. 254, 2004.
- [188] B. J. Jin, S. Im, and S. Y. Lee, "Violet and UV luminescence emitted from ZnO thin films grown on sapphire by pulsed laser deposition," *Thin Solid Films*, vol. 366, p. 107, 2000.
- [189] P. Hsieh, Y. Chen, M. Lee, K. Kao, M. Kao, and M. Houng, "The effects of oxygen concentration on ultraviolet luminescence of ZnO films by sol-gel technology and annealing," *Journal of sol-gel science and technology*, vol. 47, p. 1, 2008.
- [190] C. Klingshirn, "ZnO: from basics towards applications," *Physica Status Solidi B*, vol. 244, no. 9, p. 3027, 2007.

# List of Figures

1.1	Renewable energy share of global electricity production in 2013 [1]. . . .	10
1.2	Schematic structure of a single junction silicon thin film solar cell in a) superstrate configuration ( <i>pin</i> ) and b) substrate configuration ( <i>nip</i> ). . .	13
1.3	The hexagonal wurtzite structure of ZnO. Left: Perspective view perpendicular to the <i>c</i> -axis. Right view: View along the <i>c</i> -axis. reprinted from [18], with permission from Elsevier. . . . .	16
1.4	a) Optical spectra and b) Schematic electronic structure of a typical transparent conducting oxide. Shaded areas denote occupied states. . .	18
1.5	Modified Thornton model for the growth of sputtered ZnO:Al layers. Reprinted from Thin Solid Films [42], with permission from Elsevier. . .	22
1.6	Loss processes in a standard solar cell: (1) lattice thermalisation loss, (2) non-absorbed below band gap photons, (3) recombination loss, (4) and (5) junction and contact voltage losses [45]. . . . .	24
2.1	Processes occurring at the target surface due to the impact of high energy particles [18]. . . . .	30
2.2	Schematic cross section of the magnetron sputtering gun. . . . .	32
2.3	Top view of the ZnO target with the Er <sub>2</sub> O <sub>3</sub> pellet placed on the erosion area. . . . .	34
2.4	Comparison in photoluminescence of ZnO:Er:Yb measured at RT and at LT (-196°C). Excitation source: 325 nm. . . . .	46
2.5	Schematic of the set-up used to measure the LT PL of the samples, excitation source: 325 nm. For short wavelengths detection ( $\lambda < 700$ nm) the BSUV filter and the Color filter were replaced by the long pass filter. . .	47
2.6	Schematic of the set-up used to measure the UC PL of the samples. Excitation source: 980 nm. . . . .	48
2.7	Typical <i>J-V</i> curve of solar cell under illumination [70]. . . . .	50
3.1	Schematic light path in a silicon thin film deposited on a periodic (left) and random (right) textured TCO surface. . . . .	55
3.2	SEM images of two typical TCO structures a) APCVD grown SnO <sub>2</sub> :F (Asahi-U) and b) sputtered and etched ZnO . . . . .	56
3.3	Laser processed patterns (left) and the processing parameters used (right) for the 9 samples. . . . .	59
3.4	Transmittance and reflectance of the as-deposited AZO (500 nm) film. .	60
3.5	Confocal microscope images of the 9 laser textured AZO samples. On the top, 3D confocal images and on the bottom real 2D image. . . . .	61

*List of Figures*

3.6	Confocal microscope image with an overlapped line (left) which indicates the extracted profile (right) of sample 9. . . . .	62
3.7	Schematic of the cross section of the lineal patterned AZO indicating the groove depth ( $h$ ) and the pitch between lines (period). . . . .	63
3.8	Confocal microscope images of the laser textured samples seen through the 20 $\times$ objective (left) and through the 150 $\times$ objective (right). The white labels contain the sample name, the pitch between lines (period) and the peak fluence. . . . .	66
3.9	Diffused transmittance of the 5 linear patterned samples L6, L10, L11, L12, L16 and of Asahi-U. . . . .	67
3.10	Total reflectance of a-Si solar cells deposited on L6, L10, L11, L12, L16, over non-textured glass and over Asahi-U. . . . .	68
3.11	Schematic light path in a silicon thin film deposited on a textured glass surface. . . . .	68
3.12	SEM image recorded at a tilted angle of 60 $^\circ$ of Soda-Lime glass surface after sand blasting at an air pressure of $6 \times 10^5$ Pa. . . . .	69
3.13	AIT process scheme: a) as-deposited Al on glass, b) same sample after annealing and c) resultant glass after etching. . . . .	70
3.14	Reflectance of the Borofloat 33 glass measured on both sides. Higher UV reflectance is seen on the tin side. . . . .	72
3.15	Confocal microscope images of 250 nm evaporated Al on glass a) as-deposited, b) after annealing 20 min and c) after annealing 30 min (time needed for the reaction to occur). The two insets correspond to the samples photographs. . . . .	74
3.16	$\sigma_{rms}$ values estimated from AFM over $15 \times 15 \mu\text{m}^2$ images for different annealing time and Al thickness. . . . .	75
3.17	Haze factor of the resultant glass substrates after applying the AIT method varying the Al thickness and the time of annealing. . . . .	76
3.18	XPS spectrum of the reacted film after the annealing. . . . .	77
3.19	Silicon phosphate spots (whitish colour) formed on the Borofloat 33 glass substrate after etching the reaction products with $\text{H}_3\text{PO}_4$ at 210 $^\circ\text{C}$ . . . . .	77
3.20	XPS spectra of Borofloat 33 glass, the Al film after the reaction, the glass surface after etching with hot $\text{H}_3\text{PO}_4$ and after etching first with hot $\text{H}_3\text{PO}_4$ and then with $\text{HF}:\text{HNO}_3$ . . . . .	78
3.21	SEM images recorded at a tilt angle of 60 $^\circ$ of the different textures achieved by depositing the Al by resistive thermal evaporation. a) Texture E, $\sigma_{rms}=56$ nm, b) Texture E1, $\sigma_{rms}=70$ nm and c) Texture E2, $\sigma_{rms}=90$ nm . . . . .	81
3.22	Haze factor (left) and SEM image (right), of the resultant texture after applying the AIT method on the samples with Al deposited by e-beam evaporation. . . . .	82
3.23	SEM images recorded at a tilt angle of 60 $^\circ$ of the textured glass substrates achieved by sputtering the Al at different powers: a) Texture S1, 60 W. b) Texture S2, 100 W c) Texture S3, 150 W and d) Texture S4, 200 W. . . . .	83

3.24 Haze values of textured glass substrates achieved by sputtering the Al at different dc powers. S1 at 60 W, S2 at 100 W, S3 at 150 W and S4 at 200 W. . . . . 84

3.25 SEM image of textured glass achieved by sputtering the Al at 150 W of rf power. Texture S ( $\sigma_{rms}=145$  nm). . . . . 85

3.26 SEM image of sputtered Al on 600°C substrate. . . . . 85

3.27 SEM image recorded at a tilt angle of 60° of the resultant texture after applying the AIT on the samples with spray deposited Al. . . . . 86

3.28 The AFM image (left) and the SEM micrograph (right) of texture E,  $\sigma_{rms}=56$  nm. . . . . 87

3.29 The AFM image (left) and the SEM image (right) of texture S,  $\sigma_{rms}=145$  nm. . . . . 88

3.30 Haze of texture E and texture S. . . . . 89

3.31 SEM (tilted at 60°) image of AZO3 (1000 nm). . . . . 89

3.32 SEM (tilted at 60°) micrographs of a) texture E, b) E+AZO1 (500 nm), c) E+AZO2 (700 nm), d) E+AZO3 (1000 nm). The  $\sigma_{rms}$  values were obtained from AFM. . . . . 90

3.33 SEM (tilted at 60°) images of a) texture S, b) S+AZO1 (500 nm), c) S+AZO2 (700 nm), d) S+AZO3 (1000 nm). The  $\sigma_{rms}$  values were obtained from AFM images. . . . . 91

3.34 Cross sectional SEM images of AZO3 (1000 nm) deposited on a) smooth glass, b) texture E and c) texture S. . . . . 92

3.35 Cross sectional TEM images of AZO2 (700 nm) deposited on smooth glass and electron diffraction patterns at three different zones. . . . . 94

3.36 Cross sectional TEM images of AZO2 (700 nm) deposited on texture E and electron diffraction patterns at three different zones. . . . . 95

3.37 Cross sectional TEM images of AZO2 (700 nm) deposited on texture S and electron diffraction patterns at three different zones. . . . . 96

3.38 XRD patterns of the AZO films deposited over smooth and textured glasses. 98

3.39 Haze values of the samples a) Texture E, texture E + three different AZO thicknesses and Asahi-U substrate. b) Texture S + three different AZO thicknesses and Asahi-U substrate. . . . . 100

3.40 PSD plots for a) Texture E, E + AZO1, E+AZO2, E+AZO3, and Asahi-U. b) Texture S, S+AZO1, S+AZO2, S+AZO3, and Asahi-U. . . . . 101

3.41 (1-R) spectra for smooth glass, texture E and texture S with AZO3/a-Si:H (200 nm)/Ag (300 nm). . . . . 103

3.42 SEM image of AZO (800 nm) deposited on texture S2. . . . . 104

3.43 SEM images of etched AZO on AIT glass dipping in HCl (0.5% and 2%) solution for 2 and 10 seconds. The two bottom images are non-tilted micrographs. . . . . 105

3.44 Haze values of as-deposited AZO on AIT glass and of the same sample after dipping in HCl (0.5%, 1% and 2%) solution during 2 and 10 seconds. 106

3.45 SEM images and haze factor of etched AZO on smooth glass dipping in HCl (0.5% and 2%) solution during 10 seconds. . . . . 107

3.46 SEM tilted micrographs of texture E1 and E2 with 800 nm thick AZO. . 109



*List of Figures*

3.47	Comparative reflectance curves of the devices deposited on E1, E2, non-textured Borofloat glass and Asahi-U substrate. . . . .	110
3.48	Comparison between the external quantum efficiency curves obtained for the devices on each of the substrates tested. . . . .	111
3.49	$J-V$ curves under AM1.5G illumination for the solar cells deposited on different substrates. . . . .	112
3.50	Comparison between dark $J-V$ curves for a-Si:H solar cells deposited on different substrates. . . . .	113
3.51	Comparative reflectance curves of solar cells fabricated on texture E and texture S, non-textured Borofloat glass and Asahi-U substrate. . . . .	115
3.52	Comparison between the external quantum efficiency curves obtained for the devices on each of the substrates tested. . . . .	116
3.53	$J-V$ curves under AM1.5G illumination for the a-Si:H solar cells deposited on different substrates. . . . .	117
3.54	Left graph corresponds to the haze values of textures S1, S2, S1+AZO, S2+AZO and Asahi-U. The right images correspond to the SEM images of S1+AZO and S2+AZO surfaces. . . . .	118
3.55	Comparative reflectance curves of tandem solar cells fabricated on texture S1 and S2, non-textured Borofloat glass and Asahi-U substrate. . . . .	120
3.56	$J-V$ curves under AM1.5G illumination for the tandem solar cells deposited on different substrates. . . . .	121
4.1	Fraction of the solar spectrum effectively available for current generation in a crystalline silicon absorber after the two main optical losses, namely thermalization and transmission [45]. . . . .	124
4.2	Schematic energy diagrams showing photon adsorption and subsequent downshifting, downconversion and upconversion [45]. . . . .	125
4.3	Fraction of sunlight effectively absorbed by a crystalline silicon device and fraction of the lost energy potentially recovered by UC and DC mechanisms [45]. . . . .	125
4.4	UC mechanisms and their relative efficiencies following Auzel [138]. Excitation or de-excitation are indicated by vertical arrows (red and blue, respectively). Curved black arrows indicate energy transfer and horizontal grey lines are real existing energy levels. . . . .	127
4.5	Scheme of the different energy transfer mechanisms between two ions. S is the sensitizer (the ion donating energy) and A is the activator (the ion accepting energy) [138]. . . . .	128
4.6	Energy level scheme of 4f states of trivalent lanthanides in $\text{LaCl}_3$ [146]. . . . .	129
4.7	$C_{4v}$ point symmetry of six-fold coordinated $\text{Er}^{3+}$ ion [150]. . . . .	131
4.8	Generic scheme of Er/Yb energy transfer; full vertical arrows represent the radiative decay, the dashed ones depict upconversion processes and the curly lines indicate multi-phonon relaxation. Energy transfer processes are sketched by Yb-to-Er solid arrows. Russel-Saunders $^{(2S+1)}L_J$ notation was employed to refer to the f states: spin ( $S$ ), orbital ( $L$ ) and angular momentum ( $J$ ) quantum numbers. . . . .	133

4.9 Upconversion spectra of the Er<sub>2</sub>O<sub>3</sub> pellet under 980 nm laser illumination. 134

4.10 XRD patterns and average grain size and *c*-parameter values of 200 nm of ZnO:Er thin films with different Er content and deposited at different substrate temperatures. . . . . 136

4.11 Optical band gap energies deduced from the plot of  $(\alpha h\nu)^2$  against  $h\nu$ . . 137

4.12 XRD patterns and average grain size and *c*-parameter values of 200 nm of post-annealed (PA) ZnO:Er thin films deposited with 1 and 3 Er pellets and at different substrate temperatures. . . . . 139

4.13 Low temperature PL intensity of post-annealed ZnO:Er thin films deposited with 1 and 3 Er pellets at different substrate temperatures. Excitation source: 325-nm line from a He-Cd laser. . . . . 140

4.14 RT PL intensity of 800 nm thick ZnO:Er post-annealed in air atmosphere and under oxygen flow. Excitation wavelength: 355 nm. The inset is a scheme of trivalent Er energy transitions. . . . . 141

4.15 XRD patterns plotted on a logarithmic scale of the as-deposited and annealed films: (a) EZO and EZOA, (b) EYZO and EYZOA, and (c) OEYZO and OEYZOA. The peaks that appear in all samples at  $2\theta=31.05^\circ$  and  $2\theta=37.42^\circ$  correspond to instrumental artifacts. . . . . 144

4.16 XPS O 1s peak Gaussian deconvolution for (a) EZO, (b) EZOA, (c) EYZO, (d) EYZOA, (e) OEYZO and (f) OEYZOA. Black points indicate XPS spectra and red line represents the fitted function. . . . . 147

4.17 Transmittance of EZO, EZOA, EYZO, EYZOA, OEYZO and OEYZOA. The inset table contains the integrated transmittance values in the range 400-800 nm. . . . . 149

4.18 RT PL spectra of the different samples considered for the present study. The 325-nm line from a He-Cd laser was employed to excite the samples, being the PL emission acquired in the near-UV and visible ranges. Open symbols indicate as-deposited samples, whereas continuous lines account for the annealed ones. . . . . 150

4.19 (a) Upconversion PL spectra of the samples under study. 980 nm was selected as the excitation wavelength, and resulting PL spectra were acquired through the visible range. The observed peaks belong to the  $^4F_9/2 \rightarrow ^4I_{15/2}$  Er transition. (b) Upconversion spectra displayed in (a), corrected taking into account the total rare-earth (Er and Yb) atomic concentration for each sample. Open symbols indicate as-deposited samples, whereas full symbols account for the annealed ones. . . . . 153

4.20 X-ray diffraction patterns of as-deposited (AS DEP) ZnO:Er:Yb and that of films annealed in air (AIR), vacuum (VAC) and laser-annealed at three different laser powers (LAS1, LAS2, LAS3). . . . . 157

4.21 Transmittance spectra for the as-deposited ZnO:Er:Yb, the air- and vacuum-annealed samples and the three laser-annealed ones. The inset table contains the integrated transmittance values in the range 400-800 nm. . . . . 159

*List of Figures*

4.22	Photoluminescence spectra corresponding to the as-deposited sample as well as the vacuum-, air- and laser-annealed ones, under 325-nm laser excitation. The spectra were acquired at -196°C. The inset displays the 980 nm PL emission. . . . .	162
4.23	Upconversion PL spectra in logarithmic scale of the as-deposited sample, the air-annealed, the vacuum-annealed and the three laser-annealed samples. 980 nm was used as the excitation wavelength. . . . .	163
4.24	On the left, image of the laser treated 10×10 cm <sup>2</sup> ZnO:Er:Yb sample and the right table contains a summary with the name of the samples and the process parameters for the laser annealing. . . . .	164
4.25	Confocal microscope images of samples 5A, 6A, 7A and 12A taken with an objective 20× (left images) and 150× (right images). . . . .	166
4.26	Profile taken from the confocal image of sample 7A with 150× objective. The inset is the confocal image and the black line indicates the profile. . . . .	167
4.27	The top image contains a <i>Rs</i> map of the 10 ×10 cm <sup>2</sup> as-deposited samples. The bottom graph is the plot of $\Delta Rs/Rs$ where $\Delta Rs=Rs$ before – <i>Rs</i> after the laser annealing. . . . .	168
4.28	UC PL in logarithmic scale of the as-deposited, air annealed and laser annealed samples 5A, 6A, 7A, 12A and 16A. Laser excitation at 980 nm. . . . .	169
4.29	Image of the sample with the corresponding irradiated areas. The right table contains a summary with the name of the samples and the process parameters for the laser annealing. . . . .	171
4.30	Confocal microscope images from all the laser treated ZnO:Er:Yb samples and the as-deposited one. . . . .	172
4.31	SEM images of samples 13B, 14B and 15B. . . . .	173
4.32	X-ray diffraction patterns in logarithmic scale of all the laser treated samples along with the as-deposited (4B) and the air annealed sample. . . . .	174
4.33	X-ray diffraction patterns in logarithmic scale of the as-deposited sample, the air annealed sample and the laser annealed 6B, with the 2θ values from 20.75° on the left and from 31° to 37° on the right. . . . .	175
4.34	X-ray diffraction patterns grouped according to the laser parameters and plotted together with the as-deposited sample and the air annealed sample. . . . .	177
4.35	Conventional PL recorded at -196°C of the laser treated ZnO:Er:Yb samples, the air annealed sample and the as-deposited one in the range a) 340-480 nm, b) 600-700 nm in the left graph and its zoomed portion in the right graph and c) 800-1100 nm in the left graph and its zoomed portion in the right graph. Laser source: 325 nm. . . . .	179
4.36	Upconversion PL of the laser treated ZnO:Er:Yb samples, the air annealed sample and the as-deposited one. Laser source: 980 nm. . . . .	180
5.1	SEM micrographs of two textured glass surfaces. Left: texture achieved by depositing the Al by evaporation. Right: texture achieved by depositing the Al by sputtering. . . . .	187

# List of Tables

2.1	Targets and pellets classified by chapters. Chapter 3: Al films as a part of the Aluminium Induced Texturing method to texture glass substrates and AZO films as front TCOs over the textured surfaces. Chapter 4: Targets and pellets used to create transparent and conducting upconverters. . . . .	33
2.2	Lasers used for the sample treatments and their characteristics classified by chapters. In Chapter 3 the laser was used to texture the ZnO:Al films and in Chapter 4 it was employed to annealed the rare earth doped ZnO samples. . . . .	37
3.1	Roughness $\sigma_{rms}$ , groove depth ( $h$ ), integrated transmittance ( $T$ ) in the range 400-800 nm, haze at 600 nm, horizontal sheet resistance ( $Rsh$ ) and vertical sheet resistance ( $Rsv$ ) of the 9 laser textured samples with that of Asahi-U glass. . . . .	62
3.2	Sample names with the corresponding power, peak fluence and period used to create the lineal patterns on AZO (1000 nm) film. . . . .	64
3.3	Roughness $\sigma_{rms}$ , groove depth ( $h$ ), integrated transmittance ( $T$ ) in the range 400-800 nm, haze at 600 and sheet resistance ( $Rs$ ) of the 5 samples and Asahi-U glass. . . . .	65
3.4	Schott Borofloat 33, Corning 1737F, and Soda-Lime glass properties (1 mm thick). . . . .	71
3.5	Sample names, type of substrate and AZO thickness of the samples studied in this section (Sec. 3.3.2). Texture E was obtained from evaporated Al and texture S from the sputtered Al. . . . .	87
3.6	Surface roughness ( $\sigma_{rms}$ ), resistivity ( $\rho$ ), sheet resistance ( $Rs$ ), integrated transmittance ( $T$ ) in the range 400-800 nm, haze at 600 nm, and figure of merit values ( $\Phi$ ) of the AZO layers deposited on smooth and textured glass along with that of Asahi-U substrate. . . . .	99
3.7	Average solar cell parameters values under AM1.5G illumination for the cells on different substrates. . . . .	112
3.8	Average solar cell parameters values under AM1.5G illumination for the cells on different substrates. . . . .	117
3.9	Surface roughness ( $\sigma_{rms}$ ), Sheet resistance ( $Rs$ ), Integrated transmittance $T$ (400-800 nm), Haze at 600 nm of the AZO layers deposited on smooth and textured glass along with that of Asahi-U substrate. . . . .	119
3.10	Average solar cell parameters values under AM1.5G illumination for the cells on different substrates. . . . .	121

*List of Tables*

4.1	Electrical resistivity of the films. . . . .	138
4.2	Sample names with the corresponding description: material of the film, thickness, sputtering conditions and post-annealing treatment. . . . .	142
4.3	Average crystallite size and lattice parameter values obtained from XRD measurements. *The peak corresponding to the (102) planes reflection did not appear in the ZO diffraction pattern. . . . .	145
4.4	Atomic concentration of Er and Yb in the as-deposited EZO, EYZO and OEYZO films, estimated from the XPS data analysis. . . . .	146
4.5	Resistivity ( $\rho$ ), carrier concentration ( $n$ ), mobility ( $\mu$ ) and optical band gap ( $E_g$ ) of the as-deposited and annealed films. . . . .	148
4.6	Samples name with the post-annealing description. . . . .	156
4.7	Values of the $c$ -parameter for the as-deposited, air annealed, vacuum annealed films and the films irradiated with three different laser powers. . . . .	158
4.8	Values of lattice parameters for the as-deposited, air annealed, vacuum annealed films and the 15 samples irradiated with at different laser parameters. . . . .	176
4.9	Values of the $R_s$ and the integrated $T$ in the range 400-1100 nm of the sixteen samples. . . . .	178

# List of symbols, acronyms and abbreviations

## List of symbols

### Latin alphabet

$A$ .....	Absorptance
$a$ .....	Lattice parameter
$B$ .....	Magnetic field
$a - Si : H$ .....	Hydrogenated amorphous silicon
$c$ .....	Lattice parameter; speed of light
$^{\circ}C$ .....	Degrees Celsius
$c - Si : H$ .....	Hydrogenated crystalline Silicon
$d$ .....	Distance between (hkl) lattice planes, film thickness, period size
$D$ .....	Grain size
$e$ .....	Microstrain
$Eff$ .....	Energy conversion efficiency
$E_g$ .....	Band gap energy
$E_v$ .....	Valence band energy
$h$ .....	Planck's constant, groove depth

*Symbols, acronyms and abbreviations*

$I$ .....	Electric current
$i - type$ .....	intrinsic (not doped)
$J$ .....	Current density, total angular momentum
$J_0$ .....	Saturation current density
$J_{mp}$ .....	Maximum power current density
$J_{sc}$ .....	Short circuit current density
$k_B$ .....	Boltzmann constant
$L$ .....	Total orbital angular momentum
$m^*$ .....	Effective mass
$n$ .....	Carrier concentration, refractive index, number of electrons
$m$ .....	Diffraction order
$n - type$ .....	Negatively doped
$p$ .....	Pressure
$P$ .....	Power
$P_0$ .....	Power density of incident light
$p - type$ .....	Positively doped
$pm - Si : H$ .....	Polymorphous hydrogenated silicon
$q_e$ .....	Fundamental electrical charge
$R$ .....	Reflectance
$R_{OC}$ .....	Parallel resistance

$R_s$ .....	Sheet resistance
$R_{sh}$ .....	Sheet resistance horizontal
$R_{sv}$ .....	Sheet resistance vertical
$R_{SC}$ .....	Series resistance
$S$ .....	Total spin angular momentum
$T$ .....	Transmittance; temperature
$T_d$ .....	Difussed Transmittance
$V$ .....	Voltage
$V_H$ .....	Hall Voltage
$V_{mp}$ .....	Maximum power voltage
$V_{oc}$ .....	Open circuit voltage
$W$ .....	Watt

**Greek alphabet**

$\alpha$ .....	Absorption coefficient
$\beta$ .....	Breadth
$\beta_G$ .....	Gaussian breadth
$\beta_L$ .....	Lorentzian breadth
$\Delta E_{BM}$ .....	Burstein-Moss band gap broadening
$\epsilon_0$ .....	Vacuum permittivity
$\epsilon$ .....	Relative permittivity



*Symbols, acronyms and abbreviations*

$\Phi$ .....	Figure of Merit
$\Phi_{sp}$ .....	Spectrophotometer workfunction
$\theta$ .....	Angle
$\lambda$ .....	Wavelength
$\mu$ .....	Mobility
$\mu c - Si : H$ .....	Hydrogenated crystalline Silicon
$\nu$ .....	Frequency
$\rho$ .....	Resistivity
$\sigma$ .....	Conductivity, Particle diameter
$\sigma_{rms}$ .....	Root mean square roughness
$\tau$ .....	Lifetime
$\omega$ .....	Angular frequency
$\omega_p$ .....	Plasma frequency

**List of acronyms**

<i>AFM</i> .....	Atomic Force Microscopy
<i>AIT</i> .....	Aluminium Induced Texturing
<i>AM1.5G</i> .....	Solar spectrum at an air mass of 1.5
<i>APCVD</i> .....	Atmospheric Pressure Chemical Vapour Deposition
<i>APTE</i> .....	<i>Addition de Photon par Transferts d'Energie</i>
<i>AZO</i> .....	Aluminium doped ZnO

<i>BBR</i> .....	Band to Band Recombination
<i>BE</i> .....	Binding Energy
<i>BVE</i> .....	Broad Visible Emission
<i>CCD</i> .....	Charge Coupled Device
<i>CCiT</i> .....	Centres Científics i Tecnològics
<i>CIEMAT</i> ...	Centro de Investigaciones Energéticas, Medioambientales y Tecnológicas
<i>CW</i> .....	Continuous Wave
<i>dc</i> .....	Direct Current
<i>DC</i> .....	Downconversion
<i>DPSS</i> .....	Diode pump solid state
<i>DS</i> .....	Downshifting
<i>EQE</i> .....	External Quantum Efficiency
<i>ESA</i> .....	Excited State Absorption
<i>ETU</i> .....	Energy Transfer Upconversion
<i>FF</i> .....	Fill Factor
<i>FIB</i> .....	Focus Ion beam
<i>FTO</i> .....	Fluorine doped Tin oxide
<i>FWHM</i> .....	Full Width at Half Maximum
<i>GES</i> .....	Grup d'Energia Solar
<i>GSA</i> .....	Grown State Absorption

*Symbols, acronyms and abbreviations*

<i>ITO</i> .....	Indium Tin Oxide ( $\text{In}_2\text{O}_3:\text{SnO}_2$ )
<i>J - V</i> .....	Current-voltage characteristics
<i>JCPDS</i> .....	Joint Committee on Powder Diffraction Standards
<i>KE</i> .....	Kinetic Energy
<i>LPCVD</i> .....	Low Pressure Chemical Vapour Deposition
<i>LT</i> .....	Low Temperature
<i>NIR</i> .....	Near InfraRed
<i>OPO</i> .....	Optic Parametric Oscillator
<i>PECVD</i> .....	Plasma Enhanced Chemical Vapour Deposition
<i>PET</i> .....	Polyethylene Terephthalate
<i>PL</i> .....	Photoluminescence
<i>PMT</i> .....	Photomultiplier Tube
<i>PSD</i> .....	Power Spectral Density
<i>PV</i> .....	Photovoltaics
<i>RE</i> .....	Rare Earth
<i>rf</i> .....	Radio Frequency
<i>RT</i> .....	Room Temperature
<i>S - Q</i> .....	Shockley-Queisser
<i>SEM</i> .....	Scanning Electron Microscopy
<i>SR</i> .....	Spectral Response

<i>TCO</i> .....	Transparent Conducting Oxide
<i>TEM</i> .....	Transmission Electron Microscopy
<i>UB</i> .....	Universitat de Barcelona
<i>UC</i> .....	Upconversion
<i>UPM</i> .....	Universidad Politécnica de Madrid
<i>UV</i> .....	UltraViolet
<i>VIS</i> .....	Visible
<i>XPS</i> .....	X-ray Photoelectron Spectroscopy
<i>XRD</i> .....	X-ray Diffraction

## List of abbreviations

<i>at.</i> .....	Atomic
<i>et.al</i> .....	From latin, <i>et alii</i> (and others)
<i>Eq.</i> .....	Equation
<i>Fig.</i> .....	Figure
<i>i.e.</i> .....	From latin, <i>id est</i> (that is)
<i>min.</i> .....	Minutes
<i>Sec.</i> .....	Section
<i>vol.</i> .....	Volume
<i>wt.</i> .....	Weight



# Curriculum Vitae

## Personal Data

Name: **Marta Llusçà Jané**  
Date of Birth: November 20, 1983 (Barcelona, Catalunya)  
Nationality: Spain  
Cell Phone: (0034) 655 395 350  
e-mail: martallusca@gmail.com

## Academic Background

- 2011-2015      **Physics Ph.D.** (Solar Energy Group, Universitat de Barcelona): *Novel light management techniques for thin film solar cells: Nano textured substrates and transparent conducting upconverters*. Directed by Joan Bertomeu and Aldrin Antony.
- 2010            **Master's Degree in Physical Engineering** (Universitat de Barcelona): Master project on photovoltaic: *Transparent and conducting ZnO:Er for a-silicon solar cells*.
- 2010            **BSC Physics** (Universitat de Barcelona).  
Course 2007-2008. Exchange student in Physics at Uppsala Universitet, Uppsala, Sweden. Grant: Socrates/Erasmus.
- 2009            Mathematics teaching certificate CAP (equivalent to the English PGCE), Universitat de Barcelona.

## Professional Background

## *Curriculum Vitae*

- September 2009 - December 2010 Internship at Seismic Risk Department of the Geological Institute of Catalonia (IGC), Barcelona.
- August 2009 - September 2009 Research internship at Helmholtz Institute of Berlin (HMB), Germany. Investigation of the influence of Na incorporation in CIGS (Cu (In, Ga) Se<sup>2</sup>) solar cells grown on Titanium substrates. Supervisor: Melanie Nichterwitz.
- June 2009 - July 2009 Research internship at the Institute of Materials Science of Barcelona (ICMAB). Optimization and characterization of Indium-Tin-Oxide thin films deposited by means of sputtering on silicon and glass substrates. Supervisor: Gervasi Herranz.

### **Experimental Skills**

- Vacuum Technology: Working experience with Ultra-High Vacuum thin film deposition equipment in Clean Room environment (sputtering, thermal evaporation).
- Optical and Structural Characterisation: UV/VIS/NIR Spectrophotometer, SEM, TEM, XRD, AFM, XPS, and PL.
- Electrical Characterisation: Hall effect measurements, Four point probe, solar cells characterisation.

### **Language Skills**

- Catalan: Native language.
- Spanish: Native language.
- English: Fluent.
- French: Basic.

## Scientific publications

- Growth differences of AZO on different glass textures and their application in thin film solar cells. Proceedings of 29th European Photovoltaic Solar Energy Conference and Exhibition (2014) 1912 -1916. M. Llusçà, L. Morrone, A. Caballero, A. Antony, J.M. Asensi, J. Andreu, J. Bertomeu.
- Graded index at the TCO/p interface for silicon thin film solar cells using Nb doped TiO<sub>2</sub> Proceedings of the 29th European Photovoltaic Solar Energy Conference and Exhibition, (2014) 1941-1943. A. Antony, M. Llusçà, F. Rojas Tarazona, L. Morrone, A. Caballero, J.M. Asensi, J. Andreu, J. Bertomeu.
- Growth and properties of ZnO:Al on textured glass for thin film silicon solar cells. M. Llusçà, Aldrin Antony and Joan Bertomeu. Journal of Photoenergy (2014) <http://dx.doi.org/10.1155/2014/406495>.
- New strategies in laser processing of TCOs for light management improvement in thin-film silicon solar cells. S. Lauzurica, M. Llusçà, D. Canteli, M.I. Sánchez-Aniorte, J. López-Vidrier, S. Hernández, J. Bertomeu, C. Molpeceres. Proceedings SPIE 9180, Laser Processing and Fabrication for Solar, Displays, and Optoelectronic Devices III, 918006 (October 8, 2014); <http://dx.doi.org/10.1117/12.2061712>.
- Textured Glass Substrates for Thin Film Silicon Solar Cells. M. Llusçà, J.D. Santos, S. Fernández, J.P. González, J.J. Gandía, J. Cárabe, A. Antony, J.M. Asensi, J. Bertomeu. Proceedings of 28th European Photovoltaic Solar Energy Conference and Exhibition (2013) 2170-2174.
- Up-conversion effect of Er- and Yb-doped ZnO thin films. M. Llusçà, J. López-Vidrier, A. Antony, S. Hernández, B. Garrido and J. Bertomeu. Thin Solid Films (2014) <http://dx.doi.org/10.1016/j.tsf.2014.03.078>.



**Presentations at conferences**

- EUPVSEC 29th European PV Solar Energy Conference and Exhibition Poster presentation: Growth differences of AZO on different glass textures and their application in microcrystalline silicon solar cells. M. Llusçà, L. Morrone, A. Caballero, A. Antony, J.M. Asensi, J. Andreu, J. Bertomeu.
- SPIE Optics + Photonics 2014, 17th-21st August 2014, San Diego Convention Center, San Diego, California, United States. Invited talk: New strategies in laser processing of TCOs for light management improvement in thin-film silicon solar cells. S. Lauzurica, M. Llusçà, D. Canteli, M.I. Sánchez-Aniorte, J. López-Vidrier, S. Hernández, J. Bertomeu, C. Molpeceres.
- E-MRS spring meeting 2014, Lille, France Poster presentation: Influence of annealing methods on the properties of ZnO:Er:Yb up-converters. M. Llusçà, J. López-Vidrier, I. Sánchez, A. Antony, S. Lauzurica, C. Molpeceres, S. Hernandez, B. Garrido, J. Bertomeu.
- ALBA synchrotron, new instrumentation for Nanoscience and Molecular Materials Characterization, 14th-15th November 2013. ALBA Synchrotron, Cerdanyola del Vallès, Barcelona, Spain. Poster presentation: Photoluminescence emission in transparent ZnO:Er thin films for a-Si solar cells. M. Llusçà, A. Antony, J. Bertomeu.
- EUPVSEC 28th European PV Solar Energy Conference and Exhibition. September 29th-4th October 2013, Parc des Expositions Paris Nord Villepinte, Paris, France. Oral presentation: Textured glass substrates for thin film silicon solar cells. M. Llusçà, J.D. Santos, S. Fernández, J.P. González, J. J. Gandía, J. Cárabe, A. Antony, J.M. Asensi, J. Bertomeu.
- Workshop on pulsed laser deposition and sputtering. 24th-25th January 2013. Institut de Ciència dels Materials de Barcelona (ICMAB) Barcelona, Spain. Oral presentation: Transparent conducting ZnO:Er thin films for a-Si solar cells. M. Llusçà, A. Antony, J. Bertomeu.

- 2nd International conference on Optoelectronic Materials and Thin films for Advanced Technology (OMTAT 2013), 3rd-5th January, 2013, Kochi, Índia. Invited talk: Novel Approaches for the light absorption enhancement in Silicon thin film Solar cells. A. Antony, M. Llusà, J. Bertomeu.
- XXVII Trobades científiques de la mediterrània: Energies Renovables i Emmagatzematge d'Energia, September 29th-1st October 2011 Maó, Menorca, Spain. Oral Presentation: Capes conductores i transparents de ZnO dopat amb Er per a cèl·lules solars de silici amorf. M. Llusà, A. Antony, J. Bertomeu.
- E-MRS fall meeting 2011, Warsaw University of Technology, Poland  
Poster presentation: Transparent and conducting ZnO: Er thin films deposited by rf magnetron sputtering. M. Llusà, A. Antony, J. Bertomeu.



# Acknowledgements

Doncs ara sí que ja he arribat al final, al final de 4 anys de recerca al Grup d'Energia Solar de la Universitat de Barcelona acompanyada de persones fantàstiques que han fet immillorable el llarg camí que és fer una tesi.

En primer lloc voldria donar les gràcies al Dr. Joan Bertomeu per haver-me brindat l'oportunitat de realitzar un doctorat sota la seva supervisió, gràcies Joan per haver confiat en mi i per el teu suport i disponibilitat en tot moment. Also many thanks to Dr. Aldrin Antony for his many explanations, ideas, advices and corrections, it has been a pleasure work under your supervision. Gràcies també als dos directors del departament de Física Aplicada i Òptica i a tots els professors, especialment al Dr. Arturo Lousa i al Dr. Joan Esteve per iniciar-me en el món de la recerca amb l'assignatura del Laboratori Avançat de Física.

També vull donar les gràcies a tots els companys del Grup d'Energia Solar i del departament, que bé que m'ho he passat amb vosaltres! cafès, cerveses, congressos, sopars, xerrades pels passadissos, calçotades... realment heu fet que el meu pas pel departament fos increïble! En especial vull agrair a la meva ex-companya de despatx i amiga Paz la seva ajuda incondicional i sobretot la infinitat de moments memorables! Tambien a Álvaro y a Luigi, que paciencia que tenéis antes de que dé una charla! i com no, a la resta de companys que han passat en un moment o altre pel departament com la Leyre, el Paolo, l'Oriol, el Jofre, l'Eric, l'Arevik, la Laura, el Francesc, el Camilo, el Jorge, el Shazad... y a Fredy que además ha realizado las imágenes de TEM de esta tesis.

Aquesta feina no hagués estat possible sense la col·laboració de l'equip de Secretaria ni tampoc sense tot el personal del Serveis Científicotècnics de la UB, especialment al Dr. Lorenzo Calvo de XPS, al Dr. Xavier Alcobé de XRD i al Dr. Tariq Jawhari de les mesures de fotoluminescència. També gràcies a la Judith Linacero del la Plataforma de Nanotecnologia del Parc Científic de Barcelona per les imatges amb el SEM.

Una part d'aquesta tesi ha estat realitzada en col·laboració amb al-

## *Acknowledgements*

tres grups i altres centres de recerca, es per això que vull agrair al Dr. Sergi Hernández i al Julià Lòpez del grup de MIND del Departament d'Electrònica la seva disponibilitat per a realitzar mesures, la seva gran ajuda, i les seves explicacions. Tambien agradecer al CIEMAT por el depósito de las células solares y por impulsarme a dar una charla en el EU-PVSEC. Gracias Dr. José Domingo y gracias Dr. Julio Cárabe. Quiero también mencionar las numerosas colaboraciones con el Centro Láser de la UPM, Dr. Carlos Molpeceres, Dra. Isabel Sanchez, Dra. Sara Lauzurica y David canteli, ha sido un placer trabajar con vosotros.

També vull donar les gràcies a totes aquelles persones que m'han acompanyat durant aquest període fora de la Universitat, a les meves estimades amigues, Mònica, Adri, Alba, Irene i Elena. Quantes coses que hem viscut aquests 4 anys! viatges, festes, casaments, naixements, tesis... gràcies per ser com sou!

I sobretot agrair el suport incondicional de la meva família. Papes, això no hagués estat possible sense vosaltres, gràcies per haver confiat en mi i per tots els vostres consells tan savis. Gràcies també a la Ores i al Jorx, a l'Olga i la Sílvia, a la Paula i l'Àlex i sobretot a la iaia Olga, l'avi Ramon i al iaio Pepitu. Però realment, la persona que ha patit la tesi més que ningú ha sigut la meva parella Gerard, estic segura que ja saps que és l'upconversion, el sputtering i l'erbiium jaja! Gràcies per tot Gerard, per escoltar-me, per aconsellar-me, per cuidar-me tant i perquè amb tu he passat les millors estones d'aquests 4 anys. Gràcies. I ja per últim m'agradaria dedicar aquesta tesi a la iaia Cuca, que de ben segur estaria molt orgullosa de veure-la acabada.